1. Report No.	2. Government Accession No.	3. Recipient's Catalog No.
NASA TN D-7907		

4. Title and Subtitle	5. Report Date
EFFECTS OF SPANWISE BLOWING ON THE PRESSURE FIELD AND VORTEX-LIFT CHARACTERISTICS OF A 44° SWEPT TRAPEZOIDAL WING	June 1975
	6. Performing Organization Code

7. Author(s)	8. Performing Organization Report No.
James F. Campbell	L-10047
	10. Work Unit No.
	505-06-14-01

9. Performing Organization Name and Address	11. Contract or Grant No.
NASA Langley Research Center Hampton, Va. 23665	
	13. Type of Report and Period Covered
	Technical Note

12. Sponsoring Agency Name and Address	14. Sponsoring Agency Code
National Aeronautics and Space Administration Washington, D.C. 20546	

15. Supplementary Notes

16. Abstract

The present investigation was conducted to measure the effects of spanwise blowing on the surface pressures of a 44° swept trapezoidal wing. Wind-tunnel data were obtained at a free-stream Mach number of 0.26 for a range of model angle of attack, jet thrust coefficient, and jet location. Results of this study showed that the sectional effects of spanwise blowing were strongly dependent on angle of attack, jet thrust coefficient, and span location; the largest effects occurred at the highest angles of attack and thrust coefficients and on the inboard portion of the wing. Full vortex lift was achieved at the inboard span station with a small blowing rate, but successively higher blowing rates were necessary to achieve full vortex lift at increased span distances. Spanwise blowing increased lift throughout the angle-of-attack range, delayed wing stall to higher angles of attack, and improved the induced-drag polars. The leading-edge suction analogy can be used to estimate the section and total lifts resulting from spanwise blowing.

17. Key Words (Suggested by Author(s))

Spanwise blowing
Vortex lift
Pressure distributions

18. Distribution Statement

Unclassified – Unlimited

New Subject Category 02

EFFECTS OF SPANWISE BLOWING ON THE PRESSURE FIELD AND VORTEX-LIFT CHARACTERISTICS OF A 44° SWEPT TRAPEZOIDAL WING

James F. Campbell
Langley Research Center

SUMMARY

The present investigation was conducted to measure the effects of spanwise blowing on the surface pressures of a 44° swept trapezoidal wing. Wind-tunnel data were obtained at a free-stream Mach number of 0.26 for a range of model angle of attack, jet thrust coefficient, and jet location. Results of this study showed that the sectional effects of spanwise blowing were strongly dependent on angle of attack, jet thrust coefficient, and span location; the largest effects occurred at the highest angles of attack and thrust coefficients and on the inboard portion of the wing. Full vortex lift was achieved at the inboard span station with a small blowing rate, but successively higher blowing rates were necessary to achieve full vortex lift at increased span distances. Spanwise blowing increased lift throughout the angle-of-attack range, delayed wing stall to higher angles of attack, and improved the induced-drag polars. The leading-edge suction analogy can be used to estimate the section and total lifts resulting from spanwise blowing.

INTRODUCTION

On thin, highly swept wings at moderate to high angles of attack, the flow is characterized by a leading-edge separation which forms a stable vortex over the wing and provides large vortex-lift increments. This characteristic of slender wings for supersonic cruise has been understood for many years (refs. 1 to 5). However, for moderately swept wings that have higher aspect ratios and are suitable for fighter aircraft, vortex breakdown can occur at low angles of attack. Thus, the wing does not achieve the large vortex-lift increments that are desirable for maneuvering.

A promising technique for enhancing the leading-edge vortex and effectively delaying vortex breakdown to higher angles of attack is that of spanwise blowing. This method consists of blowing a discrete jet spanwise over the wing upper surface and in a direction essentially parallel to the leading edge. Some original research related to this approach was performed in references 6 to 9 and demonstrated the control of separated flow regions by transverse blowing. The photographs in figure 1 were taken from reference 9 and

illustrate the leading-edge vortex that forms on a rectangular flat plate because of transverse blowing. The additional work reported in references 10 to 14 applied the concept to different types of lifting surfaces, such as swept wings, trailing-edge flaps, and rudders. To supplement this research, it is desirable to obtain detailed information concerning the wing-jet interaction for wings of interest for fighter aircraft.

Accordingly, the present investigation was initiated to evaluate the spanwise development of an augmented leading-edge vortex. This was accomplished by measuring surface pressure distributions on a moderately swept wing with spanwise blowing from the fuselage and by analyzing the experimental results with appropriate aerodynamic theory. A trapezoidal wing planform having a 44° leading-edge sweep was used for the study, which was conducted at a free-stream Mach number of 0.26. Data were acquired for a range of model angles of attack, jet thrust coefficients, and jet exit locations.

SYMBOLS

A_e nozzle exit area

b span

C_D total drag coefficient

C_L total lift coefficient

$C_{L,p}$ potential total lift coefficient

$C_{L,v}$ vortex total lift coefficient

$C_{L,tot}$ $= C_{L,p} + C_{L,v}$

C_m total pitching-moment coefficient

C_p pressure coefficient, $\frac{p - p_\infty}{q_\infty}$

ΔC_p $= C_{p,u} - C_{p,l}$

C_T nozzle thrust coefficient, $\frac{T_n}{q_\infty S}$

$C_{T,s}$ static thrust coefficient of single nozzle, $\frac{T_s}{p_a S}$

c	local chord
c_{av}	average chord, S/b
c_r	root chord (chord at wing fuselage juncture)
c_d	section drag coefficient
c_l	section lift coefficient
Δc_l	$= c_{l,\text{jet on}} - c_{l,\text{jet off}}$
$c_{l,p}$	potential section lift coefficient
$c_{l,v}$	vortex section lift coefficient
$c_{l,tot}$	$= c_{l,p} + c_{l,v}$
c_{l_α}	section lift-curve slope
c_s	section suction-force coefficient
c_t	section thrust-force coefficient
d	nozzle diameter
h	height of nozzle center line above wing surface
k_p	constant in potential-lift equation (see eq. (1))
k_v	constant in vortex-lift equation (see eq. (2))
M_∞	free-stream Mach number
p_a	ambient pressure
$p_{t,n}$	stagnation pressure in nozzle settling chambers
p_∞	free-stream static pressure

c	local chord
c_{av}	average chord, S/b
c_r	root chord (chord at wing fuselage juncture)
c_d	section drag coefficient
c_l	section lift coefficient
Δc_l	$= c_{l,\text{jet on}} - c_{l,\text{jet off}}$
$c_{l,p}$	potential section lift coefficient
$c_{l,v}$	vortex section lift coefficient
$c_{l,tot}$	$= c_{l,p} + c_{l,v}$
c_{l_α}	section lift-curve slope
c_s	section suction-force coefficient
c_t	section thrust-force coefficient
d	nozzle diameter
h	height of nozzle center line above wing surface
k_p	constant in potential-lift equation (see eq. (1))
k_v	constant in vortex-lift equation (see eq. (2))
M_∞	free-stream Mach number
p_a	ambient pressure
$p_{t,n}$	stagnation pressure in nozzle settling chambers
p_∞	free-stream static pressure

q_∞	free-stream dynamic pressure
S	wing reference area, 0.103 m^2
T_n	static thrust of both nozzles, $T_{n_1} + T_{n_2}$
T_s	static thrust of single nozzle
x	chordwise distance, measured from wing leading edge
x_n	chordwise distance of nozzle from leading edge of wing root chord (see fig. 2)
y	spanwise distance, measured from model plane of symmetry
z	vertical distance, measured from wing chord plane
α	angle of attack of model
γ	ratio of specific heats, 1.4
Λ_{le}	leading-edge sweep angle
Λ_n	sweep angle of nozzles

Subscripts:

1,2	refers to nozzles 1 (left) and 2 (right), respectively
l	condition on lower surface of wing
max	maximum
tot	total
u	condition on upper surface of wing

MODEL AND APPARATUS

The wind-tunnel model consisted of a wing-fuselage combination that had a discrete jet mounted in both sides of the fuselage and oriented to blow air over the wing upper

surface. A three-view drawing of the model is shown in figure 2, and photographs of the model installed in the wind tunnel are shown in figure 3.

The trapezoidal wing had a 44° leading-edge sweep angle and a trailing-edge sweep angle of -5.7°. The aspect ratio, based on a theoretical area of 0.103 m^2, was 2.5 and the taper ratio, 0.2. The wing had no twist, camber, or dihedral and had an airfoil section (measured streamwise) which was a circular arc with sharp leading and trailing edges. The thickness ratio was 6 percent at the fuselage-wing junction (root chord) and varied linearly to 4 percent at the wing tip. The pitching-moment reference center was taken to be at 25 percent of the theoretical root chord as shown in figure 2(a).

The wing was instrumented with 140 pressure orifices which were arranged in chordwise rows at six different span locations. (See fig. 2(b).) Pressures were measured on the lower surface of the left wing and on the upper surface of the right wing. The coordinates of all the orifices were measured with a three-dimensional digitizer and are presented in table I as values nondimensionalized by the local chord. The pressures were recorded by three automatic pressure-scanning valve units located inside the fuselage. These units are shown in figure 4, which presents a schematic of the test equipment inside the model.

The continuous-flow air system that was used to provide the desired dry high-pressure air to the two nozzles is also shown in figure 4. Each nozzle was connected to a cylindrical settling chamber, which was provided air by a 0.953-cm-diameter stainless steel supply line. The stagnation pressure in each settling chamber was recorded on a large dial pressure gauge. The size of the settling chambers necessitated the use of a fuselage fairing to cover them (shown in fig. 2(a)).

The angle of attack was measured with an accelerometer, located in the nose of the fuselage, which recorded changes in the attitude of the model with respect to the horizontal. The angle-of-attack measurements account for deflection of the model support system due to loads.

Details of the convergent nozzle geometry and location are shown in figure 5, where the subscripts 1 and 2 refer to nozzles 1 and 2, respectively. Each nozzle was made of 0.953-cm-diameter stainless steel tubing, whose inner diameter converged from 0.775 cm to the diameter d_1 or d_2 of the circular exit shown in the figure. The exit diameters were slightly different for the two nozzles. The bottom of the tubing was shaped to allow the jet to be closer to the wing surface. This configuration, shown in figure 5(a), was used for the bulk of the testing. Figure 5(b) shows the nozzle raised 1 nozzle-exit diameter farther above the wing surface than the basic position in figure 5(a).

Both nozzles were calibrated prior to tunnel installation to obtain static nozzle thrust as a function of plenum total pressure. A strain-gage balance was used to measure nozzle thrust for a range of values of plenum total pressure, and the resulting data are shown in

figure 6. The nozzle thrust for nozzle 2 is higher than that for nozzle 1 at a given nozzle stagnation pressure because d_2 is slightly greater than d_1. Thrust as a function of stagnation pressure is essentially linear, which would be expected for a convergent, choked nozzle under static conditions.

TEST CONDITIONS AND PROCEDURE

The tests were conducted at a Mach number of 0.26 in the Langley high-speed 7- by 10-foot wind tunnel which has a slotted test section. The average dynamic pressure was 4549 Pa, with a temperature of 297 K and a Reynolds number of 5.2×10^5 per meter. The tests were performed on the model without fixed transition, except for one test configuration where transition strips 0.159 cm wide were located on the fuselage nose and wing leading edges. The strips were composed of No. 80 carborundum grit and were located 1.27 cm aft of the nose and leading edges measured in a streamwise direction. The test data were not corrected for blockage and flow angularity since these are considered negligible.

Pressure data were obtained for each configuration at angles of attack from 0° to 24° at 4° increments, with nozzle thrust coefficients of 0, 0.06, and 0.12. At the maximum α, C_T was varied from 0 to 0.18 at increments of 0.02. For all of the thrusting conditions, the thrust of both nozzles was the same and was obtained by adjusting the nozzle stagnation pressure to the value in the static calibration (fig. 6). It is assumed that these static thrust levels would be essentially the same at the test condition of $M_\infty = 0.26$.

The test configurations represent different nozzle orientations and are listed in the following table:

x_n/c_r	Λ_n, deg	h/d	Transition strips
0.15	44	0.835	No
.23	44	.835	↓
.23	44	1.843	↓
.32	44	.835	↓
.32	33	.835	↓
.23	33	.835	↓
.23	33	.835	Yes

A value of 44° for Λ_n was chosen so that the jet would be parallel to the wing leading edge as was done in references 10 to 14.

FLOW VISUALIZATION

Oil-flow studies were performed on one configuration to provide an indication of the effects of spanwise blowing on wing upper surface flow patterns. The photographs presented in figure 7 were taken of the upper surface of the left wing with $x_n/c_r = 0.23$, $\Lambda_n = 33^o$, and $h/d = 0.835$. The oil was a mixture of Dow Corning 200 Fluid and lampblack. The wing was painted white to provide a suitable background for the photographs. Two floodlights were used to provide the necessary lighting for a K-24 camera which was mounted outside the test area above the model. The camera had a remote shutter release and an automatic film advance to allow more than one photograph to be taken during a run.

The procedure for obtaining the oil-flow photographs was initiated by putting oil on the left wing with the tunnel off. The model was then put at a high angle of attack and the tunnel turned on. This high angle of attack resulted in the flow over the upper surface being completely separated and prevented oil from wiping off until the test conditions were set. The model was then lowered to the desired angle of attack and a photograph was taken after the flow patterns became established. Flow establishment was determined with a television camera which provided a real time picture of the oil-flow pattern on the model planform. The nozzle total pressure was then set to obtain a desired thrust coefficient and the flow patterns were again allowed to change before taking a photograph. The tunnel was then shut off and the procedure repeated for the next test angle of attack.

PRESENTATION OF RESULTS

The results of this investigation are presented in the following figures:

DISCUSSION

The wing-surface pressure measurements obtained during the wind-tunnel tests are presented in graphical form in figures 35 to 48. Upper and lower surface pressure coefficients are plotted against $\overline{x/c}$, the nominal fraction of the local chord. (See table I.) The lower surface pressures are identified by a + inside the data symbol. The data were machine plotted and then faired with a cubic spline (with no tension); this spline was integrated to obtain section forces and moments. The spanwise variation of the section properties were then fitted with a cubic spline and integrated to obtain the total forces and moments on the wing.

Wing-Surface Flow Patterns

Photographs of oil-flow patterns on the upper surface of the left wing are shown in figure 7 for the configuration with $x_n/c_r = 0.23$, $\Lambda_n = 33^o$, and $h/d = 0.835$. Although these photographs were obtained with $\Lambda_n = 33^o$, the flow patterns are similar to those observed for the model with $\Lambda_n = 44^o$.

At $\alpha = 8.1^o$ (fig. 7(a)) the wing-jet interaction is like the "jet in a crossflow" problem, where the jet path bends downstream. With $C_T = 0$, there is a stagnation line faintly visible near the juncture of the wing leading edge and the fuselage. This is indicative of the formation of a leading-edge vortex in this region which can also be noted in the pressure data in figure 45(c). Spanwise blowing extends the stagnation line along the leading edge.

At $\alpha = 16.6^o$ (fig. 7(b)) blowing has a similar effect on the stagnation line near the leading edge. Rather than bending downstream as observed for $\alpha = 8.1^o$, the jet tends to move toward the leading edge, particularly on the outer portion of the wing, where the jet surface flow appears to coalesce. The primary reason for the change in jet exhaust trajectory with angle of attack is probably due to the wing flow that exists without jet

blowing. At $\alpha = 8.1^{\circ}$ most of the upper surface flow is attached with $C_T = 0$. At $\alpha = 16.6^{\circ}$, however, extensive flow separation exists over the outer half of the wing with $C_T = 0$. Blowing causes the wing flow field to reattach aft of the jet flow, thus completely eliminating the separated flow regions. The effects of blowing at $\alpha = 23.8^{\circ}$ (fig. 7(c)) are similar to those observed at 16.6°. Some of these trends of wing-jet interaction have been noted in the studies of references 13 and 14.

Detailed Effects of Spanwise Blowing

Because of the large quantity of data obtained during this investigation, only one of the model configurations will be used to explain the detailed effects of spanwise blowing. The particular model to be used has $x_n/c_r = 0.23$, $\Lambda_n = 44^{\circ}$, and $h/d = 0.835$. The data trends that are discussed in the following sections for this configuration are typical of the trends obtained for all the test configurations.

Chordwise distributions of C_p.- The effects of nozzle thrust coefficient and model angle of attack on wing-surface pressure distributions are presented in figures 37 and 38, respectively. The data are shown as plots of upper and lower surface C_p as a function of chordwise distance for each of the six span locations.

Spanwise blowing results in more significant effects on the wing upper surface pressure field than on the lower surface pressure field and at high angles of attack as opposed to low angles of attack. To appreciate the complicated interaction process between the wing and jet flow fields, it is desirable to first examine data for $\alpha = 0^{\circ}$ (fig. 37(a)). The first effect to note is at the inboard station ($2y/b = 0.259$) where a sizable negative pressure coefficient occurs at $x/c = 0.3$ when the jet is blowing. This effect is probably due to the close proximity of the jet exit, located at $2y/b \approx 0.2$, to the pressure orifices; the underexpanded nozzle provides a distinct high velocity flow which has expansion waves and can effectively increase local thickness. This interference pressure disappears farther out on the wing, where the jet has had time to spread. It is interesting to note that this effect at the inboard station is essentially insensitive to changes in α (see figs. 37(a) to 37(g)) and is consistent when the nozzle orientation is changed, as is the case in figure 41 where $x_n/c_r = 0.32$.

The second effect to observe in the $\alpha = 0^{\circ}$ data is noted primarily at $2y/b = 0.501$, where the spreading jet causes a decrease in $C_{p,u}$ over the aft portion of the wing section. This effect, which results from the displacement of surface streamlines due to the addition of jet fluid on the wing upper surface, is similar to an increase in wing camber. This interaction effect diminishes farther out on the wing. This trend was also observed in the experimental tests reported in reference 13.

With the angle of attack increased to 12.3° (fig. 37(d)), the pressure field reflects a lifting situation for the wing. A large pressure peak occurs on the upper surface near the

leading edge of the inboard station with $C_T = 0$. Analysis of the data shows that a larger $2y/b$ results in a decrease in the peak pressure and a rearward shift in the location. These data are indicative of the formation of a leading-edge vortex which is well organized at the inboard station but quickly weakens as it grows in the span direction. The fact that the vortex quickly dissipates explains why Wentz (ref. 3), who used a schlieren system, was not able to observe it on a 45^o delta wing.

The spanwise blowing jet affects the pressure field over most of the wing upper surface, with no noticeable effect on the lower surface pressures. The magnitude of the upper surface pressure peak is increased by spanwise blowing, and the span effects noted with no blowing are essentially the same as those with blowing. The jet-camber effect noted at $\alpha = 0^o$ is difficult to ascertain in these data.

The effects of spanwise blowing become more pronounced at the higher angles of attack. The primary reason that the effects are more pronounced is connected with the separated flow field over the wing which occurs with no blowing. With the sharp leading edge of this wing, the flow separates at the leading edge, after which it may reattach to the wing and lead to the more conventional flow separation which occurs near the trailing edge. The wing upper surface flow field is dependent, then, on the interaction between these two separation points and the reattachment point, and as a consequence, so are the wing stall characteristics. Complete stall would occur at a particular wing section when the separated leading-edge flow does not reattach but remains separated over the wing. This results in upper surface pressures that are essentially constant over the wing section. At $\alpha = 12.3^o$ (fig. 37(d)) this constant $C_{p,u}$ distribution is seen only on the outer portion of the wing near the wing tip. However, as α is increased, this completely separated flow region moves progressively inboard until at $\alpha = 23.9^o$ (fig. 37(g)) the flow is separated over the entire upper surface. Spanwise blowing causes the leading-edge vortex to reform and the flow to reattach to the wing upper surface at some point aft of the jet flow, similar to the flow condition noted in figures 1 and 7. This results in significant decreases in $C_{p,u}$, particularly at the inboard stations where the jet flow is still strong enough to cause the vortex to roll up and the vortex is still close to the wing surface. These pressure results are similar to those obtained on a rectangular flat plate in reference 10. The pressure distributions obtained with blowing appear to be similar to those obtained on highly swept delta wings which have a natural (no blowing required) leading-edge vortex (ref. 5). It is noted that at the highest angles of attack, blowing causes a slight increase in $C_{p,l}$ coupled with a slight rearward shift in the stagnation point on the wing lower surface.

Chordwise distributions of ΔC_p.- The effects of span location on the chordwise distributions of ΔC_p are shown in figure 8 for $\alpha = 20.6^o$. With no blowing $(C_T = 0)$, the highest ΔC_p values occur at the inboard station and decrease with an increase in span distance. With $C_T = 0.06$, the leading-edge vortex is formed and results in large suction

pressures and pressure gradients near the leading edge at $2y/b = 0.259$. At span stations farther outboard, the growth and displacement from the wing surface of the vortex, combined with the spreading of the jet, results in lower peak pressures but has a greater effect over more of the wing section. The effects on the ΔC_p distribution with $C_T = 0.12$ are the same as seen for $C_T = 0.06$; $C_T = 0.12$ results in higher negative values of ΔC_p.

A schematic of the wing pressure field is shown in figure 9 to illustrate the pressure distribution near the leading edge that results if the flow is separated, as in the present experiment, and to show what distribution it might have if it were attached. The attached flow condition is represented by the subsonic theory from reference 15 and is characterized by negatively increasing $C_{p,u}$ as the leading edge is approached. The experimental data show that the flow cannot negotiate the sharp leading edge; therefore, it separates. Spanwise blowing helps the separated leading-edge flow to roll up into a vortex, thus yielding the negative peaks in the $C_{p,u}$ data.

The effects of angle of attack on the chordwise distributions of ΔC_p at $2y/b = 0.5$ are illustrated in figure 10. With no blowing, ΔC_p increases with increases in α up to the stall angle for this wing section ($\approx 16^\circ$); further increase in α results in a decrease in ΔC_p. With $C_T = 0.06$, an increase in α results in a progressive increase in ΔC_p all across the chord. This implies a greater wing-section stall angle than that obtained with no blowing. The data shown for $C_T = 0.12$ have the same trends as the data for $C_T = 0.06$. The higher blowing rate does result in an effect at $\alpha = 0^\circ$ at this span station that was not apparent at the lower blowing rate. This is the jet-induced camber effect discussed previously which results in a slight compression on the forward half of the wing section and a favorable expansion on the rear half.

Section lift and drag characteristics.- The information in figures 11 to 15 will be used to discuss the effects of spanwise blowing on wing-section aerodynamic characteristics. The section data were obtained by integrating the chordwise pressure distributions using the pressure orifice locations presented in table I.

The effects of blowing on section lift characteristics are presented in figure 11 for the six span stations. An increase in C_T generally resulted in an increase in c_l all across the span, the largest effects occurring at high angles of attack, where the wing sections have experienced partial or complete stall with no blowing $(C_T = 0)$.

The largest c_l values on the wing were attained for the highest blowing rate shown $(C_T = 0.12)$ and occurred at $2y/b = 0.609$ and 0.707. The c_l at $2y/b = 0.707$ was limited due to vortex breakdown. The data also indicate that blowing increases c_{l_α} and $c_{l,max}$, as well as the angle of attack where $c_{l,max}$ occurs. In addition, blowing causes a change in the section lift behavior near stall (or $c_{l,max}$). For example, the data at $2y/b = 0.609$ and 0.707 for $C_T = 0.06$ show that these wing sections experience a

fairly abrupt loss of c_l beyond $c_{l,max}$, as compared with the high angle-of-attack data for $C_T = 0$. This type of stall pattern is typical of wings with leading-edge vortex flows (ref. 3) and results because of the sudden loss of lift due to vortex bursting on the wing.

With no blowing, c_l as a function of α is reasonably linear at low angles of attack, particularly on the inboard portion of the wing. Blowing results in nonlinear section lift curves which are characteristic of lift curves obtained on highly swept wings having a leading-edge vortex (ref. 3).

To better interpret the experimental results, theoretical estimates of the section lift characteristics were calculated by using the leading-edge suction analogy. The basic assumptions which are used in reference 1 to apply the suction analogy to a wing with a fully developed leading-edge vortex are assumed to apply here on a sectional basis. Accordingly, the potential and vortex section lifts for a section with 0-percent leading-edge suction are given by

$$c_{l,p} = \sqrt{k_p \sin\alpha \cos^2\alpha} \tag{1}$$

$$c_{l,v} = \sqrt{k_v \sin^2\alpha \cos\alpha} \tag{2}$$

where the total lift is

$$c_{l,tot} = c_{l,p} + c_{l,v} \tag{3}$$

The terms k_p and k_v are defined as:

$$k_p = c_{l_\alpha} \tag{4}$$

and

$$k_v = \frac{c_t}{\cos\Lambda_{le}\sin^2\alpha} = \frac{c_s}{\sin^2\alpha} \tag{5}$$

where c_t and c_s are the section thrust- and suction-force coefficients, respectively. Because of their dependence on section properties, the parameters k_p and k_v are functions of spanwise location. The parameters c_t and c_s, as well as c_{l_α}, were determined at different span locations on the trapezoidal wing (fig. 2) by the lifting surface theory of reference 16. Since this is a linear theory, k_v was calculated by using α^2 in equation (5) instead of $\sin^2\alpha$.

The theoretical estimates for section lift with no vortex lift $(c_{l,p})$ and with full leading-edge vortex lift $(c_{l,p} + c_{l,v})$ are presented in figure 11. Several observations

of the comparison with experiment are necessary. For the case with $C_T = 0$, the section lift is estimated reasonably well up to section stall by $c_{l,p}$. This substantiates the earlier observation that, with no spanwise blowing, this wing has little or no leading-edge vortex flow. The dashed line, which represents the estimated section lift that would result if the leading-edge vortex was fully established, has the same lift-curve shape as the data with blowing and generally estimates magnitudes reasonably well. There are some notable exceptions to this besides the obvious deterioration as the wing tip is approached. At some sections, blowing results in section lift coefficients that are higher than the estimated full vortex-lift levels. At $2y/b = 0.501$, for example, $C_T = 0.12$ results in larger c_l values throughout the α range. At $\alpha = 0^\circ$ where there is no leading-edge vortex on the wing, even with blowing, the increase in c_l is due to a jet-induced camber effect. This effect was noted previously during the discussion of the pressure data and has been observed in references 10 and 14.

At other span stations, $2y/b = 0.609$ and 0.707 for instance, there is no evidence of the jet-camber effect at $\alpha = 0^\circ$, even though the data at higher angles of attack for $C_T = 0.12$ indicate lifts that are greater than the estimated values. It is not obvious why this is so, but there is a definite difference in the wing-jet flow field at high angles of attack compared with low angles of attack as was demonstrated by the oil-flow photographs in figure 7. Some of the lift benefits may be the result of the jet feeding the vortex in a manner similar to the leading-edge blowing problem studied by Barsby (ref. 17), who showed that injecting a thin jet of air out from the leading edge strengthened the vortex and increased lift.

So far the data have shown that the amount of sectional vortex lift generated by spanwise blowing is dependent on C_T, $2y/b$, and α. One question that can be asked is what value of C_T does it take to achieve the full vortex-lift level at the various span locations? An attempt to answer this is shown in figure 12, which presents c_l as a function of C_T for the six span locations with $\alpha = 23.9^\circ$. The full vortex-lift levels, which were estimated by the suction analogy, are represented by the dashed lines.

As was observed earlier, blowing increases the section lift at all the span locations, but this figure illustrates how dramatically different the blowing effectiveness is depending, of course, on $2y/b$. The increase in c_l at low values of C_T is most effective inboard and least effective outboard near the wing tip. This is reflected in the value of C_T that is required to achieve full vortex lift at each of the span stations. For example, at $2y/b = 0.259$, $C_T \approx 0.07$ is required; at $2y/b = 0.501$, $C_T \approx 0.08$ is required; at $2y/b = 0.609$, $C_T \approx 0.11$; and at $2y/b = 0.707$, $C_T \approx 0.17$. At the two outermost stations, the full vortex-lift level was not attained with the C_T values used in the current tests.

These results suggest that blowing spanwise from the fuselage is a jet-decay problem. Thus, the development of the leading-edge vortex and the associated section lift depend on the local jet and vortex properties, as well as on free-stream Mach number and dynamic pressure. As a matter of reference, the geometries of the wing and jet are such that the jet flow must penetrate almost 62 nozzle-exit diameters to reach the wing tip. The resulting decay of the jet velocity is large enough to have a significant effect on leading-edge vortex formation.

Another way of looking at spanwise blowing effects is shown in figure 13, which presents the variation of section lift and lift-augmentation ratio along the span for a range of blowing rates. As shown earlier, blowing increases c_l all across the span. Plotting the data in this fashion gives a good perspective of the span distribution of c_l with and without vortex lift. The no blowing case $(C_T = 0)$ is typical of a wing with no vortex lift. Blowing causes the shape of the c_l distribution curve to progressively change toward the c_l distribution estimated by the suction analogy. At the higher blowing rates, the c_l values on the inboard portion of the wing are higher than the theoretical estimates; this trend was also shown in figure 12. This jet-induced effect on the inboard portion of the wing, coupled with available vortex lift on the outboard portion, suggests that higher C_T than those of this test will produce even higher lift levels.

Also shown in figure 13 is the lift-augmentation ratio $\Delta c_l/C_T$, where $\Delta c_l = c_{l,\text{jet on}} - c_{l,\text{jet off}}$. As might be expected from some of the previous results, the data for $C_T = 0.04$ yields the largest augmentation ratios and a decrease in the ratios occurs with an increase in C_T. The maximum augmented lift for a given C_T occurs between $2y/b = 0.501$ and 0.707, depending on the value of C_T. On the outboard portion of the wing near the wing tip, the ratios are essentially independent of C_T. This implies that Δc_l near the wing tip is a linear function of C_T, which is what the data showed in figure 12 at the outermost span locations.

The effects of blowing on span loading is shown in figure 14 for the same data presented in figure 13. Blowing increases the span loading, particularly on the inner portion of the wing. This effect is beneficial from a wing bending-moment standpoint. The prediction of the span loading obtained from the suction analogy is also shown.

The effect of spanwise blowing on section induced-drag characteristics is presented in figure 15 for the various span locations. Blowing improves the drag polars over most of the span, the smallest effect occurring near the wing tip. Estimates of the induced-drag polars were obtained by taking the section normal force to be the resultant section force, which would be the case with zero suction. This leads to the expressions

$$c_d = c_{l,p} \tan \alpha \tag{6}$$

for the situation with no vortex lift, and

$$c_d = c_{l,tot} \tan \alpha \tag{7}$$

for full vortex lift. The $c_{l,p}$ and $c_{l,tot}$ used in these expressions come from equations (1) and (3), respectively.

The expression for the potential flow case gives reasonable estimates of induced drag for the no blowing $(C_T = 0)$ situation except at high c_l, where section stall has begun. The improvements in drag polars due to spanwise blowing are generally estimated by the theory, which assumes that full vortex lift exists. At $2y/b = 0.501$, 0.609, and 0.707, the drag obtained for $C_T = 0.12$ is lower than the predicted level. This is consistent with the lift results at these sections that were discussed in figure 11.

Total aerodynamic characteristics.- The section data presented in the previous section (figs. 11 and 15) were integrated spanwise from $2y/b = 0.259$ to 1.0 to obtain the total force coefficients presented in figure 16. Estimates for lift were obtained by spanwise integration of the theoretical values of $c_{l,p}$ (potential lift) and $c_{l,tot}$ (potential + vortex lifts). These lift results are presented in figure 16 and were used to obtain estimates for induced drag.

Spanwise blowing results in an increase in lift and improved drag polars, which would be expected, particularly at high angles of attack where the wing without blowing $(C_T = 0)$ has experienced complete stall. Besides increasing $C_{L,max}$, blowing increases the angle of attack where $C_{L,max}$ occurs. There appears to be a small jet-camber effect at $\alpha = 0^o$ with $C_T = 0.12$, resulting in a slight increase in C_L.

The assumption of no vortex lift leads to good predictions of C_L and C_D for the no blowing case $(C_T = 0)$. The theory for full vortex lift predicts the blowing effects very well. The pitching-moment results obtained by using the moment reference center shown in figure 2 are also presented in this figure. Spanwise blowing results in an extension of the linear pitching moment obtained for $C_T = 0$ to much higher lifts. This is accomplished without adversely effecting the stability level. The estimates for pitching moment were obtained using the method described in reference 18.

Configuration Effects

The discussion thus far has been devoted to just one of the test configurations, where $x_n/c_r = 0.23$, $\Lambda_n = 44^o$, and $h/d = 0.835$. For the benefit of completeness, the effects of blowing on the longitudinal aerodynamic characteristics of the other six configurations are presented in figures 17 to 23. The effects of blowing are similar for the different configurations, although blowing effectiveness varies somewhat. The effect of transition strips was determined by adding transition strips to the configuration with

$x_n/c_r = 0.23$, $\Lambda_n = 33^\circ$, and $h/d = 0.835$. The effects of blowing on the aerodynamic characteristics of this configuration without transition strips are presented in figure 21, and with transition strips in figure 22. Figure 23 shows that there is little or no effect of the transition strips for $C_T = 0$ and 0.12.

Effect of x_n/c_r.- The effect of nozzle chordwise location x_n/c_r on the wing pressure field is illustrated in figure 24. Chordwise distributions of ΔC_p at $2y/b = 0.501$ are shown for $C_T = 0.06$ and 0.12, and at angles of attack of 12.3° and 20.5°. Moving the nozzle position rearward from $x_n/c_r = 0.15$ causes a reduction in the peak value of ΔC_p which occurs near the leading edge and an increase in ΔC_p over the midportion of the wing section. These trends are evident at both angles of attack and nozzle thrust coefficients, although the largest effects of x_n/c_r occur at $\alpha = 20.5^\circ$ with $C_T = 0.12$.

The data trends of figure 24 are reflected in the sample section lift data shown in figure 25. Increasing x_n/c_r decreases c_l throughout the angle-of-attack range at the inboard station and at intermediate angles of attack at the outboard stations. The trend at the outboard stations tends to reverse at the highest α.

The effect of x_n/c_r on the longitudinal aerodynamic characteristics is presented in figure 26 for $C_T = 0.12$. Increasing x_n/c_r causes a slight decrease in C_L at intermediate angles of attack but has essentially no effect on C_D and C_m.

Effect of Λ_n.- The effect of nozzle sweep angle Λ_n on chordwise distributions of ΔC_p is illustrated in figures 27 and 28, where x_n/c_r is 0.23 and 0.32, respectively. The data are shown for $\alpha = 12.3^\circ$ and 20.5° with $C_T = 0.06$ and 0.12, where $\Lambda_n = 44^\circ$ is parallel to the wing leading edge. Sweeping the nozzle angle forward from 44° to 33° causes a slight increase in the leading-edge pressure peak and a varying degree of adverse effect on the aft portion of the wing section.

The effect of decreasing Λ_n on the section lift characteristics (fig. 29) is adverse at $2y/b = 0.259$ for all test angles of attack, with a varying effect at the outboard stations. These trends result in unfavorable effects on the total loads as observed in figure 30. Decreasing Λ_n from 44° to 33° causes an adverse camber effect at $\alpha = 0^\circ$, which persists throughout the angle-of-attack range. This, of course, leads to higher induced drag and more negative C_m at a given C_L. Although the data results in figures 29 and 30 were obtained with $x_n/c_r = 0.23$, similar trends were obtained for the configuration with $x_n/c_r = 0.32$.

Effect of h/d.- The effect of nozzle vertical location h/d on chordwise distributions of ΔC_p is illustrated in figure 31 for two angles of attack and two blowing rates. Raising the nozzle location from $h/d = 0.835$ to 1.843 results in a slight decrease in the pressure peak near the leading edge and a varying effect on the aft portion of the wing section.

Figure 32 shows that increasing h/d increases section lift on the inboard portion of the wing and decreases c_l on the outboard portion. The effect of h/d on the longitudinal aerodynamic characteristics is presented in figure 33 for $C_T = 0.12$. Increasing h/d has no effect on C_D and C_m and causes a slight decrease in C_L. This is substantiated by the results of reference 9 which performed a nozzle position study on a 45° delta wing at $\alpha \approx 21^\circ$. For $x_n/c_r = 0.20$, these data showed that the model with $h/d = 1.0$ generated more lift than with $h/d = 1.5$ or 2.0. (See fig. 6 in ref. 9.) However, with $x_n/c_r = 0.30$, the optimum vertical position was $h/d = 1.5$, and with $x_n/c_r = 0.40$, $h/d = 2.0$.

An effort was made in figure 34 to compare the lift-producing capabilities of the different nozzle orientations for $\alpha \approx 23.9^\circ$. Generally, the configuration with $\overline{x_n/c_r} = 0.23$, $\Lambda_n = 44^\circ$, and $h/d = 0.835$ resulted in the highest increase in C_L, while the configuration with $\overline{x_n/c_r} = 0.23$, $\Lambda_n = 33^\circ$, and $h/d = 0.835$ resulted in the lowest increase.

CONCLUSIONS

The present investigation was conducted to measure the effects of spanwise blowing on the pressure distributions of a trapezoidal wing with 44° leading-edge sweep. Wind-tunnel data were obtained at a free-stream Mach number of 0.26 for a range of model angle of attack, jet thrust coefficient, and jet location. Results of this study lead to the following conclusions:

1. Spanwise blowing had significant effects on the upper surface pressure field at high angles of attack. The largest suction pressures occurred at the inboard span station near the wing leading edge and diminished outboard.

2. The pressure distributions obtained on this 44° swept wing with blowing are similar to those obtained on a highly swept wing which has a well-established leading-edge vortex without blowing. With no blowing the trapezoidal wing had very limited vortex flow.

3. Full vortex lift was achieved at the inboard span station with a small blowing rate; successively higher blowing rates were required to achieve full vortex lift at increased span distances.

4. Increased blowing rate increased span loading all across the wing; the highest loading occurred at the inboard span station, which is beneficial from a wing bending-moment standpoint.

5. The leading-edge suction analogy can be used to obtain reasonable estimates of increased section and total lift curves resulting from spanwise blowing up to wing stall. Section induced-drag polars were adequately estimated by the product of section lift coefficient and the tangent of the angle of attack; the same was true for total induced-drag polars.

6. Spanwise blowing increases total lift throughout the angle-of-attack range, thus increasing the maximum lift coefficient and the angle of attack where this lift occurs. In addition, blowing improves the induced-drag polar, and extends the linear pitching moment to high lifts.

7. Within the range of test variables, the configuration with a nozzle chordwise location at 23 percent wing root chord, a nozzle sweep angle of 44°, and a nozzle vertical location of 0.835 nozzle diameter above the wing surface resulted in the highest increases in lift.

Langley Research Center,
National Aeronautics and Space Administration,
Hampton, Va., April 3, 1975.

REFERENCES

1. Polhamus, Edward C.: A Concept of the Vortex Lift of Sharp-Edge Delta Wings Based on a Leading-Edge-Suction Analogy. NASA TN D-3767, 1966.

2. Polhamus, Edward C.: Application of the Leading-Edge-Suction Analogy of Vortex Lift to the Drag Due to Lift of Sharp-Edge Delta Wings. NASA TN D-4739, 1968.

3. Wentz, William H., Jr.; and Kohlman, David L.: Wind Tunnel Investigations of Vortex Breakdown on Slender Sharp-Edged Wings. Rep. FRL 68-013 (Grant NGR-17-002-043), Univ. of Kansas Center for Research, Inc., Nov. 27, 1969. (Available as NASA CR-98737.)

4. Polhamus, Edward C.: Predictions of Vortex-Lift Characteristics by a Leading-Edge Suction Analogy. J. Aircraft, vol. 8, no. 4, Apr. 1971, pp. 193-199.

5. Hummel, D.: Study of the Flow Around Sharp-Edged Slender Delta Wings With Large Angles of Attack. NASA TT F-15,107, 1973.

6. Werlé, H.: Partage et Rencontre d'Écoulements Fluides. Étude Effectuée à la Cuve à Huile et au Tunnel Hydrodynamique a Visualisation de l'O.N.E.R.A. La Rech. Aeron., no. 79, Nov.-Dec. 1960, pp. 9-26.

7. Cornish, J. J., III: High Lift Applications of Spanwise Blowing. ICAS Paper No. 70-09, Sept. 1970.

8. Werlé, H.; and Gallon, M.: Flow Control by Cross Jet. NASA TT F-14,548, 1972.

9. Werlé, Henri: Sur l'Écoulement au Bord d'Attaque d'un Profil Portant. La Rech. Aérospatiale, no. 4, July-Aug. 1973, pp. 197-218.

10. Dixon, C. J.: Lift Augmentation by Lateral Blowing Over a Lifting Surface. AIAA Paper No. 69-193, Feb. 1969.

11. Dixon, C. J.: Lift and Control Augmentation by Spanwise Blowing Over Trailing Edge Flaps and Control Surfaces. AIAA Paper No. 72-781, Aug. 1972.

12. Bradley, R. G.; and Wray, W. O.: A Conceptual Study of Leading-Edge-Vortex Enhancement by Blowing. AIAA Paper No. 73-656, July 1973.

13. Dixon, C. J.; Theisen, J. G.; and Scruggs, R. M.: Theoretical and Experimental Investigations of Vortex Lift Control by Spanwise Blowing. Volume I - Experimental Research. LG73ER-0169, Lockheed Aircraft Corp., Sept. 15, 1973.

14. Bradley, R. G.; Wray, W. O.; and Smith, C. W.: An Experimental Investigation of Leading-Edge Vortex Augmentation by Blowing. NASA CR-132415, 1974.

15. Woodward, F. A.: An Improved Method for the Aerodynamic Analysis of Wing-Body-Tail Configurations in Subsonic and Supersonic Flow. NASA CR-2228, Pts. I-II, 1973.

Part I – Theory and Application.

Part II – Computer Program Description.

16. Margason, Richard J.; and Lamar, John E.: Vortex-Lattice FORTRAN Program for Estimating Subsonic Aerodynamic Characteristics of Complex Planforms. NASA TN D-6142, 1971.

17. Barsby, J. E.: Calculations of the Effect of Blowing From the Leading Edges of a Slender Delta Wing. Tech. Rep. 71077, British R.A.E., Apr. 1971.

18. Lamar, John E.; and Gloss, Blair B.: Prediction of Subsonic Aerodynamic Characteristics on Interacting Lifting Surfaces With Separated Flow Around Sharp Leading and Side Edges Using Vortex-Lattice Methodology. NASA TN D-7921, 1975.

TABLE I.- PRESSURE ORIFICE LOCATIONS

(a) 2y/b = 0.259; c = 26.850 cm

x_u/c (1)	z_u/c (1)	x_l/c (1)	z_l/c (1)	x/c (2)
0.0064	0.0017	0.0045	0.0012	0.005
.0113	.0024	.0104	.0019	.010
.0248	.0037	.0259	.0038	.025
.0494	.0065	.0500	.0064	.050
.0989	.0117	.1008	.0118	.100
.2021	.0198	.2004	.0199	.200
.2998	.0253	.3014	.0257	.300
.3995	.0288	.4017	.0292	.400
.5002	.0302	.5023	.0302	.500
.5998	.0288	.5998	.0289	.600
.6991	.0253	.7048	.0251	.700
.7994	.0197	.8004	.0194	.800
.8994	.0110	.9004	.0109	.900
.9499	.0063	.9507	.0058	.950
.9699	.0041	.9705	.0036	.970

(b) 2y/b = 0.501; c = 20.317 cm

x_u/c (1)	z_u/c (1)	x_l/c (1)	z_l/c (1)	x/c (2)
0.0048	0.0015	0.0074	0.0017	0.005
.0100	.0023	.0154	.0027	.010
.0237	.0038	.0257	.0038	.025
.0500	.0065	.0521	.0065	.050
.0992	.0110	.1024	.0113	.100
.1998	.0194	.2016	.0194	.200
.3001	.0244	.3022	.0248	.300
.3975	.0278	.4013	.0282	.400
.4974	.0288	.5002	.0291	.500
.5975	.0278	.6007	.0279	.600
.6989	.0244	.6991	.0244	.700
.7993	.0187	.7999	.0186	.800
.8983	.0106	.9004	.0103	.900
.9237	.0081	.9250	.0081	.925
.9483	.0056	.9495	.0056	.950

[1]These coordinates were used in integrating the pressure data to get forces.

[2]These are nominal values of x/c used to machine plot the pressure data.

TABLE I.- PRESSURE ORIFICE LOCATIONS – Continued

(c) 2y/b = 0.609; c = 17.369 cm

x_u/c (1)	z_u/c (1)	x_l/c (1)	z_l/c (1)	x/c (2)
0.0111	0.0023	0.0080	0.0017	0.010
.0228	.0035	.0291	.0041	.025
.0478	.0061	.0501	.0062	.050
.0999	.0108	.0990	.0107	.100
.1992	.0188	.1994	.0185	.200
.4002	.0273	.4001	.0272	.400
.5971	.0271	.6004	.0270	.600
.7998	.0182	.8017	.0177	.800
.9003	.0102	.9018	.0098	.900
.9235	.0081	.9259	.0076	.925

(d) 2y/b = 0.707; c = 14.704 cm

x_u/c (1)	z_u/c (1)	x_l/c (1)	z_l/c (1)	x/c (2)
0.0095	0.0023	0.0102	0.0017	0.010
.0254	.0037	.0252	.0036	.025
.0489	.0062	.0485	.0056	.050
.1011	.0102	.0993	.0103	.100
.1989	.0181	.2004	.0180	.200
.3988	.0265	.3989	.0264	.400
.5987	.0261	.5995	.0262	.600
.8005	.0175	.7996	.0173	.800
.8992	.0099	.8993	.0095	.900
.9250	.0077	.9252	.0072	.925

[1]These coordinates were used in integrating the pressure data to get forces.

[2]These are nominal values of x/c used to machine plot the pressure data.

TABLE I.- PRESSURE ORIFICE LOCATIONS – Concluded

(e) 2y/b = 0.866; c = 10.399 cm

x_u/c (1)	z_u/c (1)	x_l/c (1)	z_l/c (1)	x/c (2)
0.0239	0.0042	0.0238	0.0033	0.025
.0477	.0063	.0491	.0050	.050
.0747	.0085	.0731	.0071	.075
.1490	.0138	.1490	.0126	.150
.2986	.0215	.3004	.0203	.300
.4499	.0250	.4511	.0240	.450
.5999	.0241	.5955	.0233	.600
.7520	.0187	.7504	.0176	.750
.7966	.0162	.7997	.0149	.800
.8494	.0128	.8483	.0115	.850

(f) 2y/b = 0.966; c = 7.694 cm

x_u/c (1)	z_u/c (1)	x_l/c (1)	z_l/c (1)	x/c (2)
0.0247	0.0052	0.0278	0.0022	0.025
.0495	.0072	.0509	.0043	.050
.0997	.0104	.0981	.0073	.100
.1985	.0157	.1961	.0132	.200
.2979	.0197	.3005	.0172	.300
.3976	.0218	.3973	.0198	.400
.5039	.0224	.4955	.0206	.500
.6022	.0214	.5971	.0196	.600
.7052	.0184	.6976	.0167	.700
.7994	.0143	.7968	.0123	.800

[1]These coordinates were used in integrating the pressure data to get forces.

[2]These are nominal values of x/c used to machine plot the pressure data.

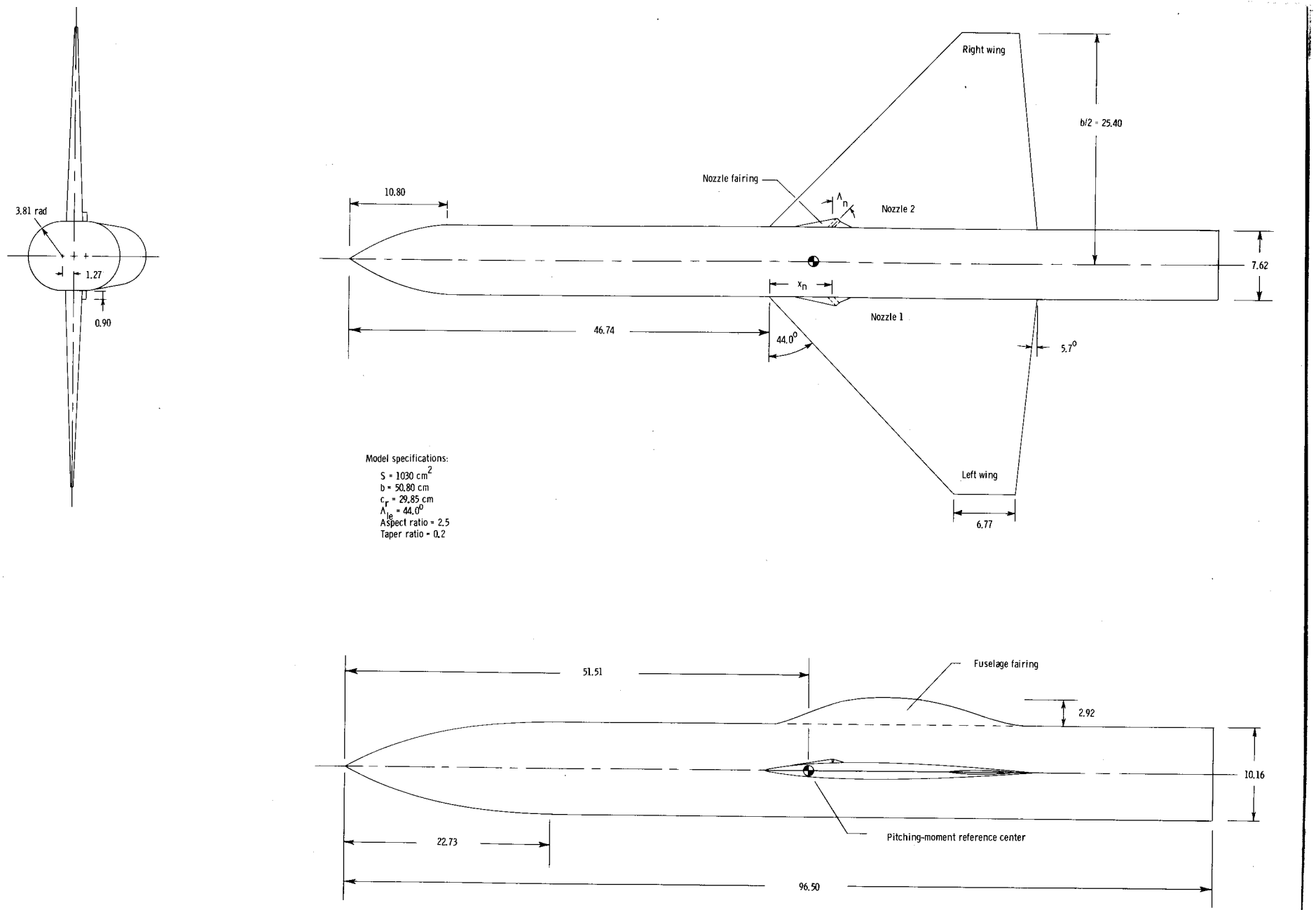

(a) Three-view drawing.

Figure 2.- Details of wind-tunnel model. (All dimensions are in centimeters.)

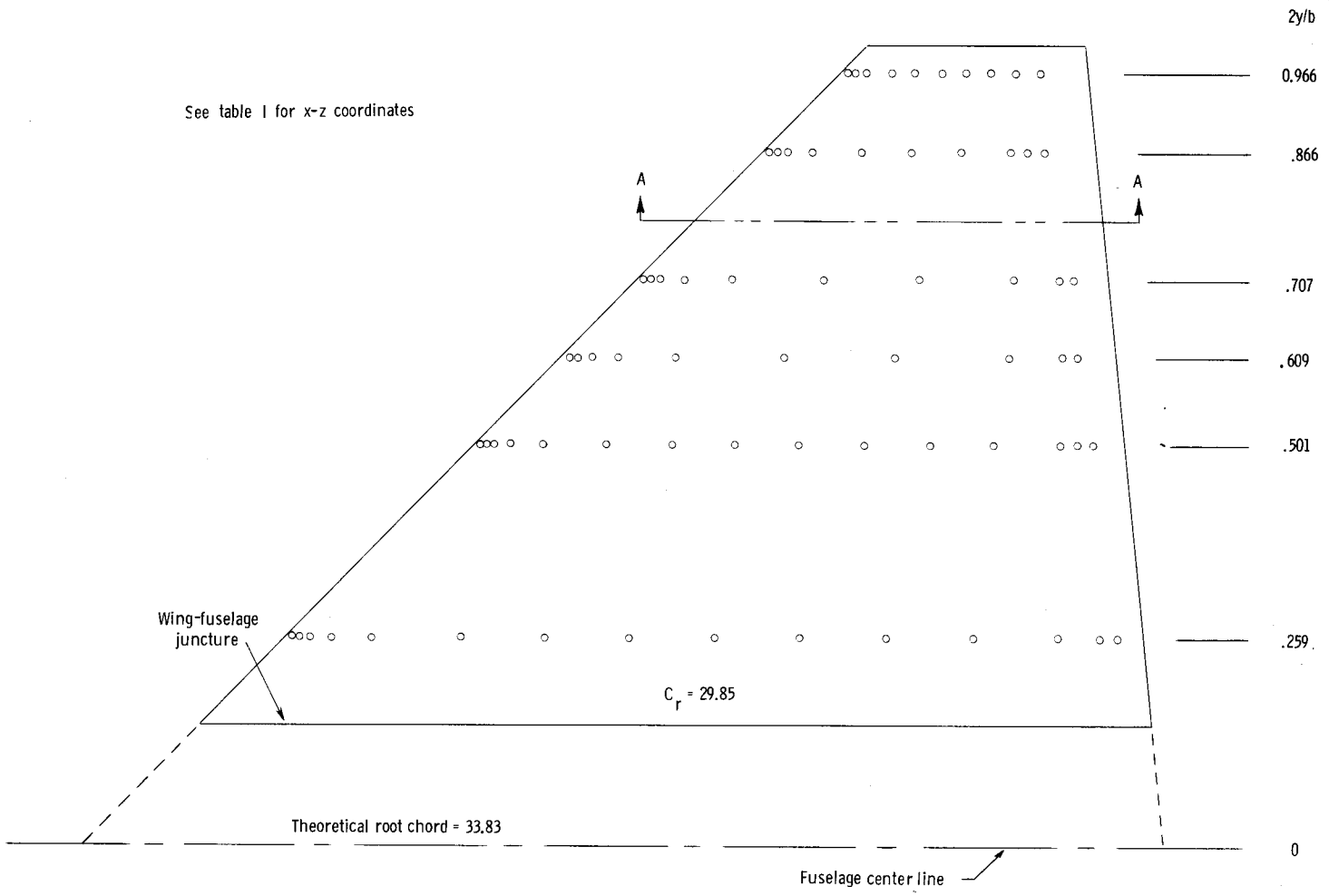

Section A-A (typical)

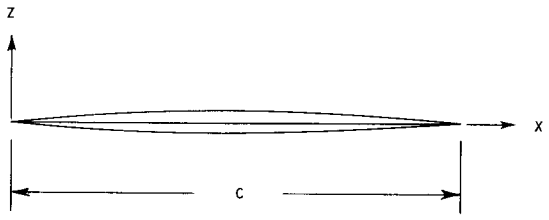

(b) Location of pressure orifices on upper surface of right wing and lower surface of left wing.

Figure 2.- Concluded.

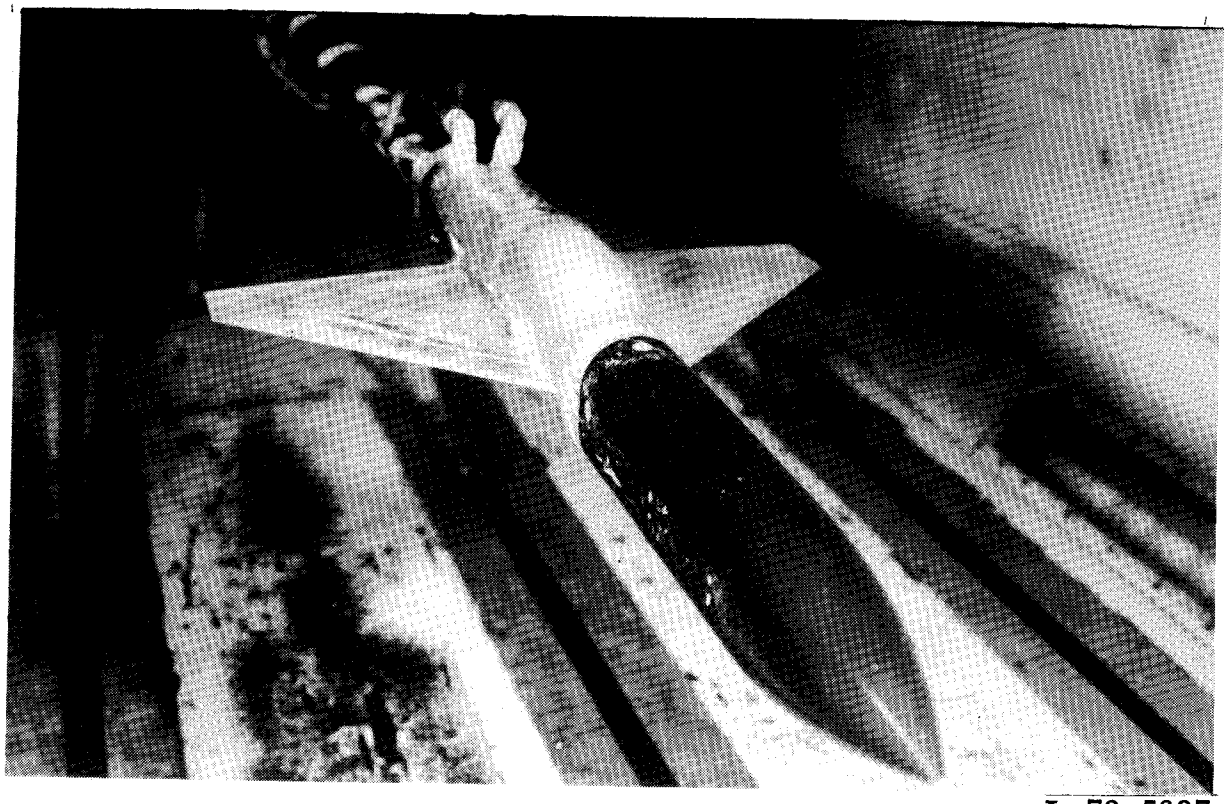

L-73-5687

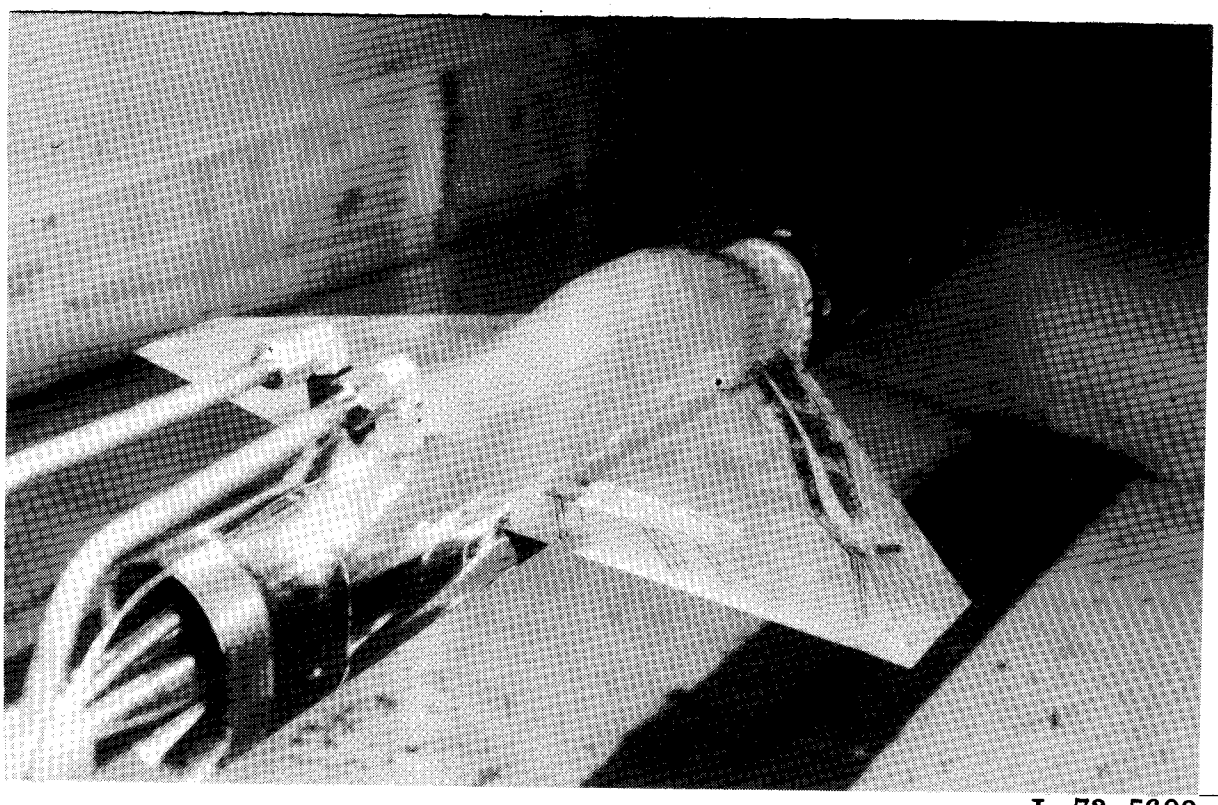

L-73-5690

Figure 3.- Photographs of model mounted in test section.

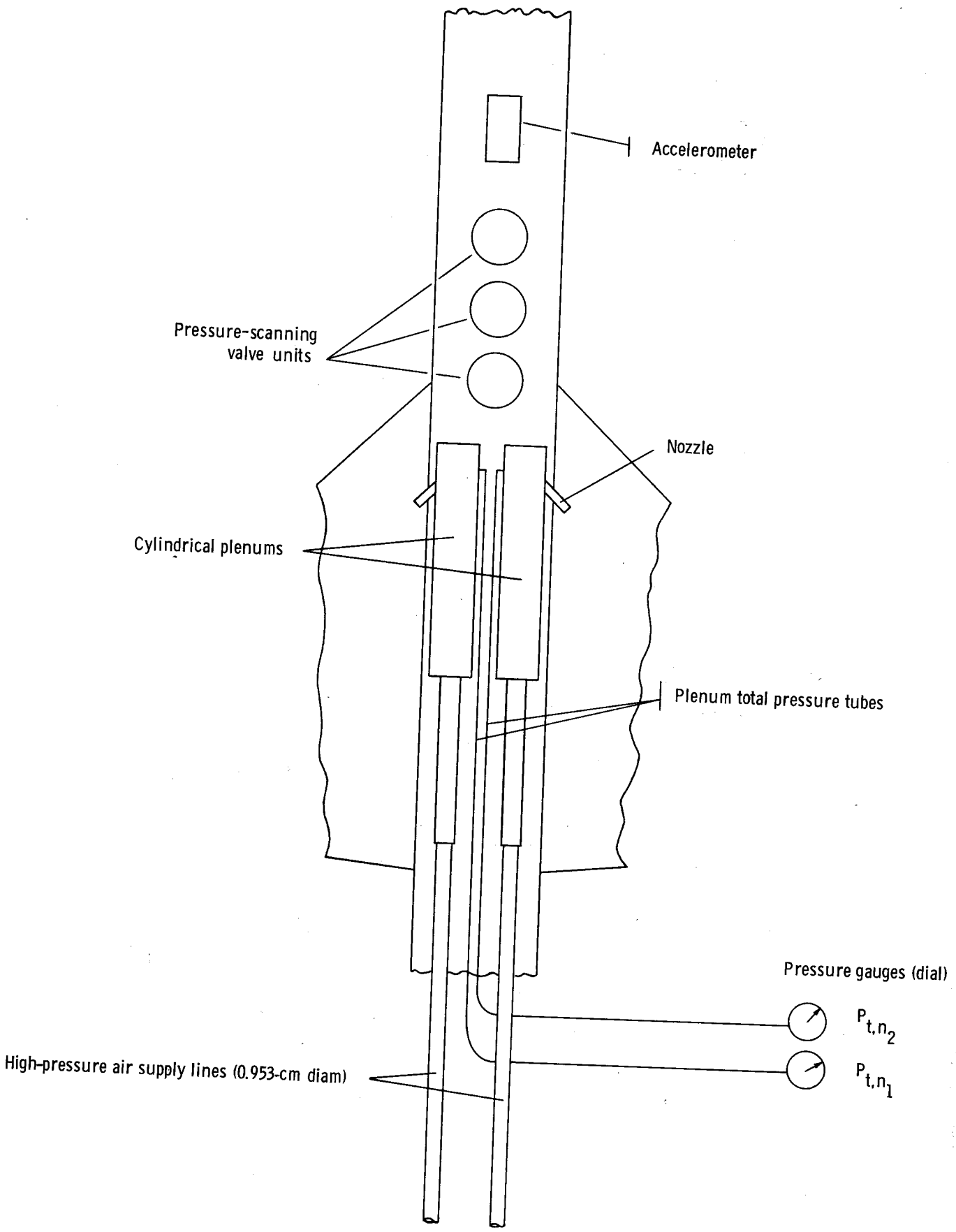

Figure 4.- Schematic of air supply system and measurement devices.

L-10047

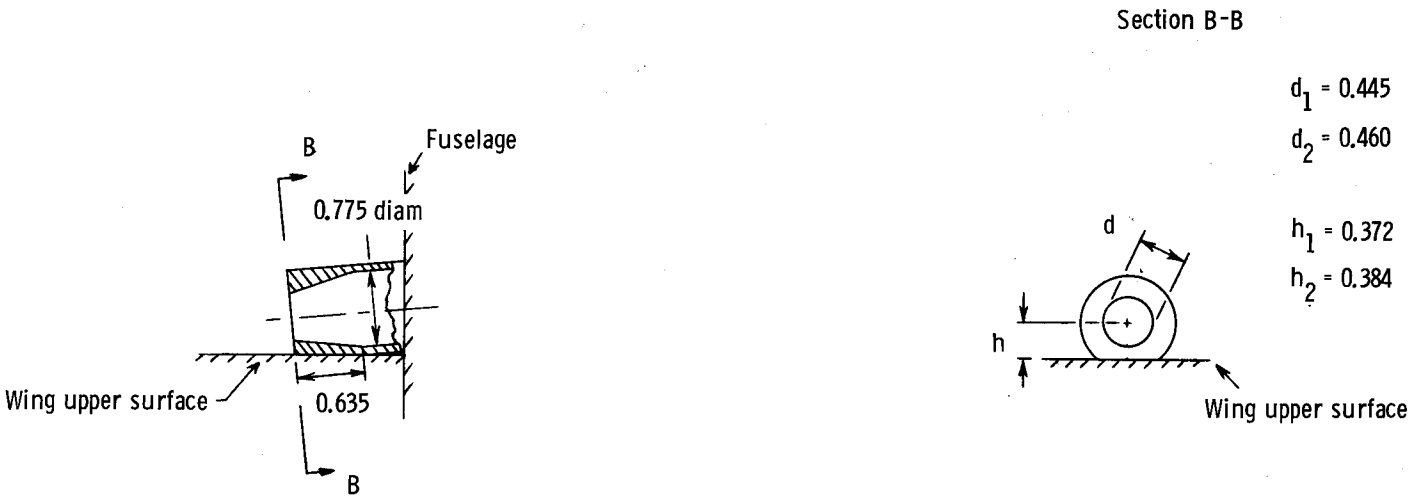

(a) h/d = 0.835.

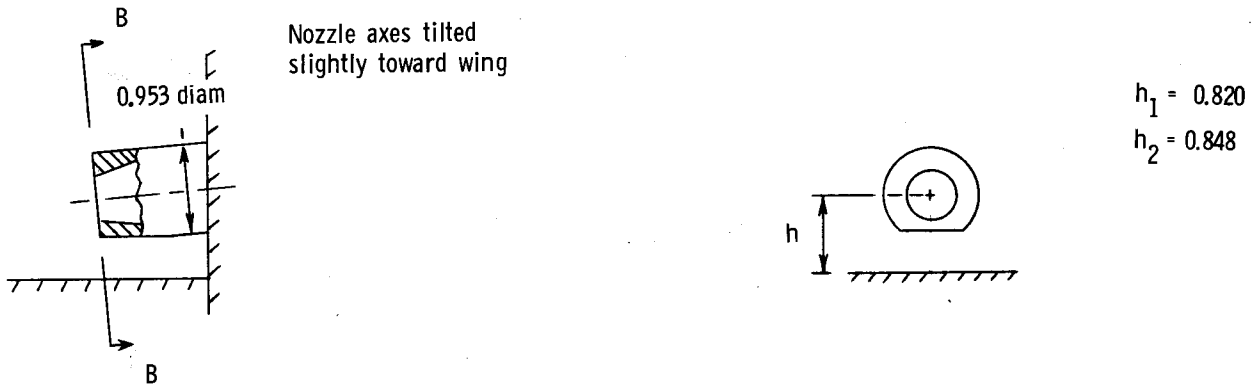

(b) h/d = 1.843.

Figure 5.- Nozzle geometry and vertical location. (All dimensions are in centimeters.)

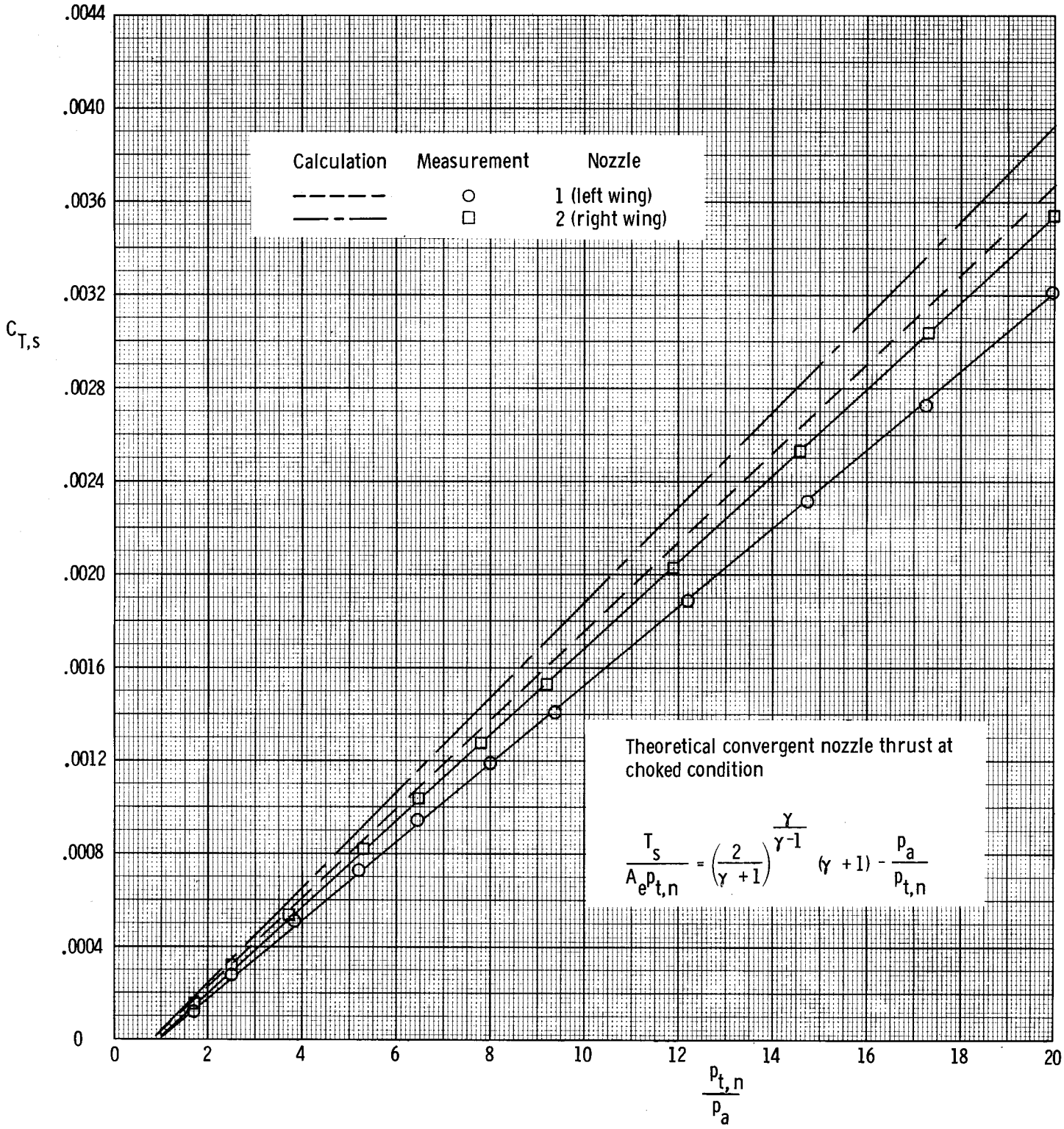

Figure 6.- Nozzle static thrust calibration.

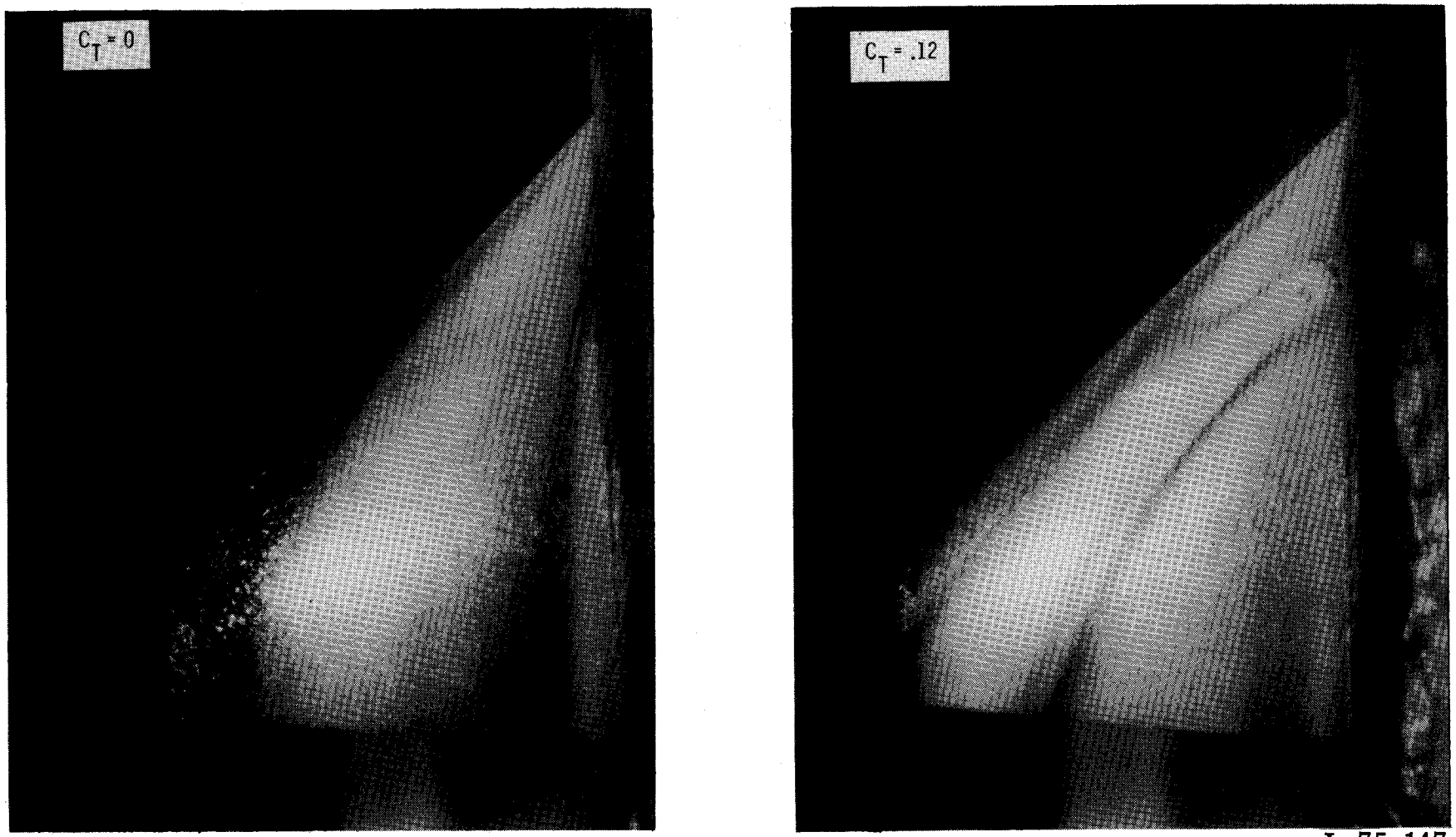

(a) $\alpha = 8.1^{o}$.

Figure 7.- Photographs of oil-flow patterns on upper surface of left wing; $x_n/c_r = 0.23$; $\Lambda_n = 33^{o}$; $h/d = 0.835$.

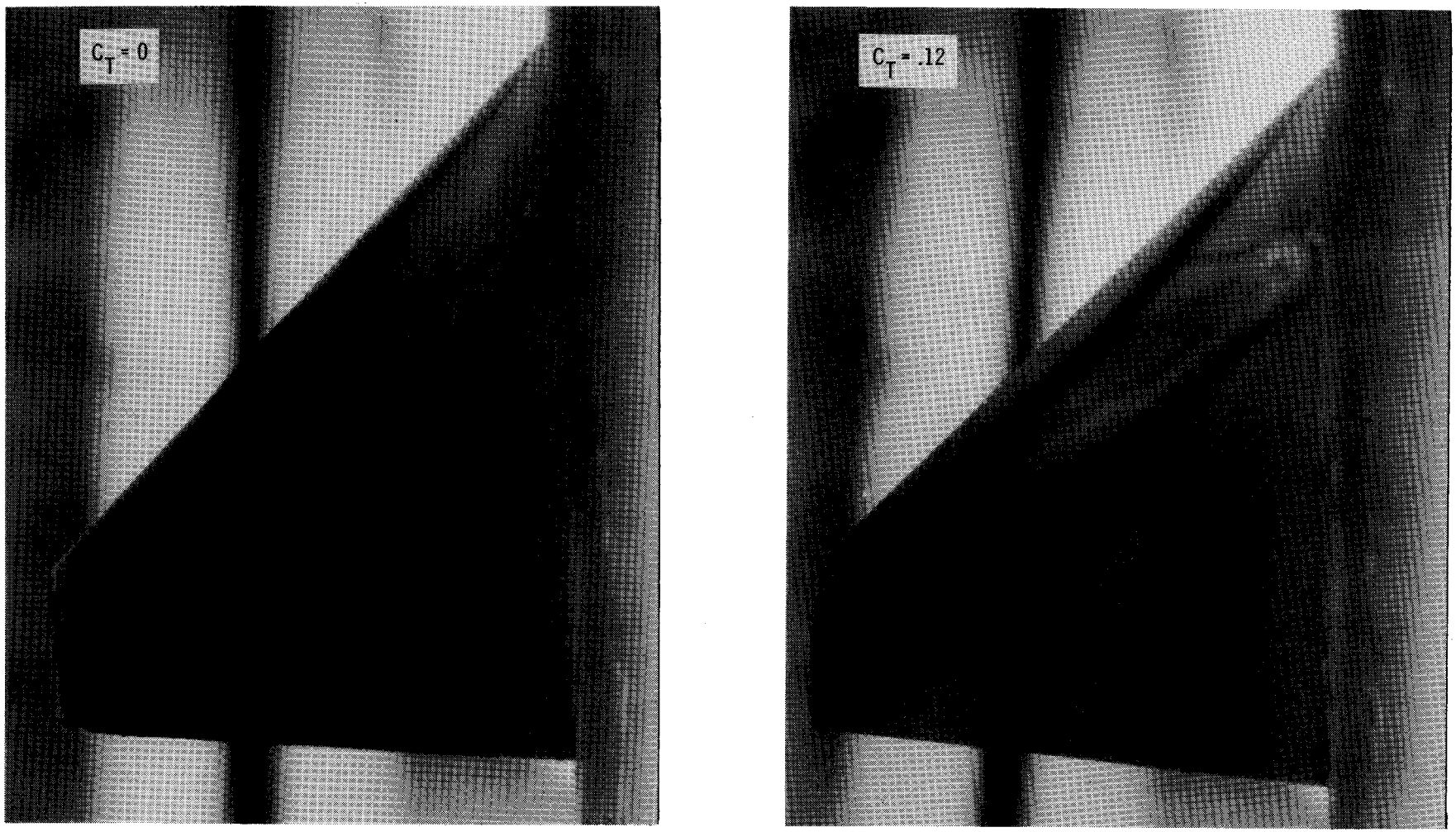

(b) $\alpha = 16.6^{o}$.

Figure 7.- Continued.

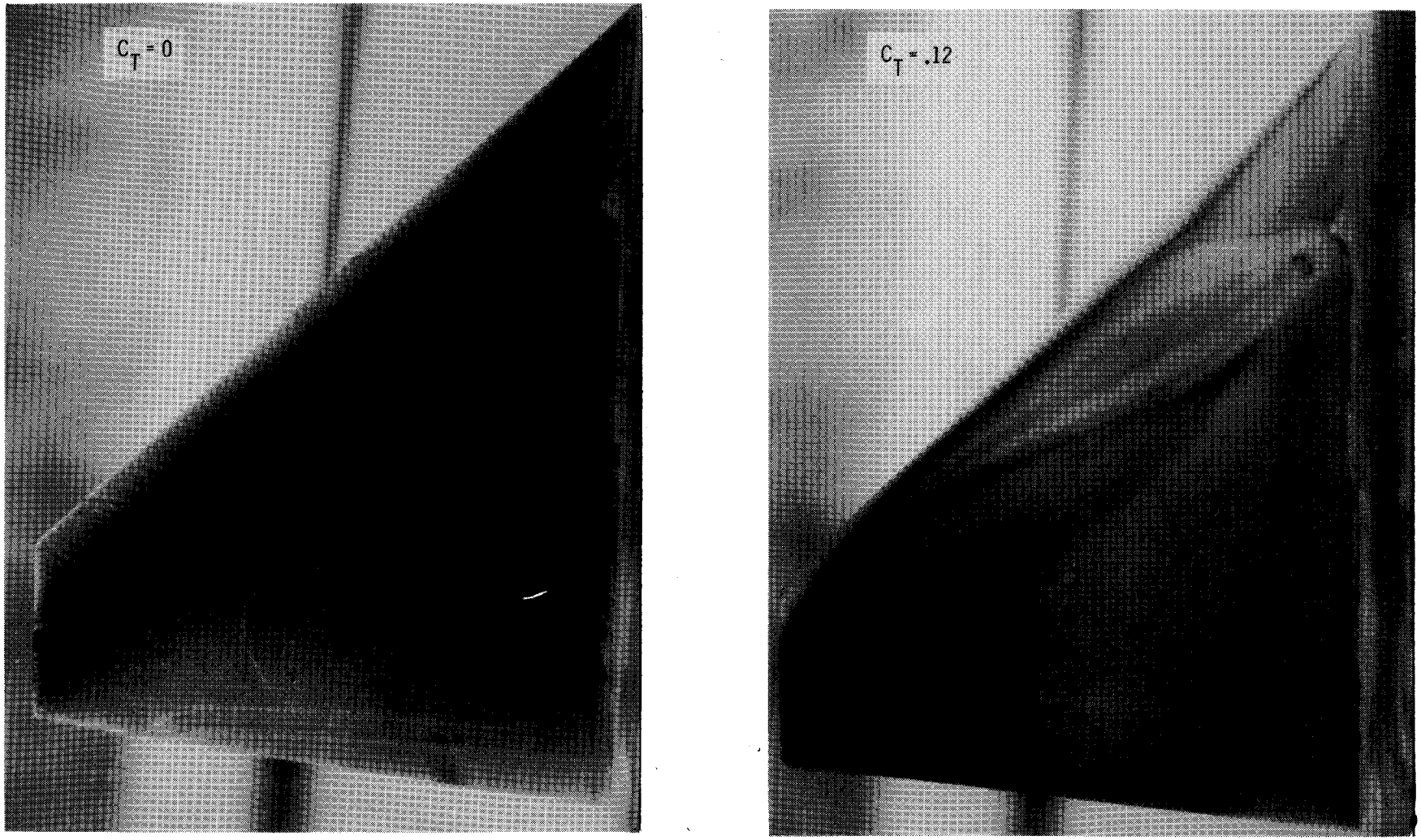

(c) $\alpha = 23.8^{\circ}$.

Figure 7.- Concluded.

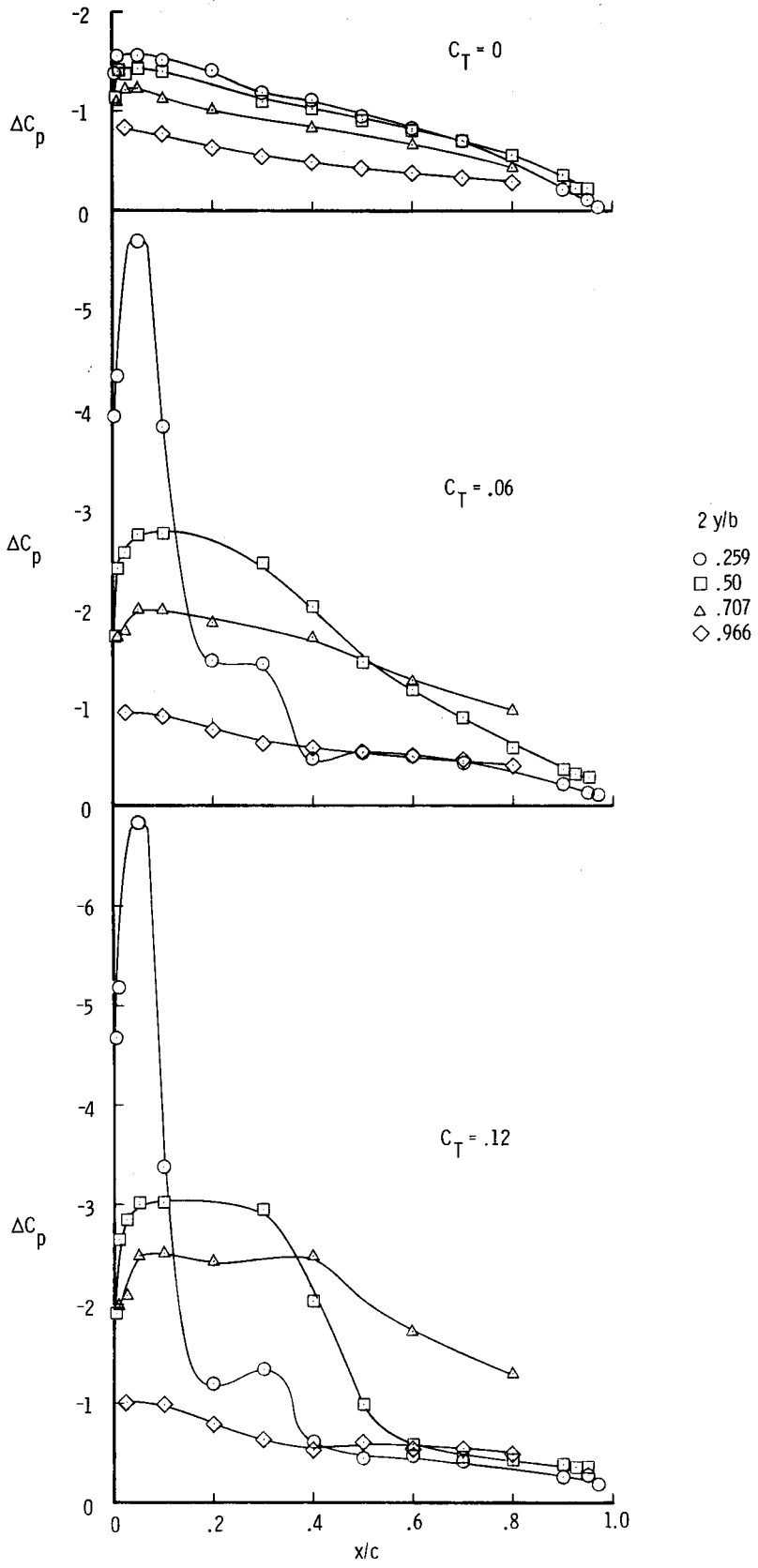

Figure 8.- Effect of span location on chordwise distributions of ΔC_p for several values of C_T; $\alpha = 20.6^o$; $x_n/c_r = 0.23$; $\Lambda_n = 44^o$; $h/d = 0.835$.

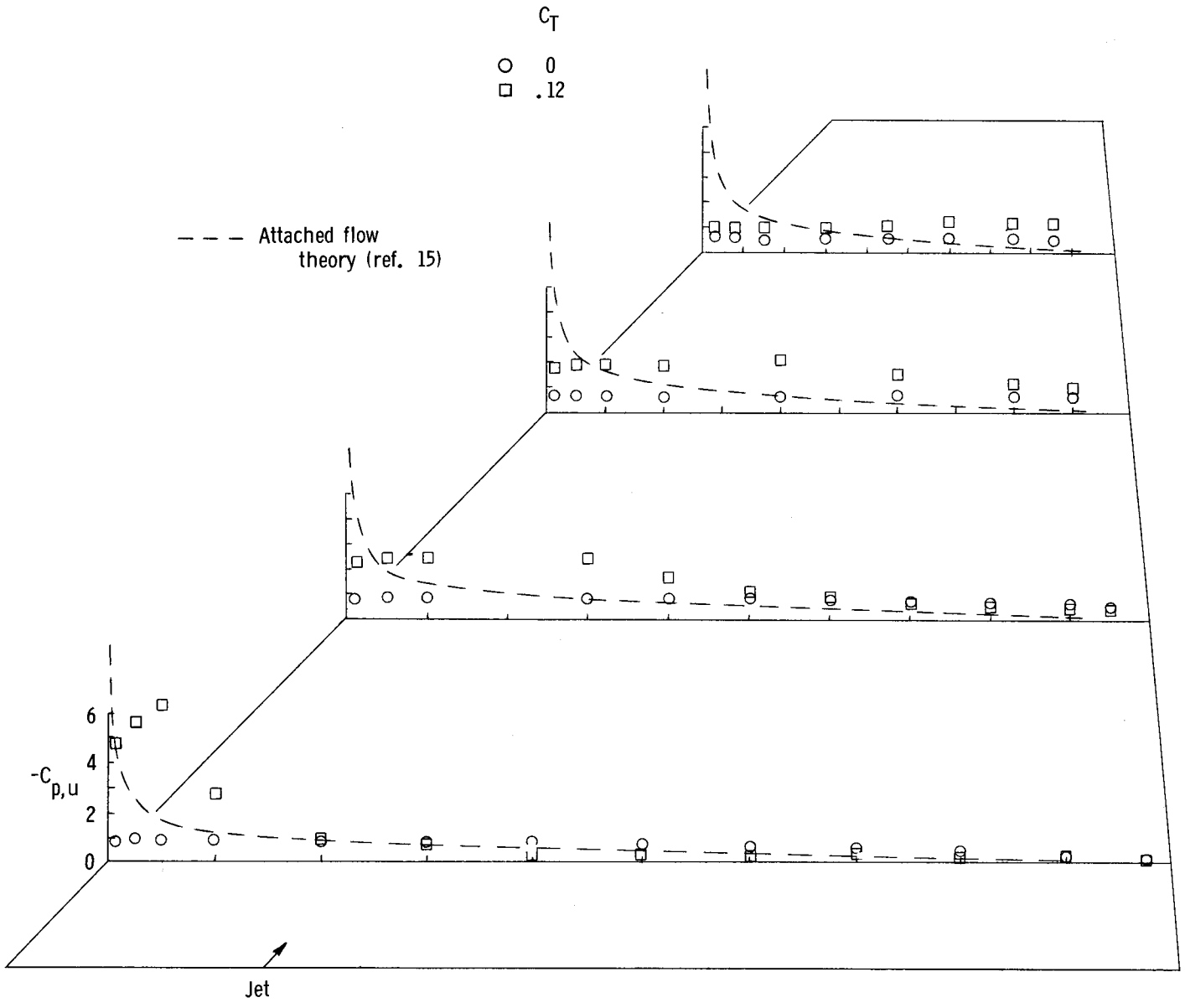

Figure 9.- Schematic of wing pressure field for $\alpha \approx 20.6^{o}$; $x_n/c_r = 0.23$; $\Lambda_n = 44^{o}$; $h/d = 0.835$.

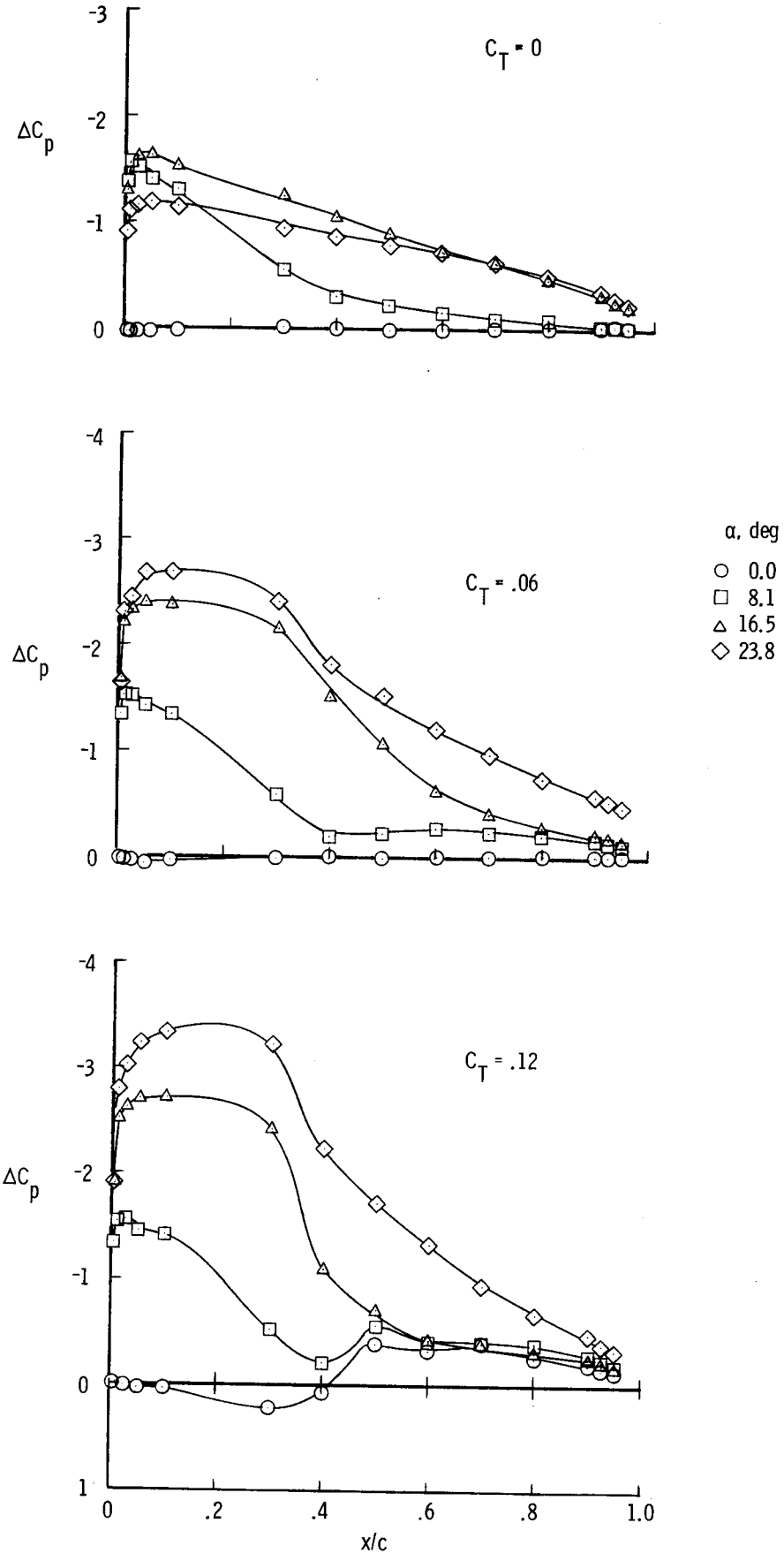

Figure 10.- Effect of angle of attack on chordwise distributions of ΔC_p at $2y/b = 0.5$ for several values of C_T; $x_n/c_r = 0.23$; $\Lambda_n = 44^o$; $h/d = 0.835$.

L-10047

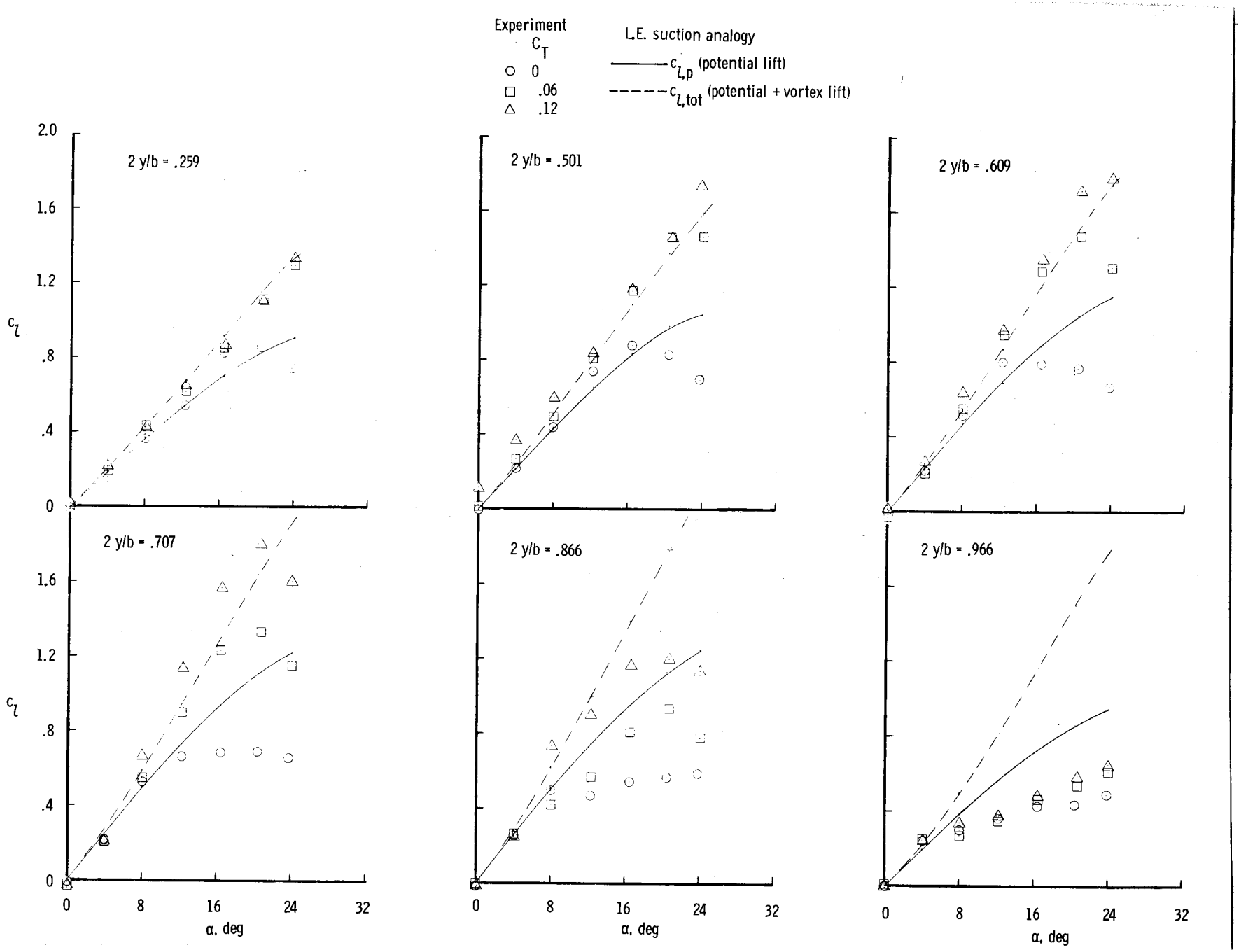

Figure 11.- Effect of spanwise blowing on section lift characteristics for different span locations on wing; $x_n/c_r = 0.23$; $\Lambda_n = 44^o$; $h/d = 0.835$.

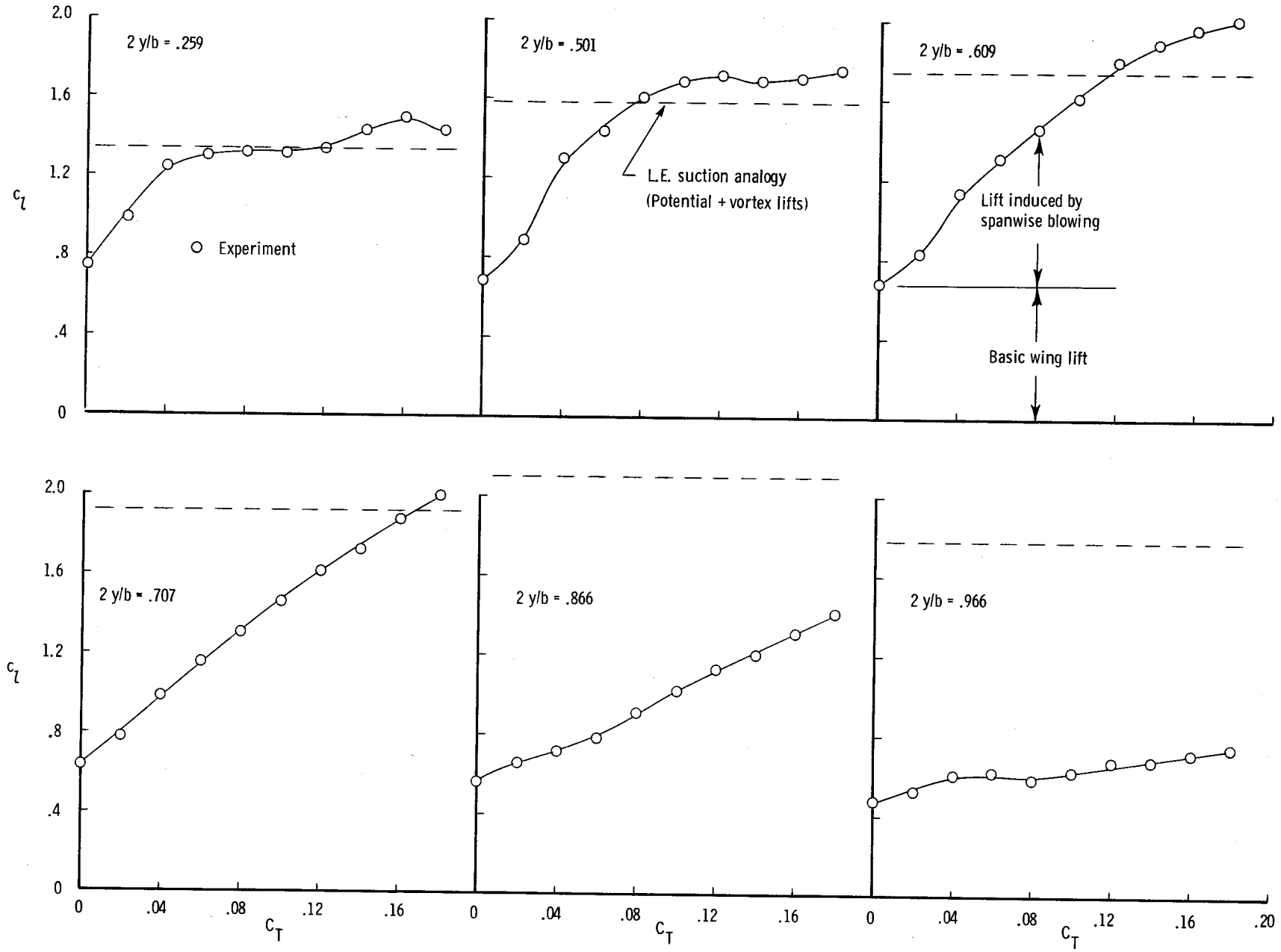

Figure 12.- Variation of section lift coefficient with C_T at various span locations on the wing; $\alpha = 23.9^o$; $x_n/c_r = 0.23$; $\Lambda_n = 44^o$; $h/d = 0.835$.

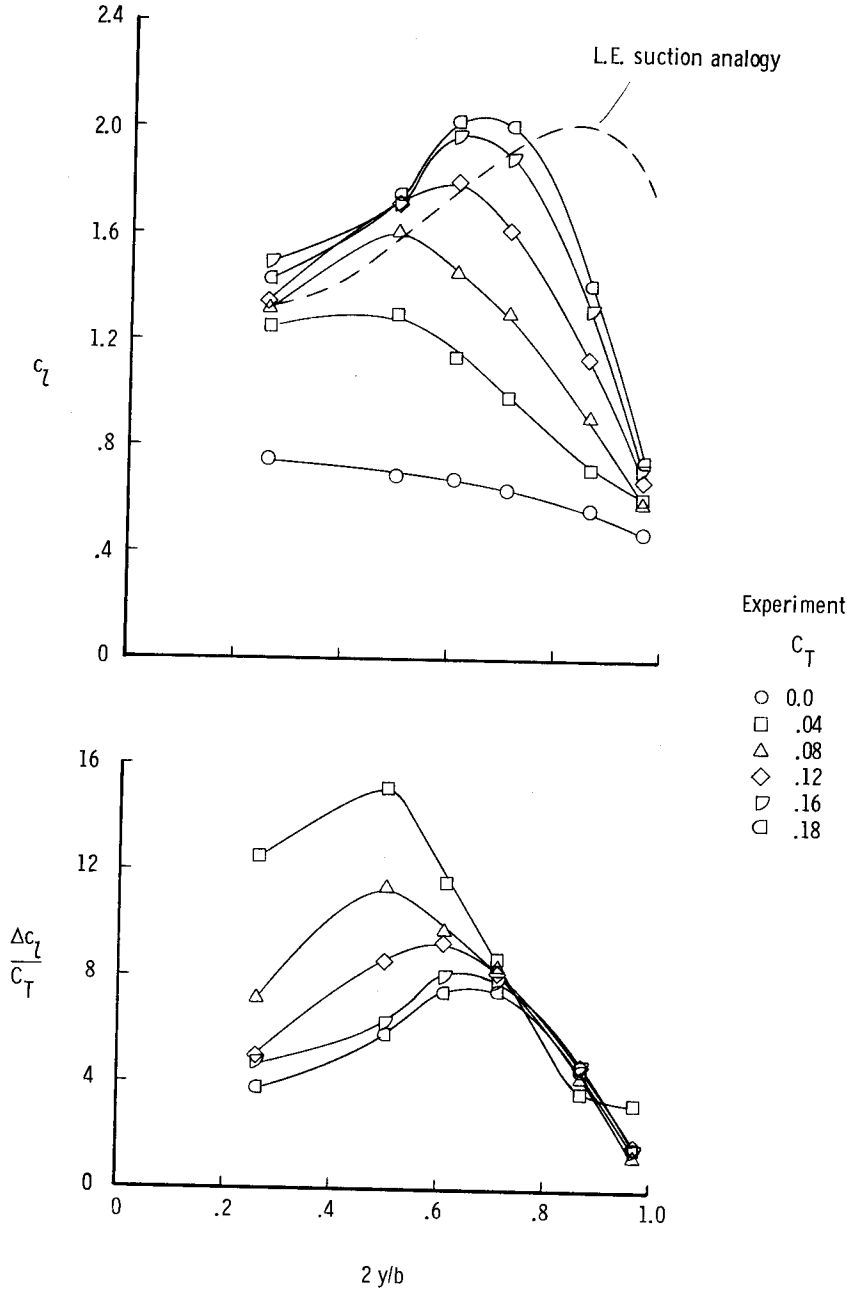

Figure 13.- Variation of section lift coefficient and lift-augmentation ratio along the span for a range of C_T; $\alpha = 23.9^o$; $x_n/c_r = 0.23$; $\Lambda_n = 44^o$; $h/d = 0.835$.

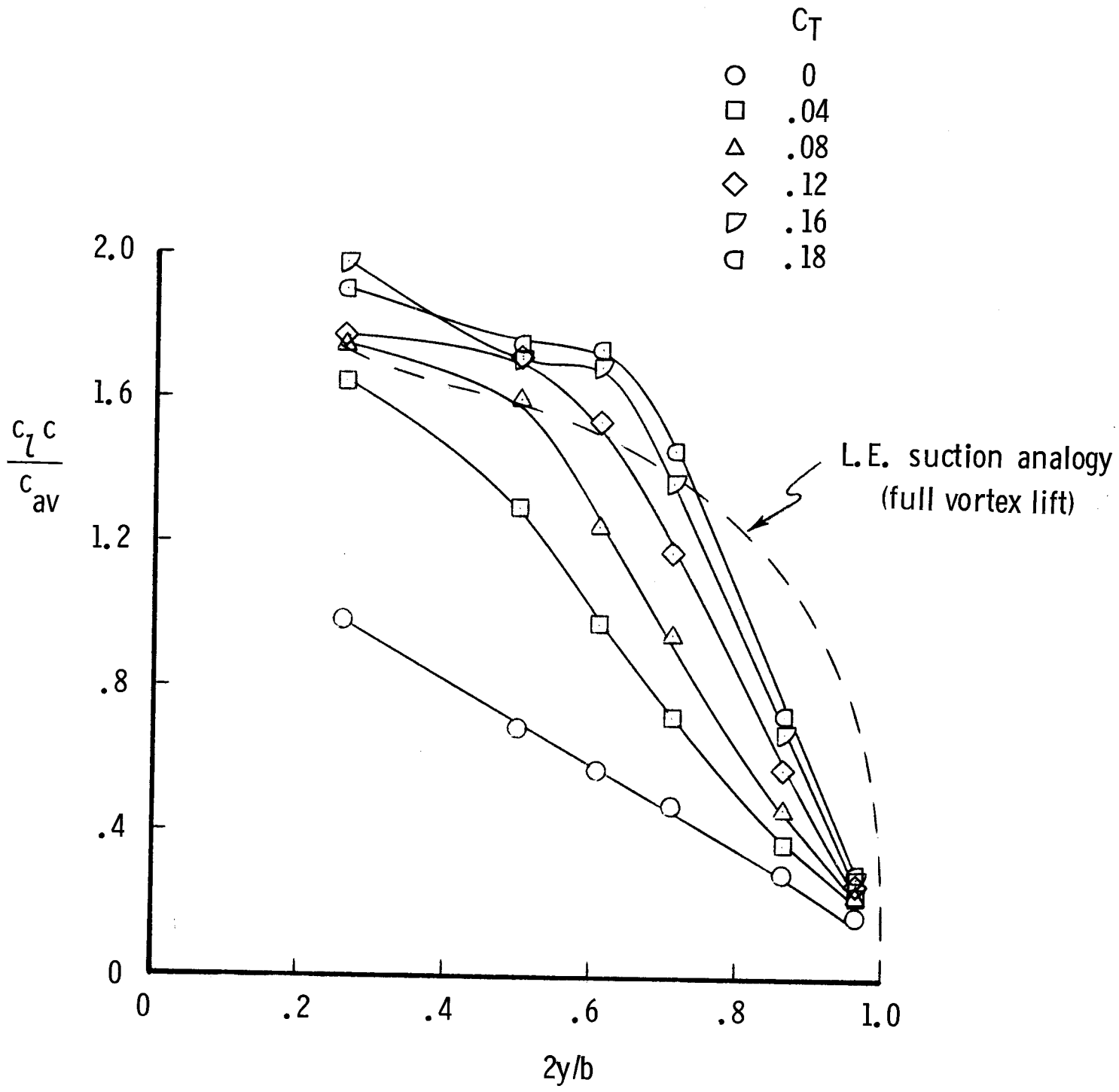

Figure 14.- Effect of blowing on span loading for the wing at $\alpha = 23.9^{o}$; $x_n/c_r = 0.23$; $\Lambda_n = 44^{o}$; $h/d = 0.835$.

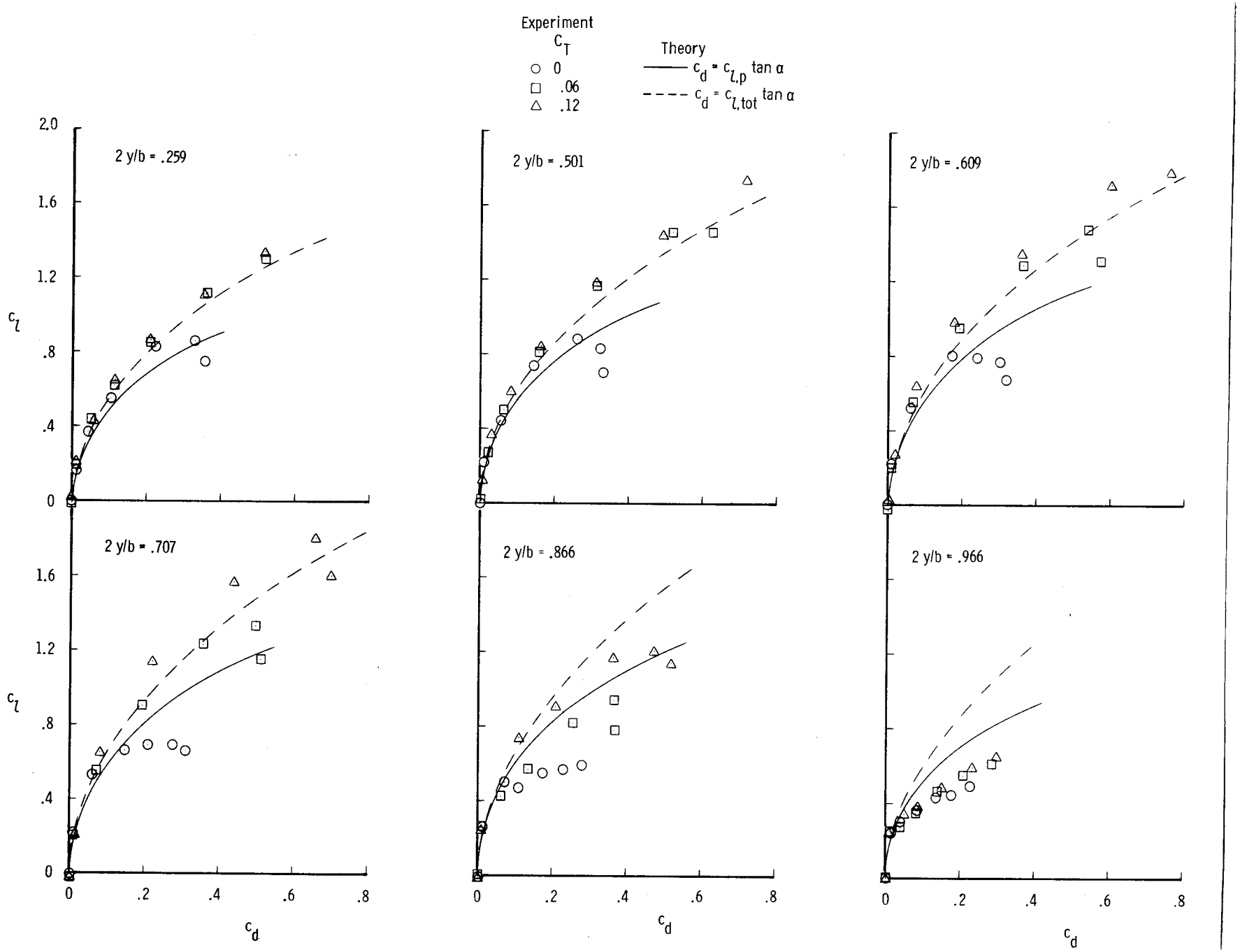

Figure 15.- Effect of spanwise blowing on section drag characteristics for different span locations on wing; $x_n/c_r = 0.23$; $\Lambda_n = 44^o$; $h/d = 0.835$.

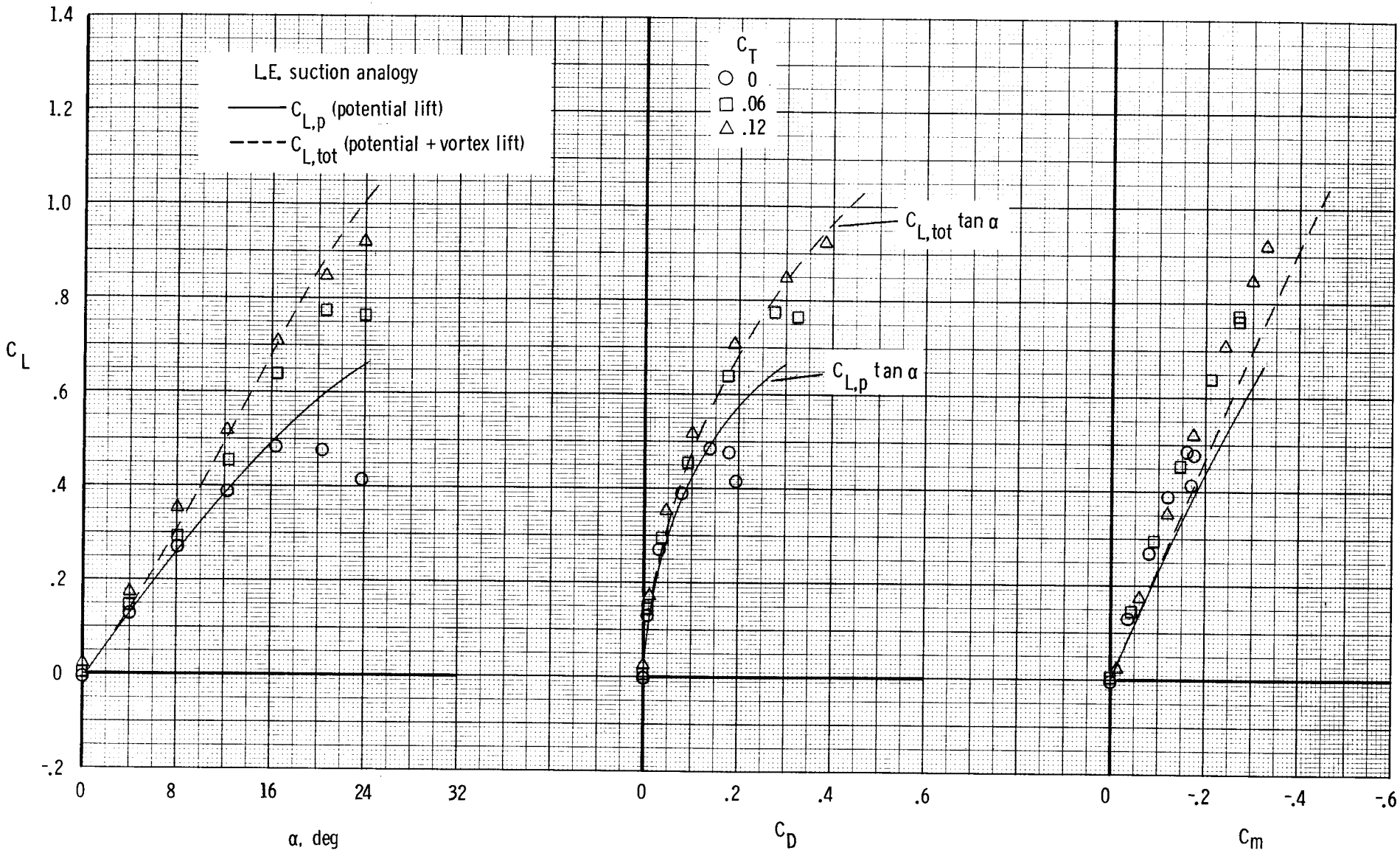

Figure 16.- Effect of spanwise blowing on longitudinal aerodynamic characteristics; $x_n/c_r = 0.23$; $\Lambda_n = 44^o$; $h/d = 0.835$.

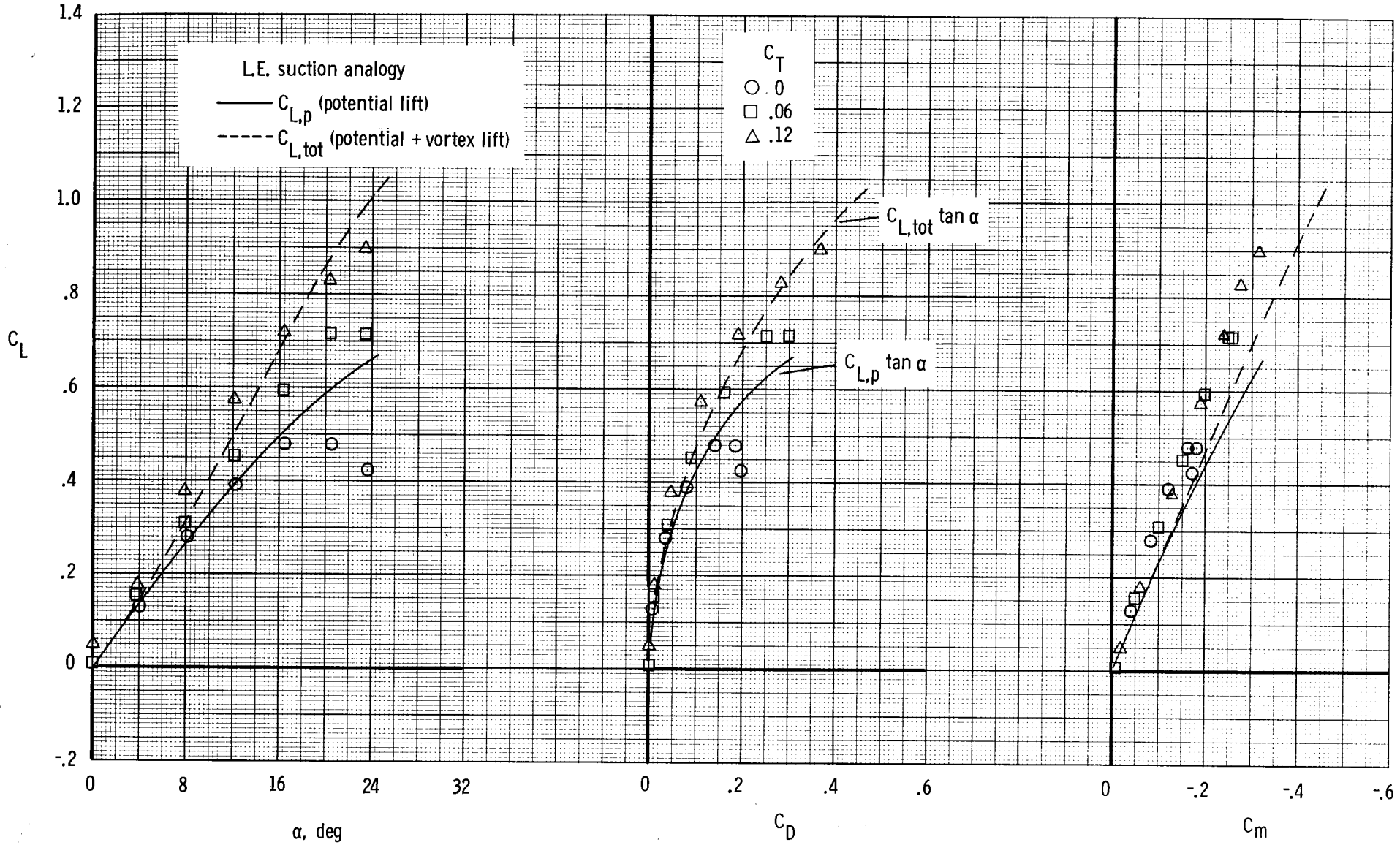

Figure 17.- Effect of spanwise blowing on longitudinal aerodynamic characteristics; $x_n/c_r = 0.15$; $\Lambda_n = 44^o$; $h/d = 0.835$.

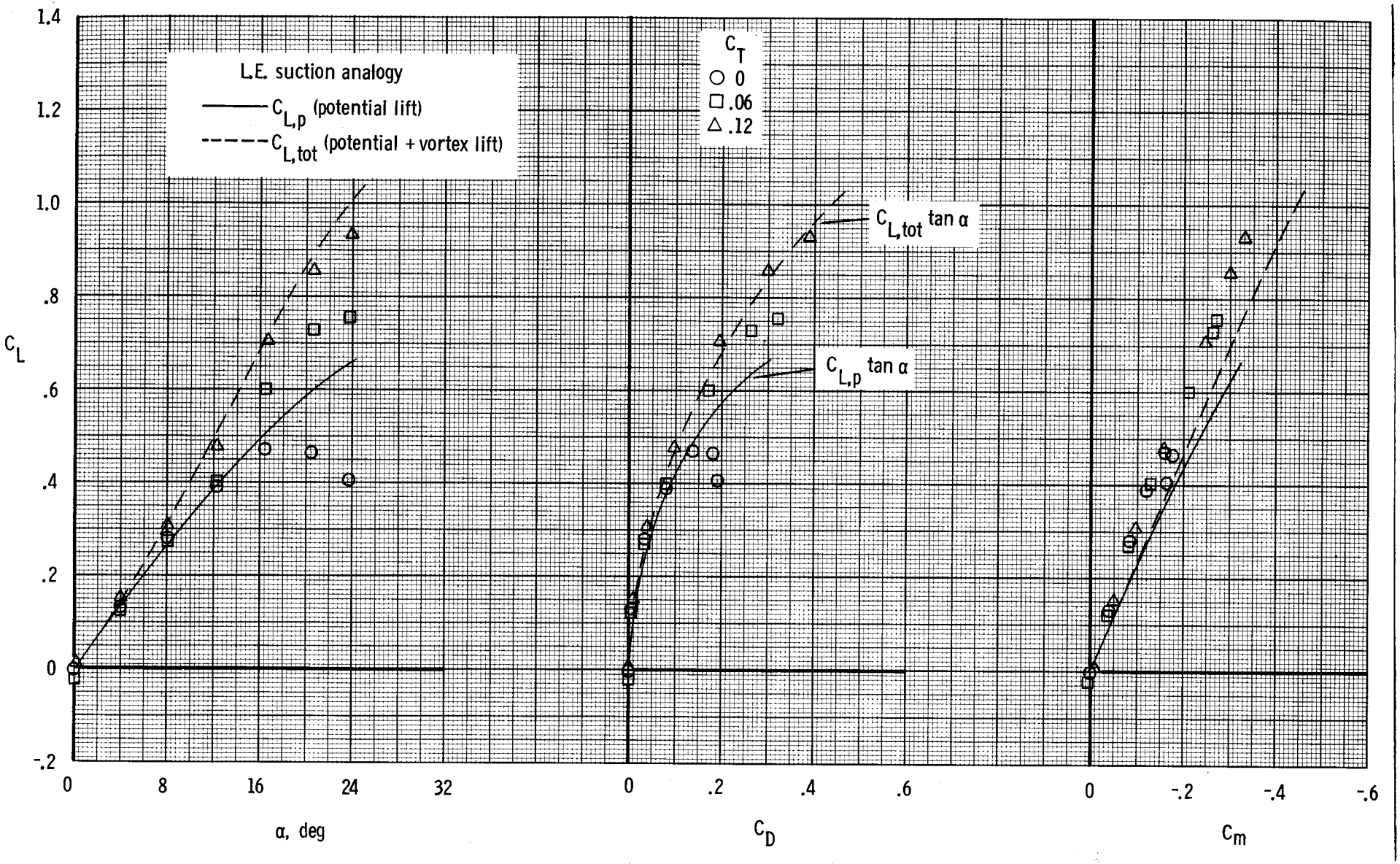

Figure 18.- Effect of spanwise blowing on longitudinal aerodynamic characteristics; $x_n/c_r = 0.23$; $\Lambda_n = 44^o$; $h/d = 1.843$.

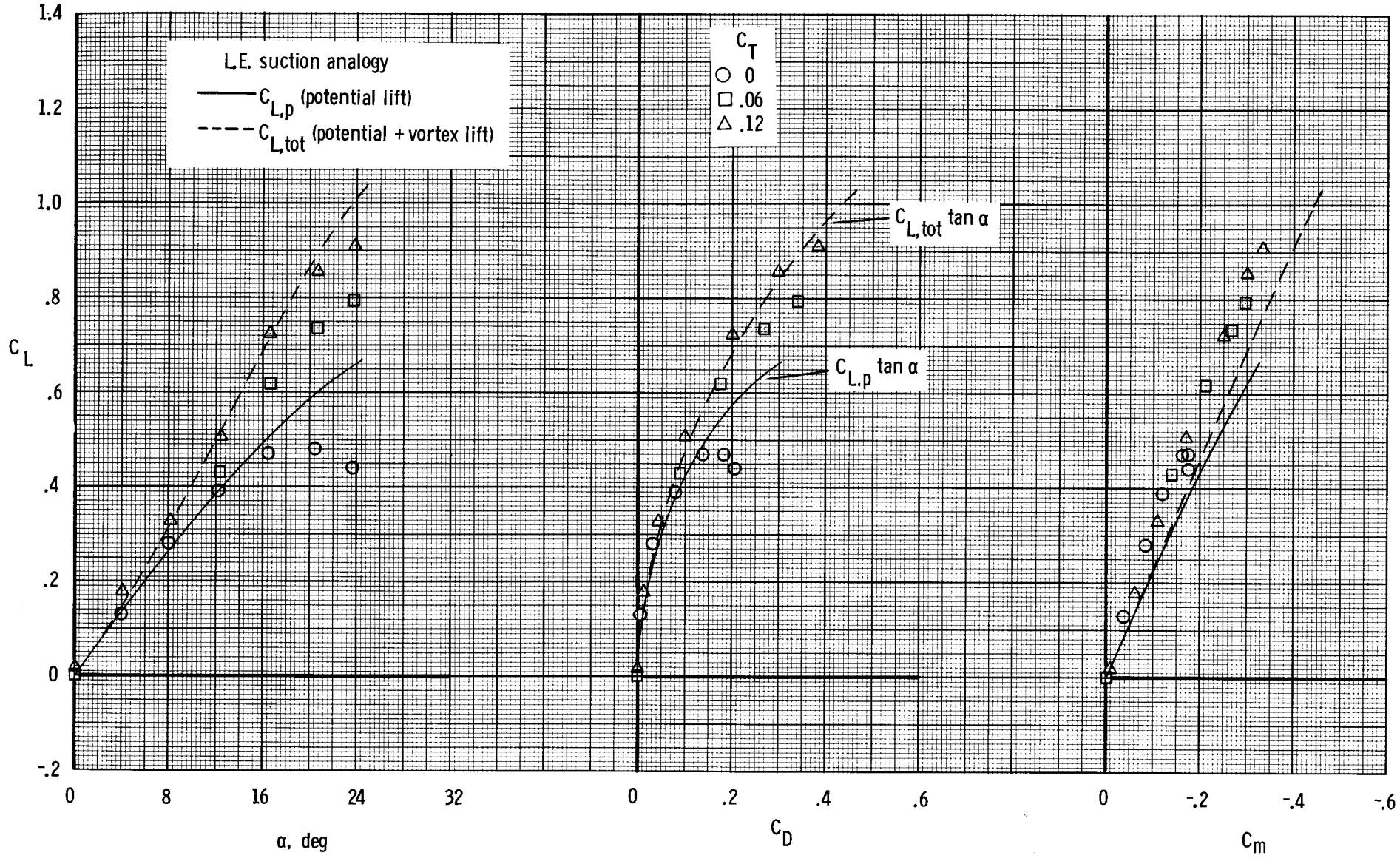

Figure 19.- Effect of spanwise blowing on longitudinal aerodynamic characteristics; $x_n/c_r = 0.32$; $\Lambda_n = 44^o$; $h/d = 0.835$.

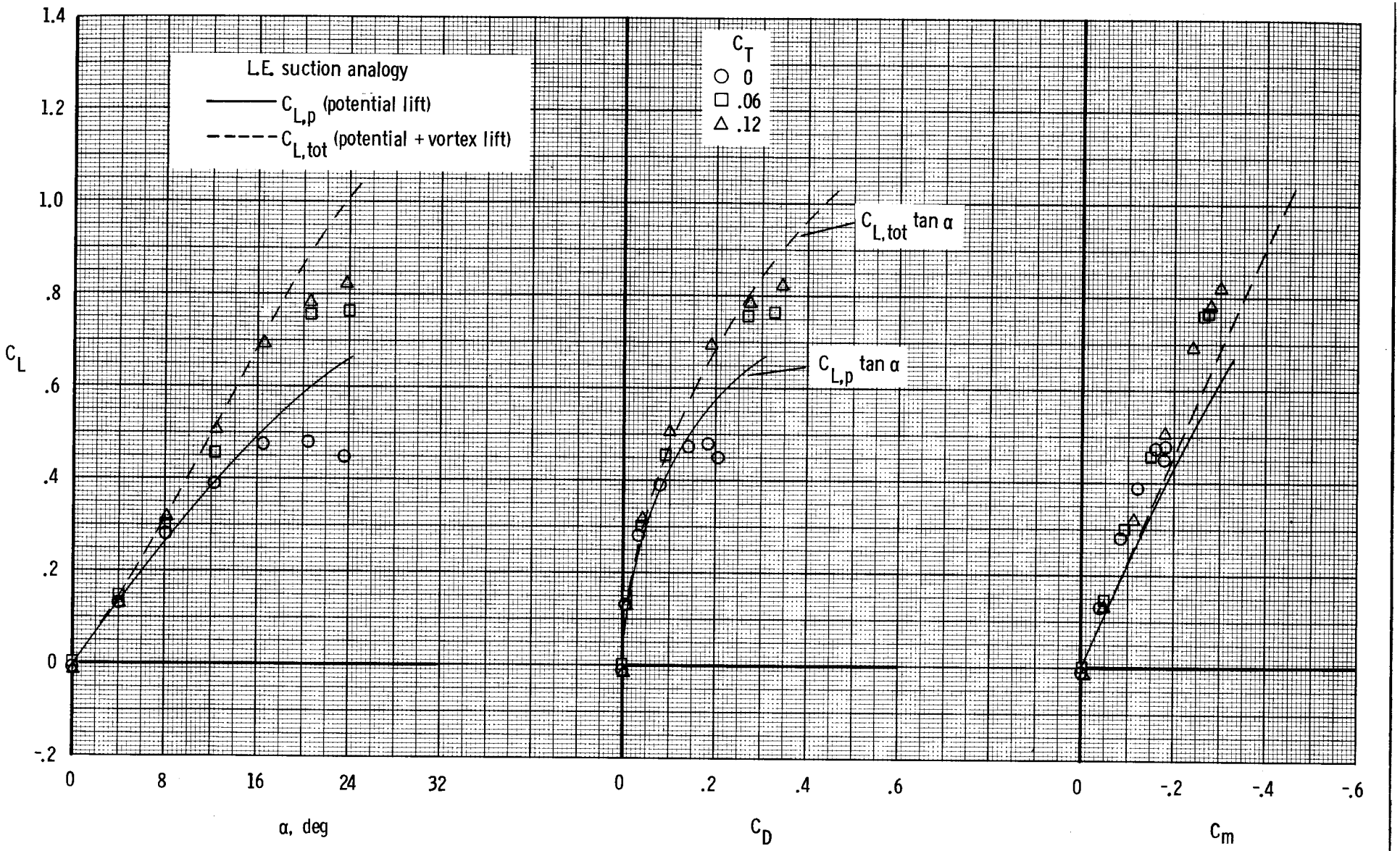

Figure 20.- Effect of spanwise blowing on longitudinal aerodynamic characteristics; $x_n/c_r = 0.32$; $\Lambda_n = 33^o$; $h/d = 0.835$.

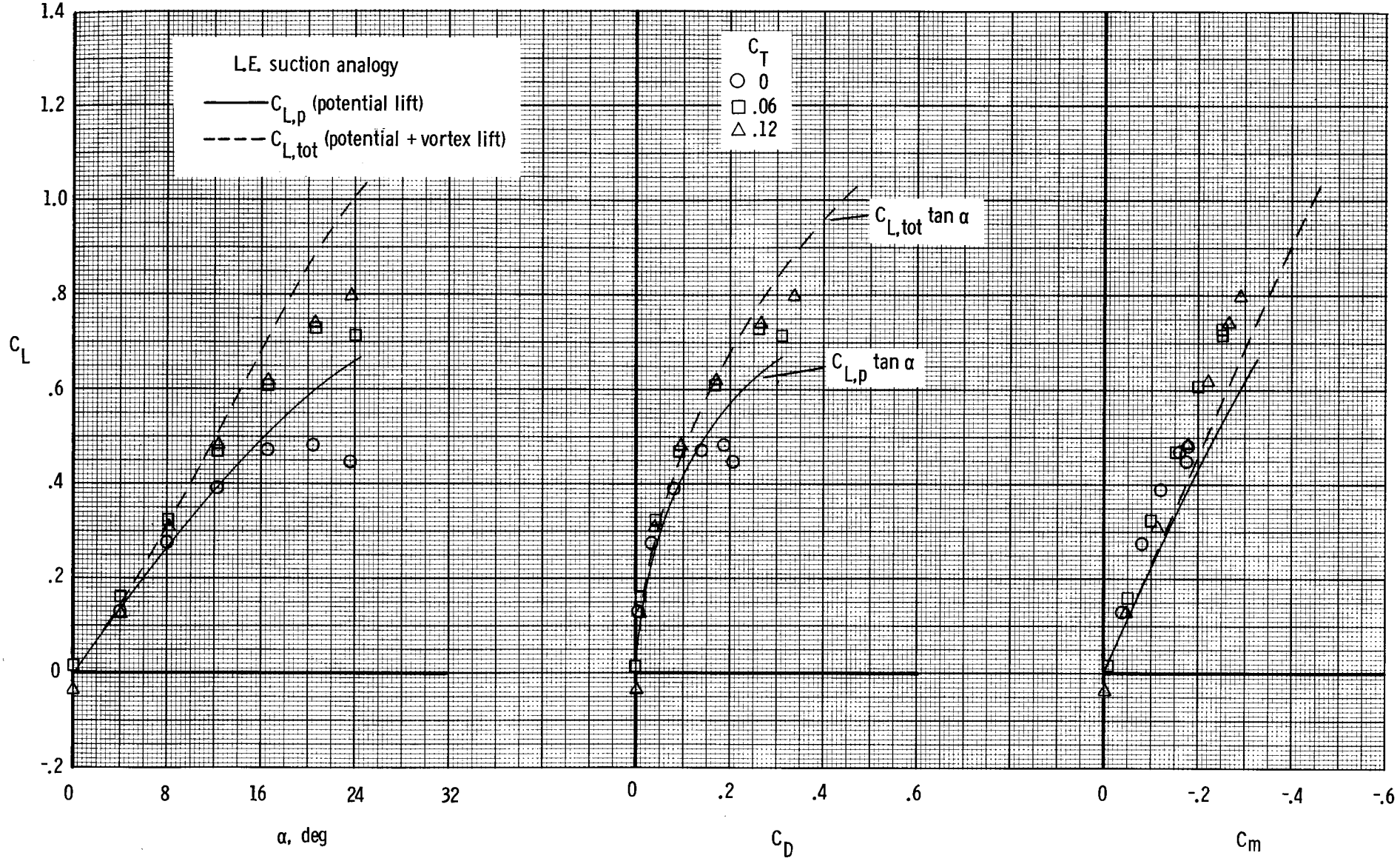

Figure 21.- Effect of spanwise blowing on longitudinal aerodynamic characteristics; $x_n/c_r = 0.23$; $\Lambda_n = 33^o$; $h/d = 0.835$.

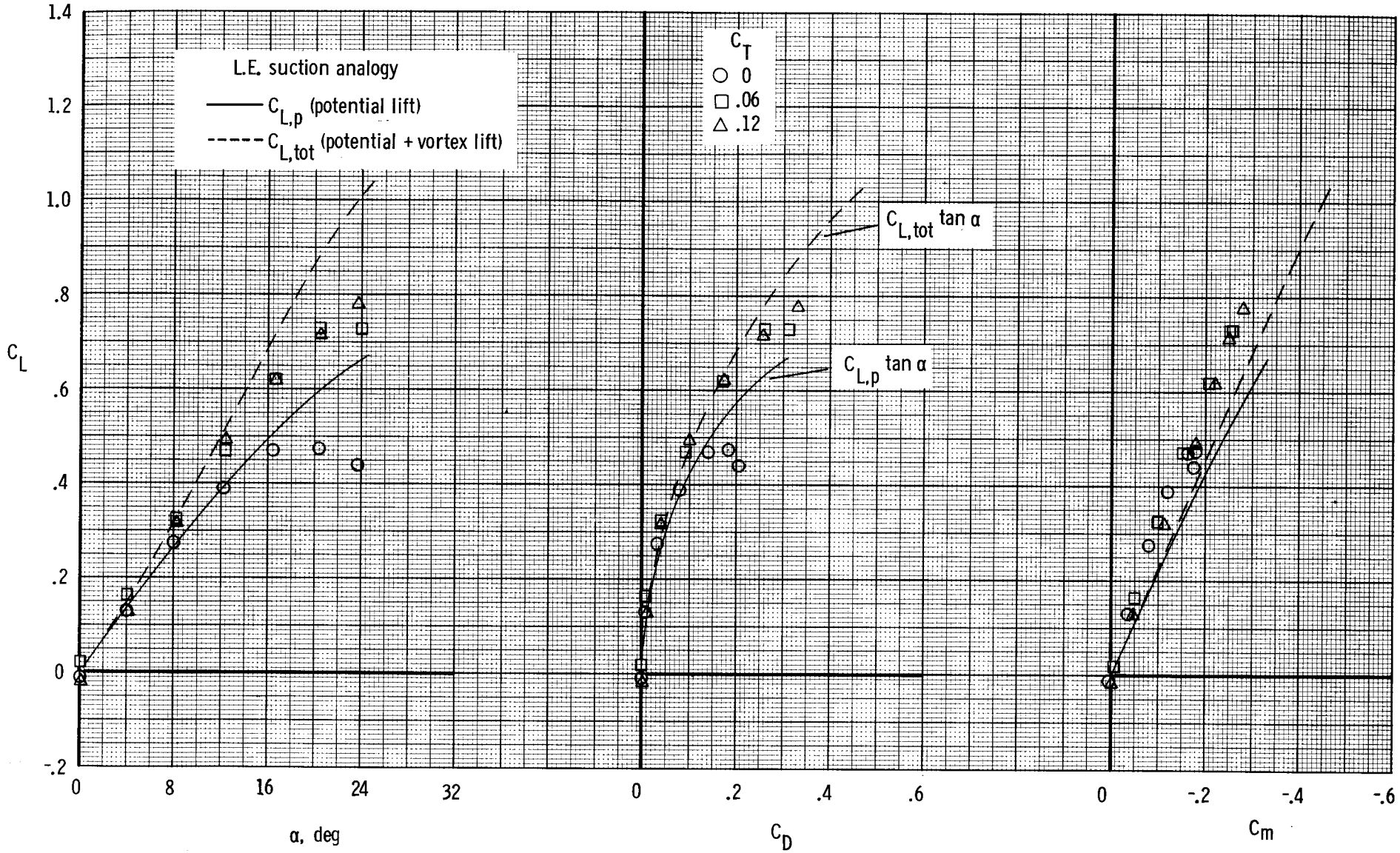

Figure 22.- Effect of spanwise blowing on longitudinal aerodynamic characteristics of model with transition strips; $x_n/c_r = 0.23$; $\Lambda_n = 33^o$; $h/d = 0.835$.

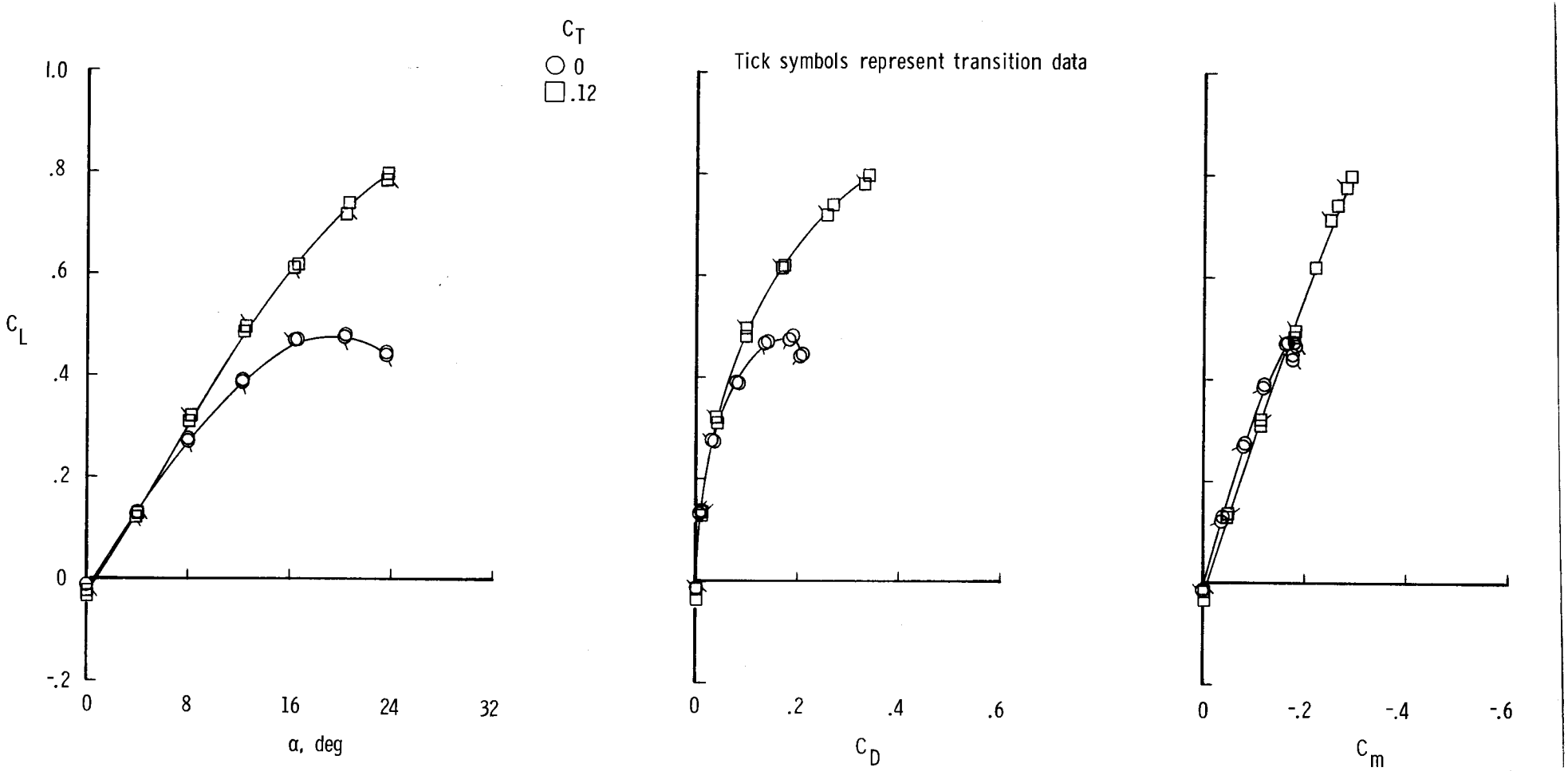

Figure 23.- Effect of transition strips on longitudinal aerodynamic characteristics with and without blowing; $x_n/c_r = 0.23$; $\Lambda_n = 33^o$; $h/d = 0.835$.

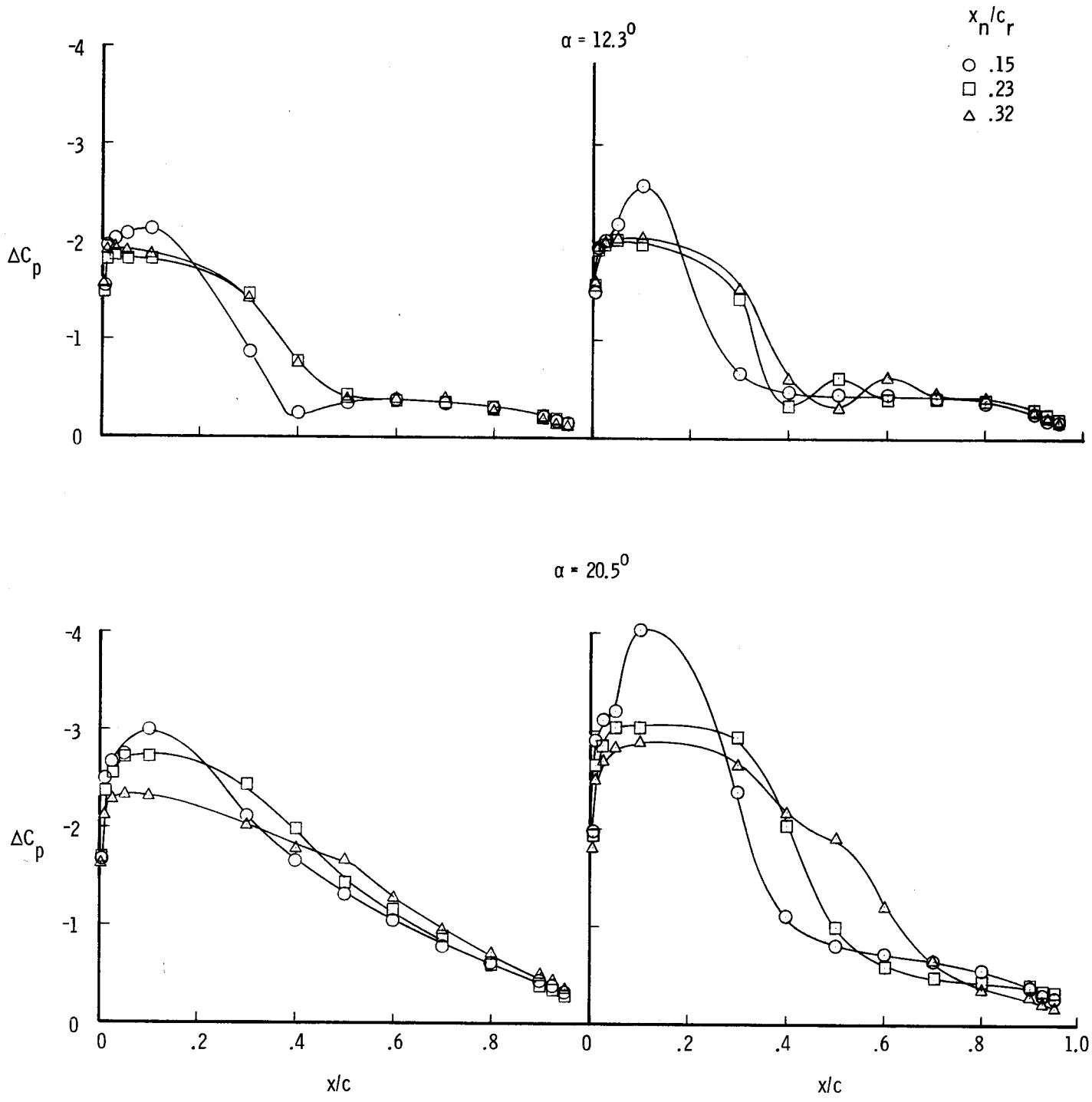

(a) $C_T = 0.06$.

(b) $C_T = 0.12$.

Figure 24.- Effect of x_n/c_r on chordwise distributions of ΔC_p at $2y/b = 0.5$ for two values of α and C_T; $\Lambda_n = 44^o$; $h/d = 0.835$.

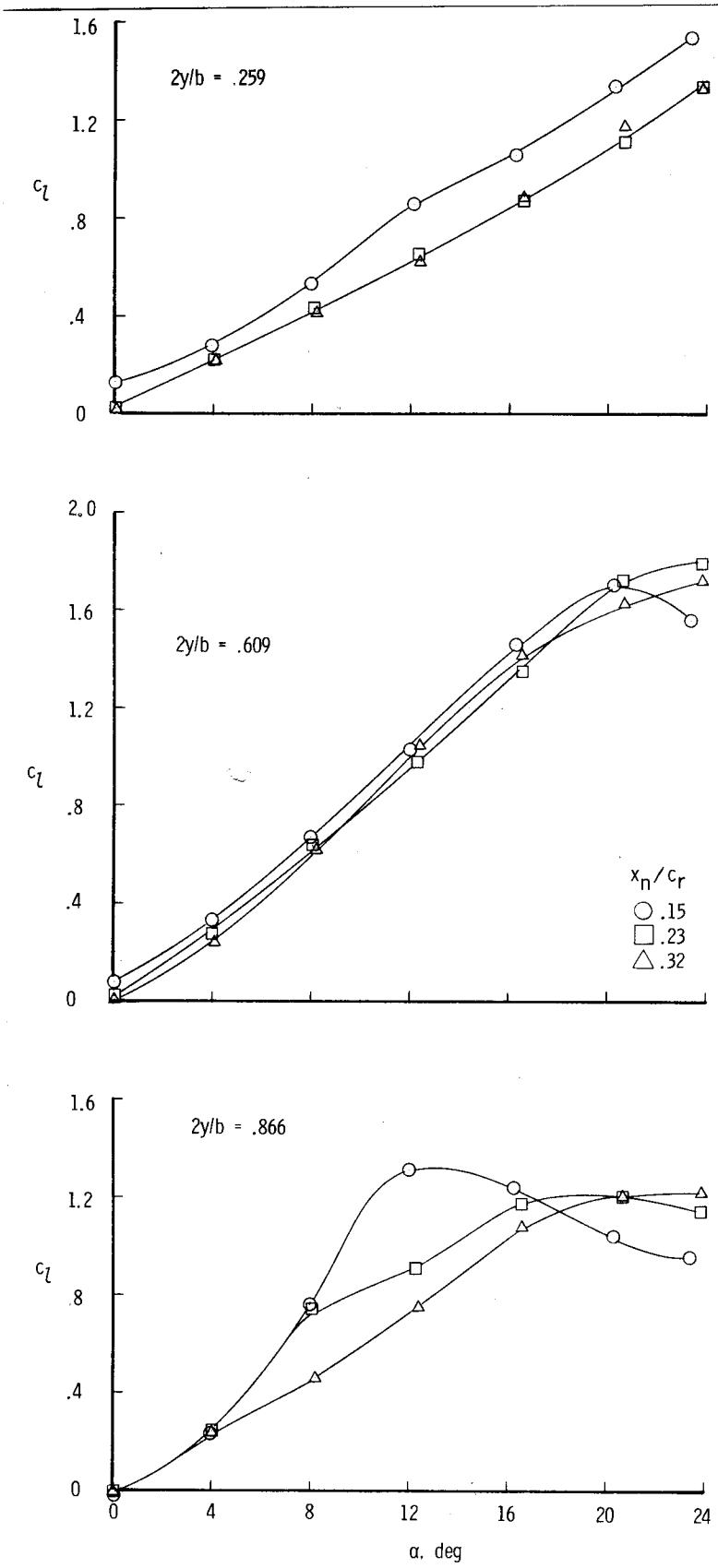

Figure 25.- Effect of $\overline{x_n/c_r}$ on section lift characteristics at several span locations with $C_T = 0.12$; $\Lambda_{\overline{n}} = 44^o$; $h/d = 0.835$.

Figure 26.- Effect of x_n/c_r on longitudinal aerodynamic characteristics for $C_T = 0.12$; $\Lambda_n = 44^o$; $h/d = 0.835$.

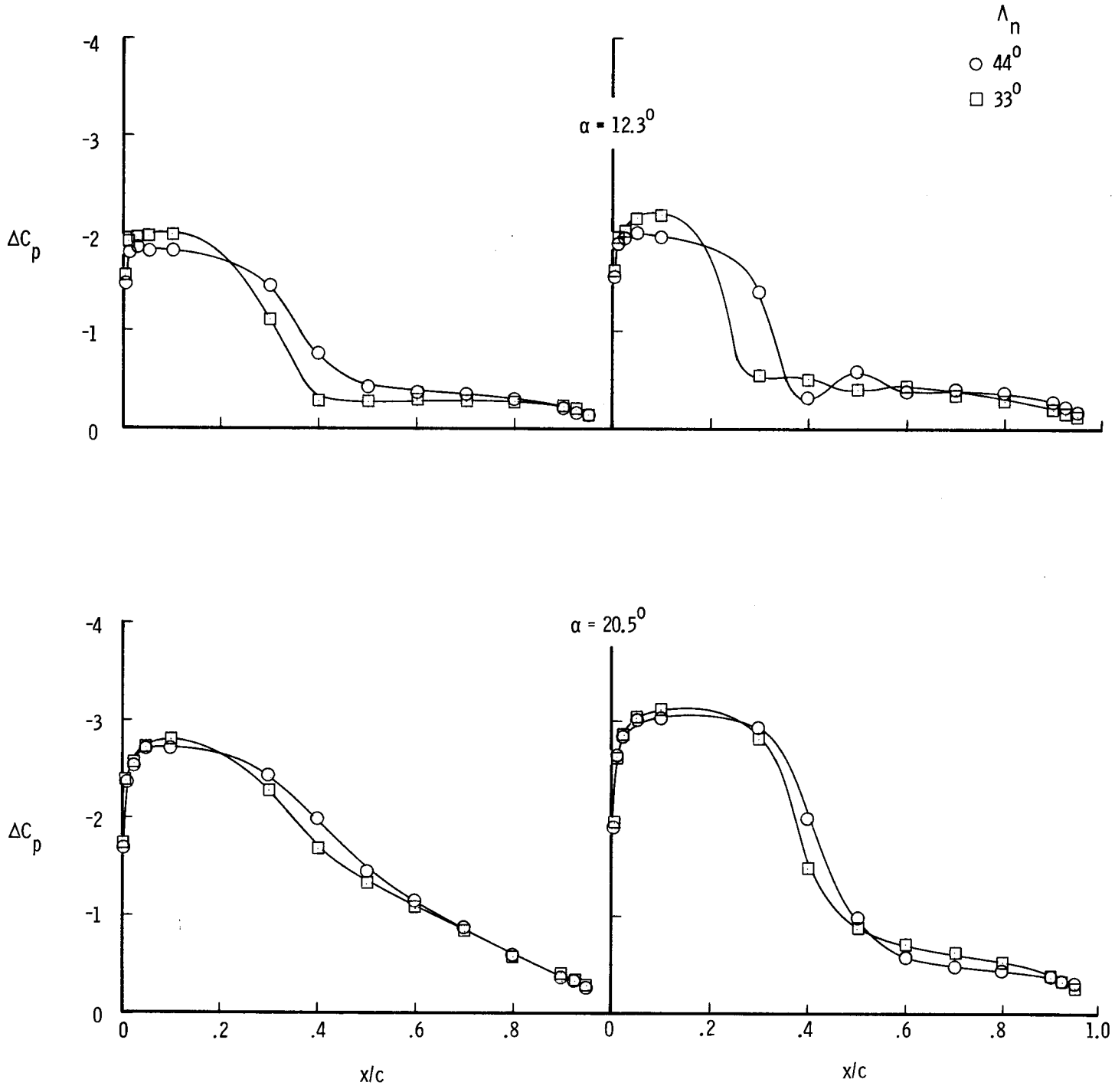

(a) $C_T = 0.06$.

(b) $C_T = 0.12$.

Figure 27.- Effect of Λ_n on chordwise distributions of ΔC_p at $2y/b = 0.5$ for two values of α and C_T; $\overline{x_n/c_r} = 0.23$; $h/d = 0.835$.

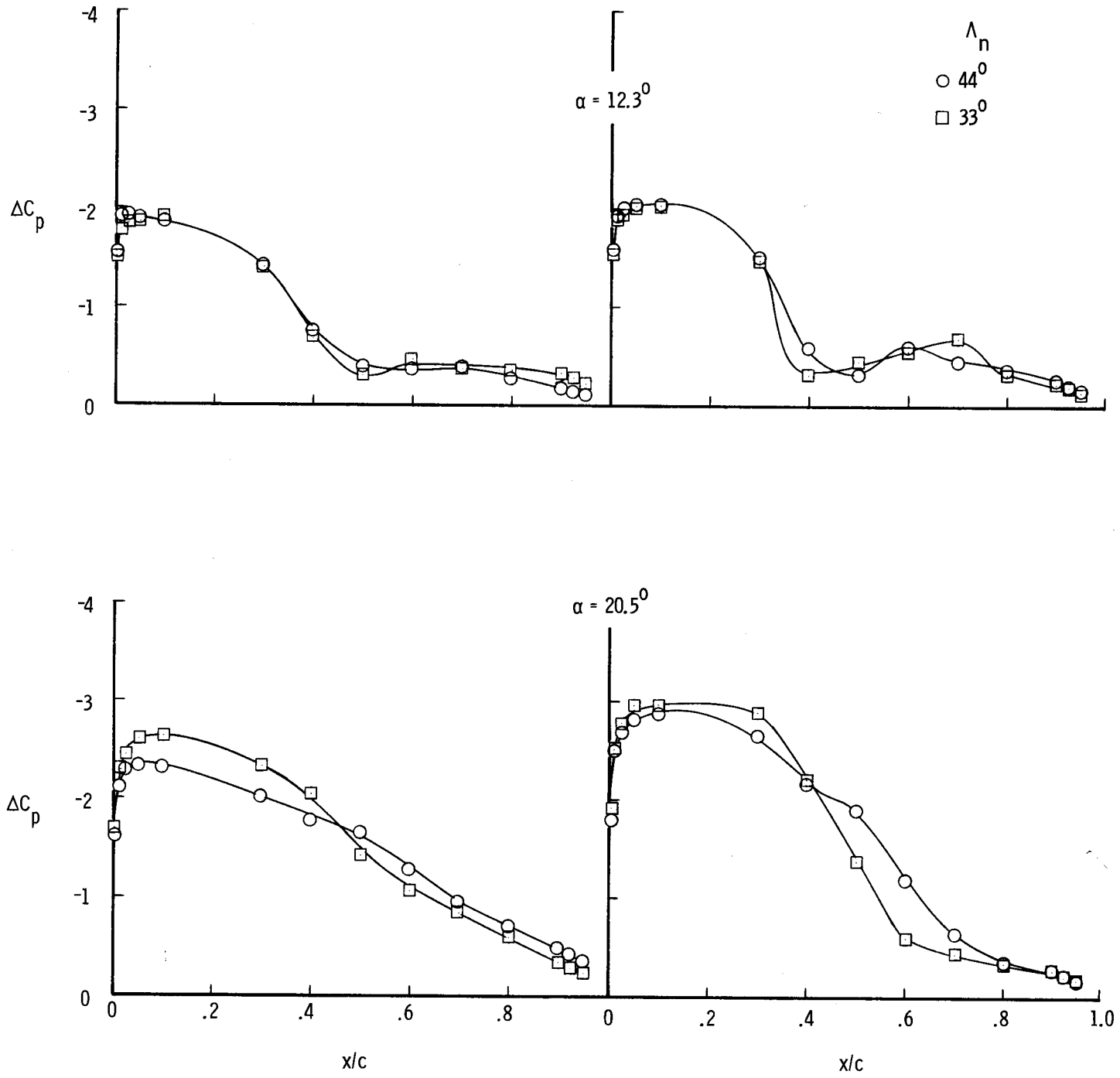

(a) $C_T = 0.06$.

(b) $C_T = 0.12$.

Figure 28.- Effect of Λ_n on chordwise distributions of ΔC_p at $2y/b = 0.5$ for two values of α and C_T; $x_n/c_r = 0.32$; $h/d = 0.835$.

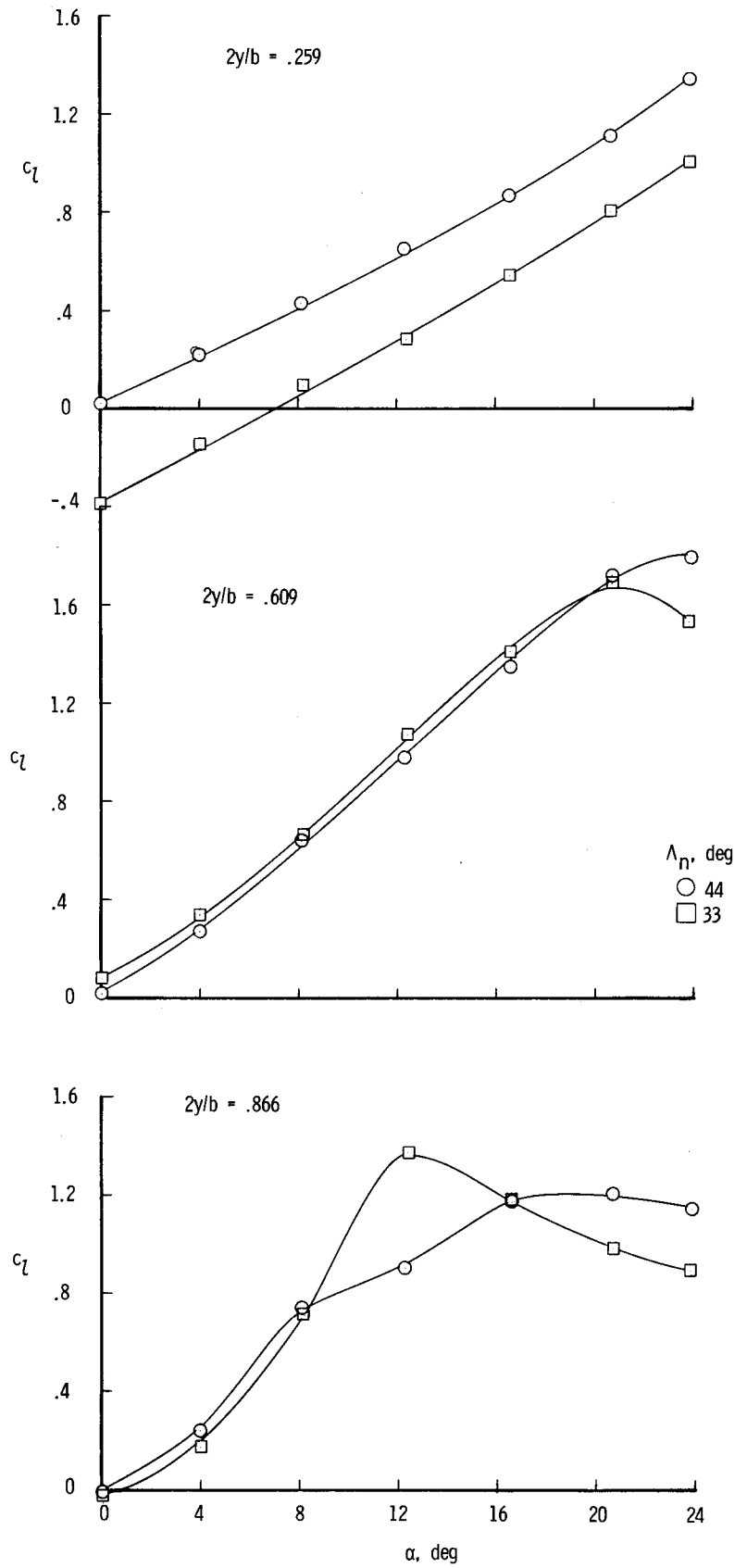

Figure 29.- Effect of Λ_n on section lift characteristics at several span locations with $C_T = 0.12$; $x_n/c_r = 0.23$; $h/d = 0.835$.

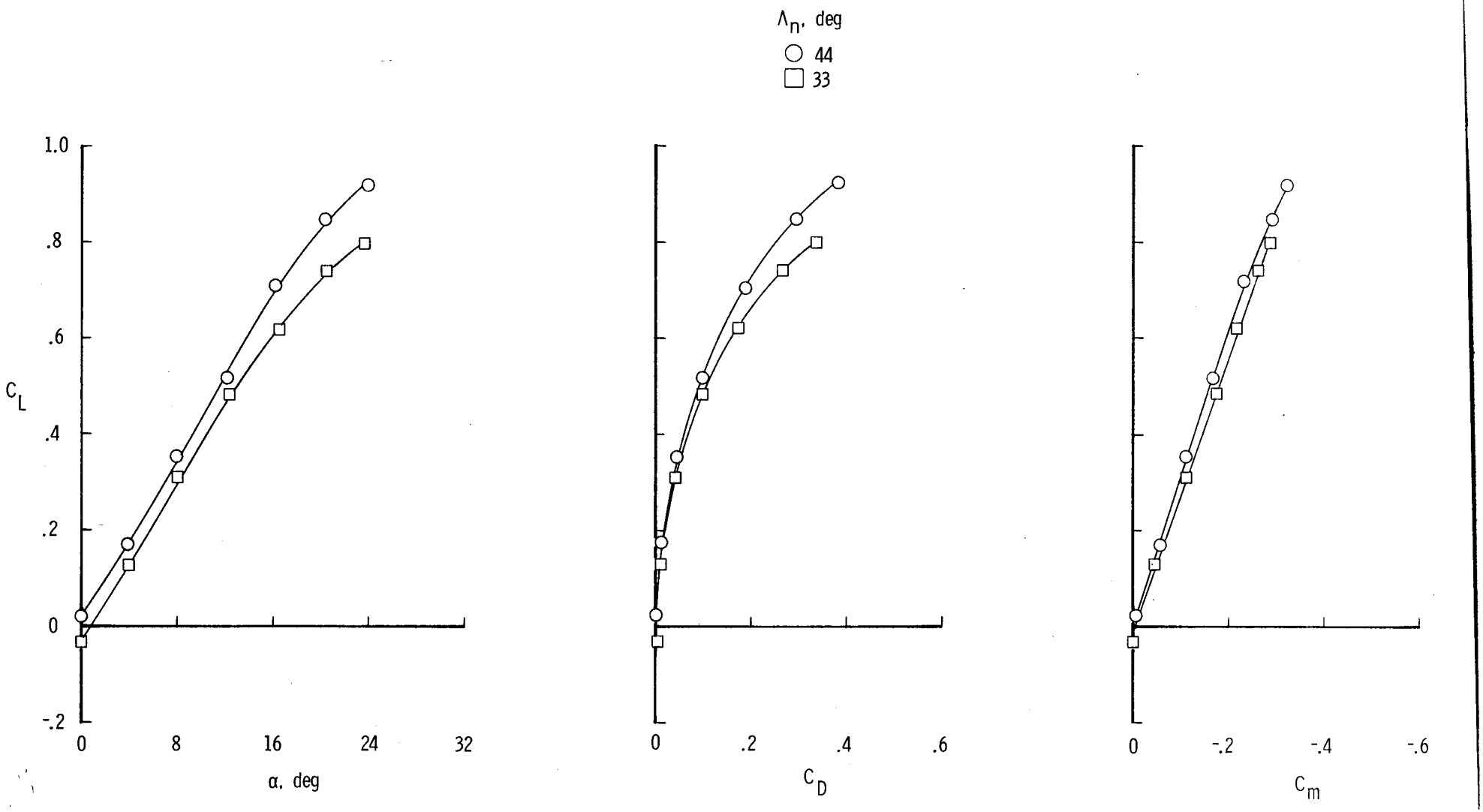

Figure 30.- Effect of Λ_n on longitudinal aerodynamic characteristics for $C_T = 0.12$; $x_n/c_r = 0.23$; $h/d = 0.835$.

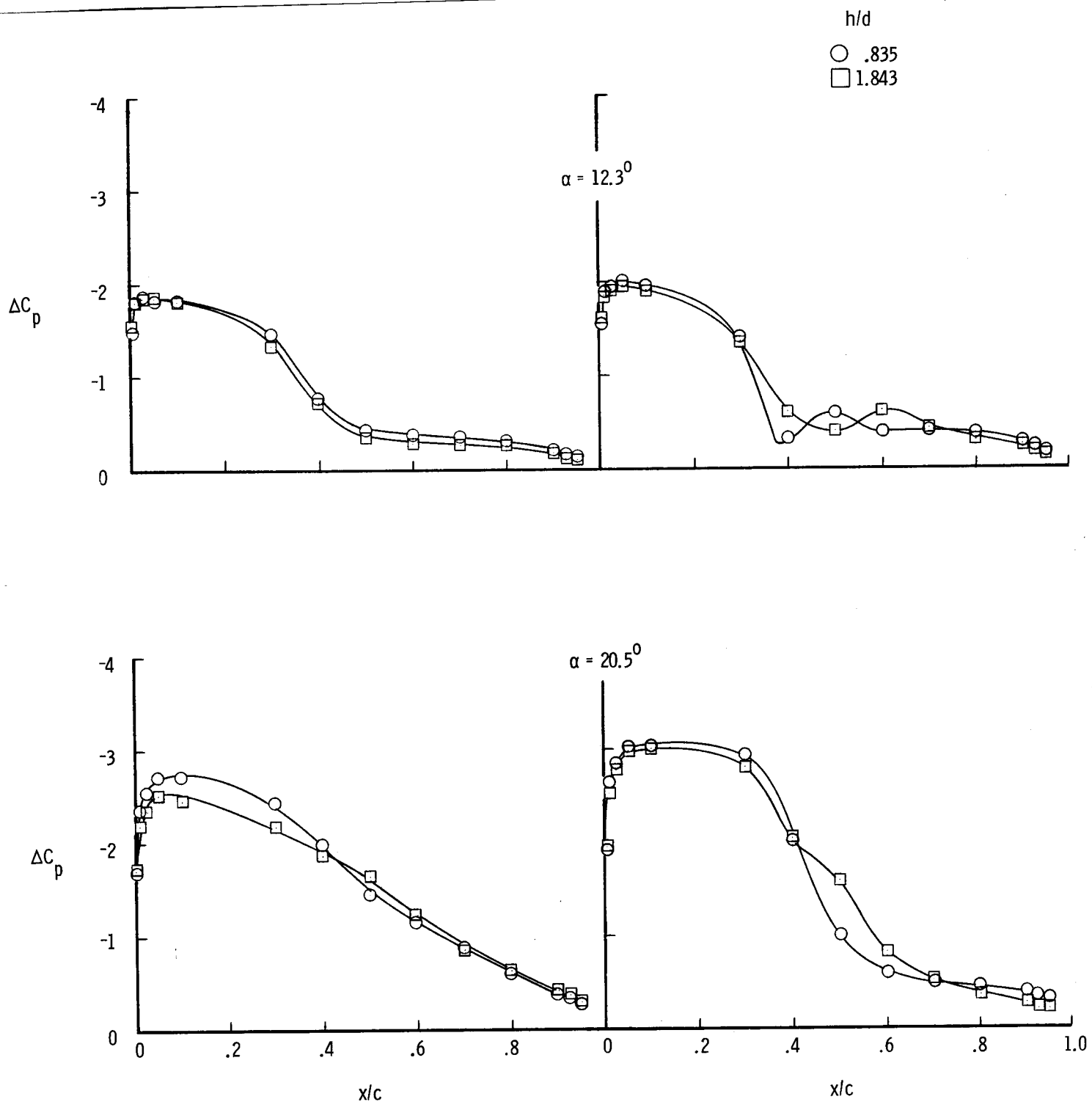

(a) $C_T = 0.06$.

(b) $C_T = 0.12$.

Figure 31.- Effect of h/d on chordwise distributions of ΔC_p at $2y/b = 0.5$ for two values of α and C_T; $\overline{x_n/c_r} = 0.23$; $\Lambda_n = 44^o$.

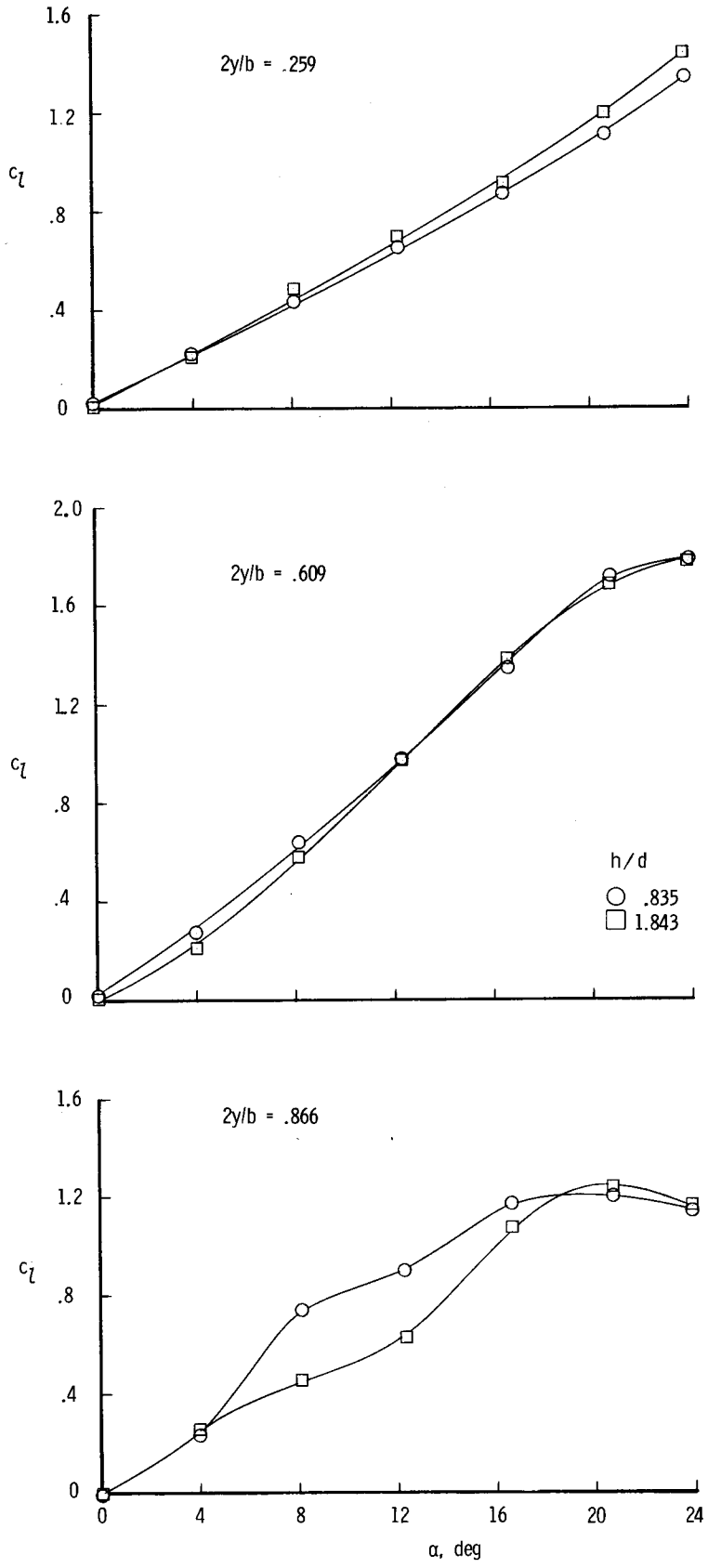

Figure 32.- Effect of h/d on section lift characteristics at several span locations with $C_T = 0.12$; $x_n/c_r = 0.23$; $\Lambda_n = 44^o$.

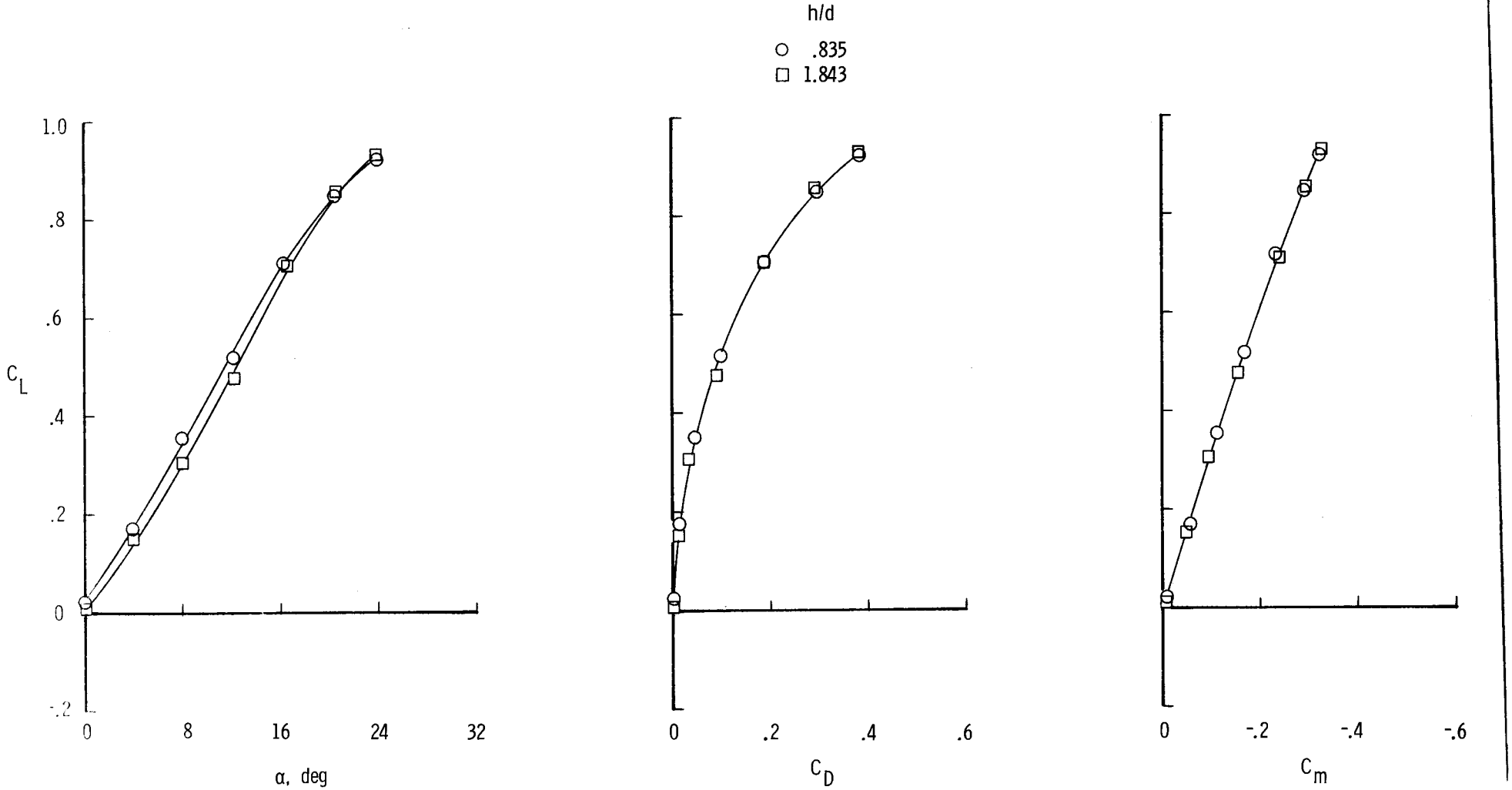

Figure 33.- Effect of h/d on longitudinal aerodynamic characteristics for $C_T = 0.12$; $x_n/c_r = 0.23$; $\Lambda_n = 44^o$.

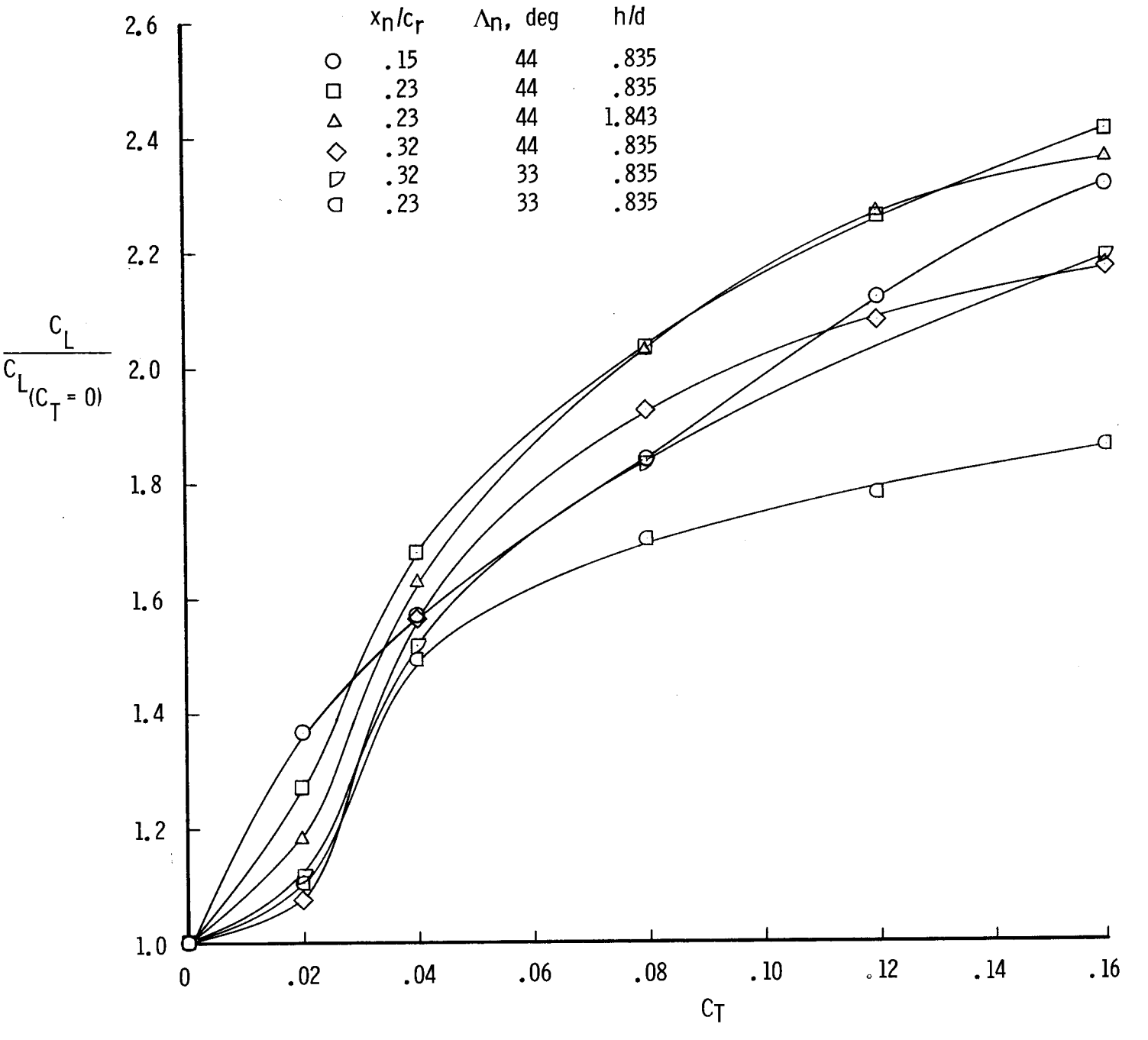

Figure 34.- Effect of nozzle orientation on capability to generate lift for a range of C_T values; $\alpha \approx 23.9^{\circ}$.

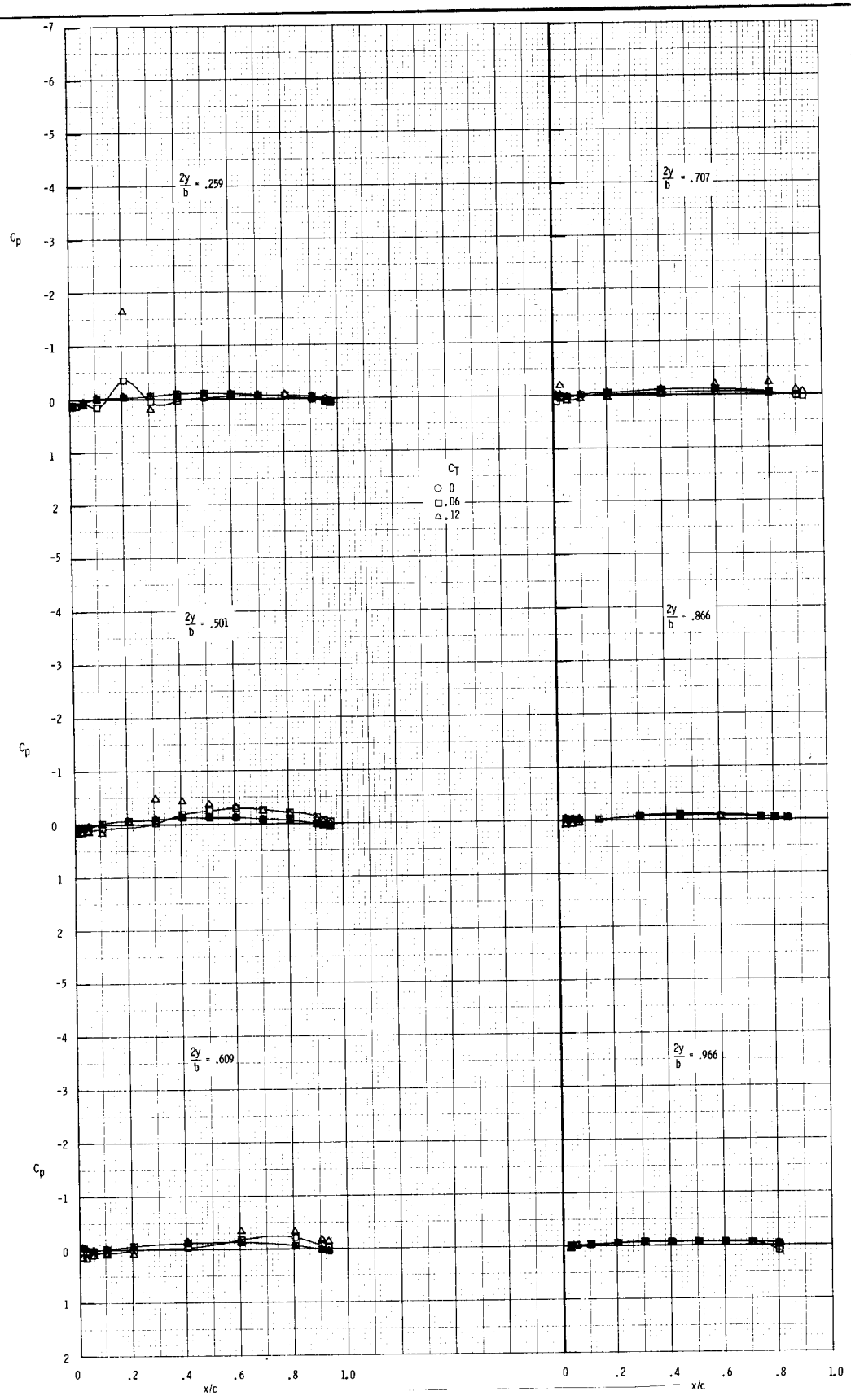

(a) $\alpha = 0.0^{\circ}$.

Figure 35.- Effect of nozzle thrust coefficients on wing-surface pressure distributions for a range of angle of attack. $x_n/c_r = 0.15$; $\Lambda_n = 44^{\circ}$; $h/d = 0.835$.

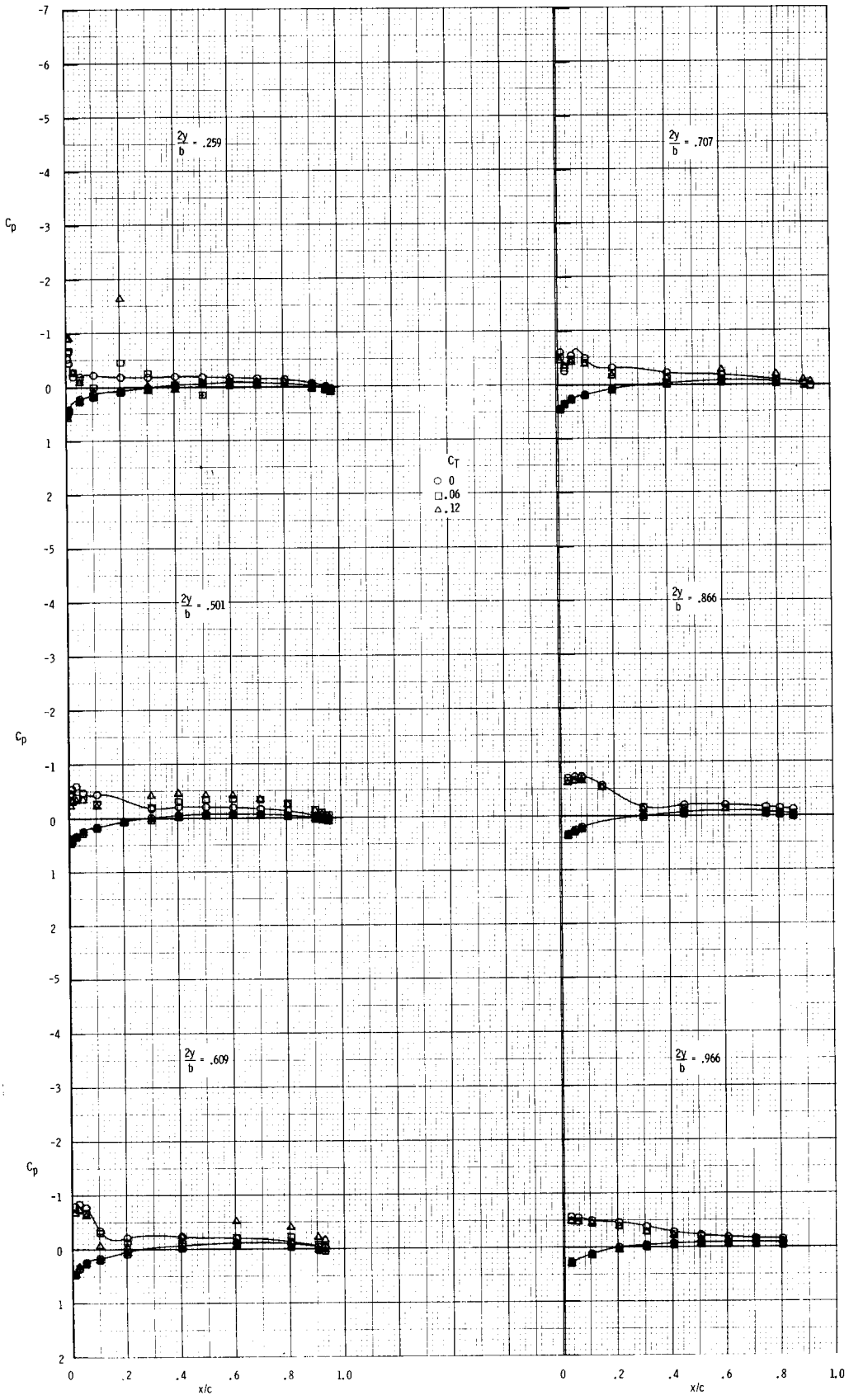

(b) $\alpha = 3.9^{o}$.

Figure 35.- Continued.

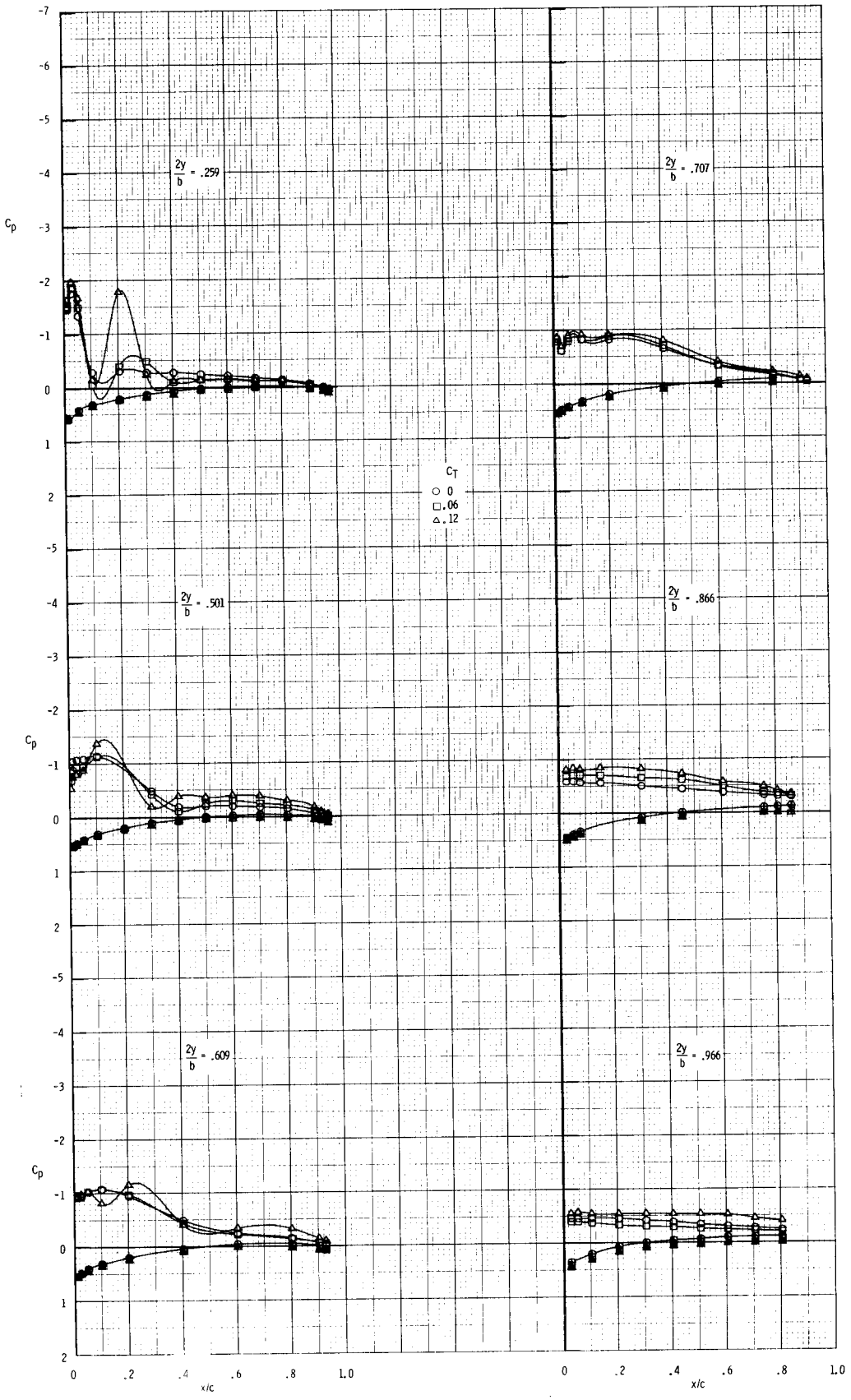

(c) $\alpha = 8.0^{\circ}$.

Figure 35.- Continued.

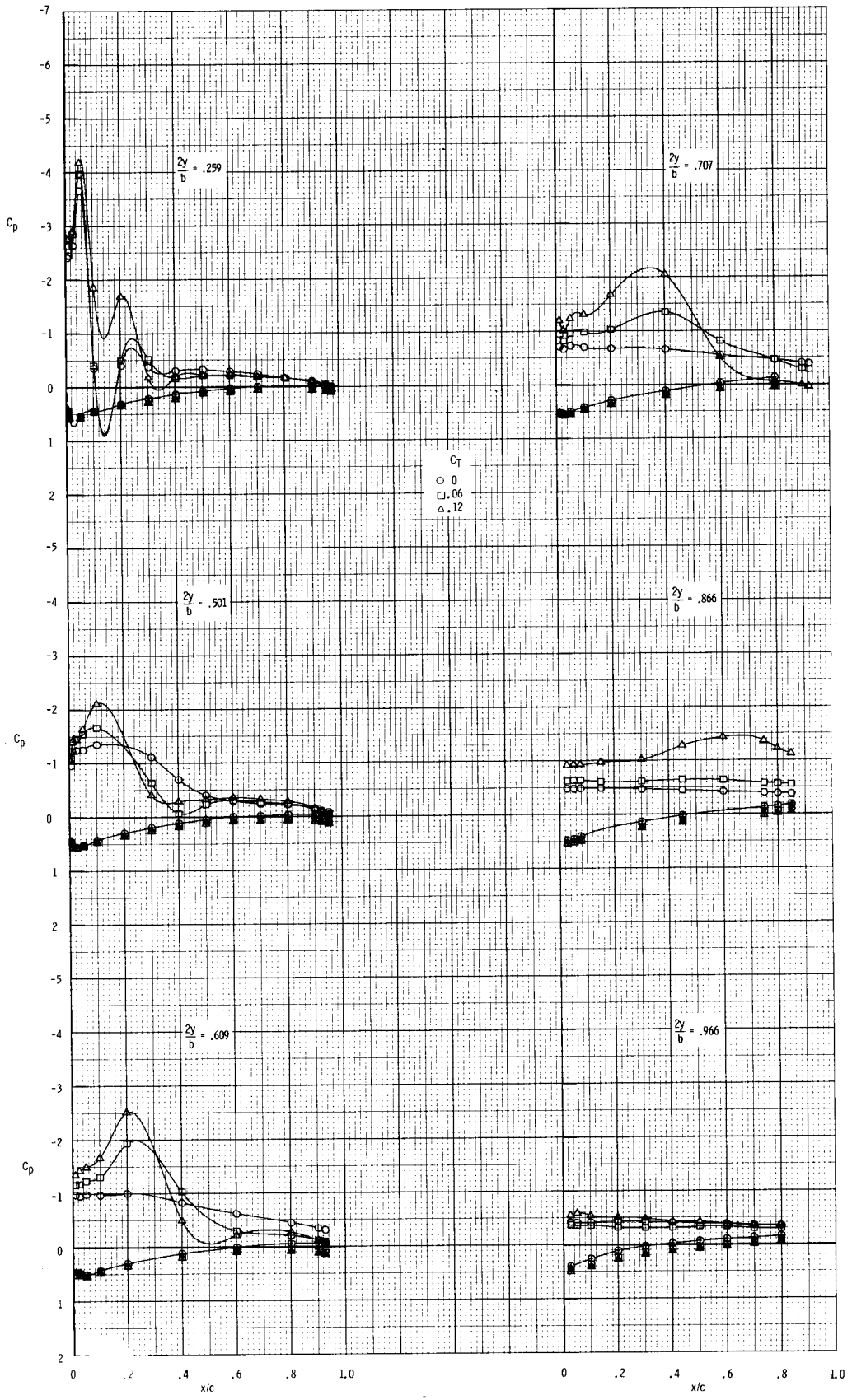

(d) $\alpha = 12.2^{\circ}$.

Figure 35.- Continued.

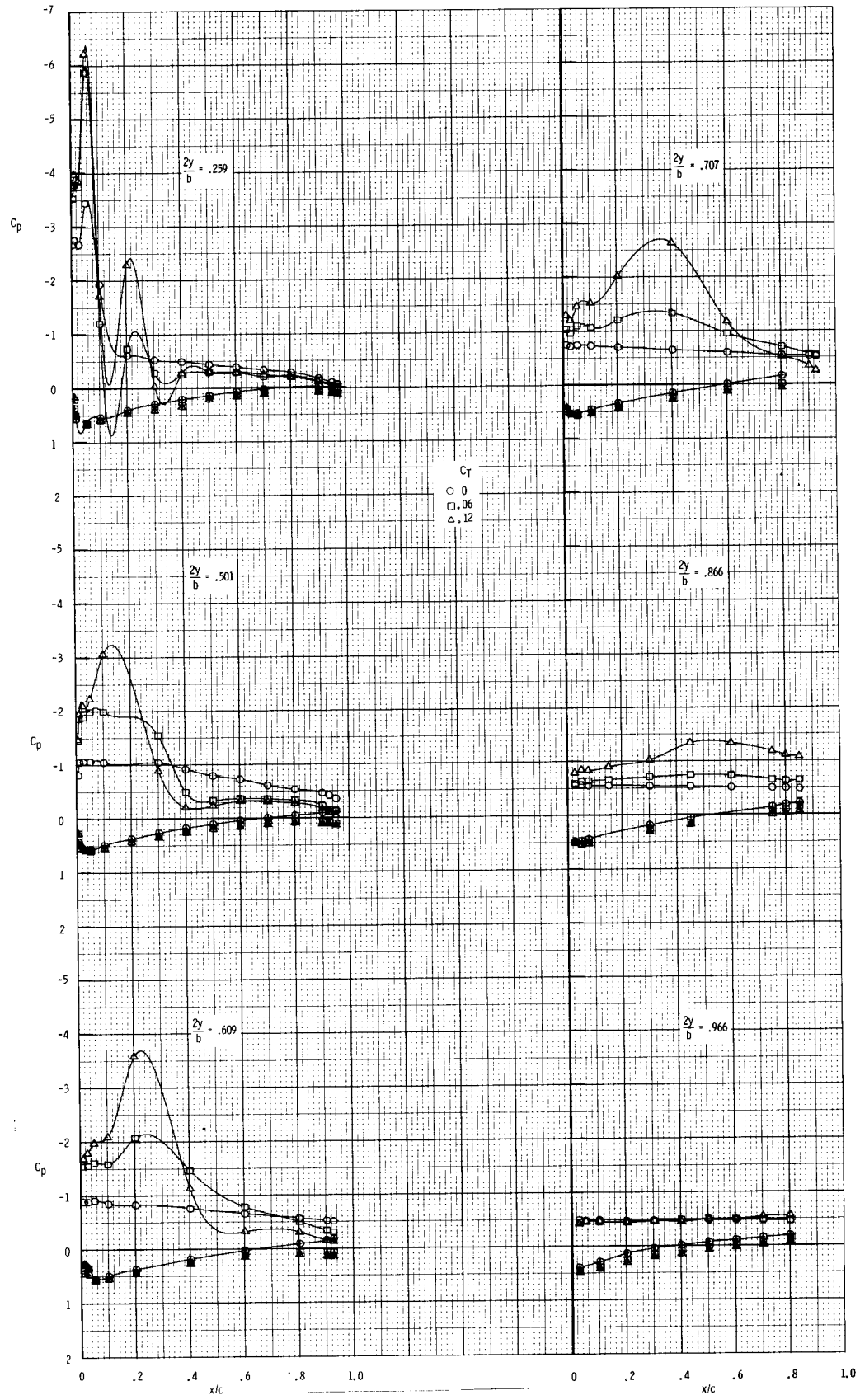

(e) $\alpha = 16.4^{o}$.

Figure 35.- Continued.

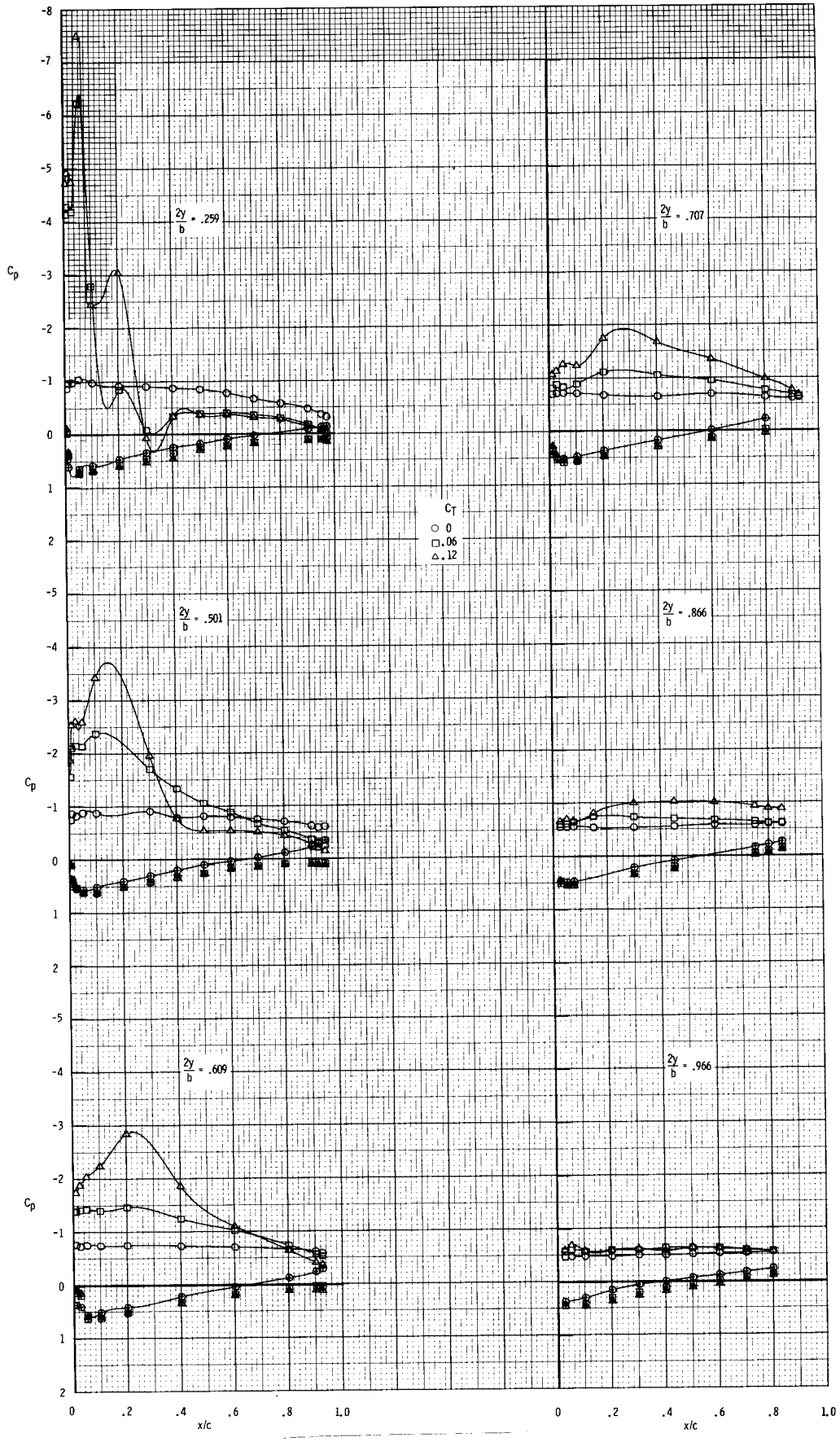

(f) $\alpha = 20.4^{\circ}$.

Figure 35.- Continued.

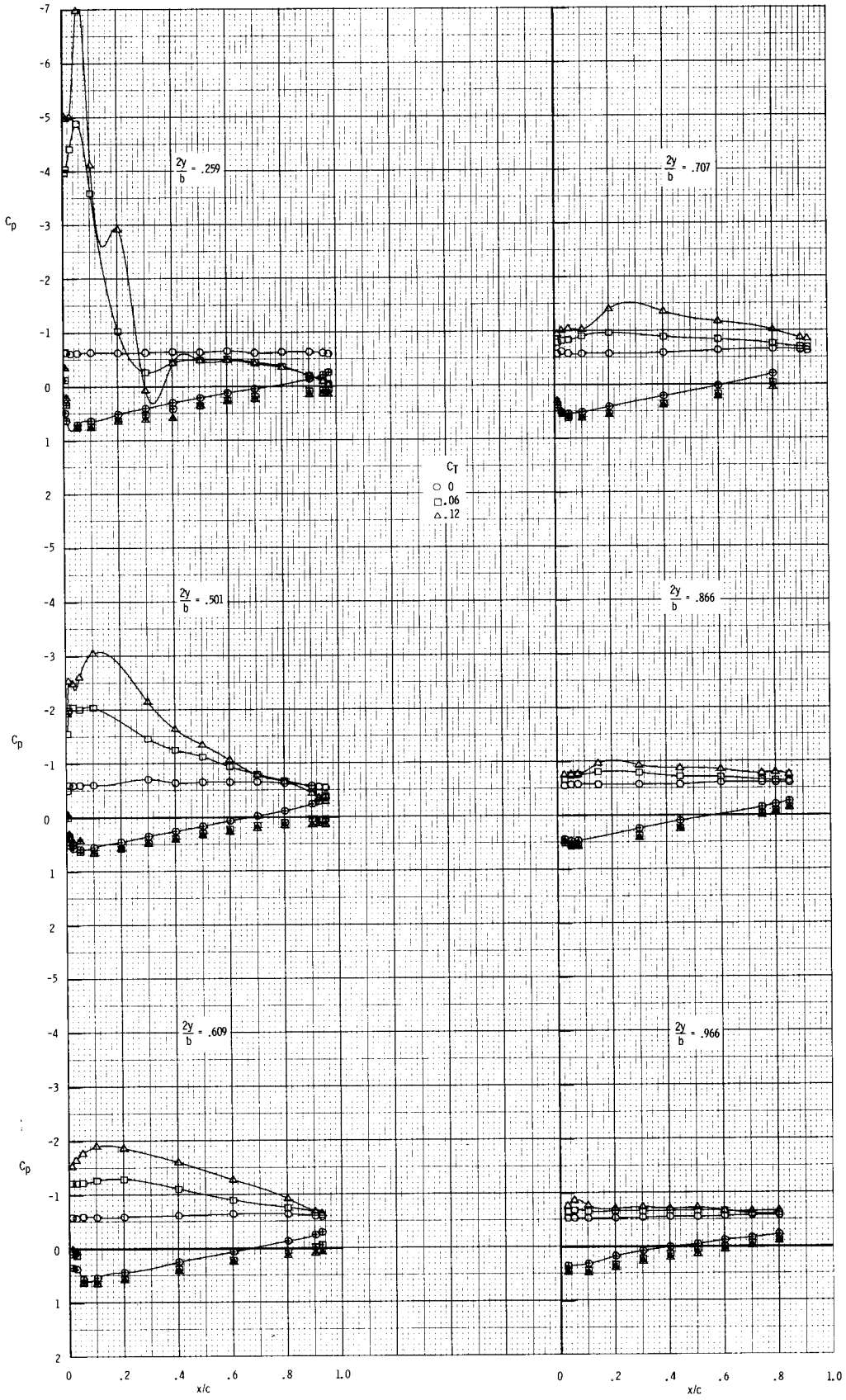

(g) $\alpha = 23.5^{o}$.

Figure 35.- Concluded.

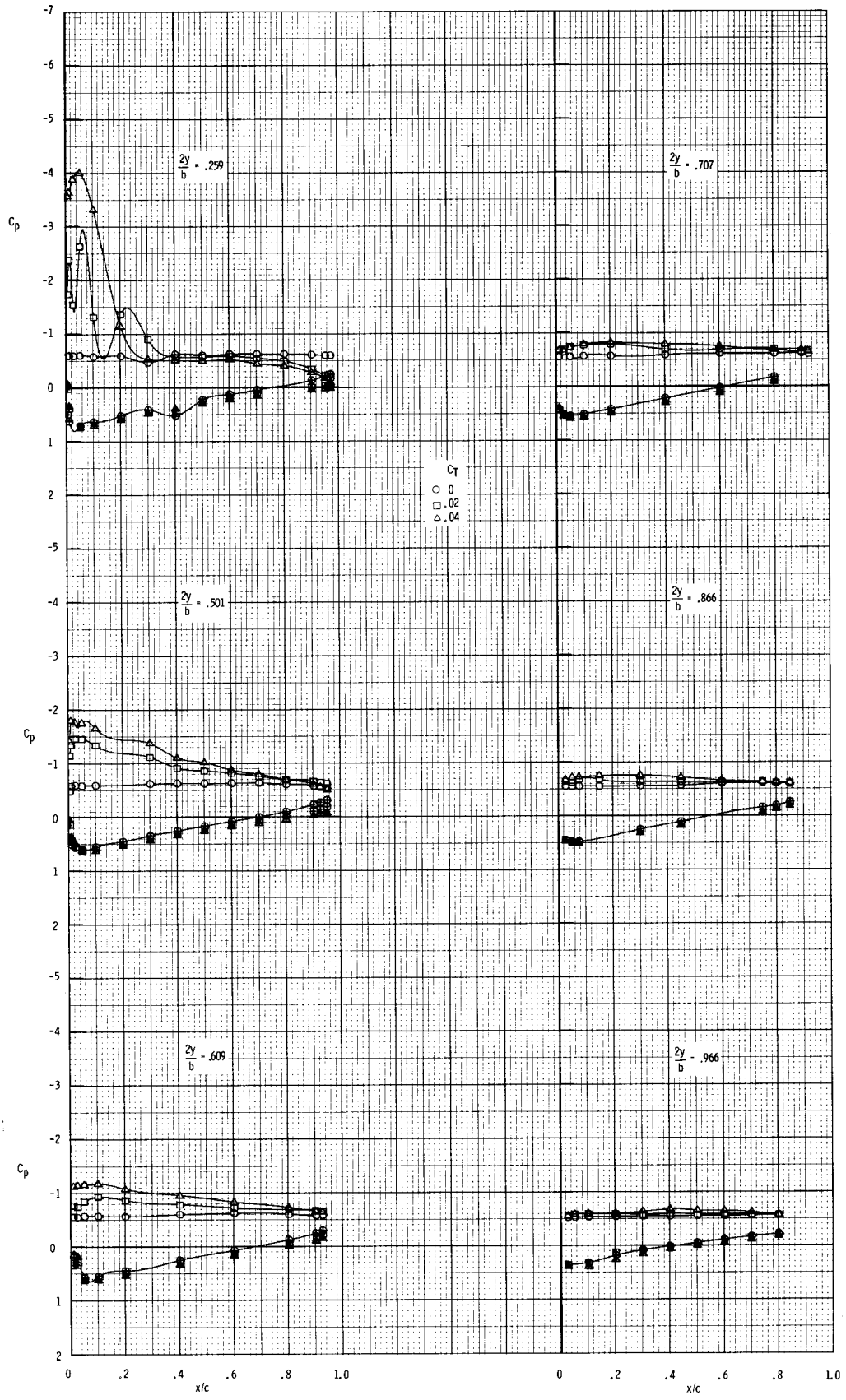

(a) C_T = 0, 0.02, and 0.04.

Figure 36.- Effect of nozzle thrust coefficient on wing-surface pressure distributions for $\alpha = 23.5^{\circ}$; $\overline{x_n/c_r} = 0.15$; $\Lambda_n = 44^{\circ}$; h/d = 0.835.

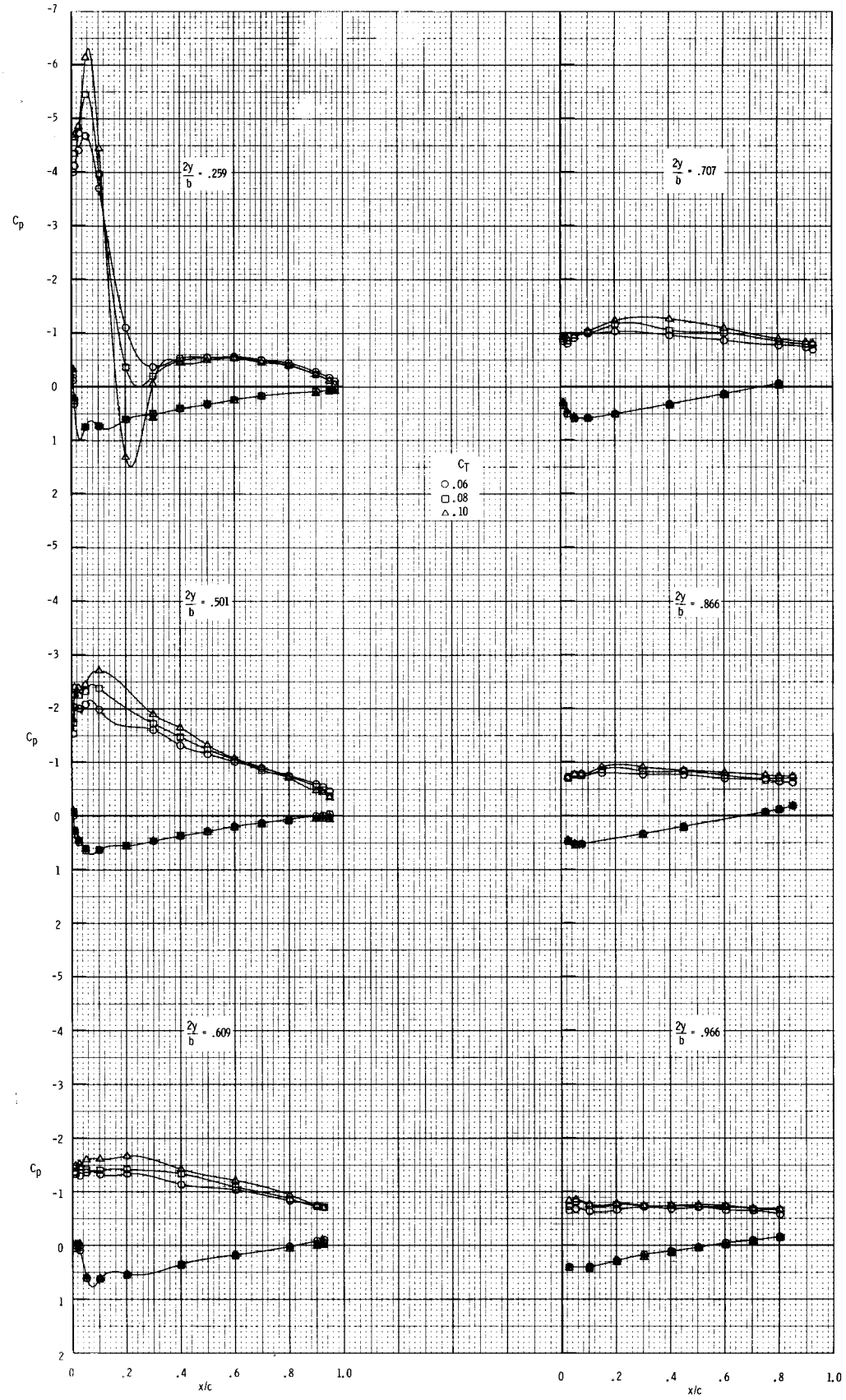

(b) C_T = 0.06, 0.08, and 0.10.

Figure 36.- Continued.

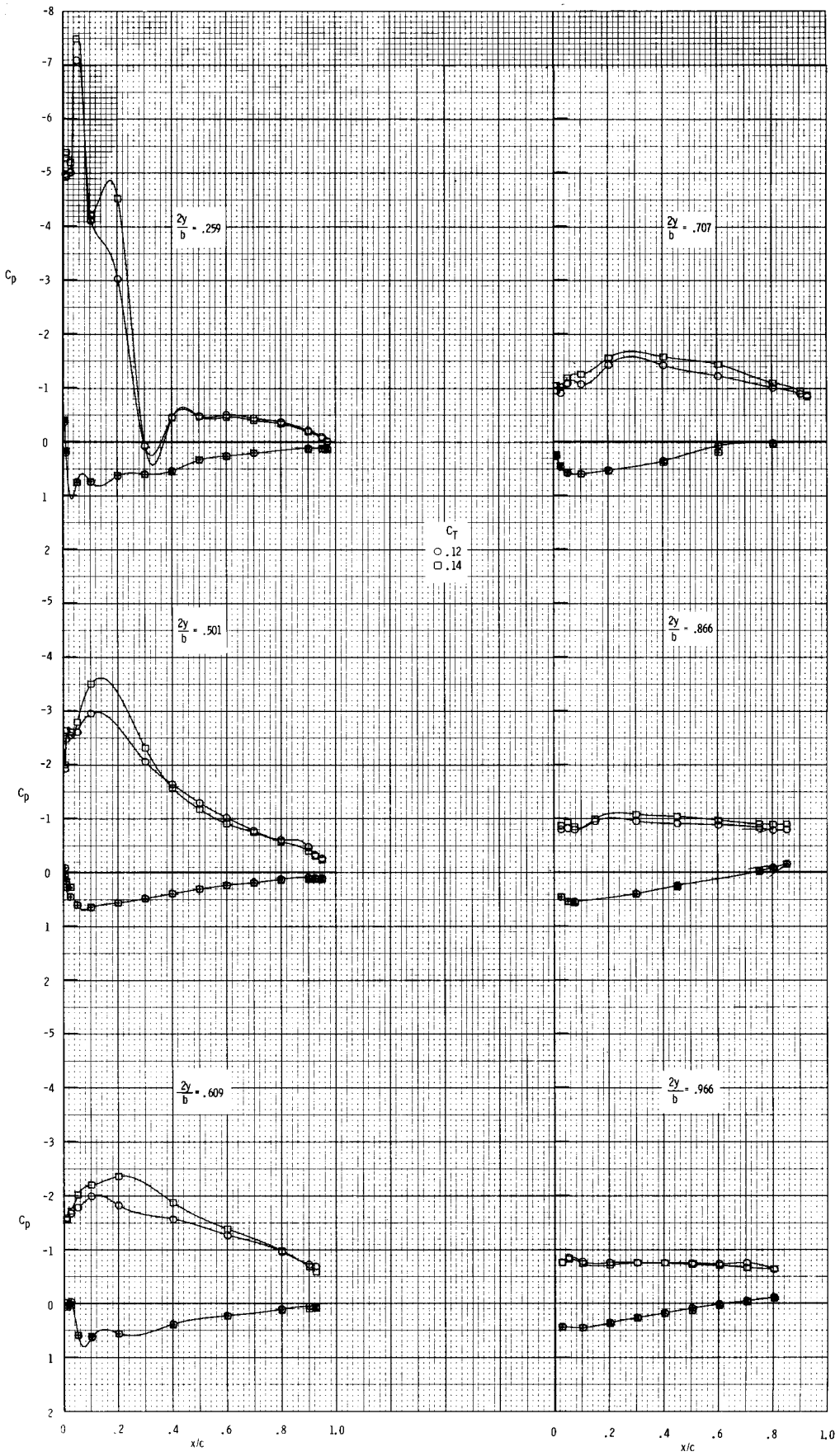

(c) C_T = 0.12 and 0.14.

Figure 36.- Continued.

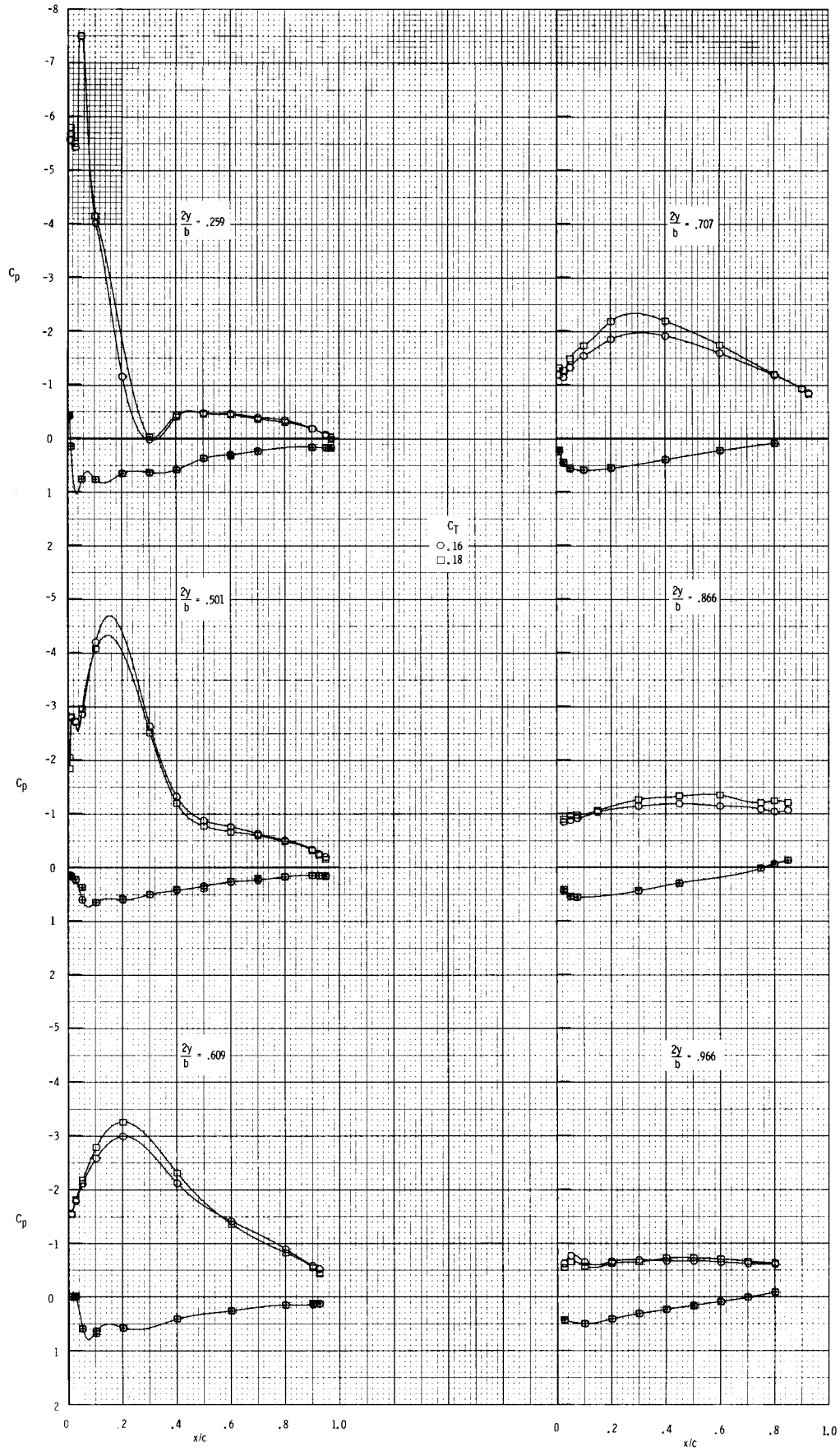

(d) C_T = 0.16 and 0.18.

Figure 36.- Concluded.

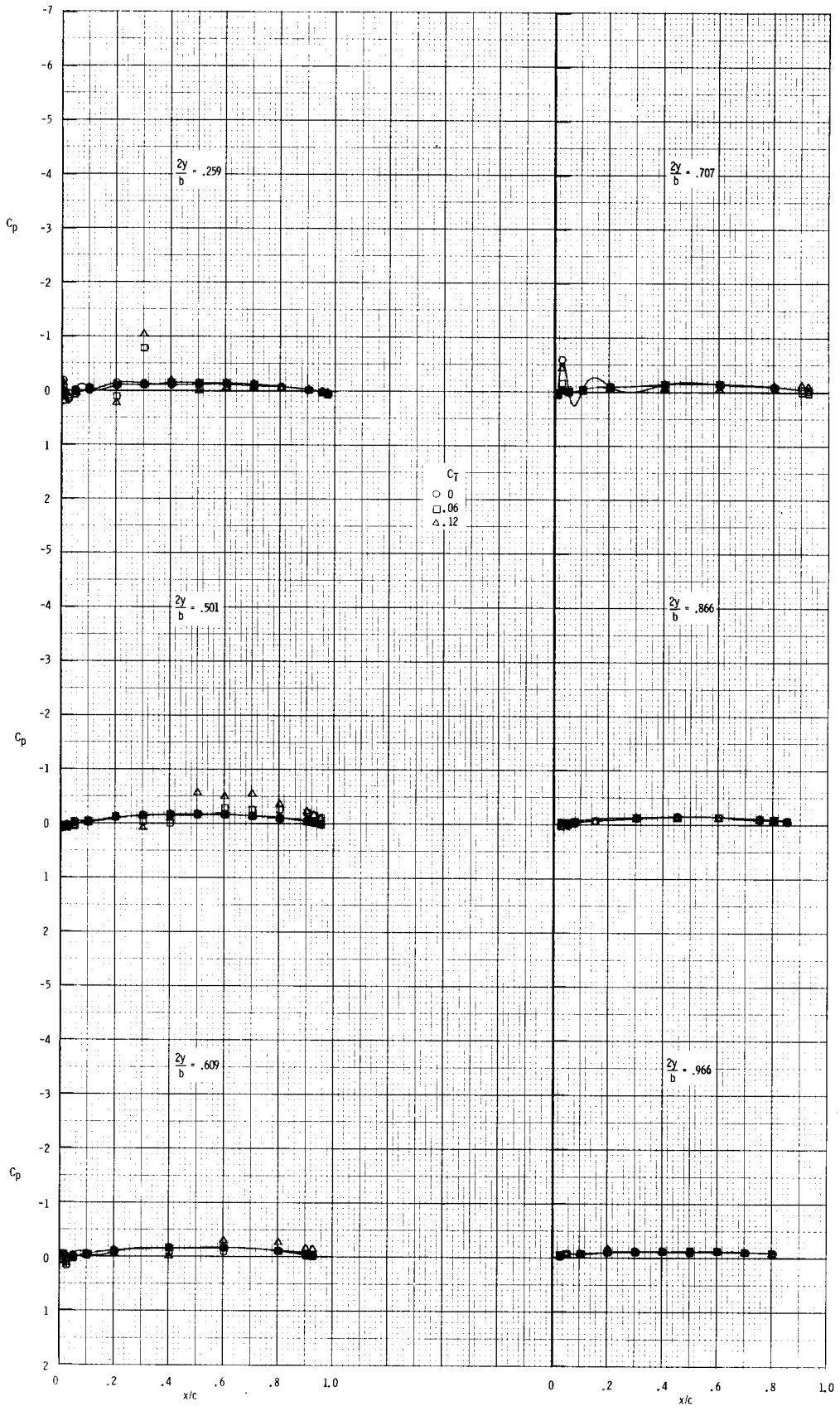

(a) $\alpha = 0.0^{\circ}$.

Figure 37.- Effect of nozzle thrust coefficient on wing-surface pressure distributions for a range of angle of attack. $\overline{x_n/c_r} = 0.23$; $\Lambda_n = 44^{\circ}$; $h/d = 0.835$.

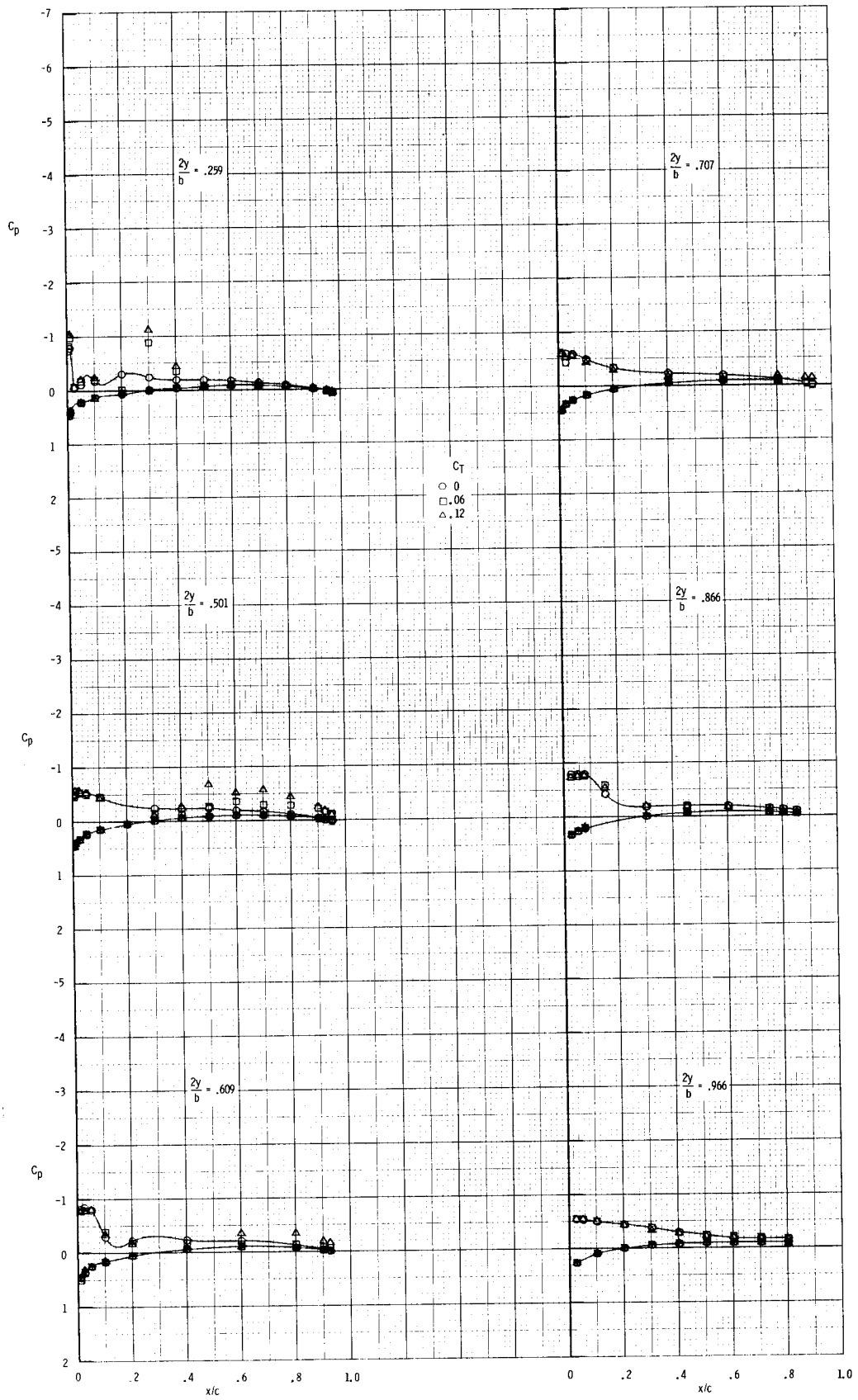

(b) $\alpha = 4.0^{\circ}$.

Figure 37.- Continued.

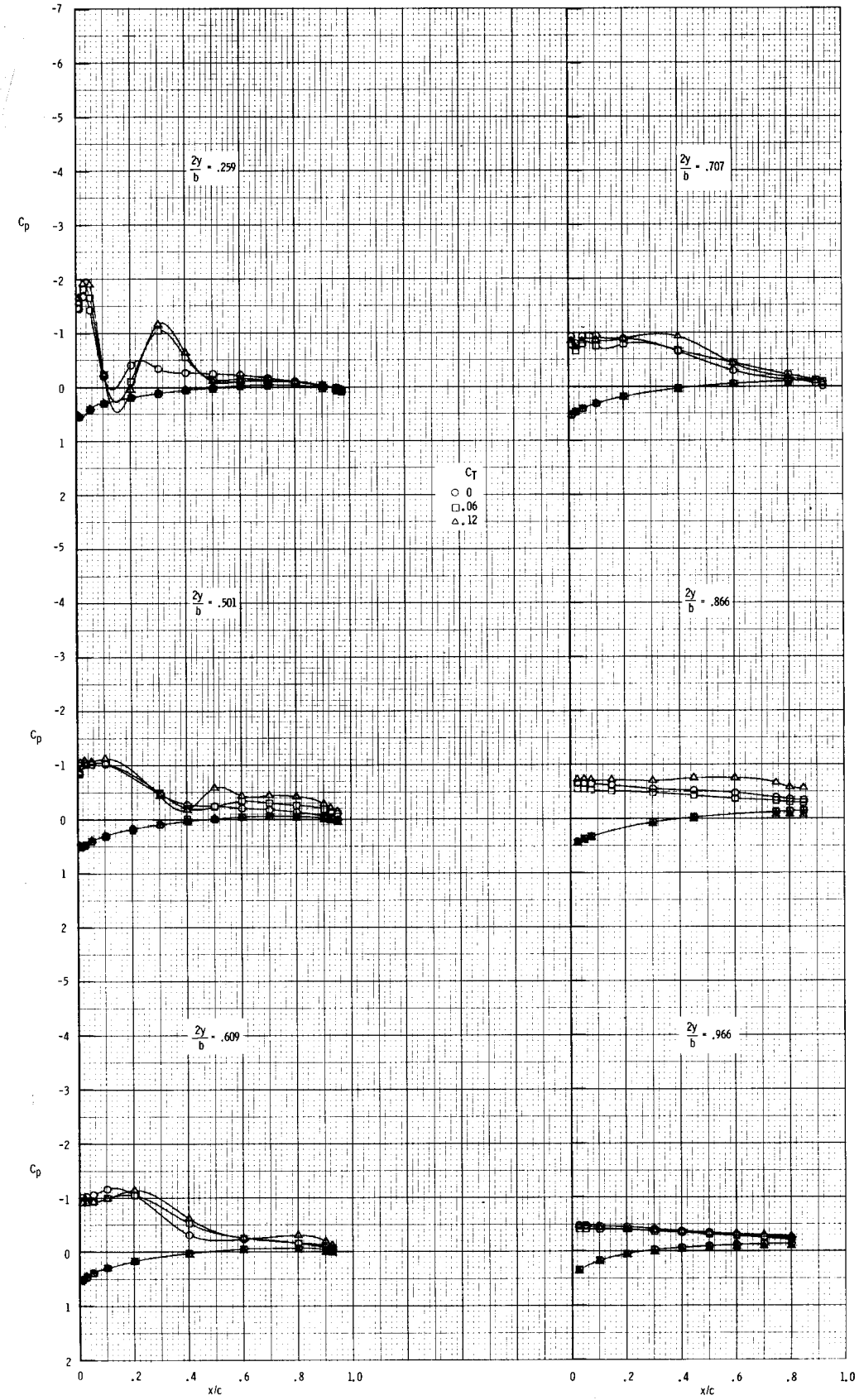

(c) $\alpha = 8.1^{o}$.

Figure 37.- Continued.

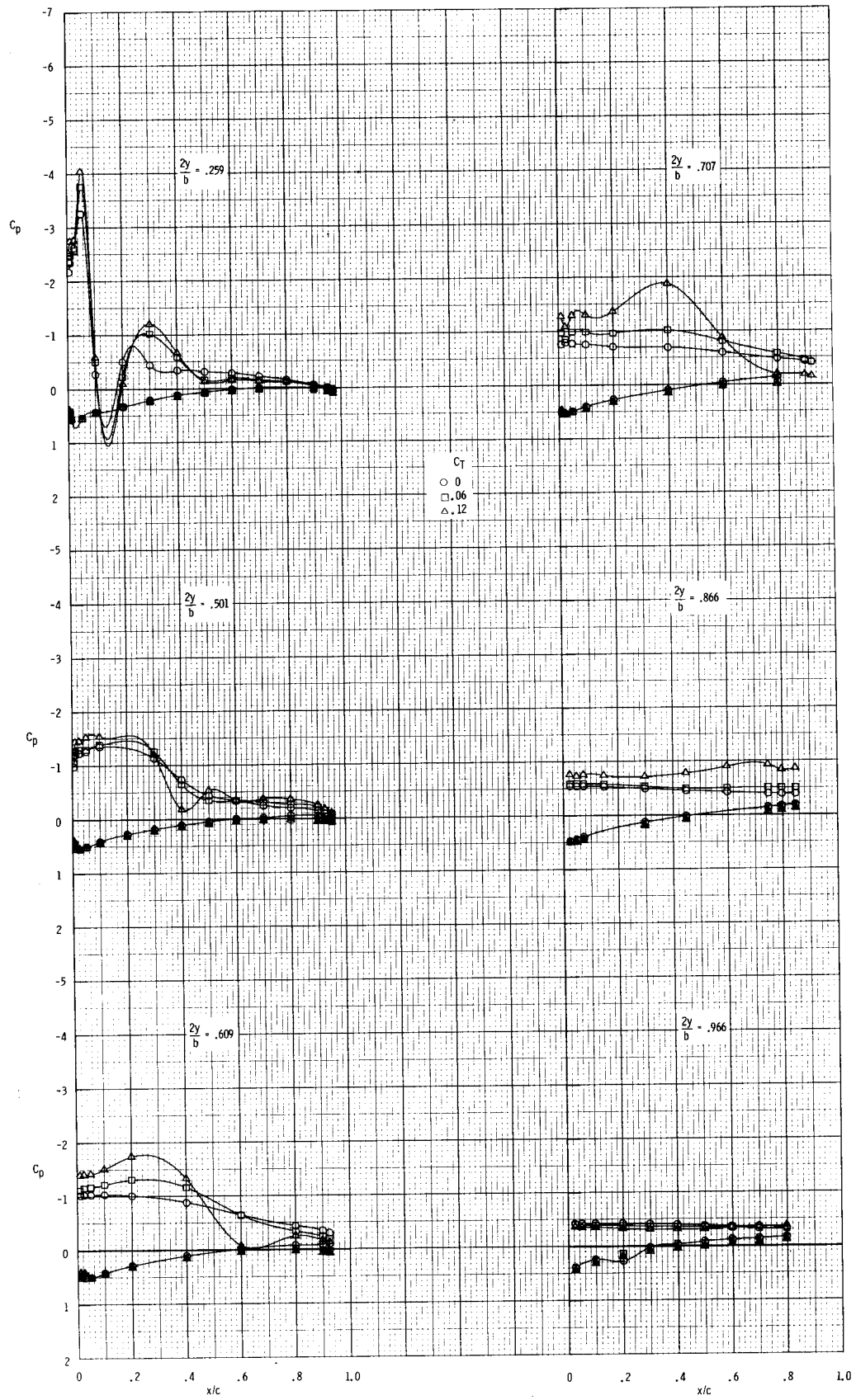

(d) $\alpha = 12.3^{\circ}$.

Figure 37.- Continued.

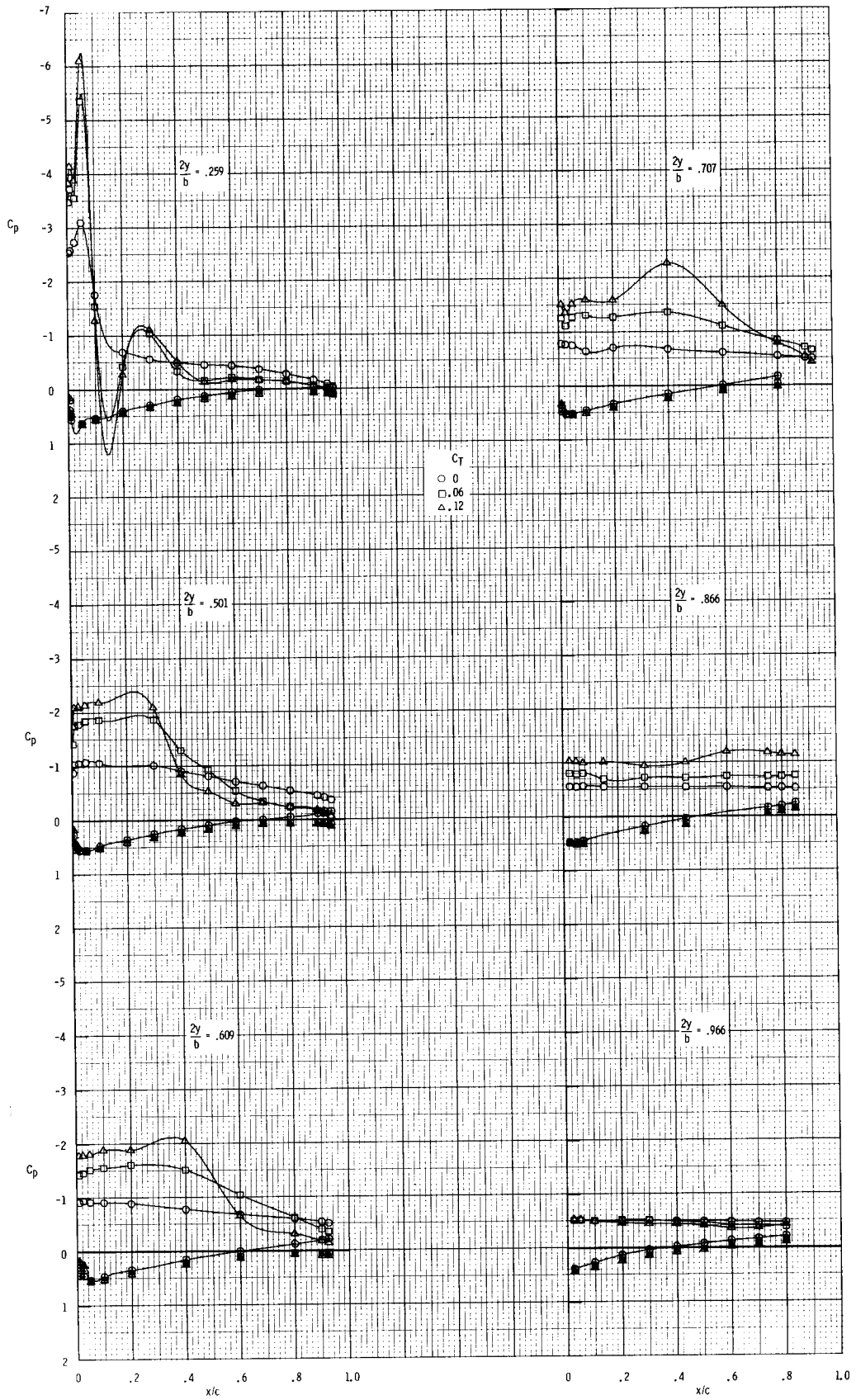

(e) $\alpha = 16.5^{\circ}$.

Figure 37.- Continued.

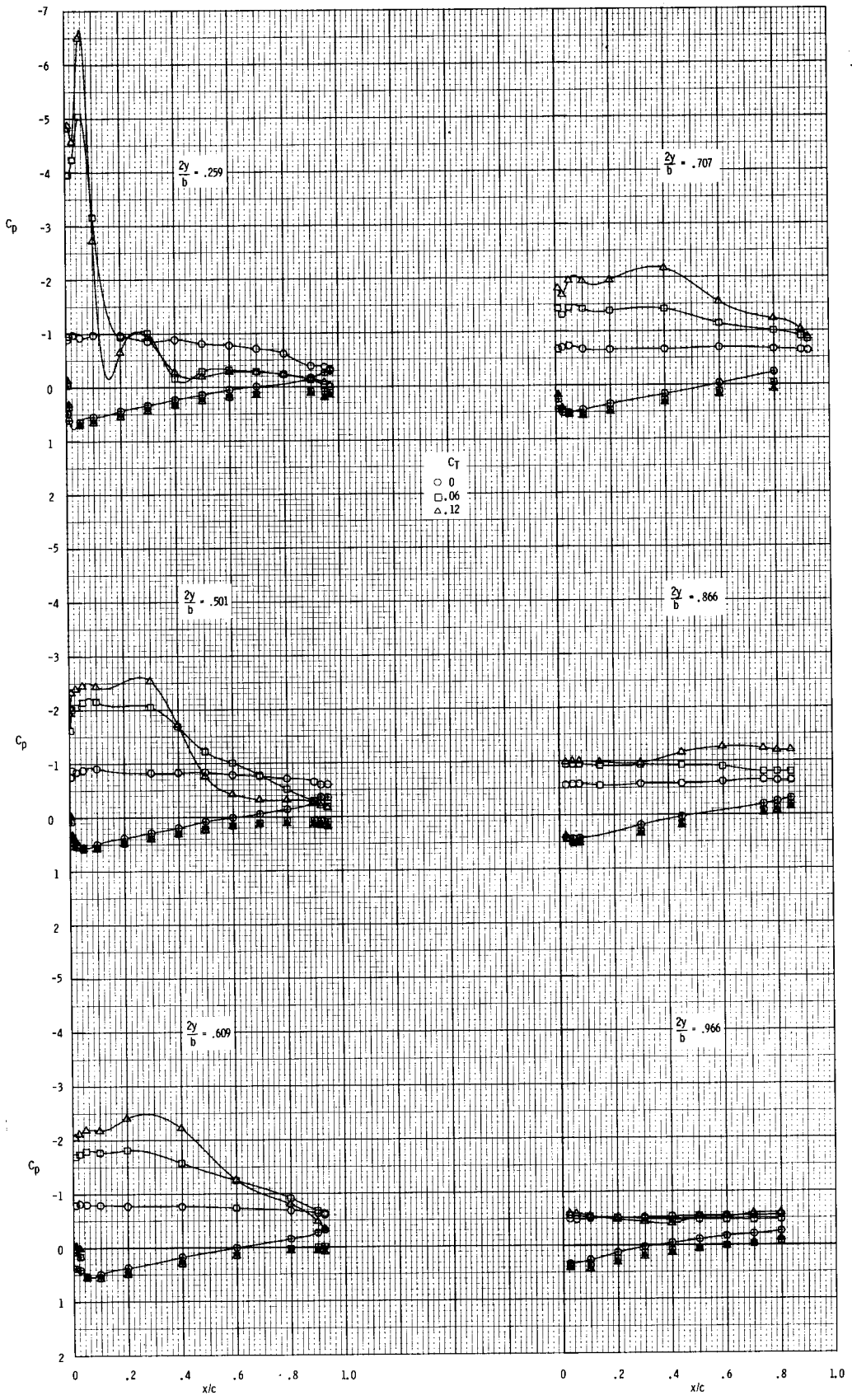

(f) $\alpha = 20.6^{O}$.

Figure 37.- Continued.

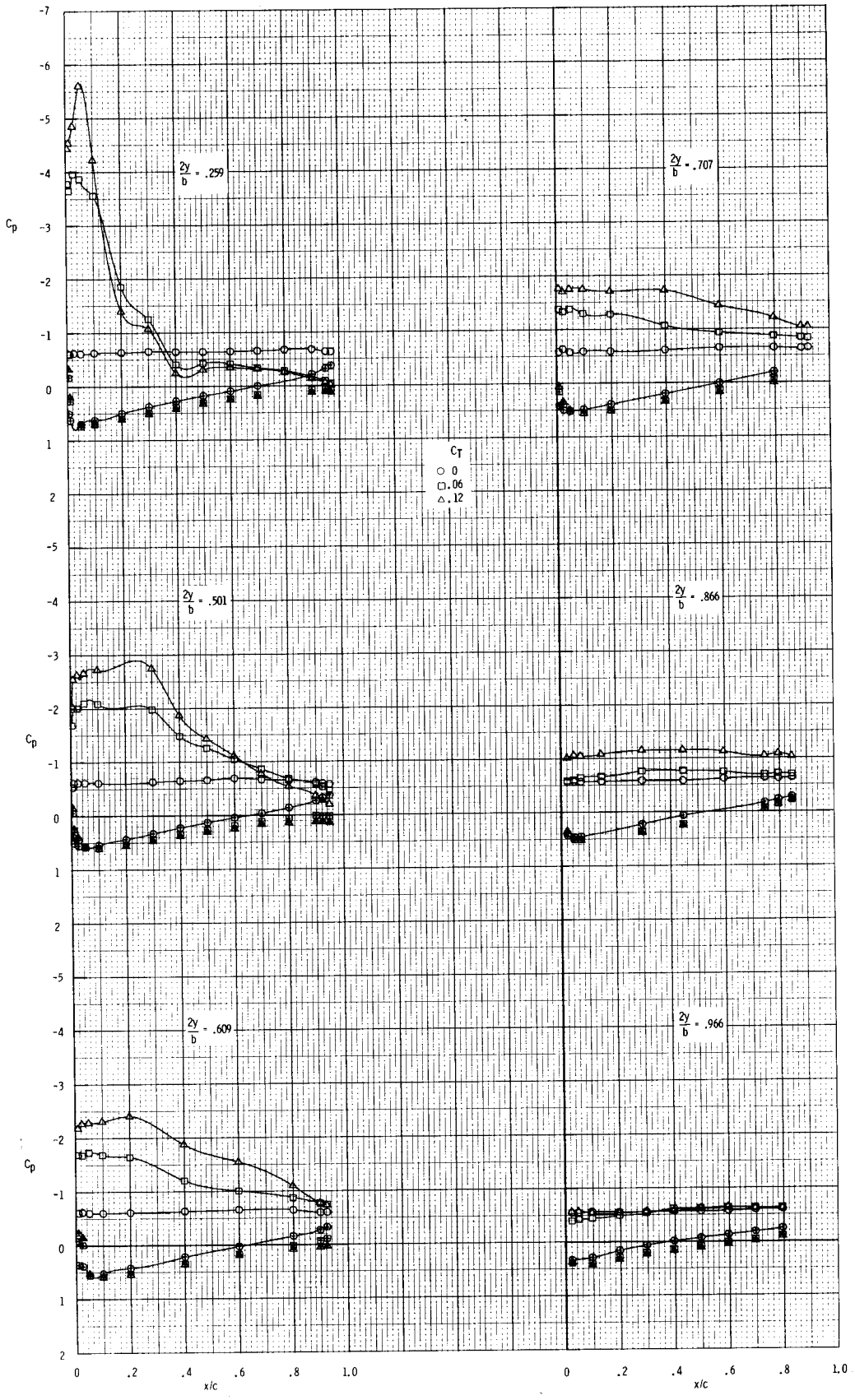

(g) $\alpha = 23.9^{\circ}$.

Figure 37.- Concluded.

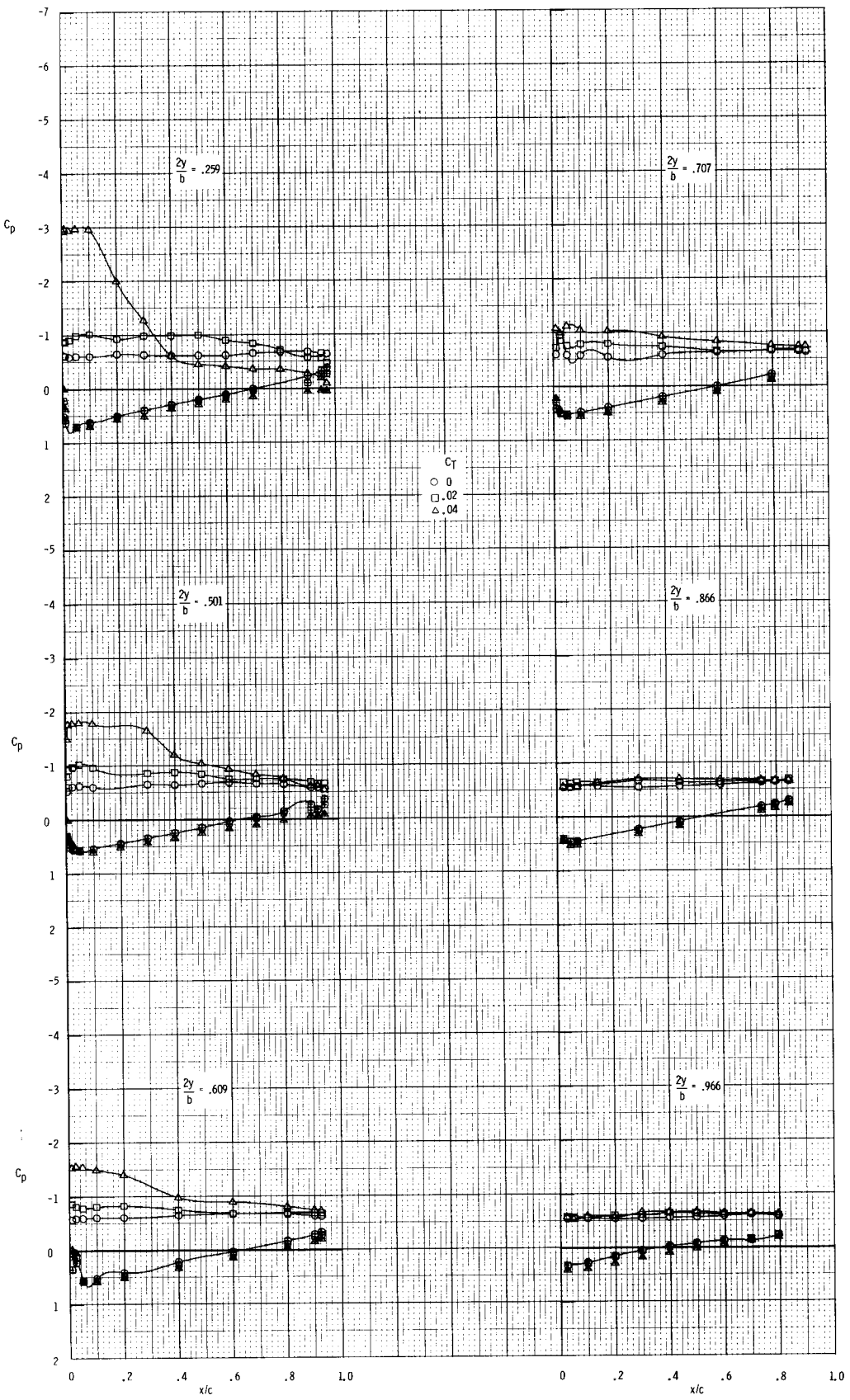

(a) C_T = 0, 0.02, and 0.04.

Figure 38.- Effect of nozzle thrust coefficient on wing-surface pressure distributions for $\alpha = 23.9^{\circ}$; $\overline{x_n/c_r} = 0.23$; $\Lambda_n = 44^{\circ}$; h/d = 0.835.

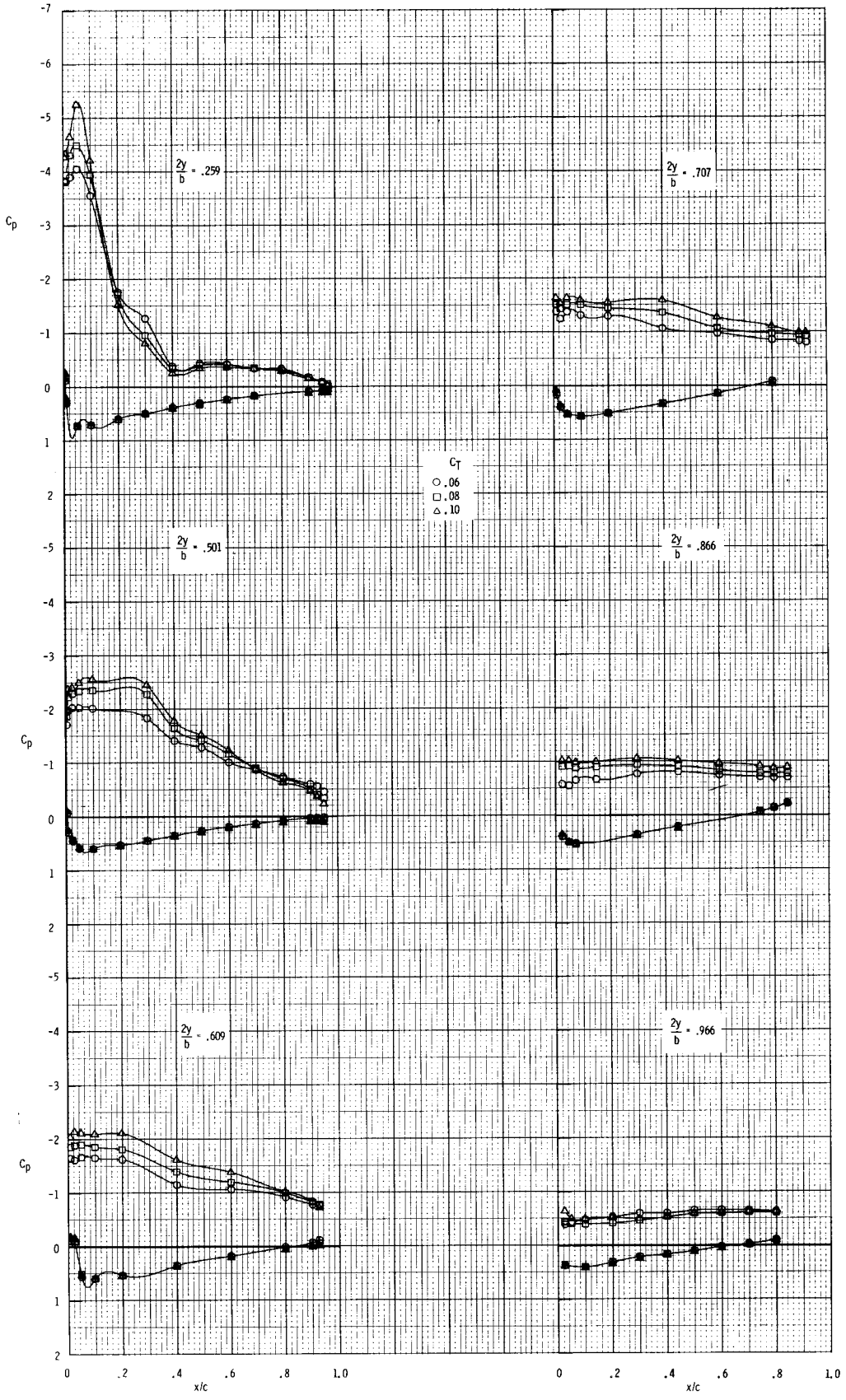

(b) C_T = 0.06, 0.08, and 0.10.

Figure 38.- Continued.

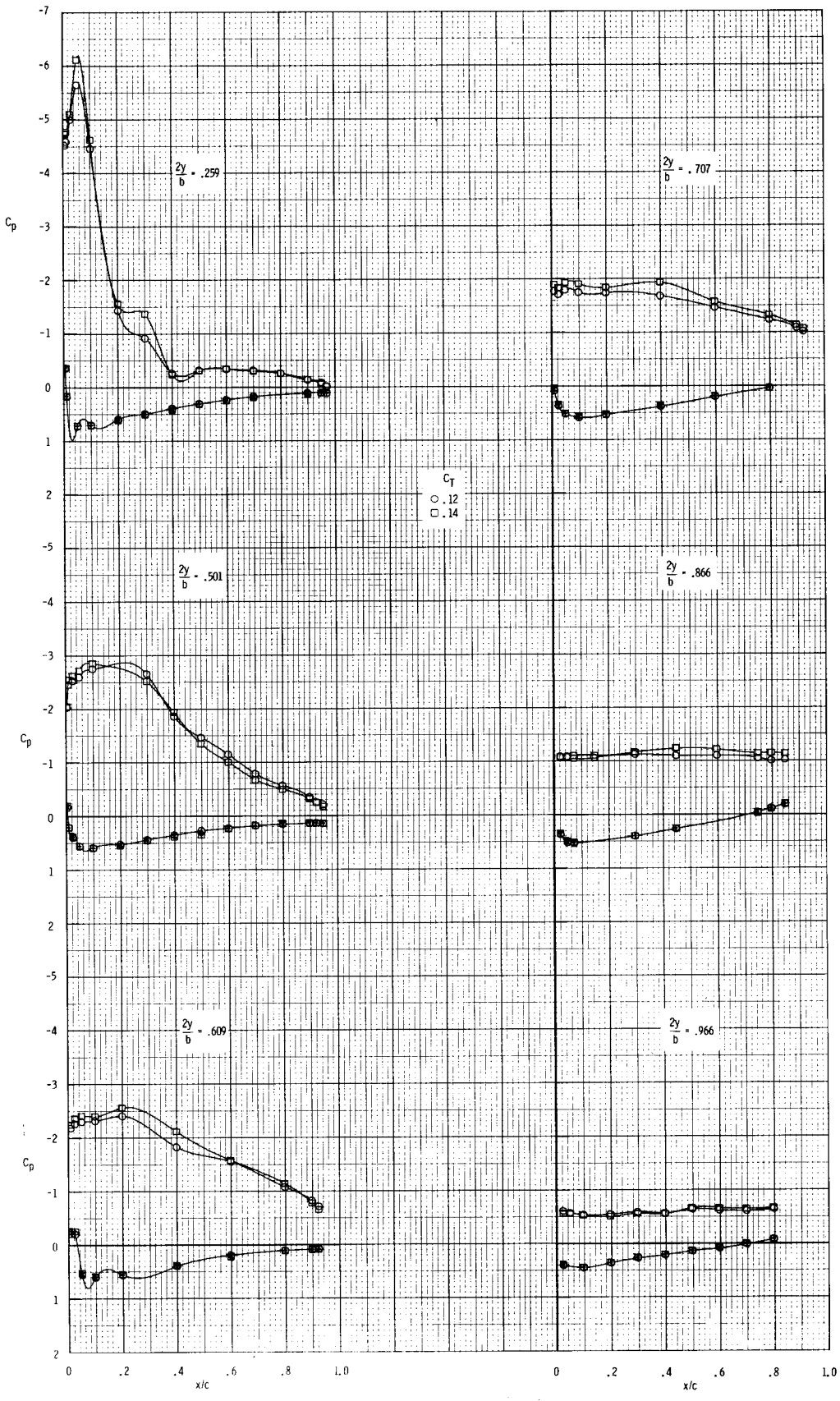

(c) C_T = 0.12 and 0.14.

Figure 38.- Continued.

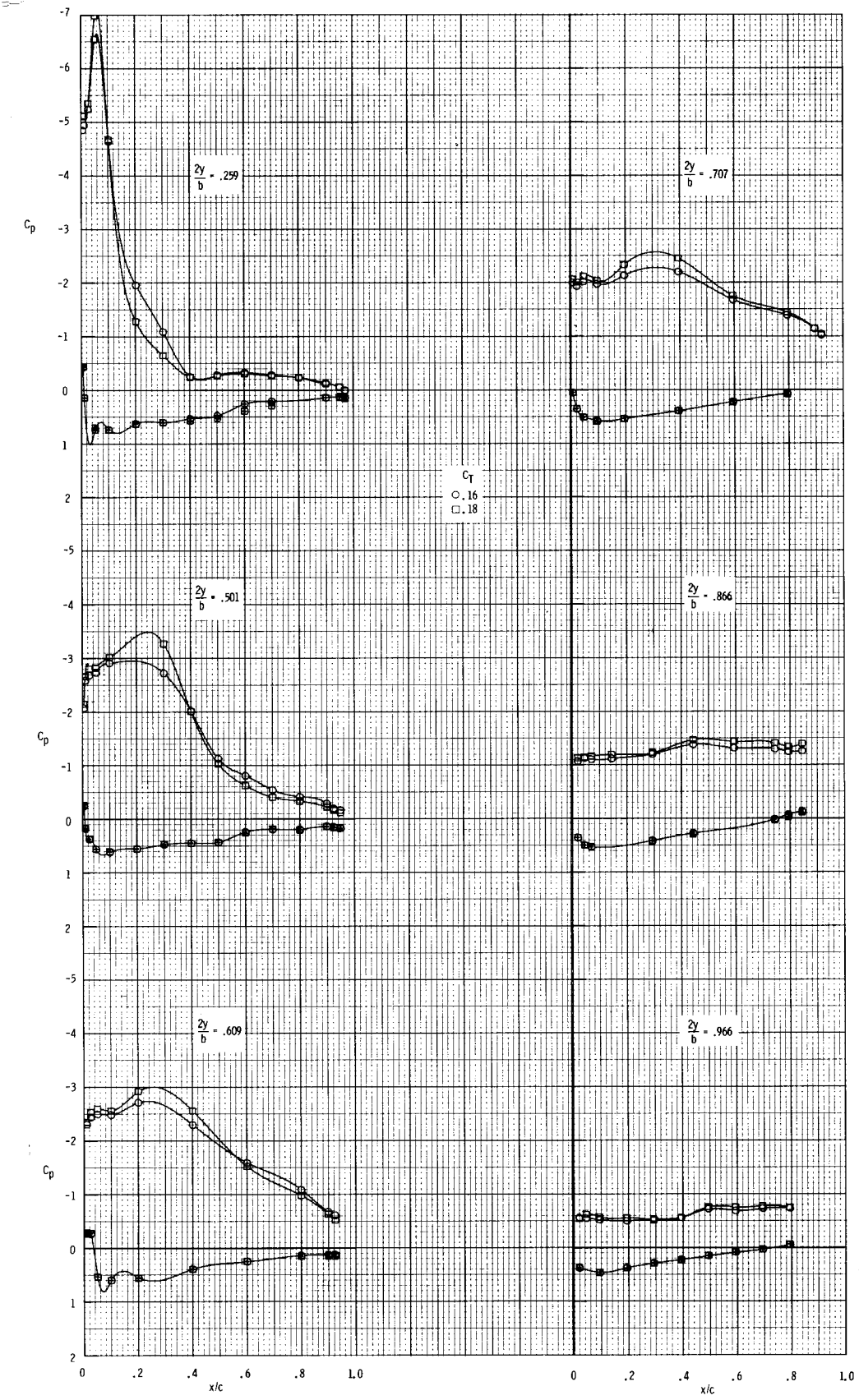

(d) C_T = 0.16 and 0.18.

Figure 38.- Concluded.

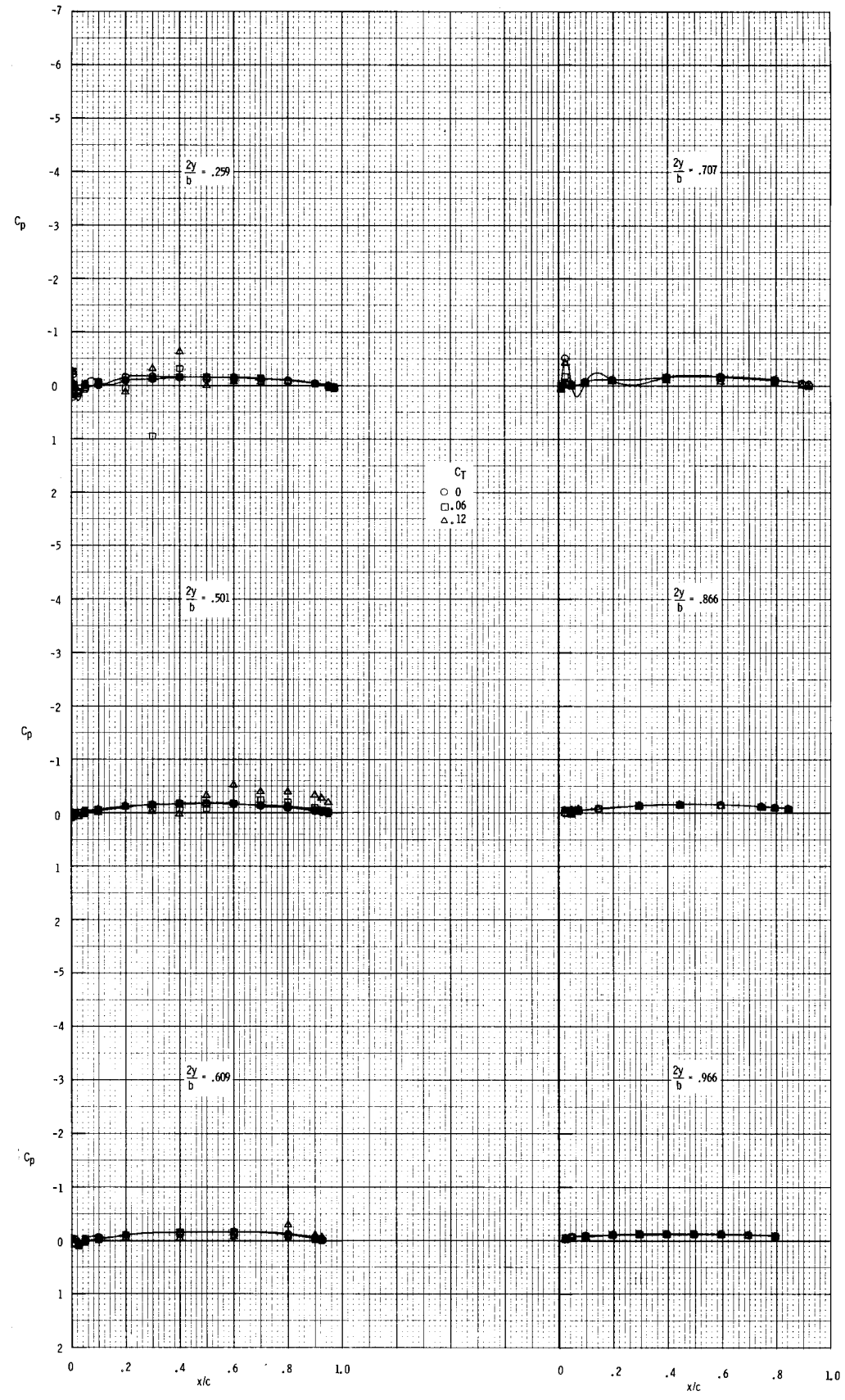

(a) $\alpha = 0.0^{\circ}$.

Figure 39.- Effect of nozzle thrust coefficient on wing-surface pressure distributions for a range of angle of attack; $\overline{x_n/c_r} = 0.23$; $\Lambda_n = 44^{\circ}$; $h/d = 1.843$.

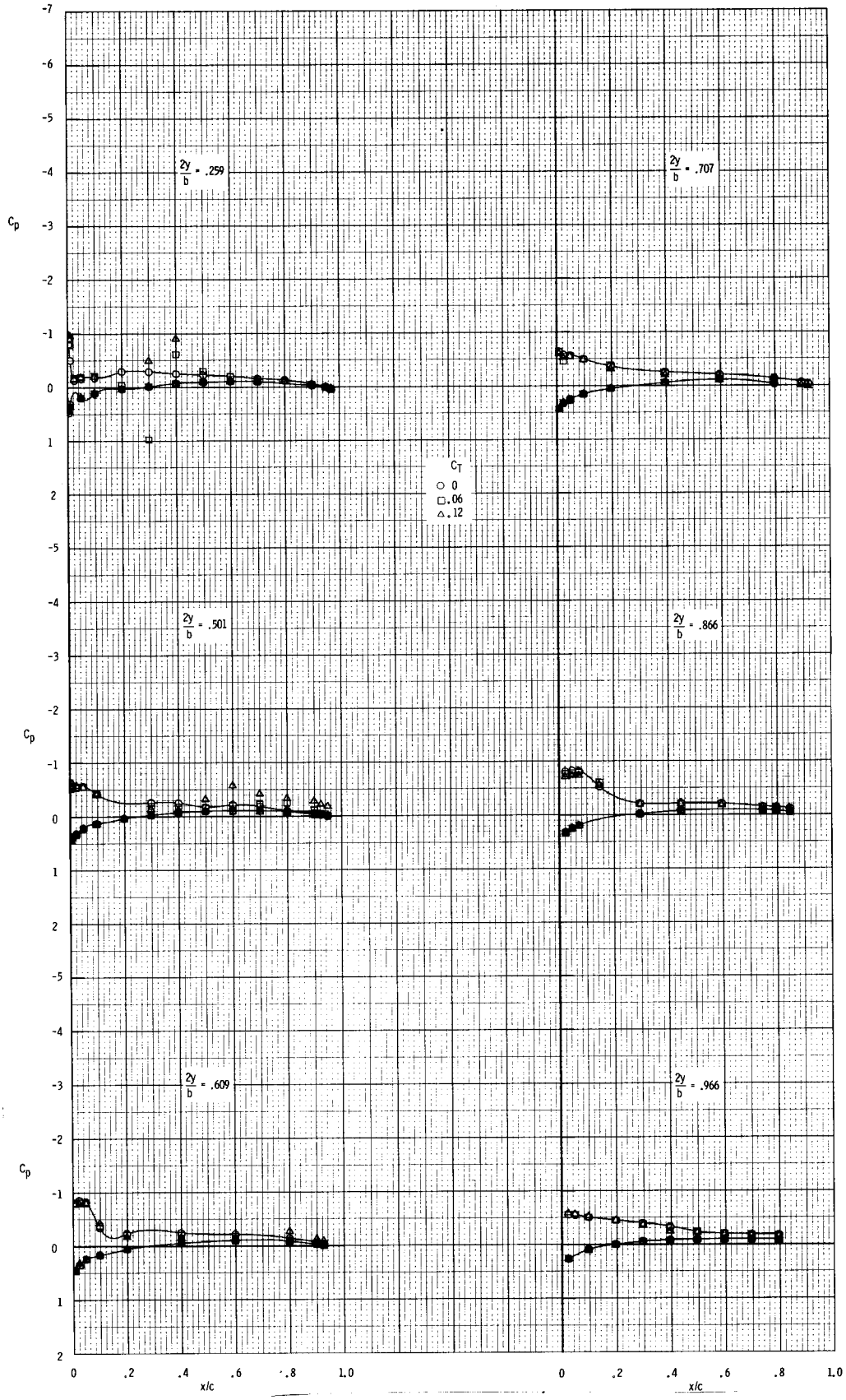

(b) $\alpha = 4.0^{o}$.

Figure 39.- Continued.

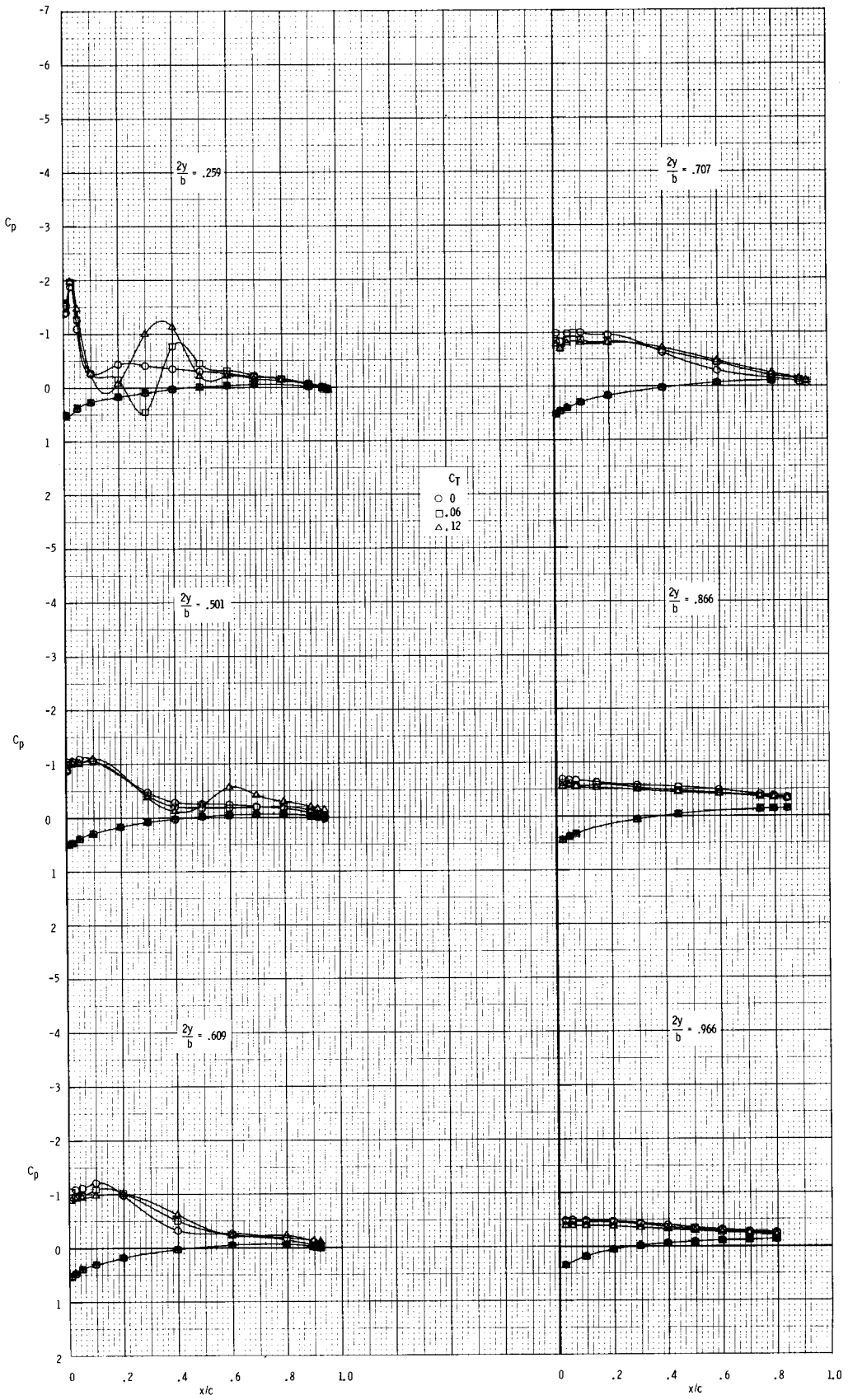

(c) $\alpha = 8.1^{o}$.

Figure 39.- Continued.

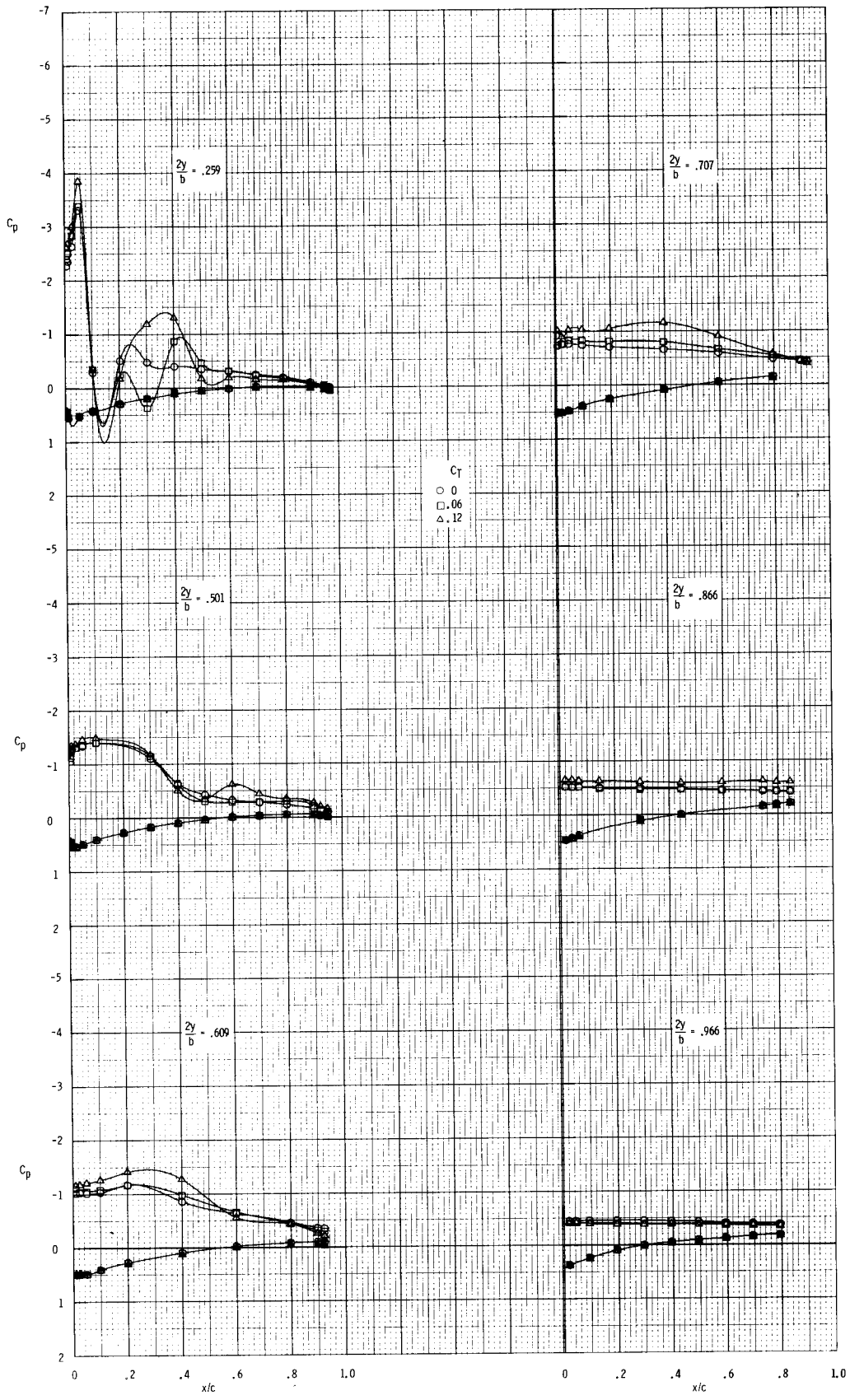

(d) $\alpha = 12.3^{\circ}$.

Figure 39.- Continued.

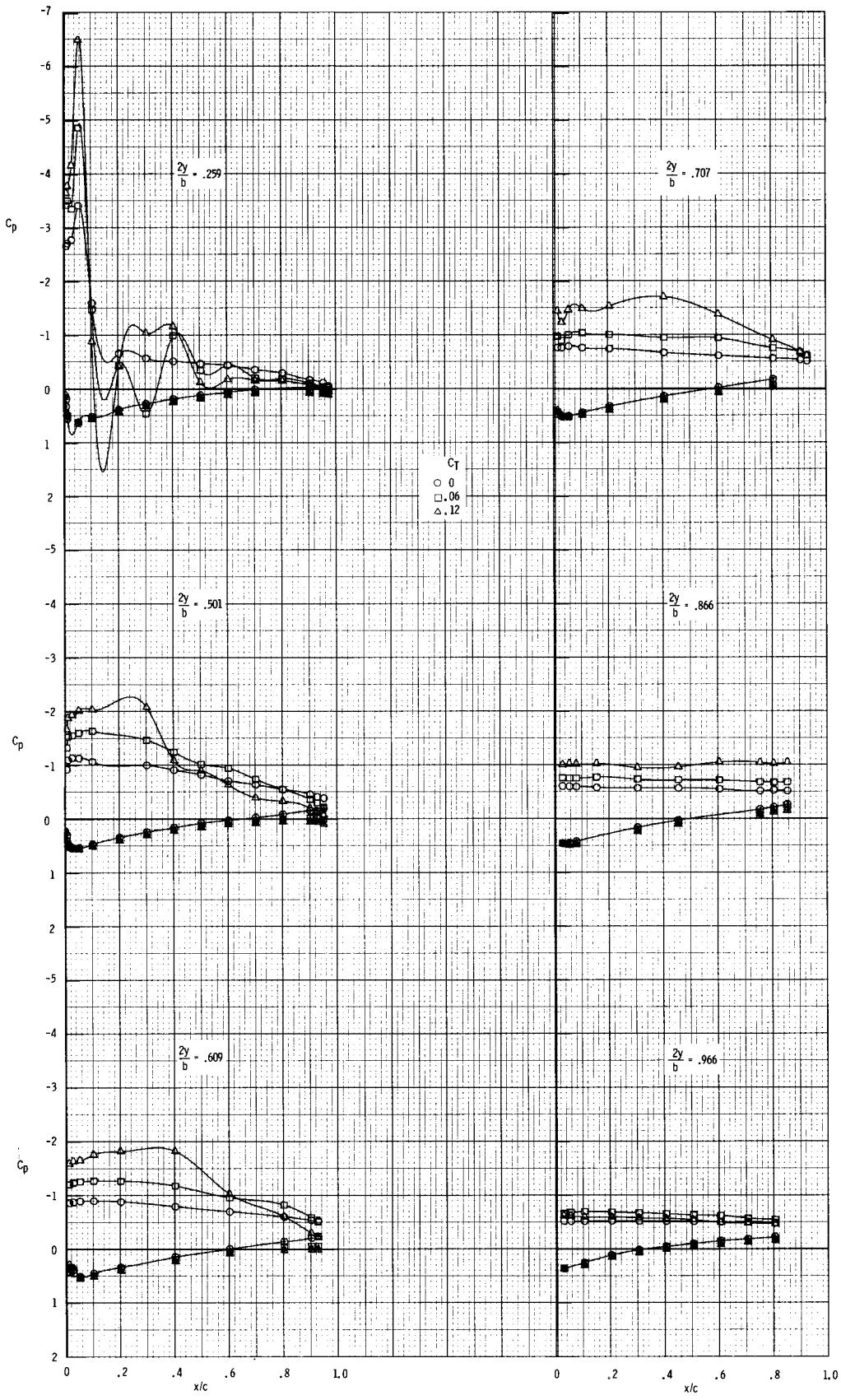

(e) $\alpha = 16.5^{\circ}$.

Figure 39.- Continued.

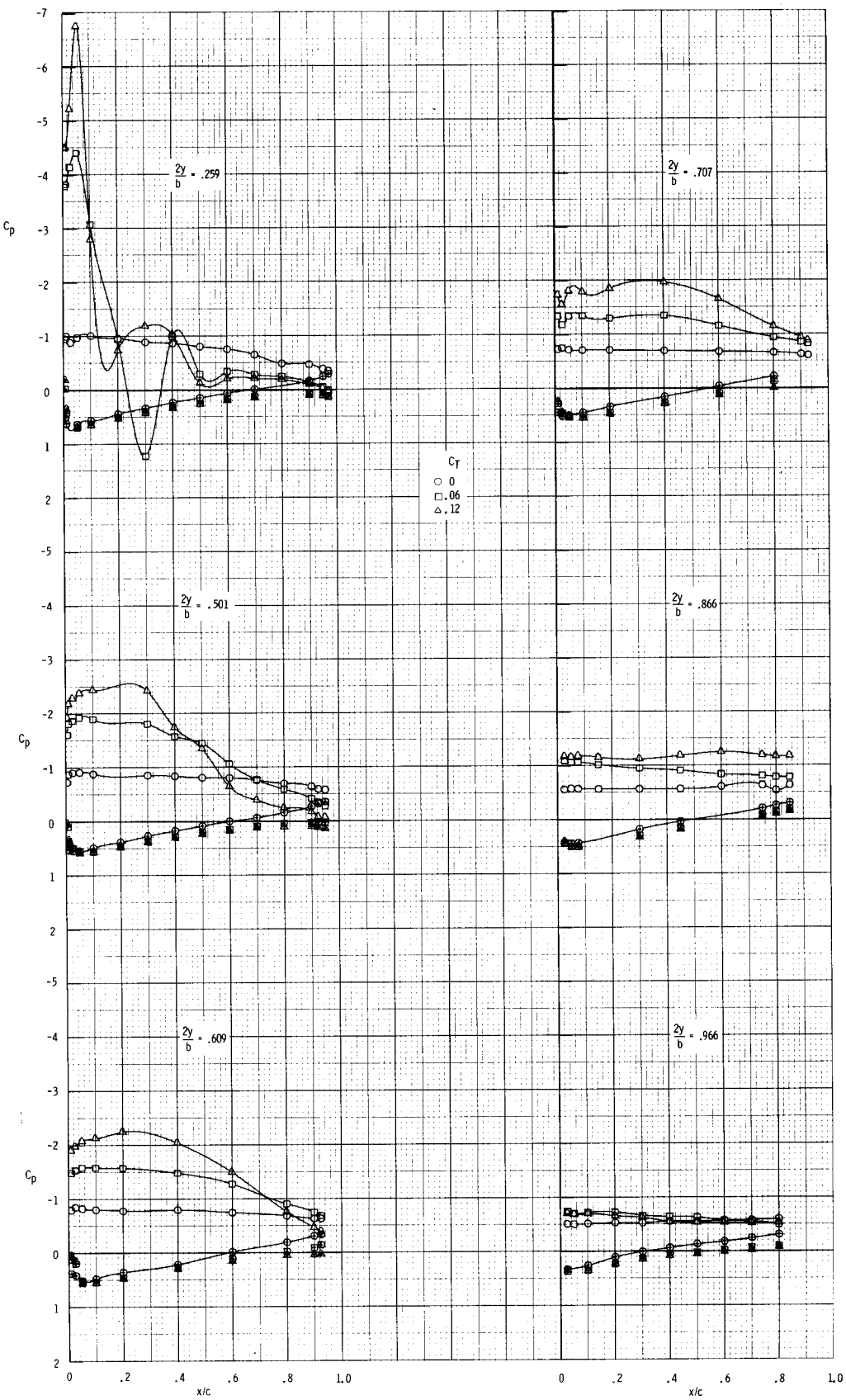

(f) $\alpha = 20.6^{\circ}$.

Figure 39.- Continued.

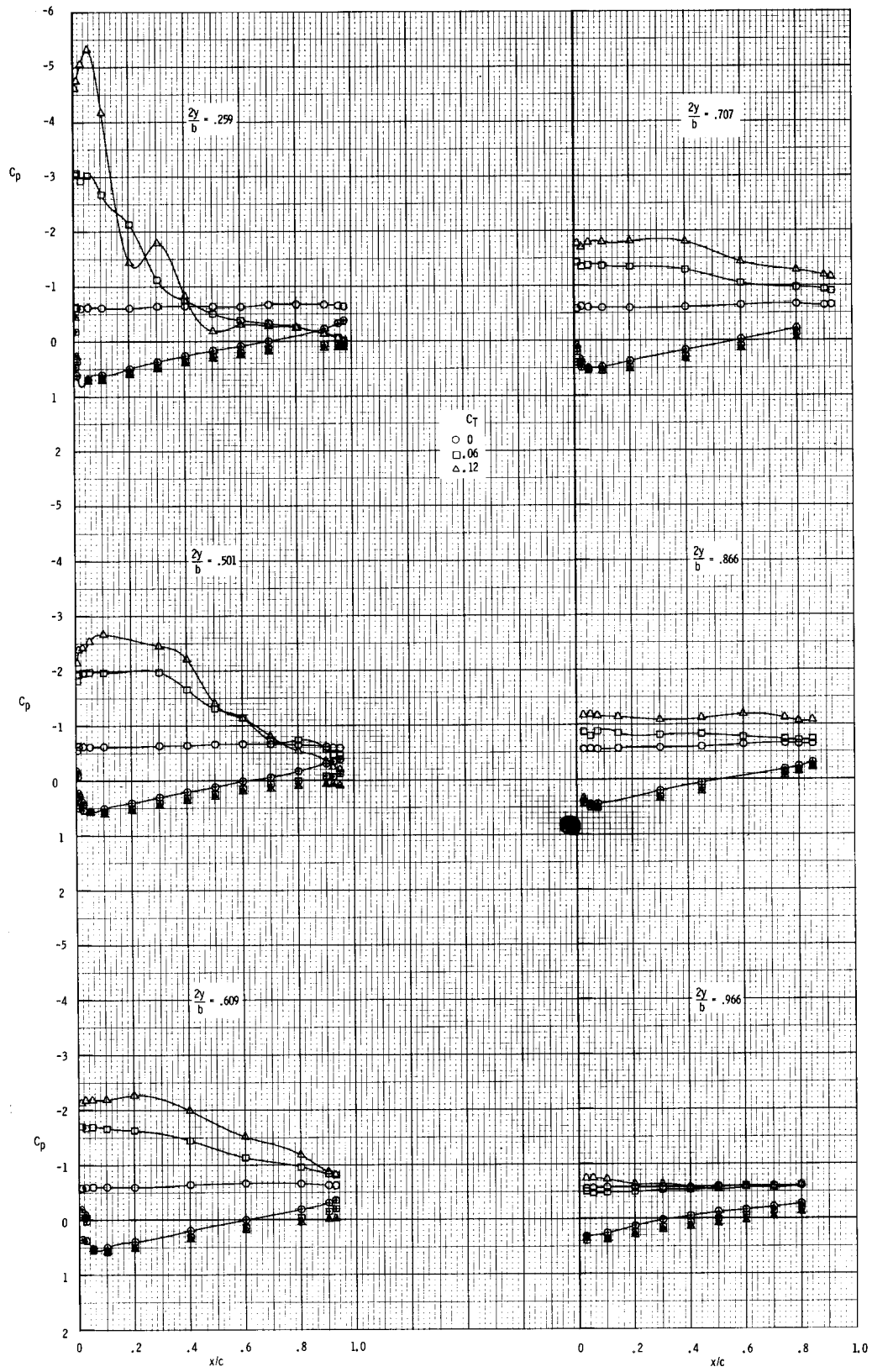

(g) $\alpha = 23.8^{\circ}$.

Figure 39.- Concluded.

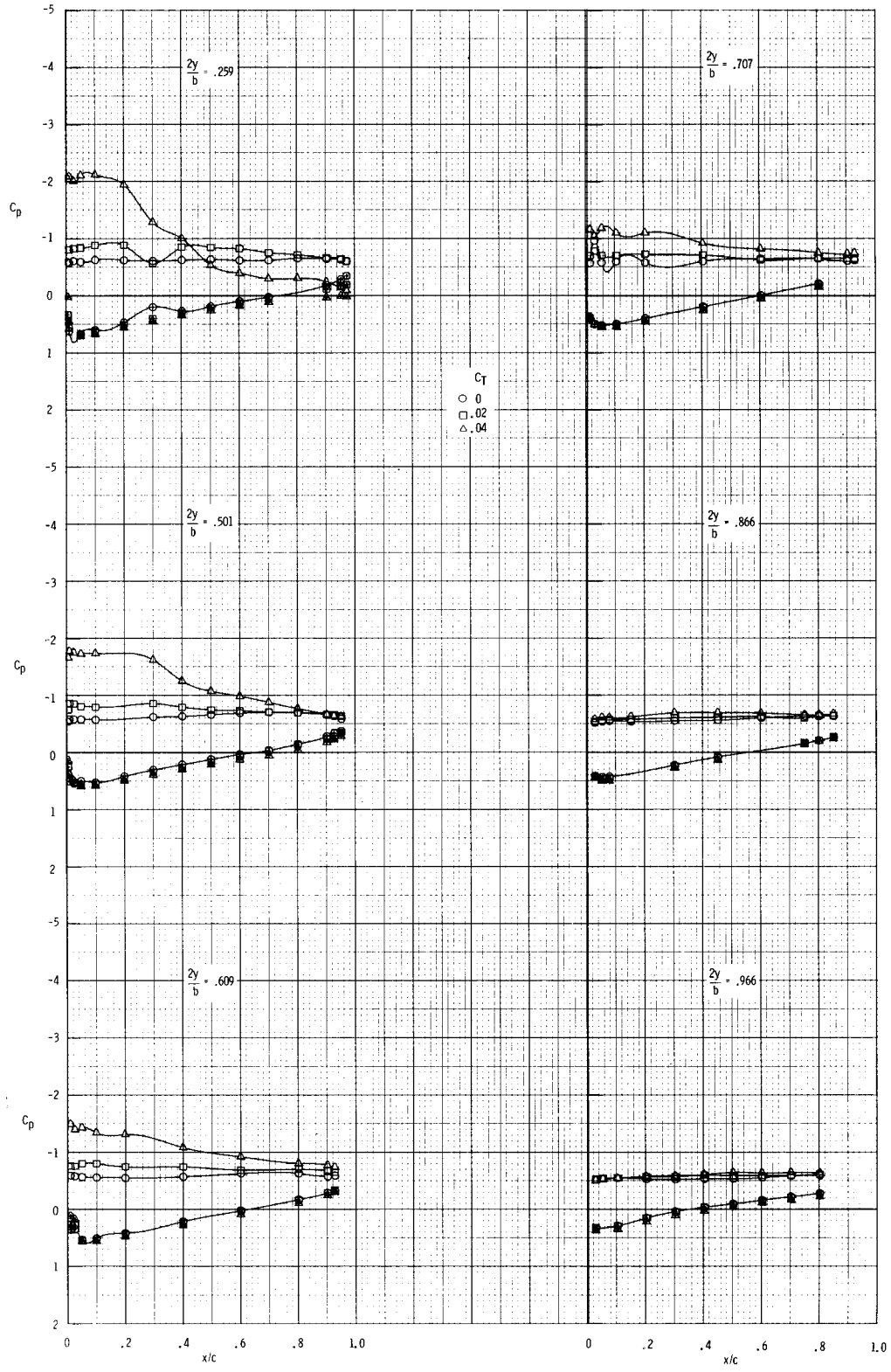

(a) C_T = 0, 0.02, and 0.04.

Figure 40.- Effect of nozzle thrust coefficient on wing-surface pressure distributions for $\alpha = 24.0^o$; $x_n/c_r = 0.23$; $\Lambda_n = 44^o$; h/d = 1.843.

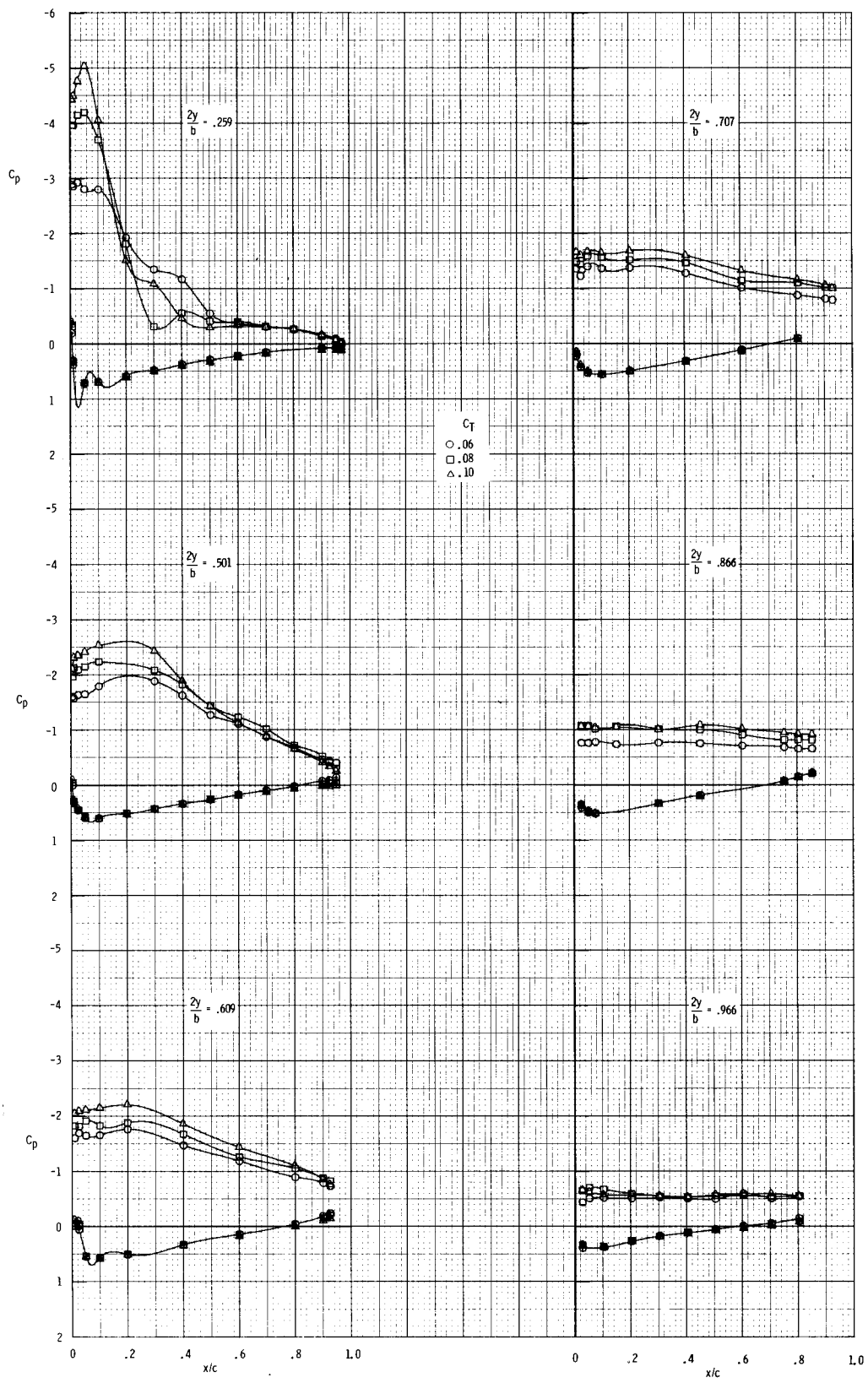

(b) C_T = 0.06, 0.08, and 0.10.

Figure 40.- Continued.

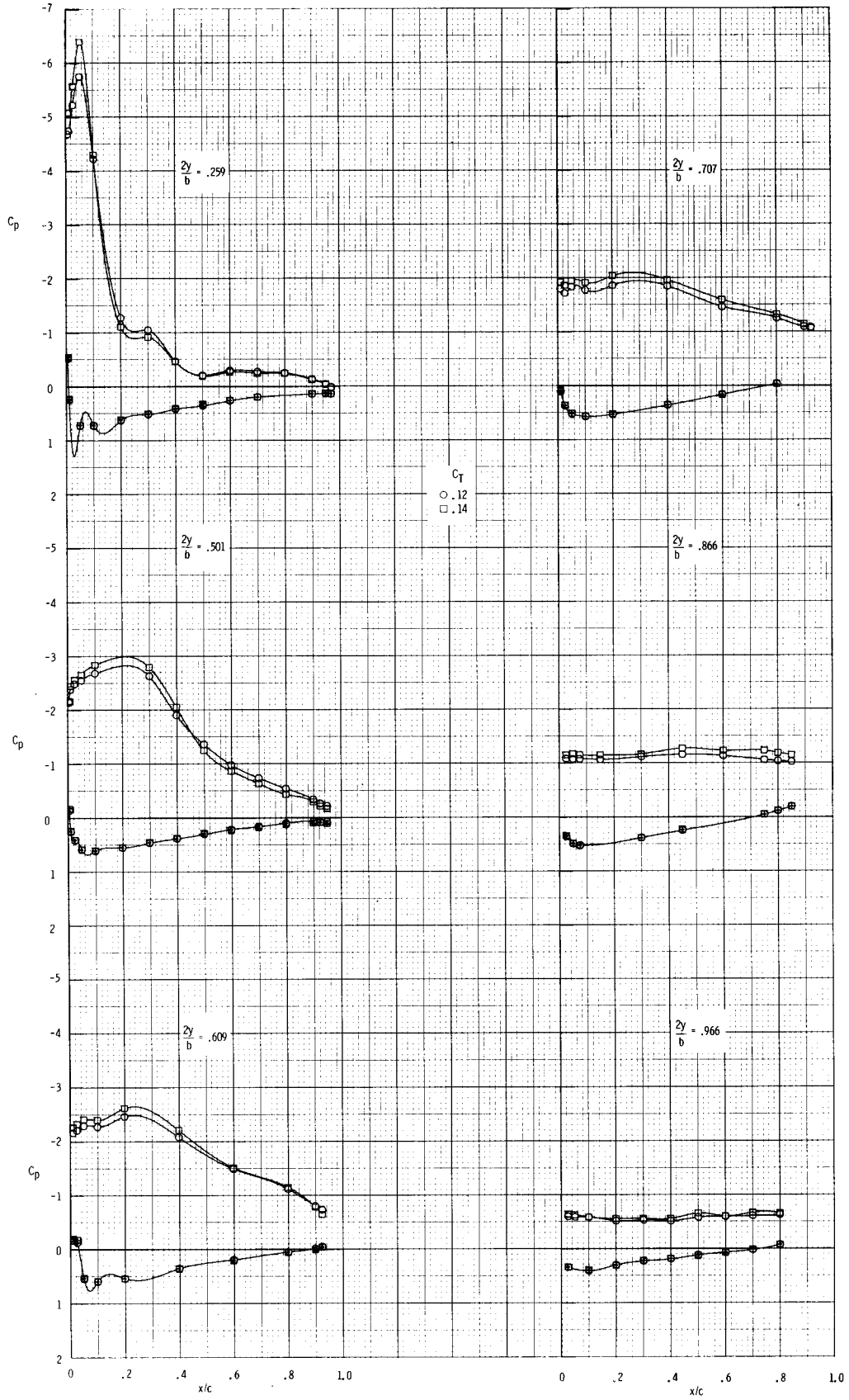

(c) C_T = 0.12 and 0.14.

Figure 40.- Continued.

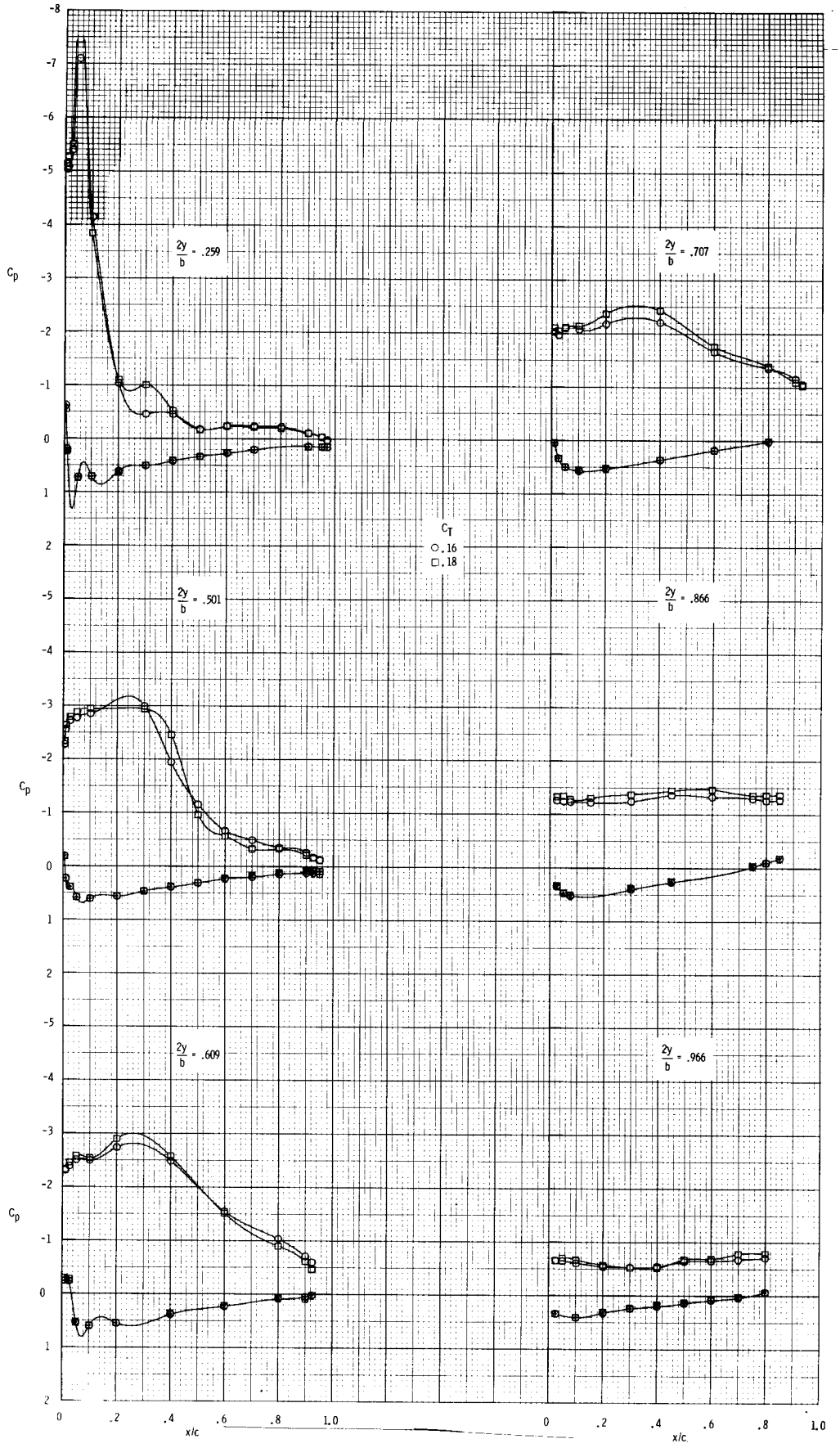

(d) C_T = 0.16 and 0.18.

Figure 40.- Concluded.

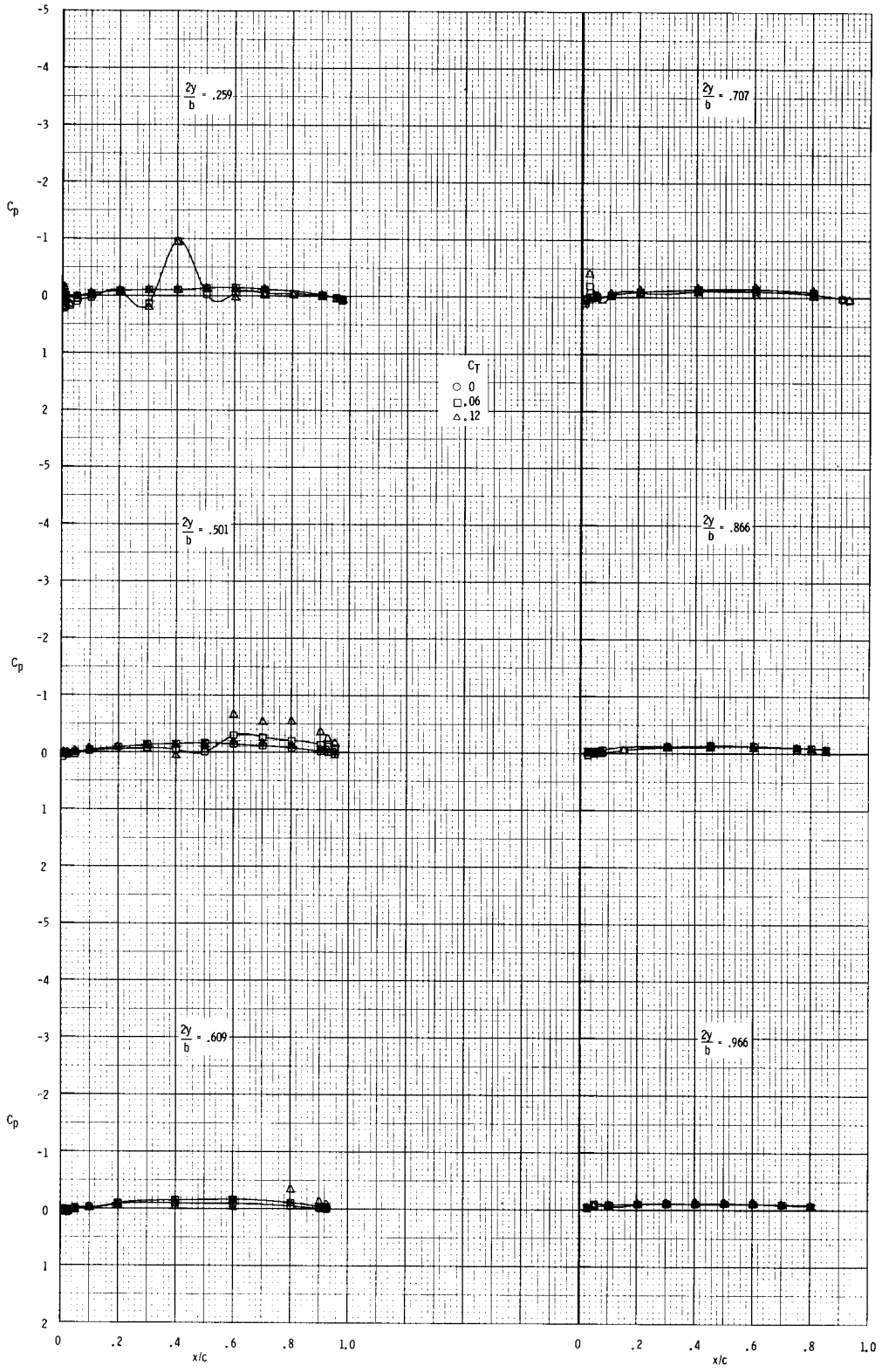

(a) $\alpha = 0.1^{o}$.

Figure 41.- Effect of nozzle thrust coefficient on wing-surface pressure distributions for a range of angle of attack. $x_n/c_r = 0.32$; $\Lambda_n = 44^{o}$; $h/d = 0.835$.

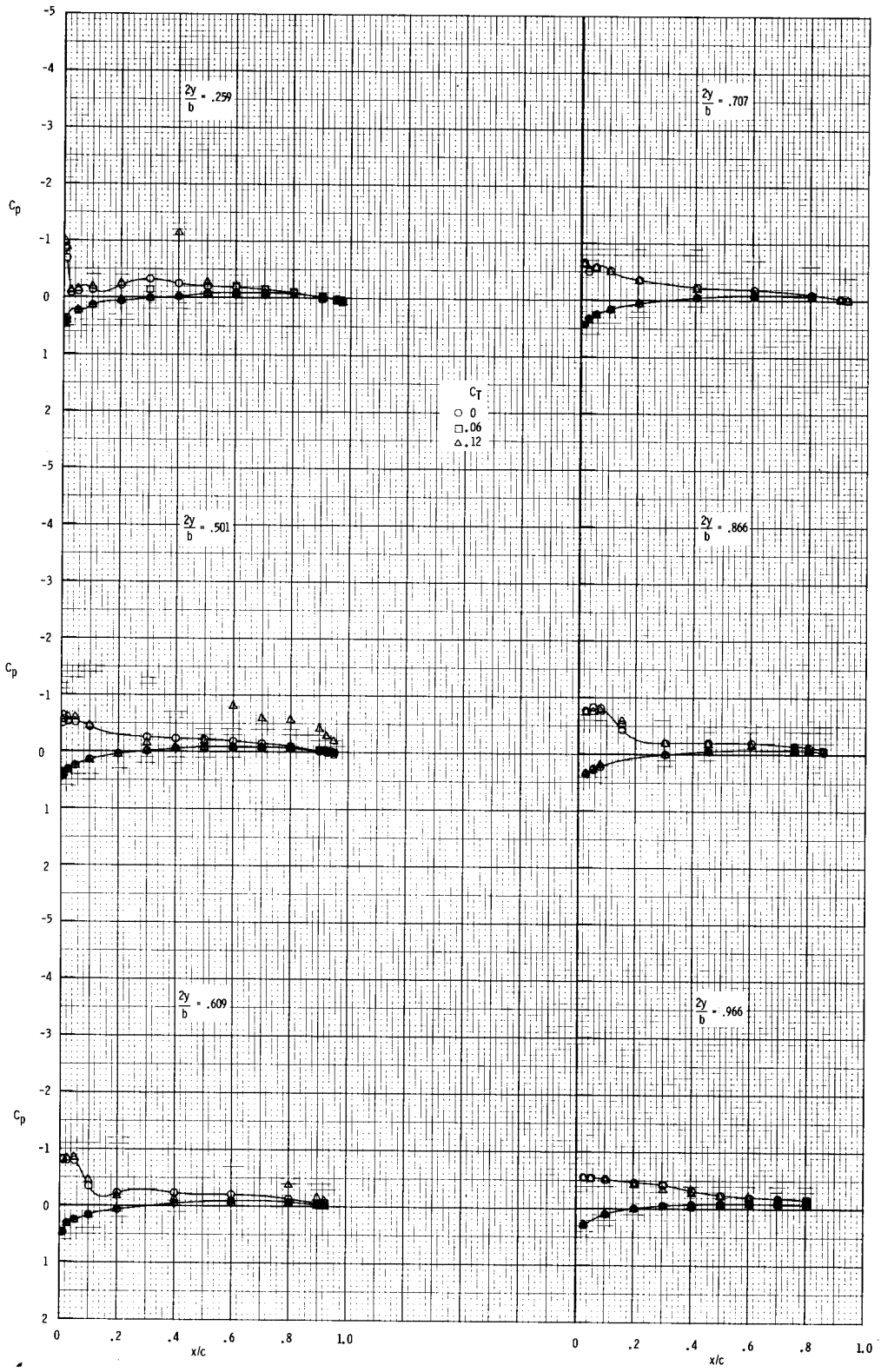

(b) $\alpha = 4.0^{\circ}$.

Figure 41.- Continued.

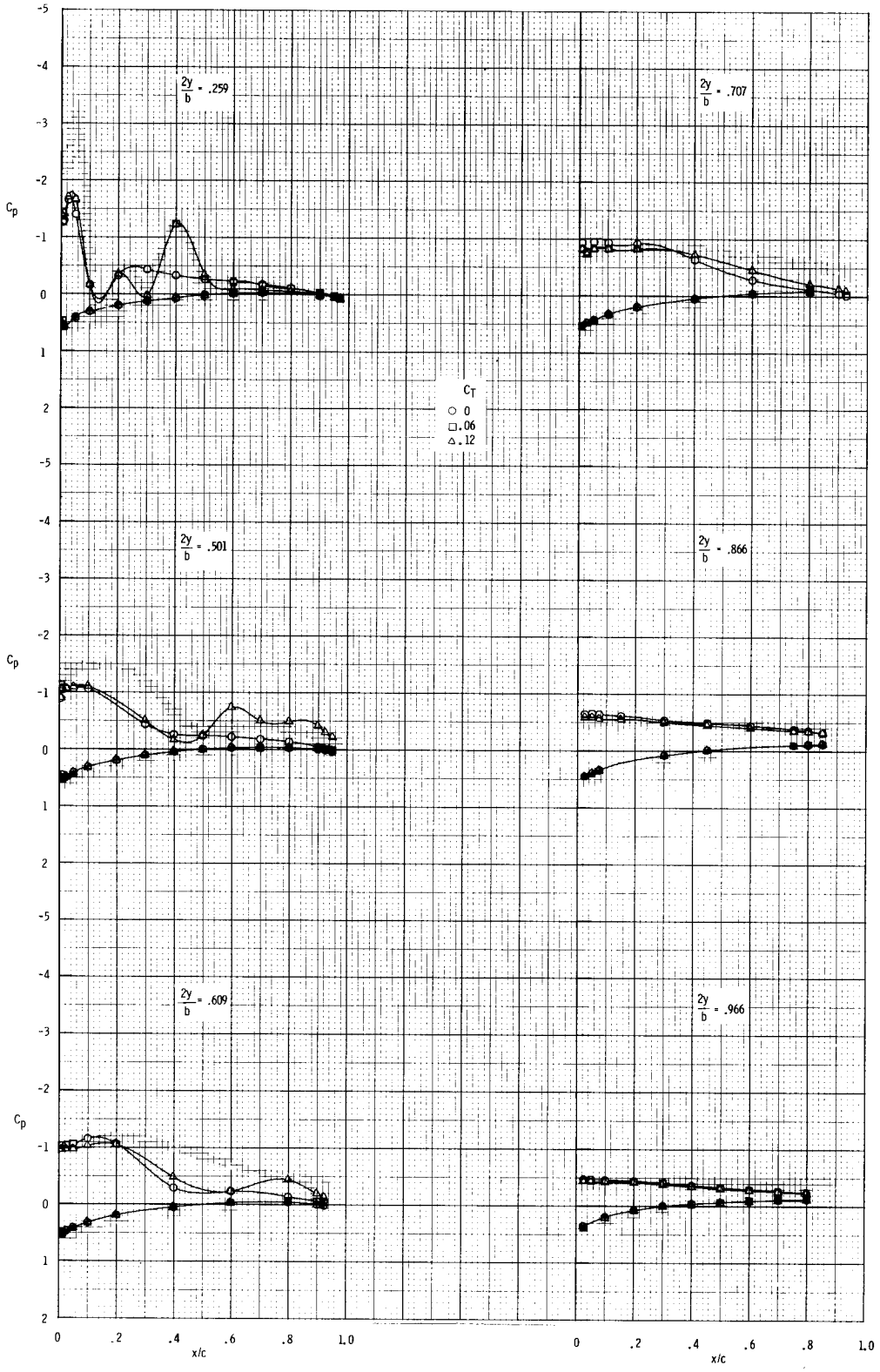

(c) $\alpha = 8.1^{\circ}$.

Figure 41.- Continued.

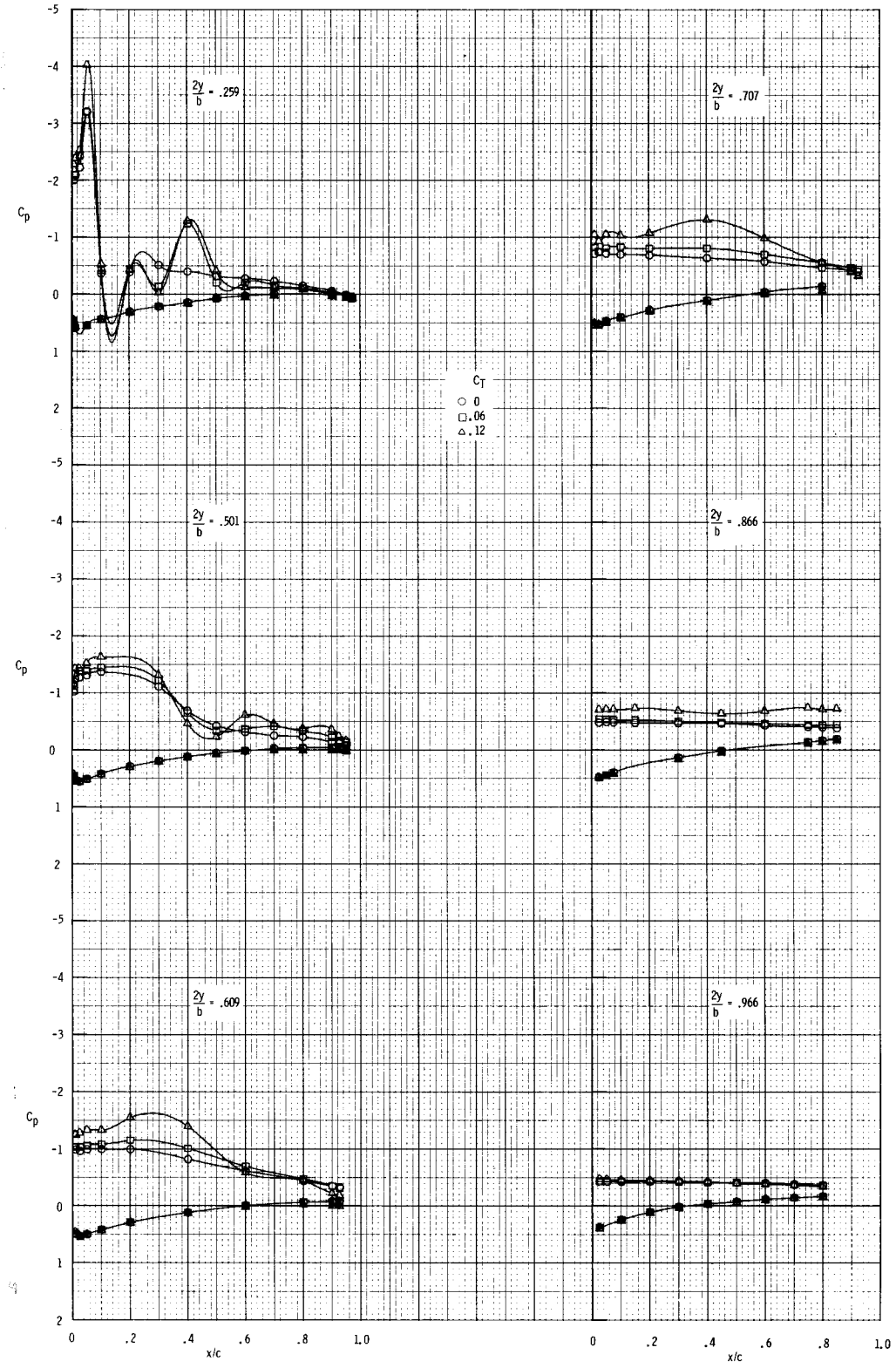

(d) $\alpha = 12.4^{\circ}$.

Figure 41.- Continued.

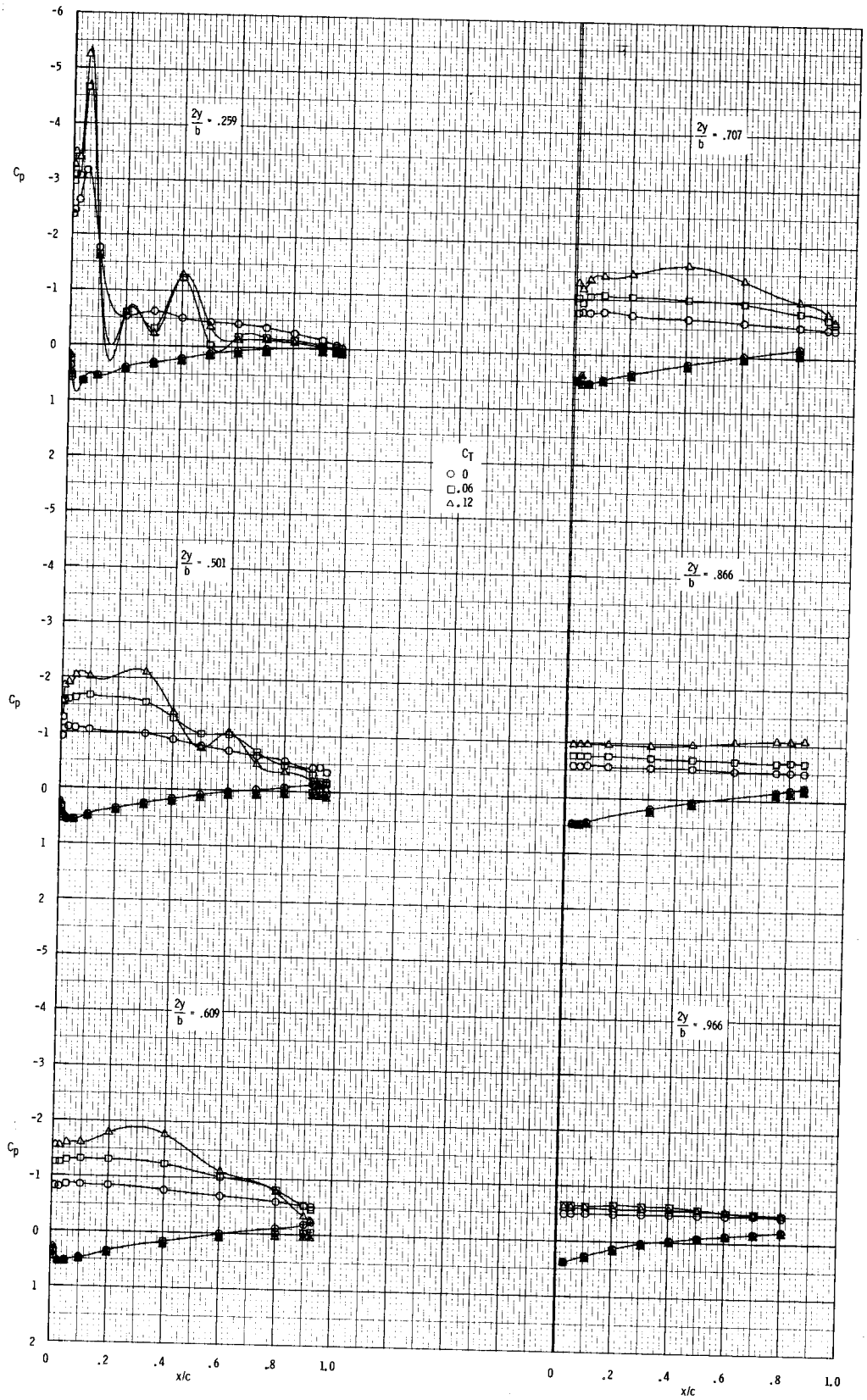

(e) $\alpha = 16.6^{o}$.

Figure 41.- Continued.

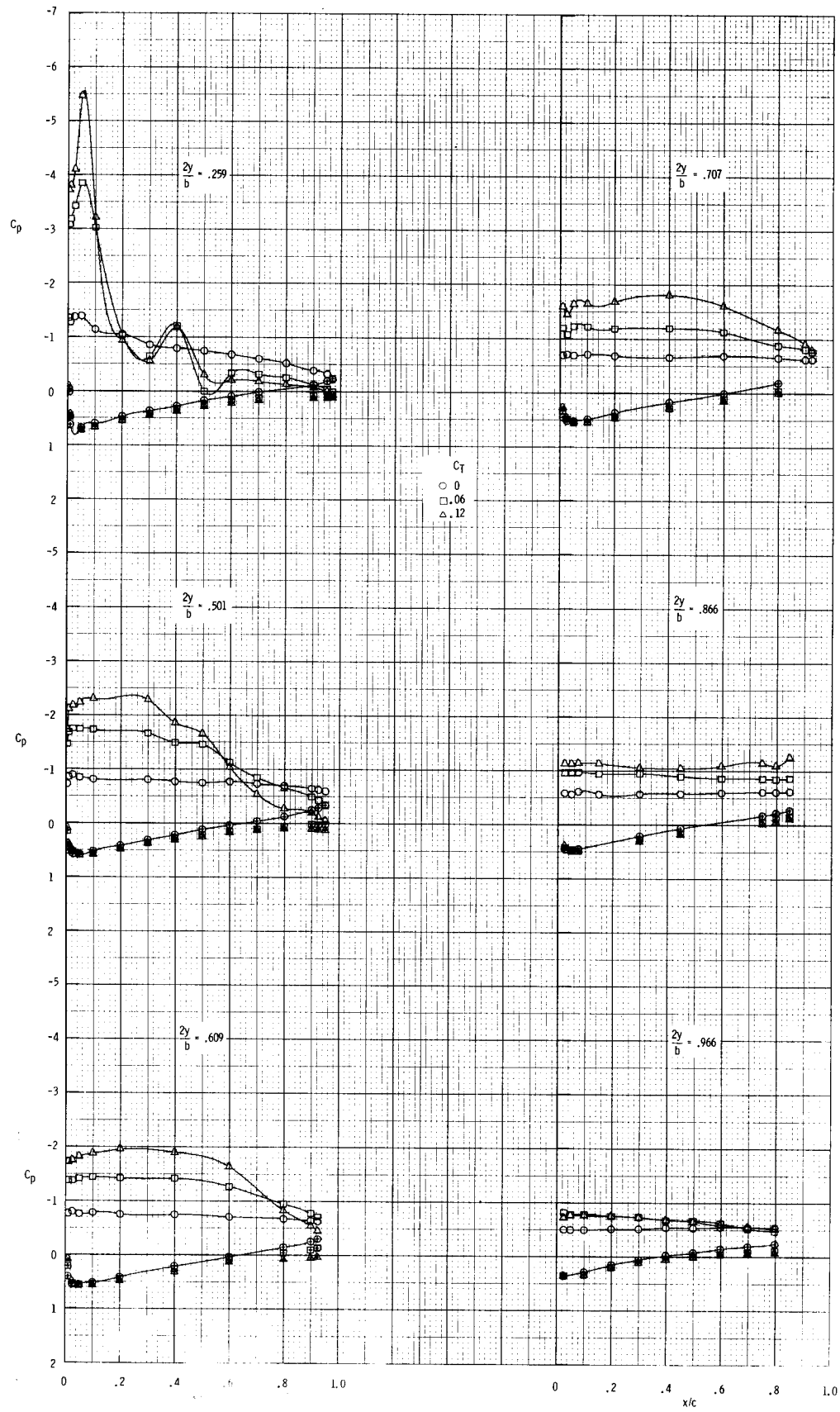

(f) $\alpha = 20.7^{o}$.

Figure 41.- Continued.

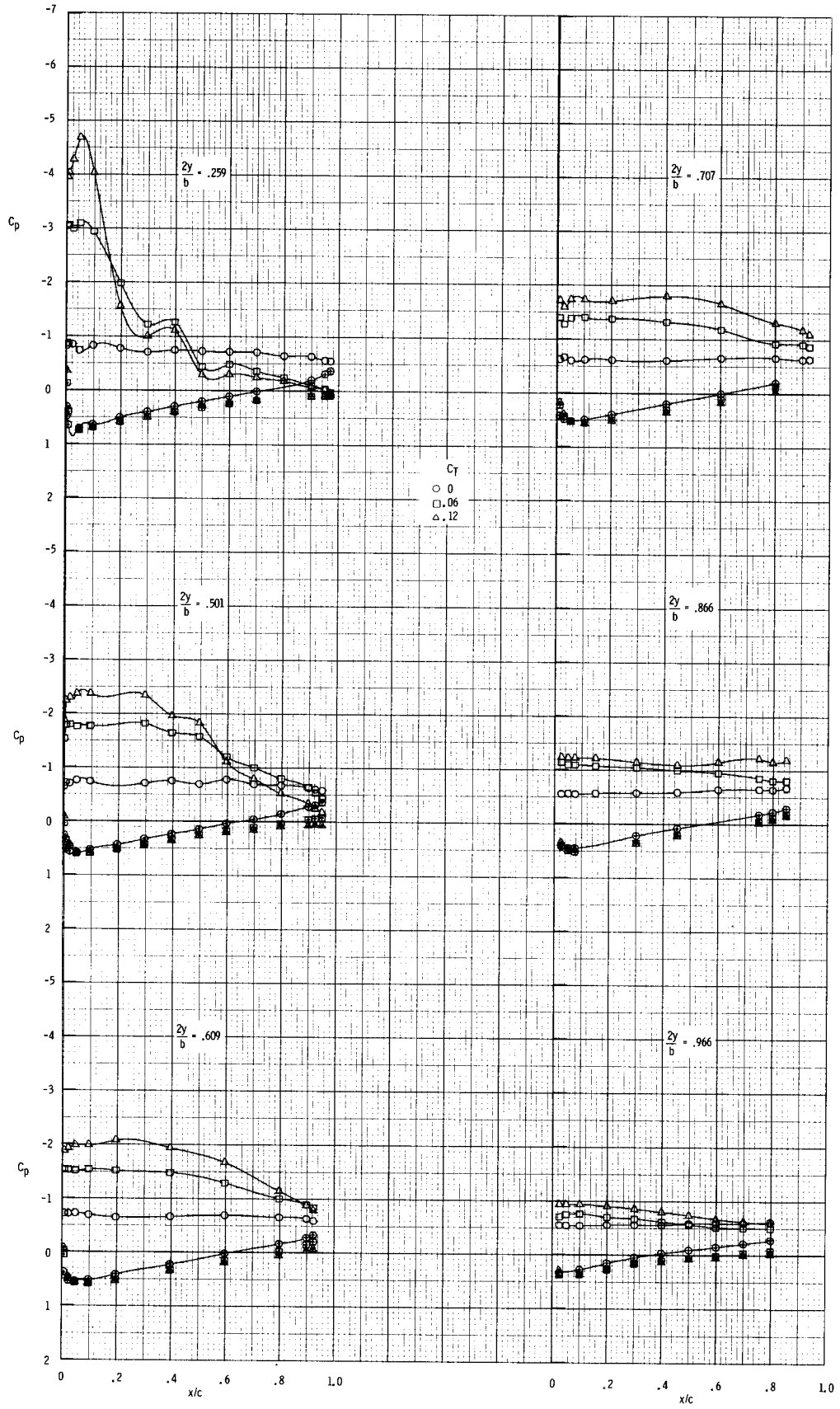

(g) $\alpha = 23.8^{o}$.

Figure 41.- Concluded.

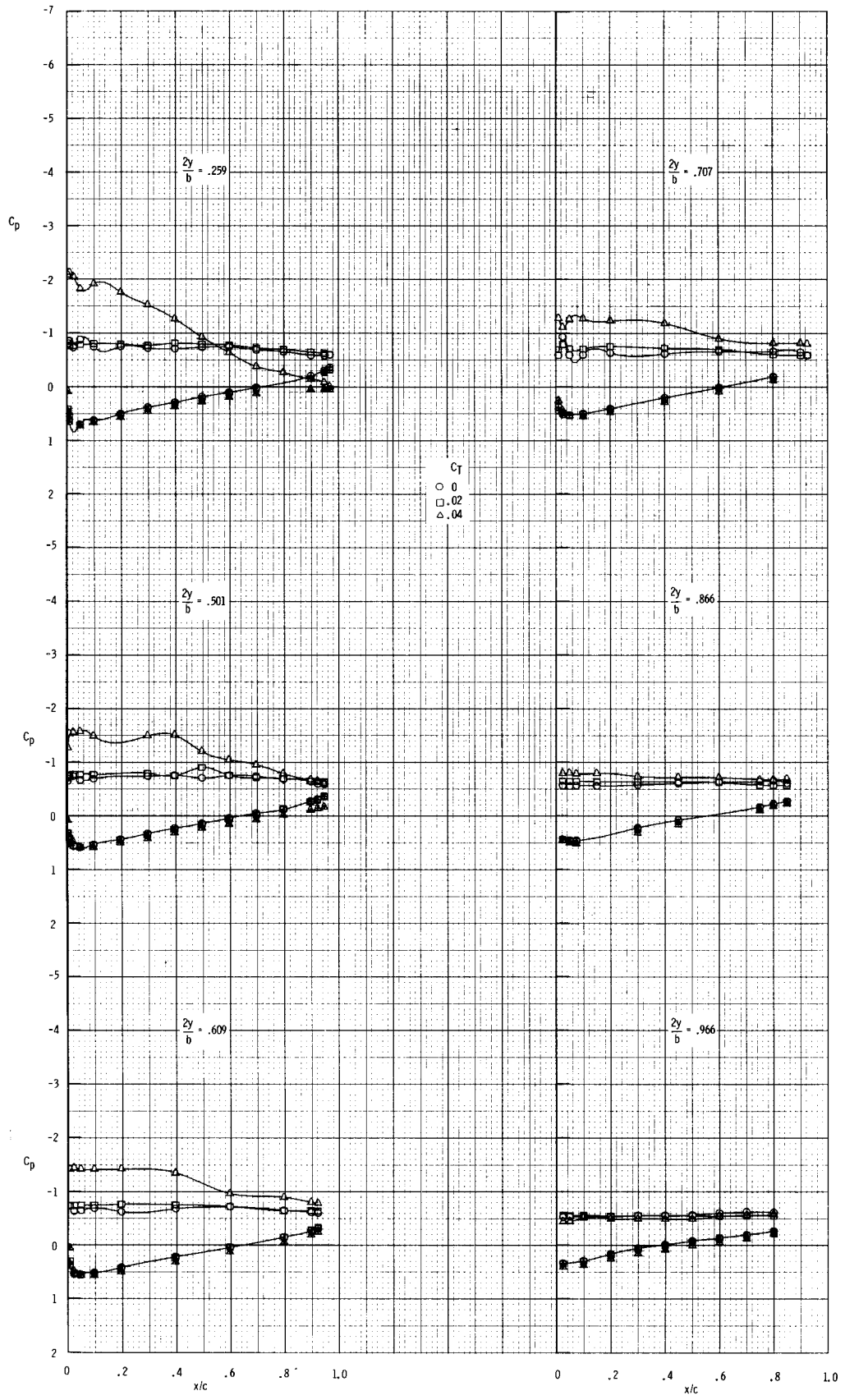

(a) C_T = 0, 0.02, and 0.04.

Figure 42.- Effect of nozzle thrust coefficient on wing-surface pressure distributions for $\alpha = 24.0^o$; $\overline{x_n/c_r} = 0.32$; $\Lambda_n = 44^o$; $h/d = 0.835$.

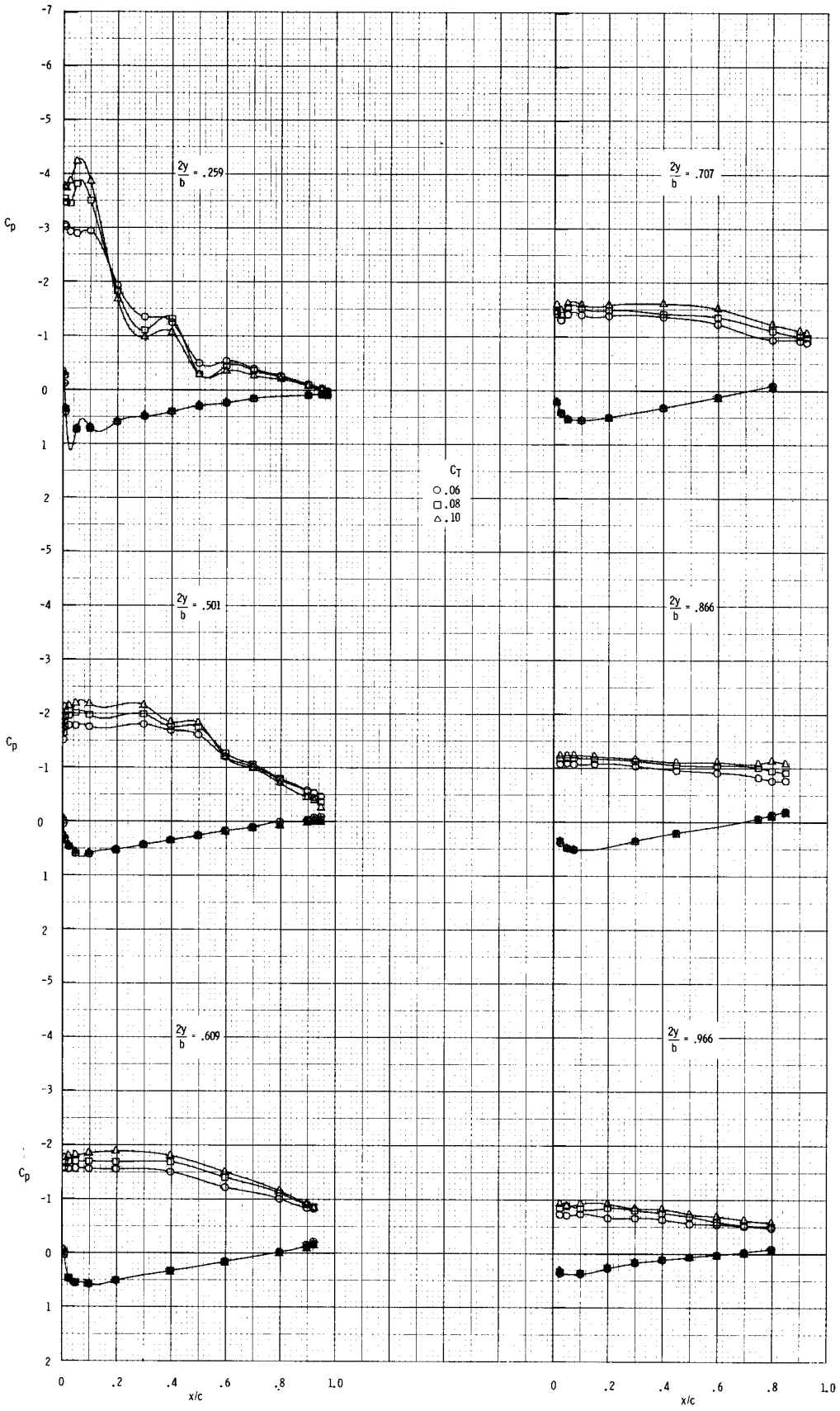

(b) C_T = 0.06, 0.08, and 0.10.

Figure 42.- Continued.

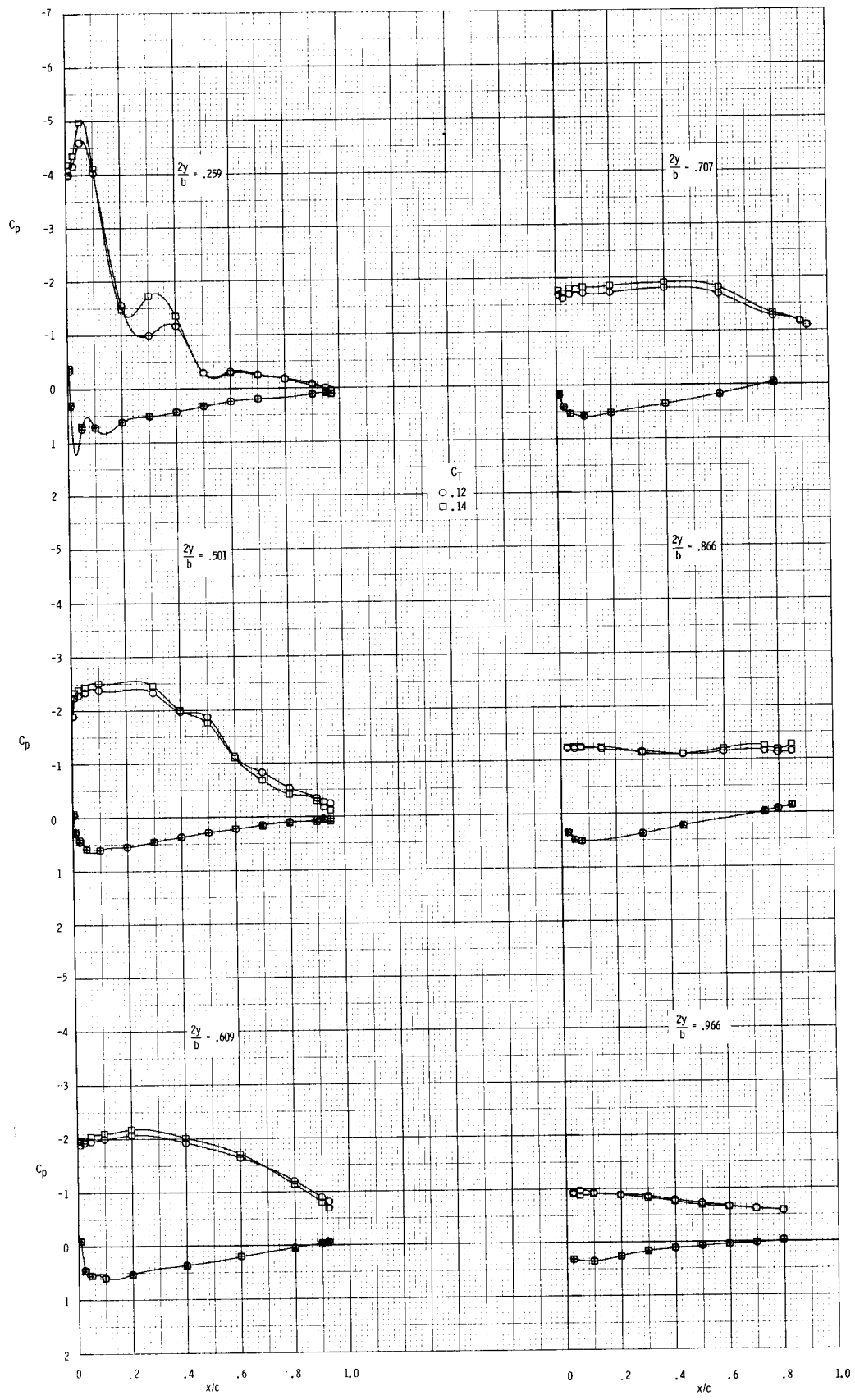

(c) C_T = 0.12 and 0.14.

Figure 42.- Continued.

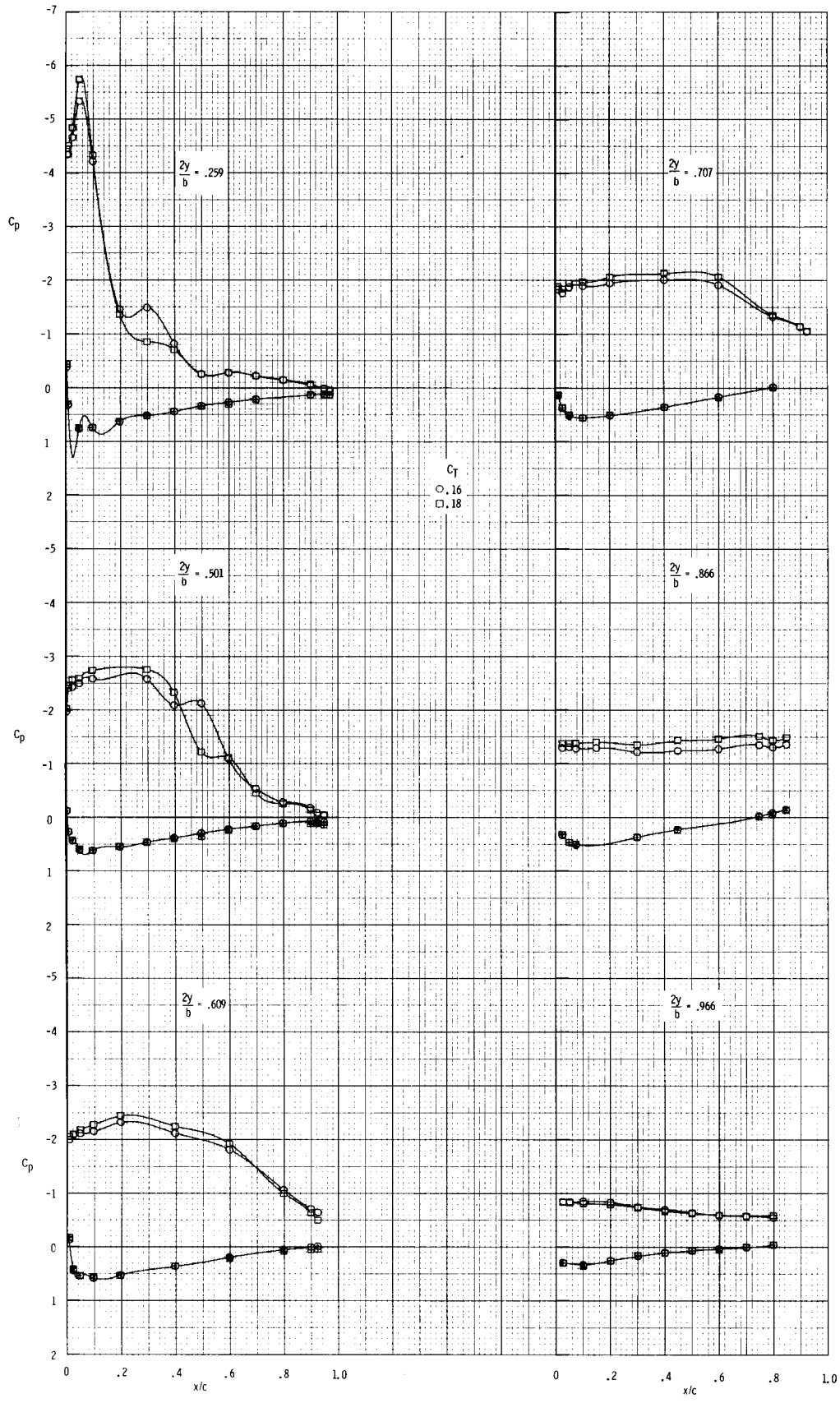

(d) C_T = 0.16 and 0.18.

Figure 42.- Concluded.

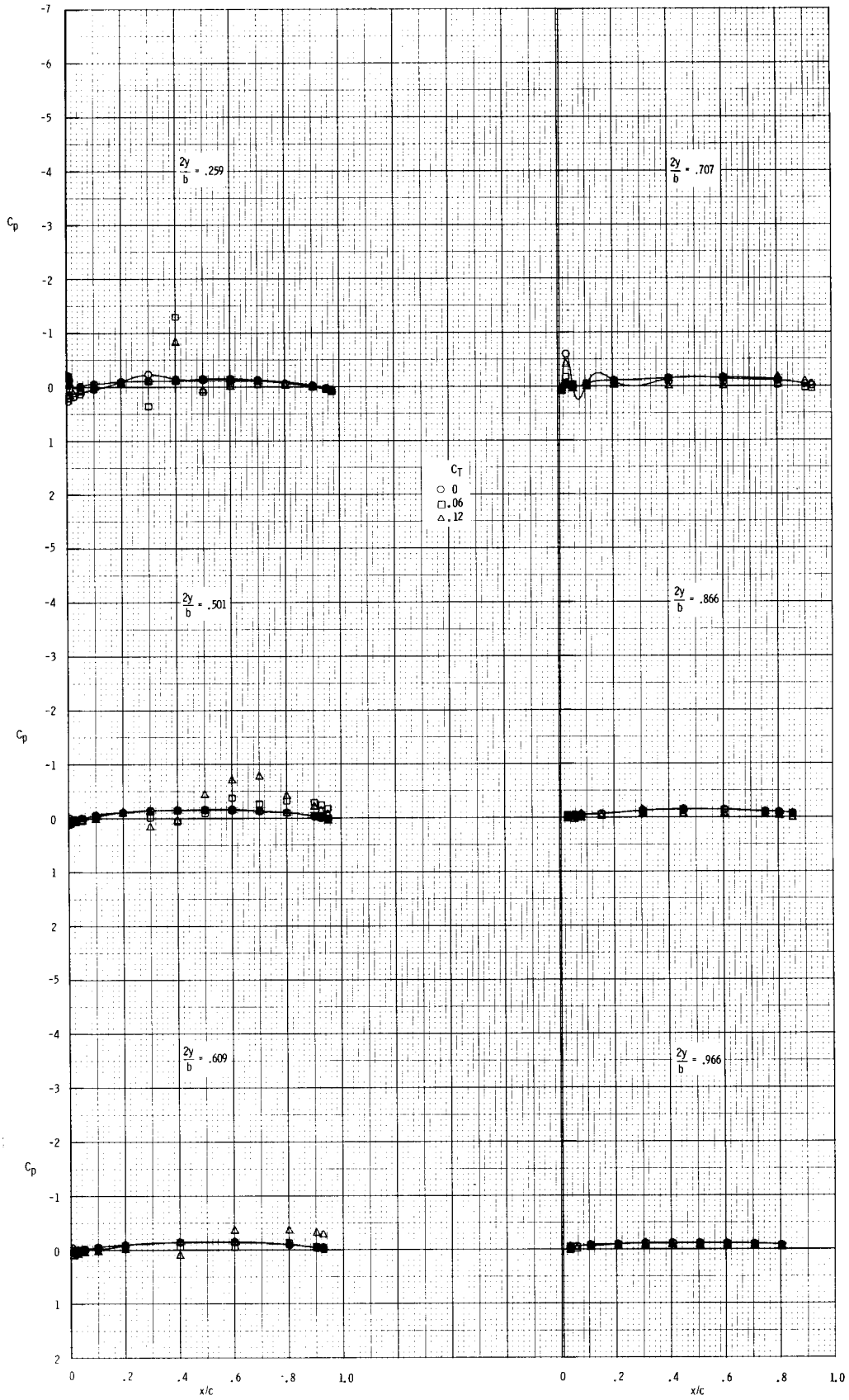

(a) $\alpha = 0.1^{\circ}$.

Figure 43.- Effect of nozzle thrust coefficient on wing-surface pressure distributions for a range of angle of attack; $\overline{x_n/c_r} = 0.32$; $\Lambda_n = 33^{\circ}$; $h/d = 0.835$.

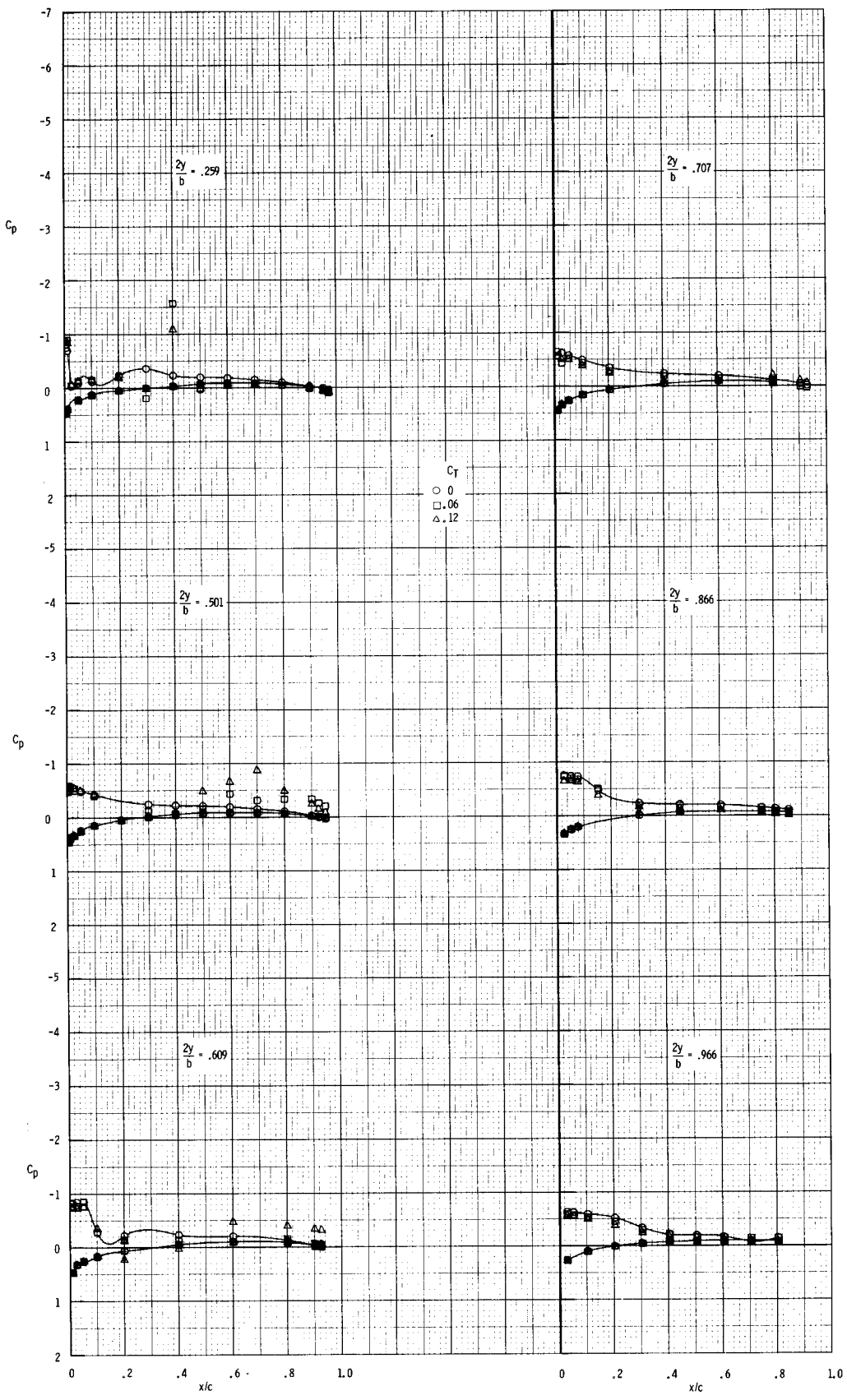

(b) $\alpha = 4.0^{o}$.

Figure 43.- Continued.

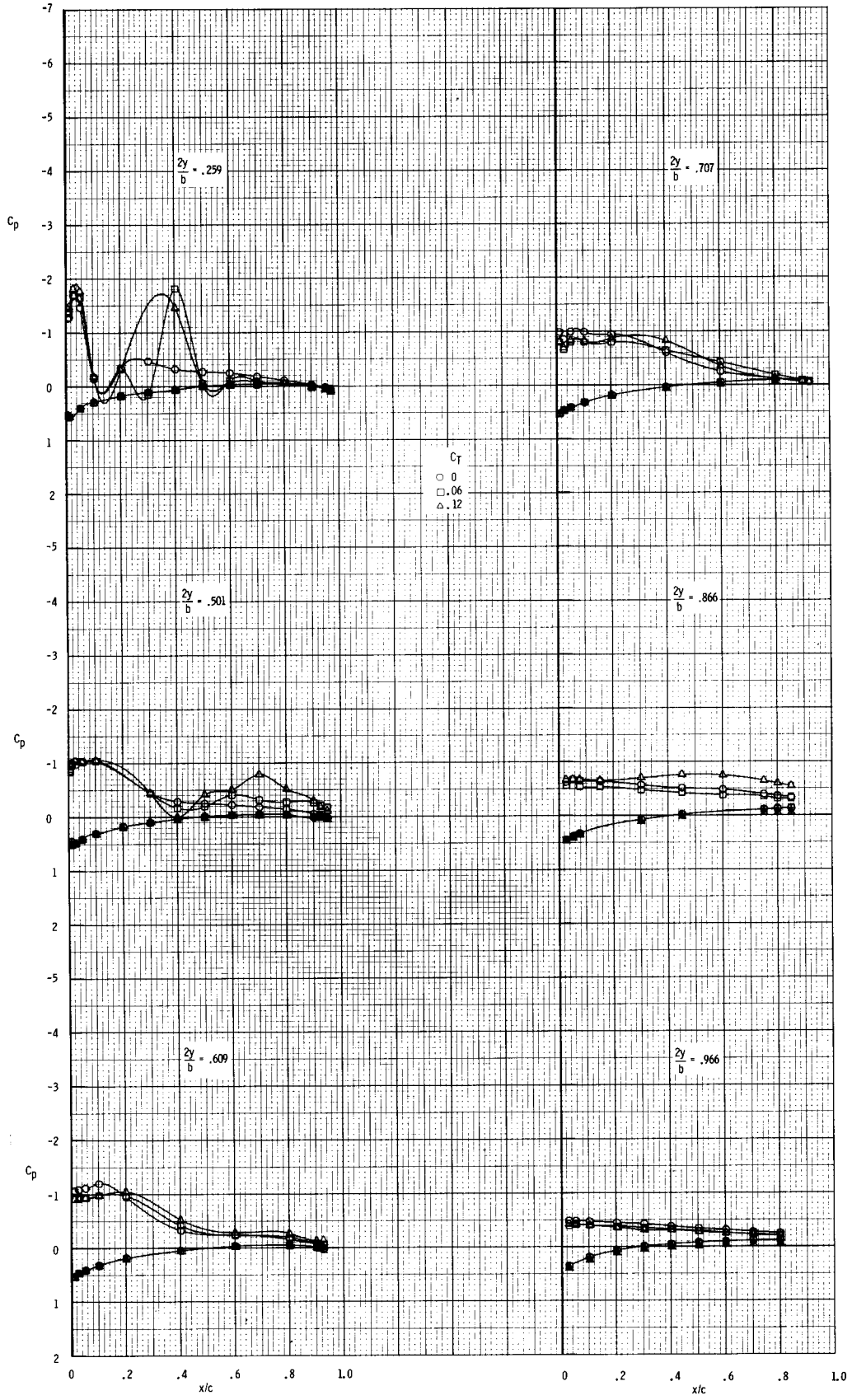

(c) $\alpha = 8.1^{\circ}$.

Figure 43.- Continued.

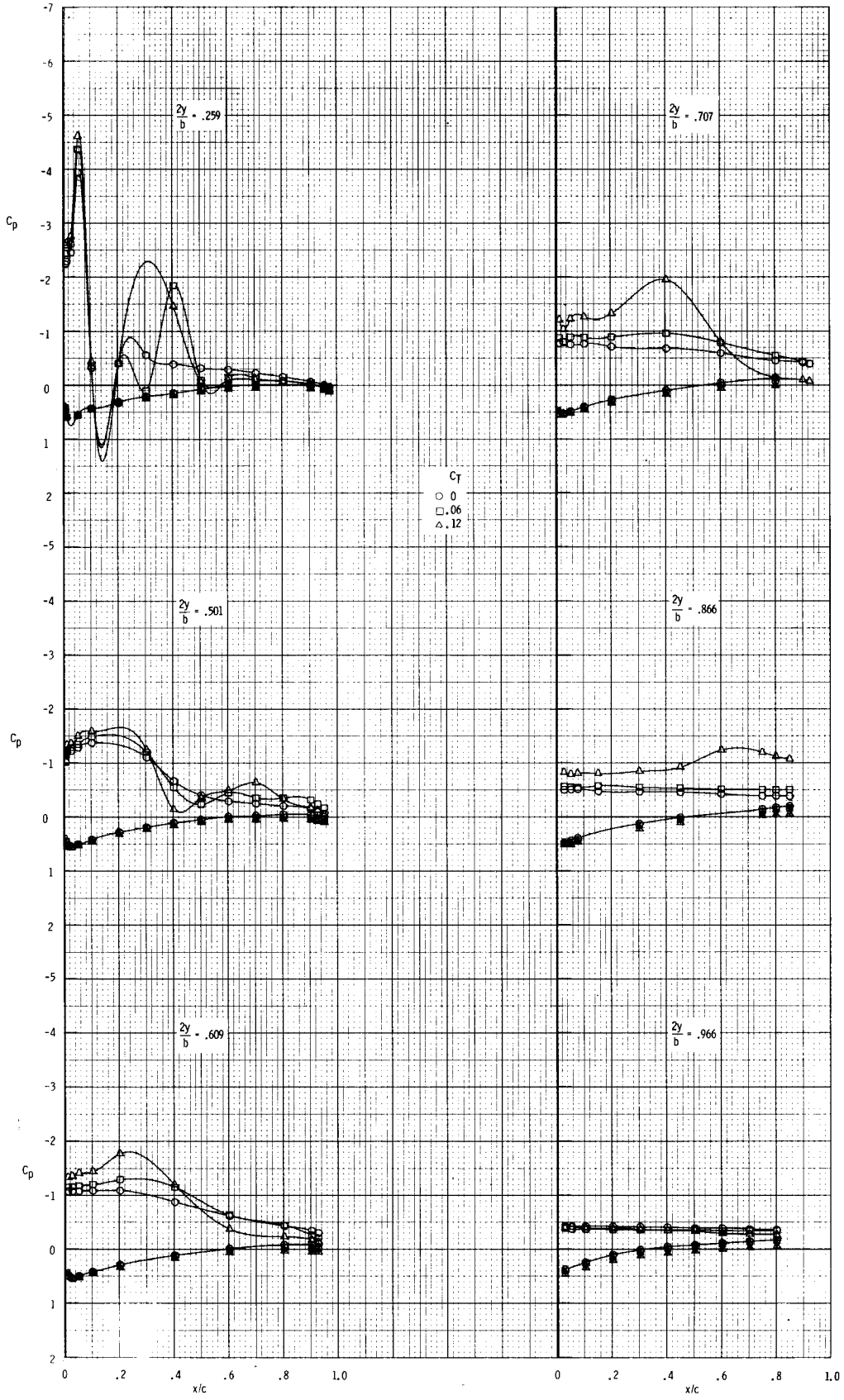

(d) $\alpha = 12.3^{o}$.

Figure 43.- Continued.

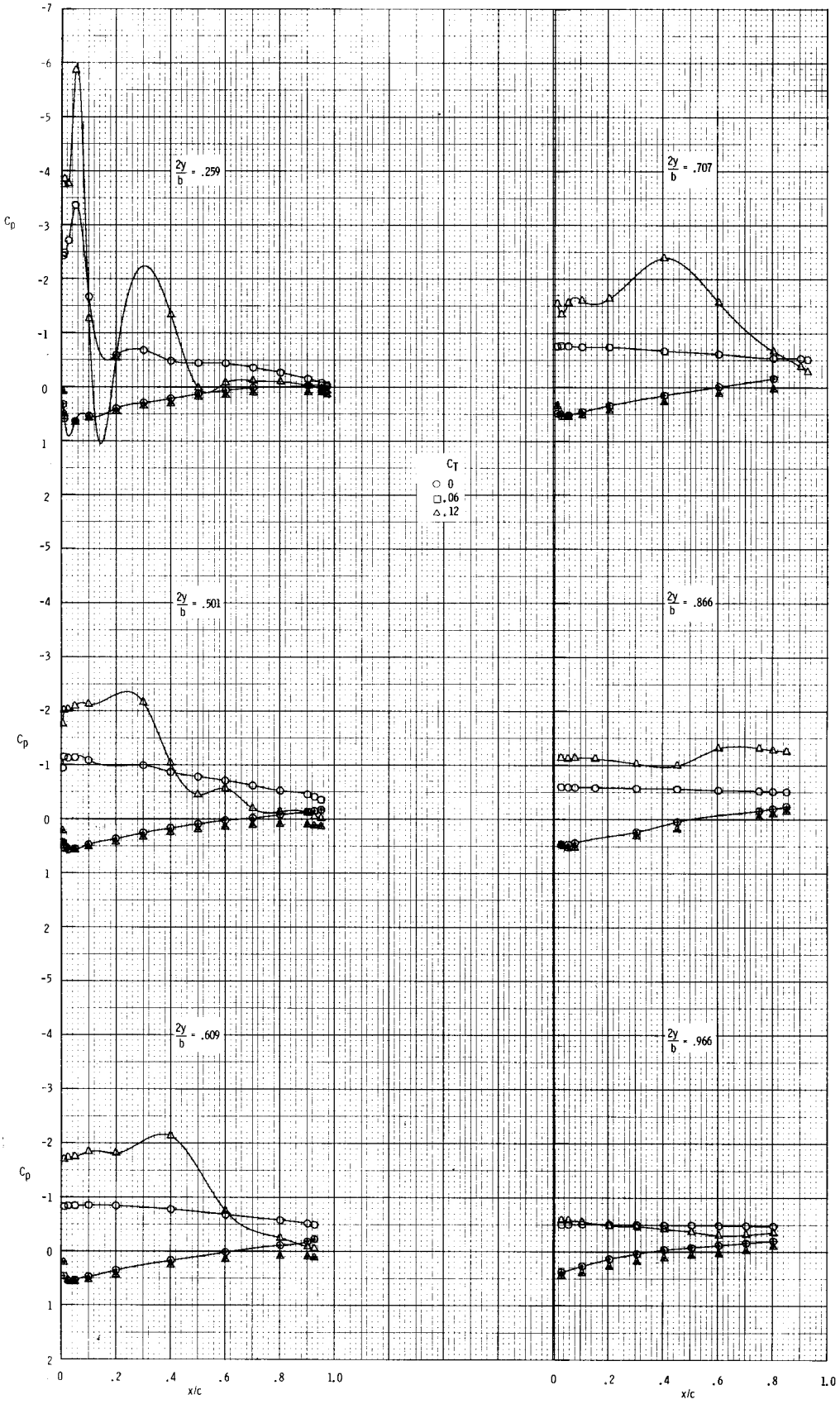

(e) $\alpha = 16.6^{\circ}$.

Figure 43.- Continued.

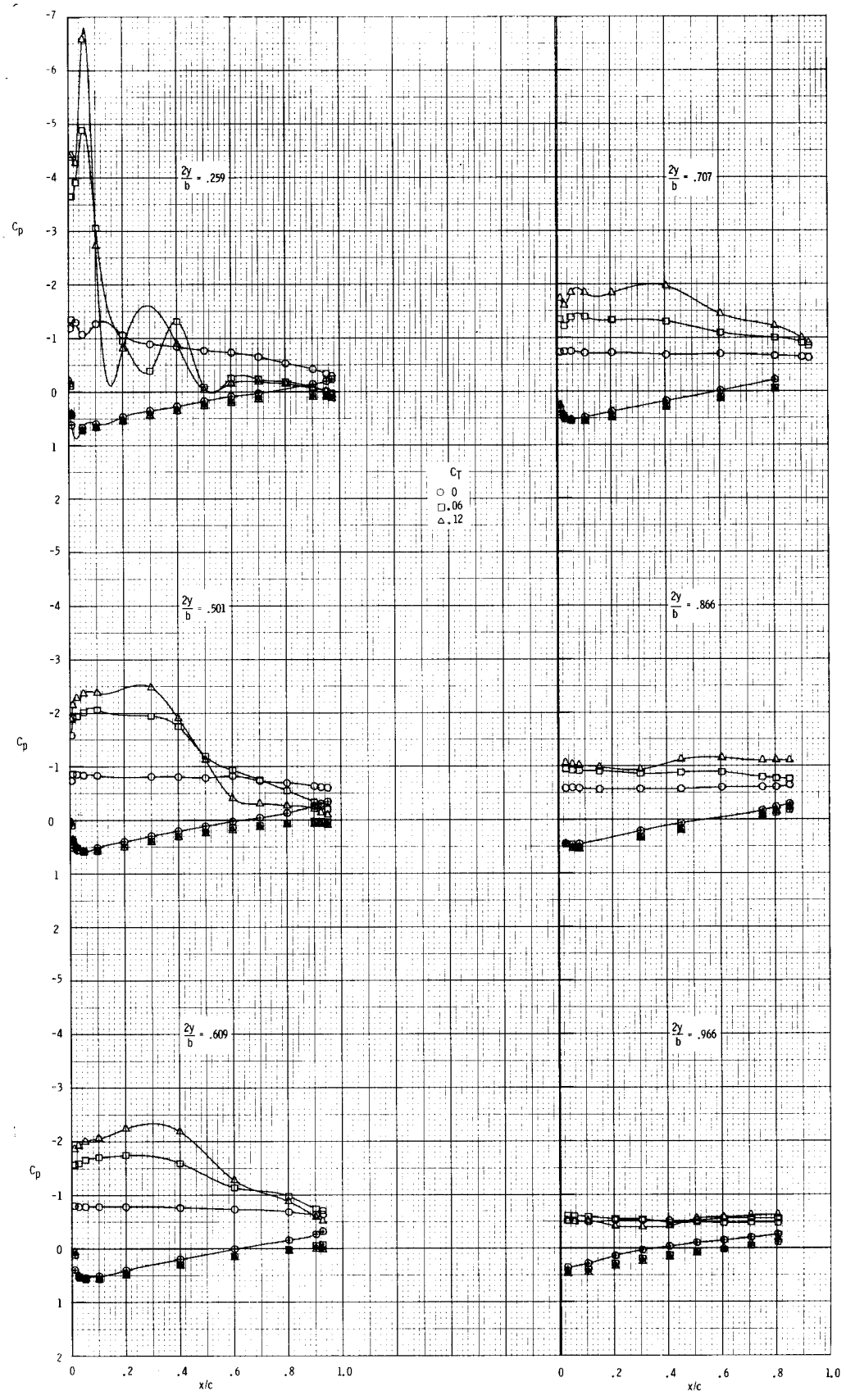

(f) $\alpha = 20.7^{\circ}$.

Figure 43.- Continued.

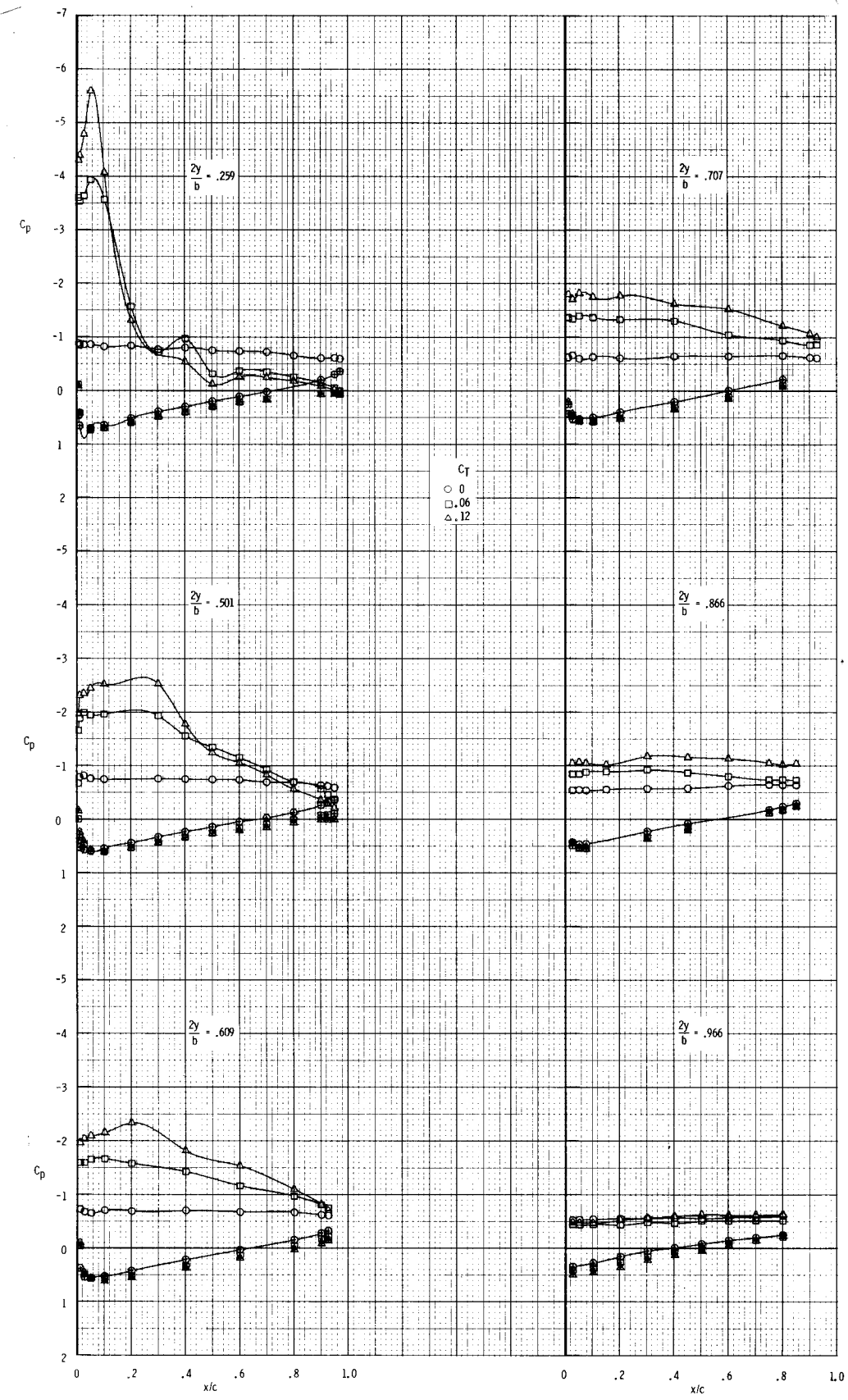

(g) $\alpha = 23.8^{\circ}$.

Figure 43.- Concluded.

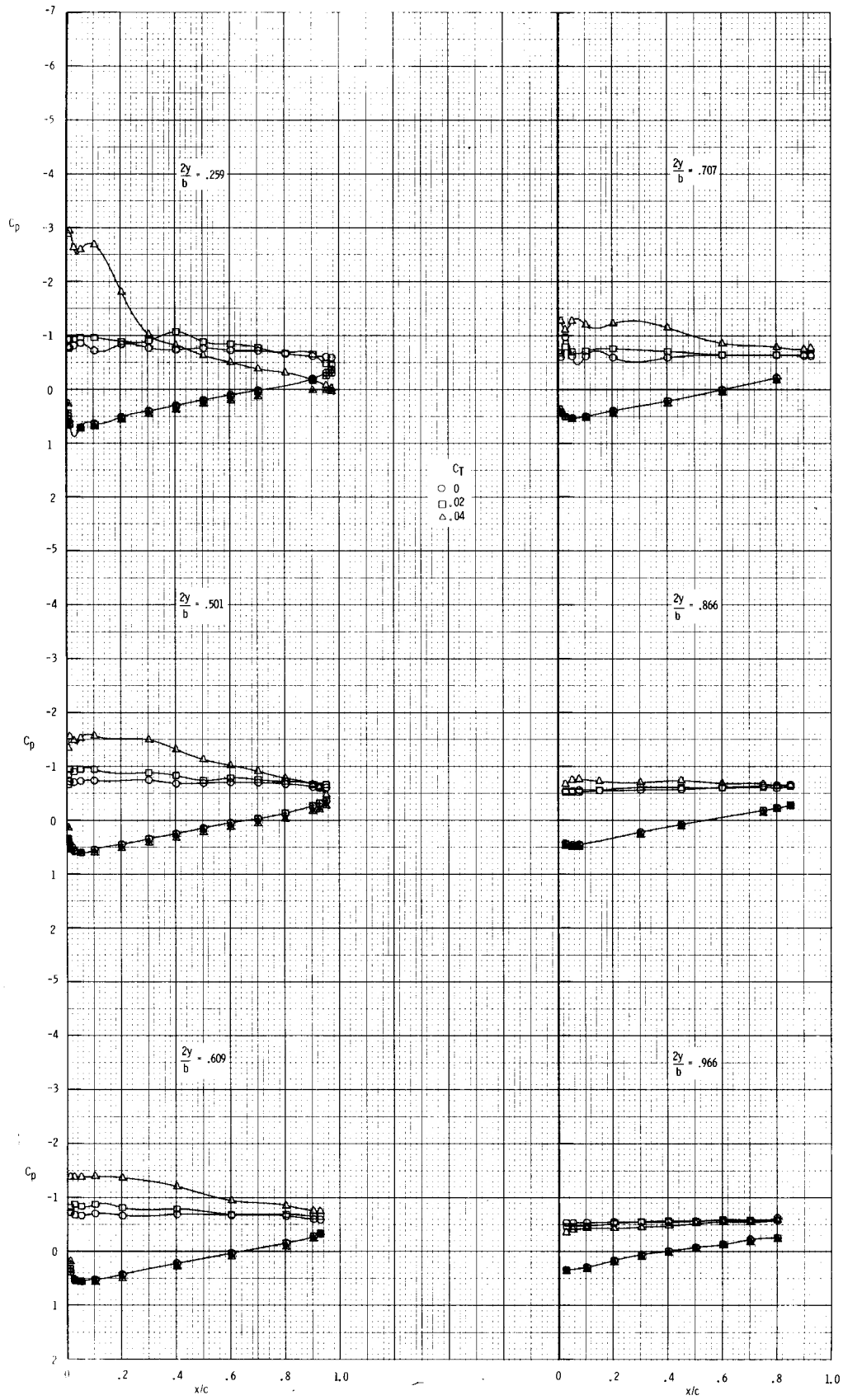

(a) C_T = 0, 0.02, and 0.04.

Figure 44.- Effect of nozzle thrust coefficient on wing-surface pressure distributions for $\alpha = 23.8^{\circ}$; $\overline{x_n/c_r} = 0.32$; $\Lambda_n = 33^{\circ}$; $h/d = 0.835$.

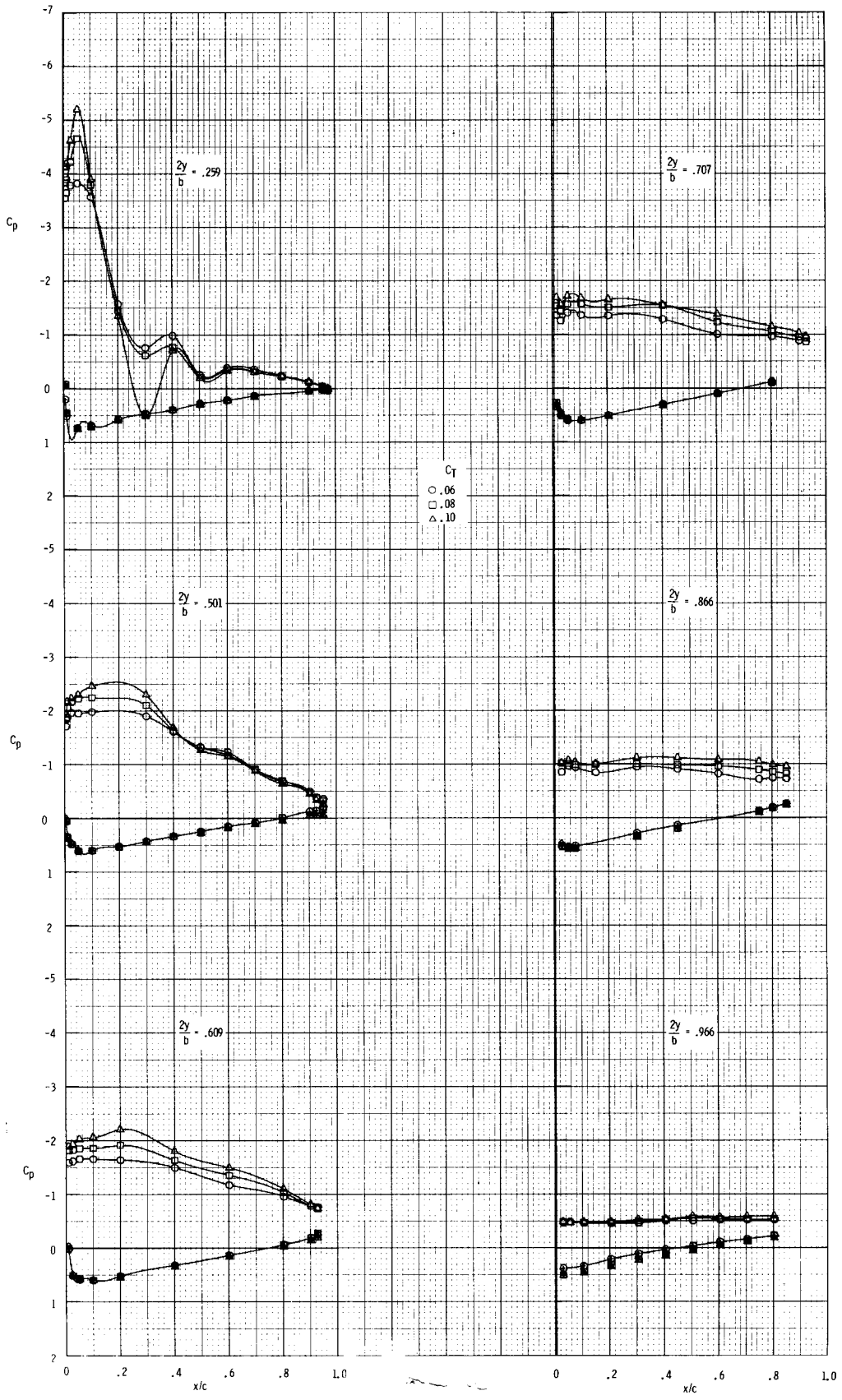

(b) C_T = 0.06, 0.08, and 0.10.

Figure 44.- Continued.

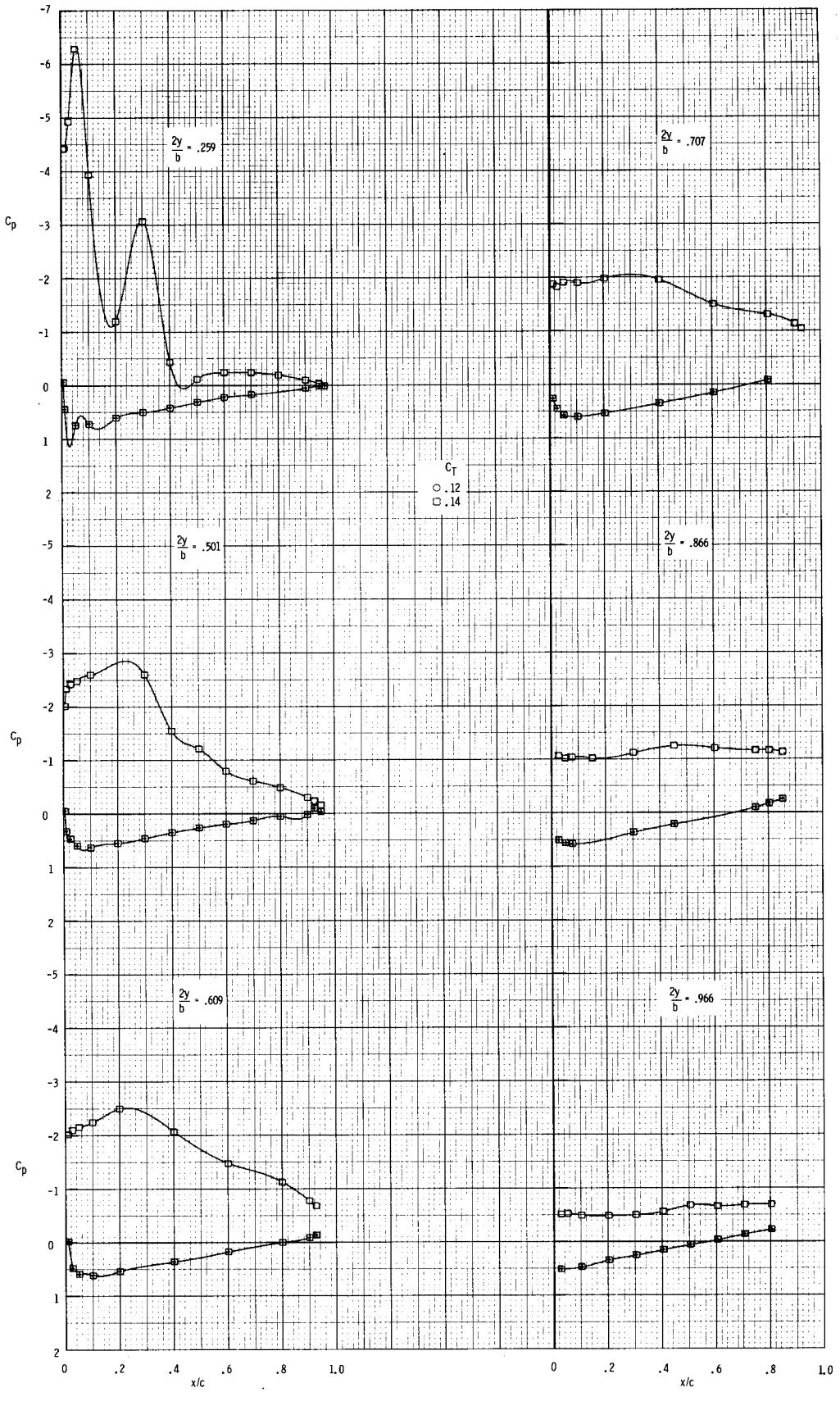

(c) C_T = 0.12 and 0.14.

Figure 44.- Continued.

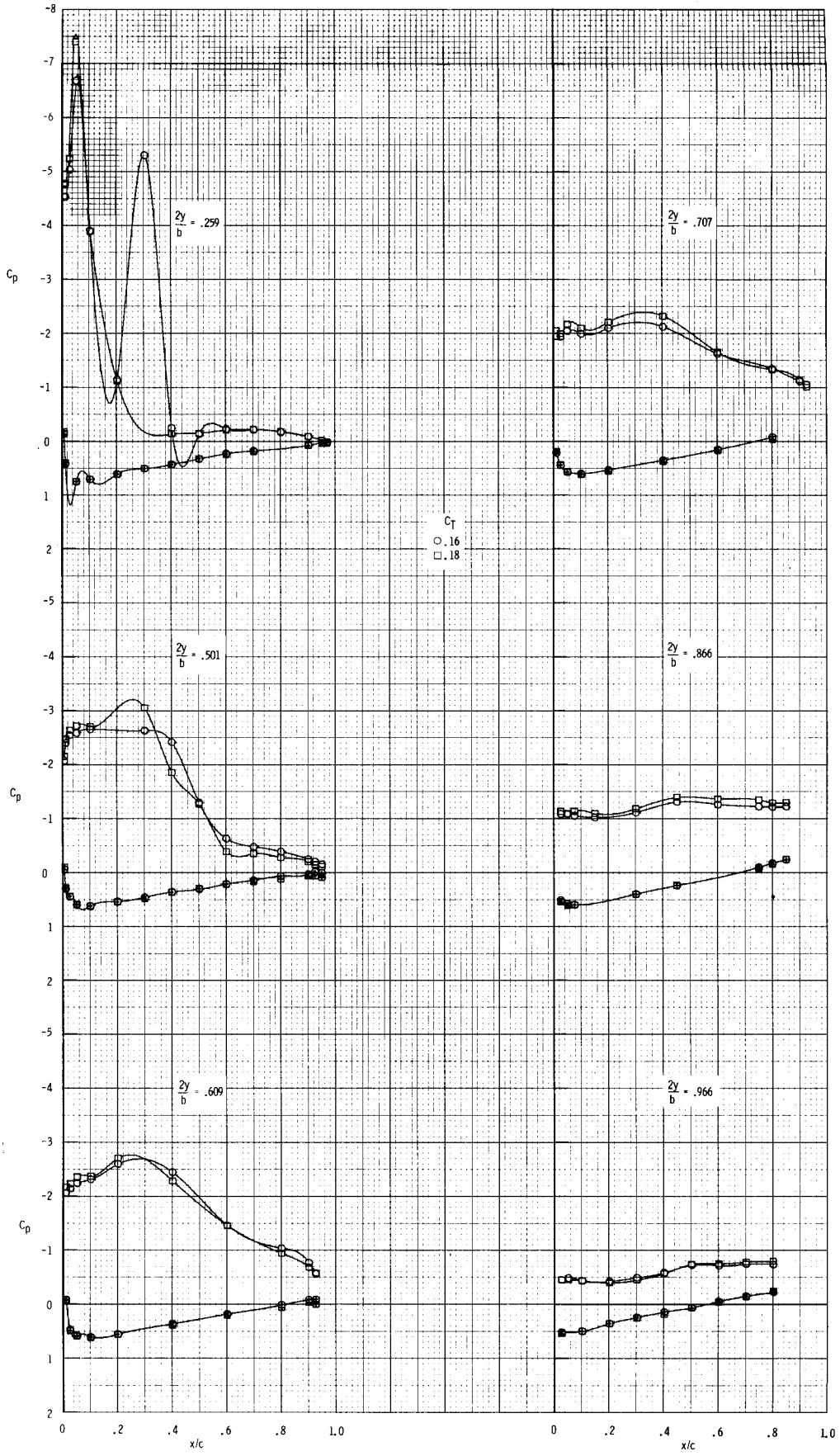

(d) C_T = 0.16 and 0.18.

Figure 44.- Concluded.

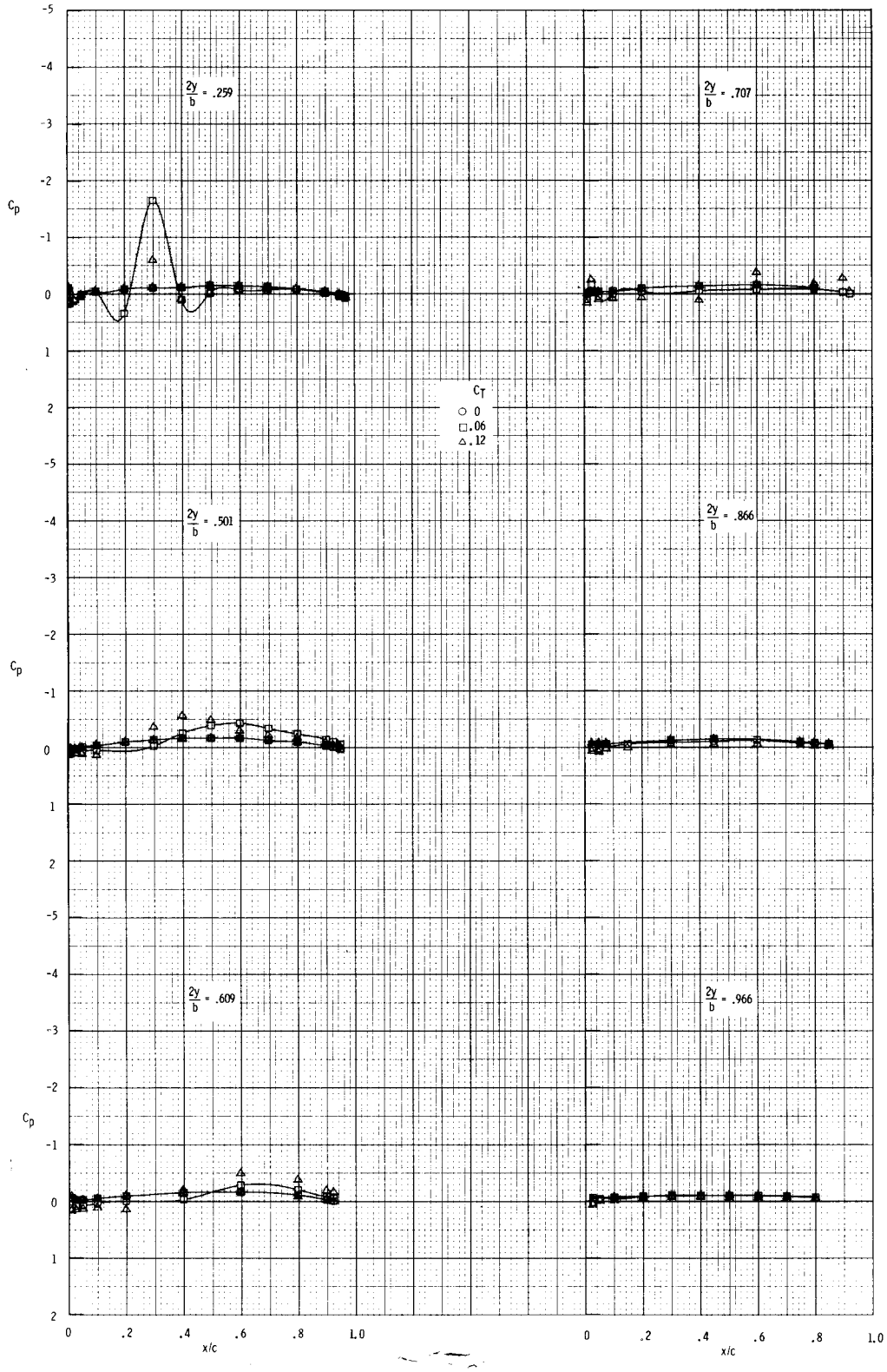

(a) $\alpha = 0.0^{\circ}$.

Figure 45.- Effect of nozzle thrust coefficient on wing-surface pressure distributions for a range of angle of attack. $\overline{x_n/c_r} = 0.23$; $\Lambda_n = 33^{\circ}$; $h/d = 0.835$.

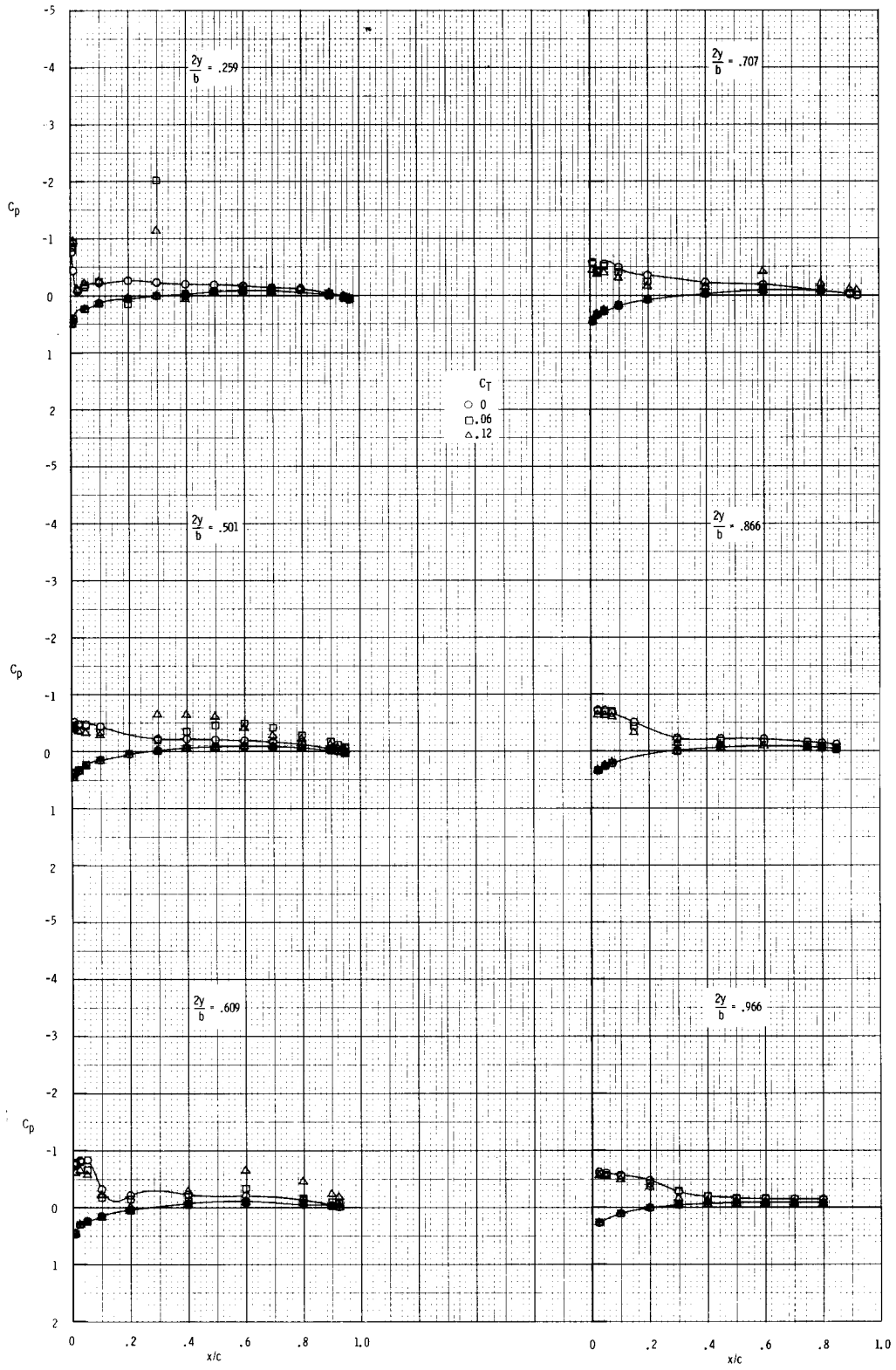

(b) $\alpha = 4.0^{o}$.

Figure 45.- Continued.

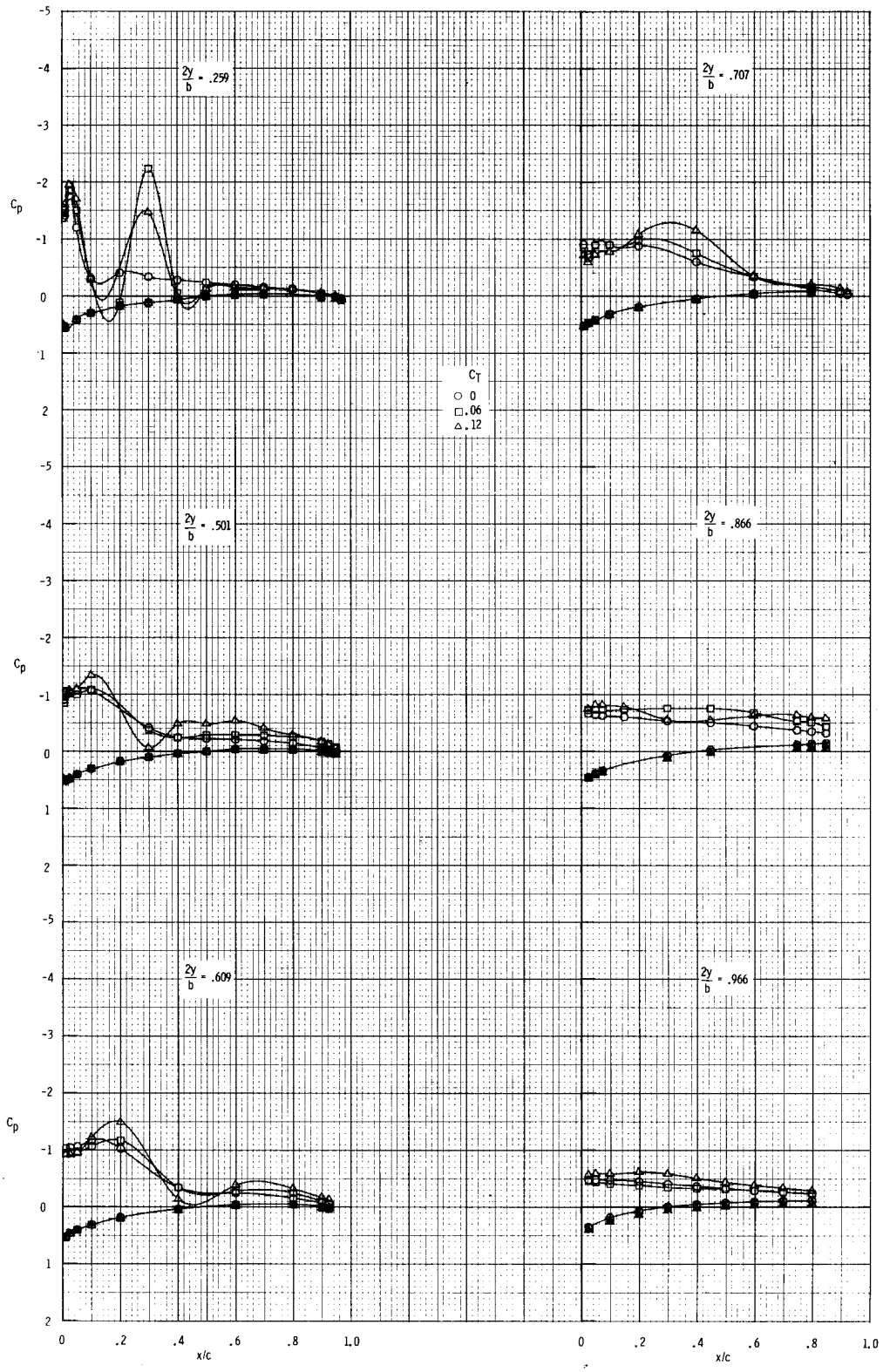

(c) $\alpha = 8.1^{\circ}$.

Figure 45.- Continued.

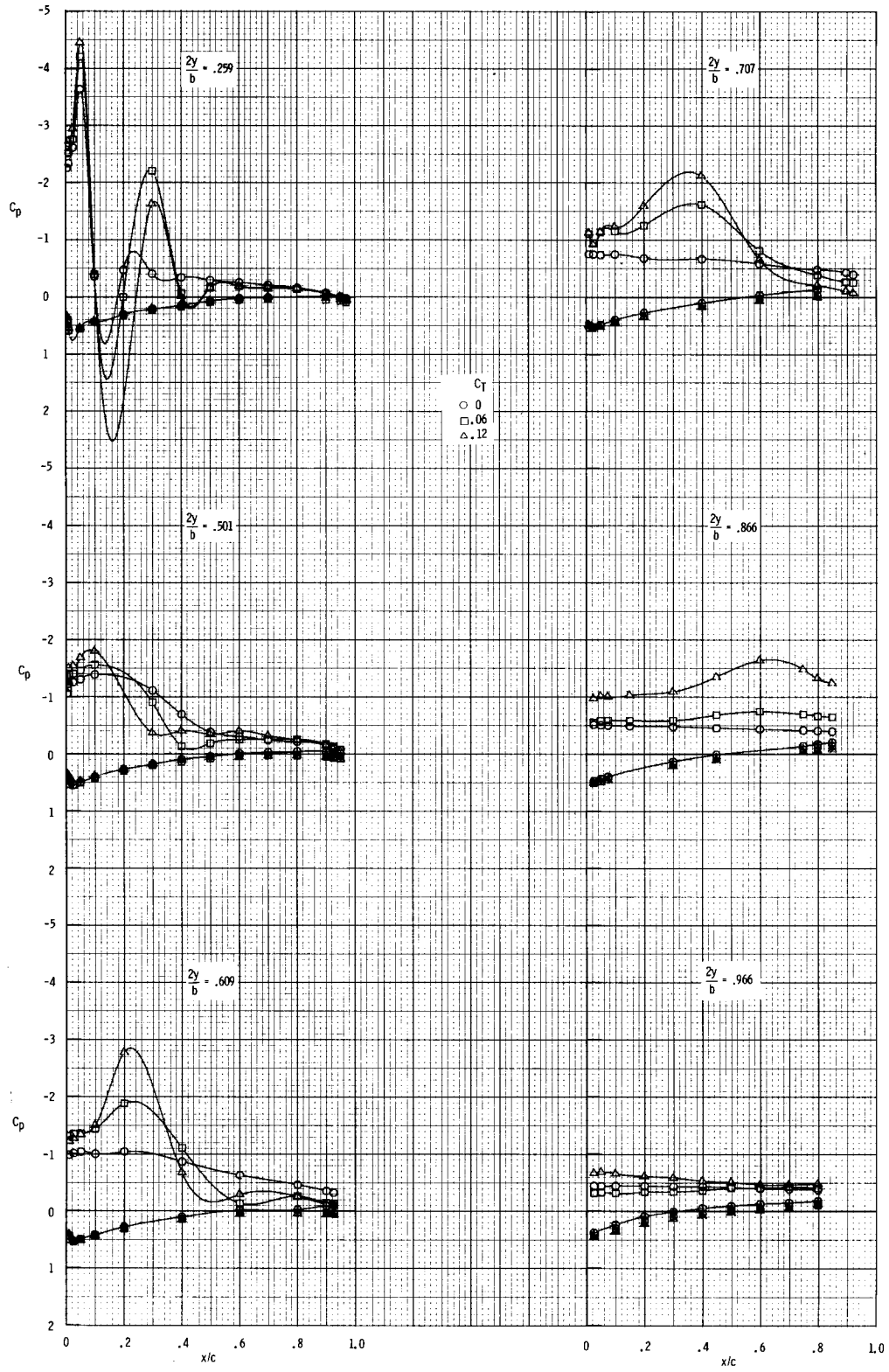

(d) $\alpha = 12.3^{o}$.

Figure 45.- Continued.

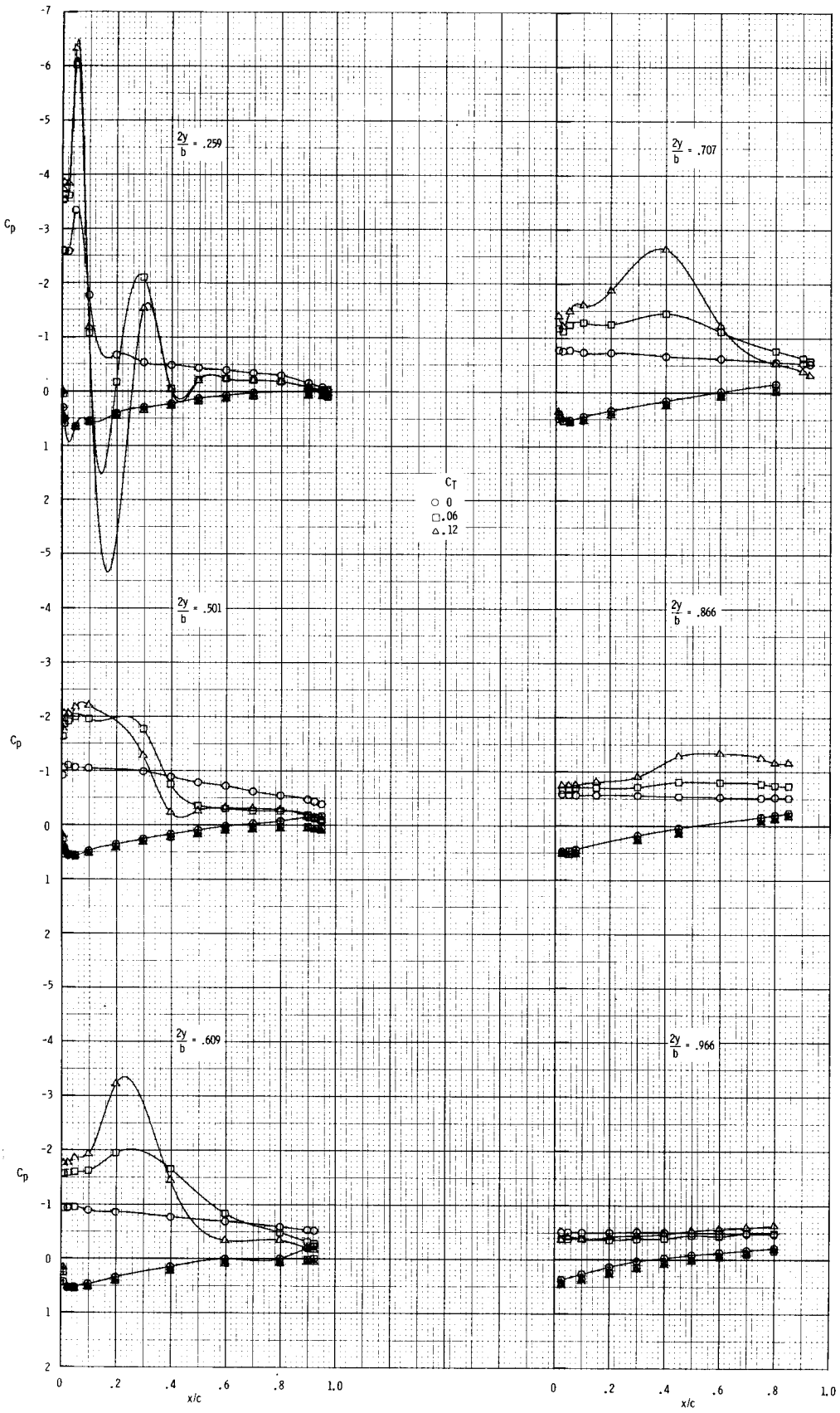

(e) $\alpha = 16.6^{\circ}$.

Figure 45.- Continued.

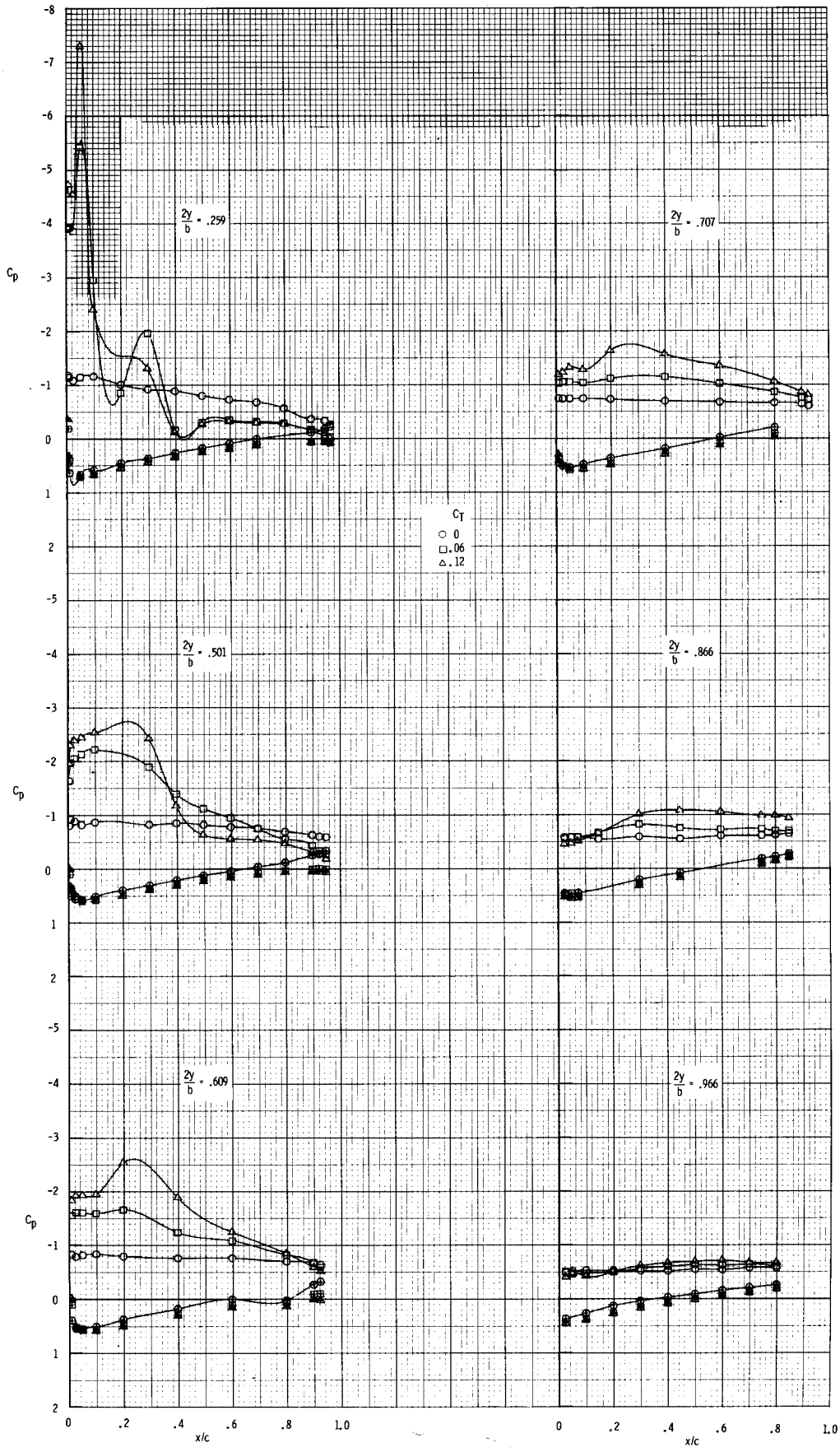

(f) $\alpha = 20.6^{o}$.

Figure 45.- Continued.

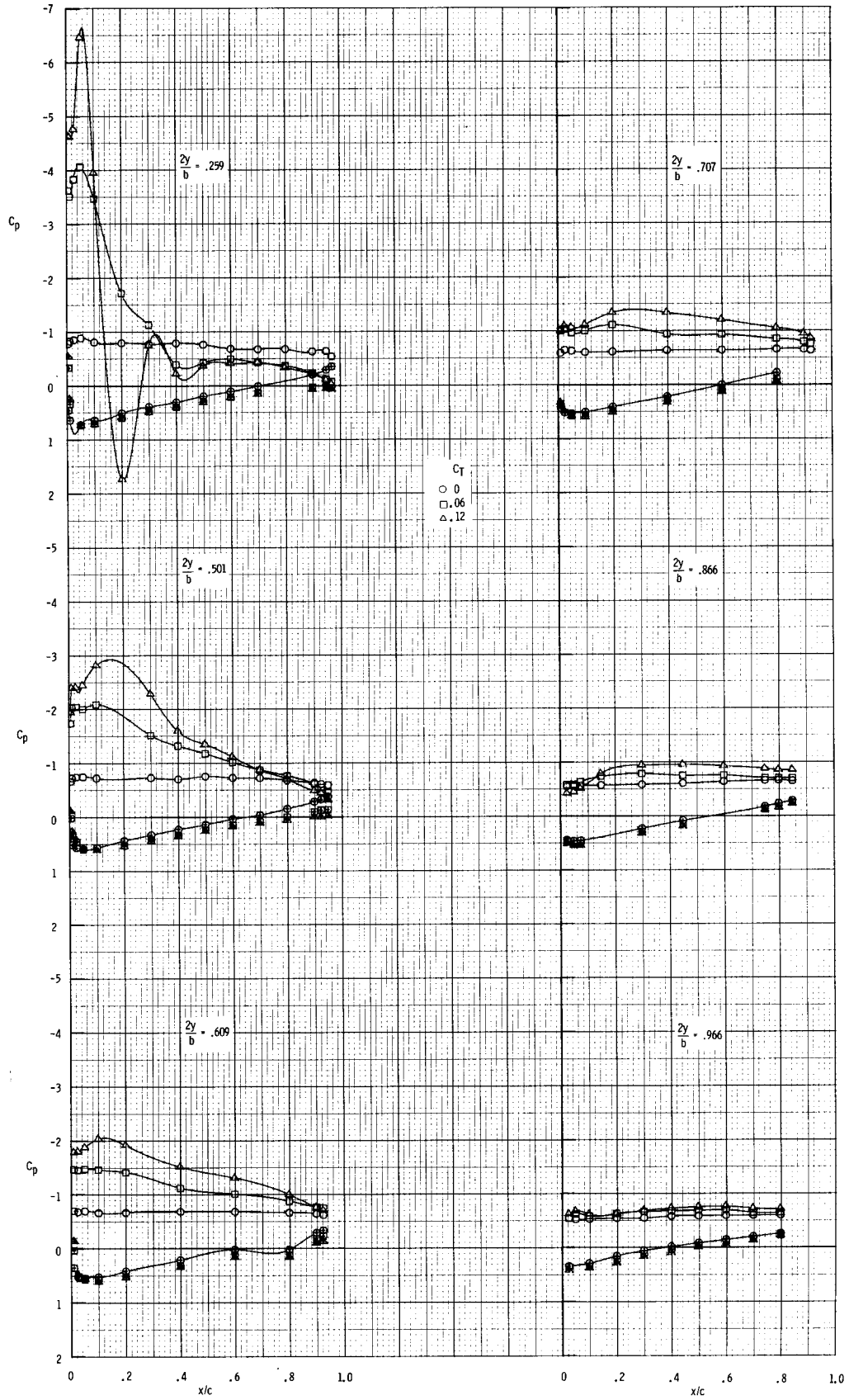

(g) $\alpha = 23.8^{o}$.

Figure 45.- Concluded.

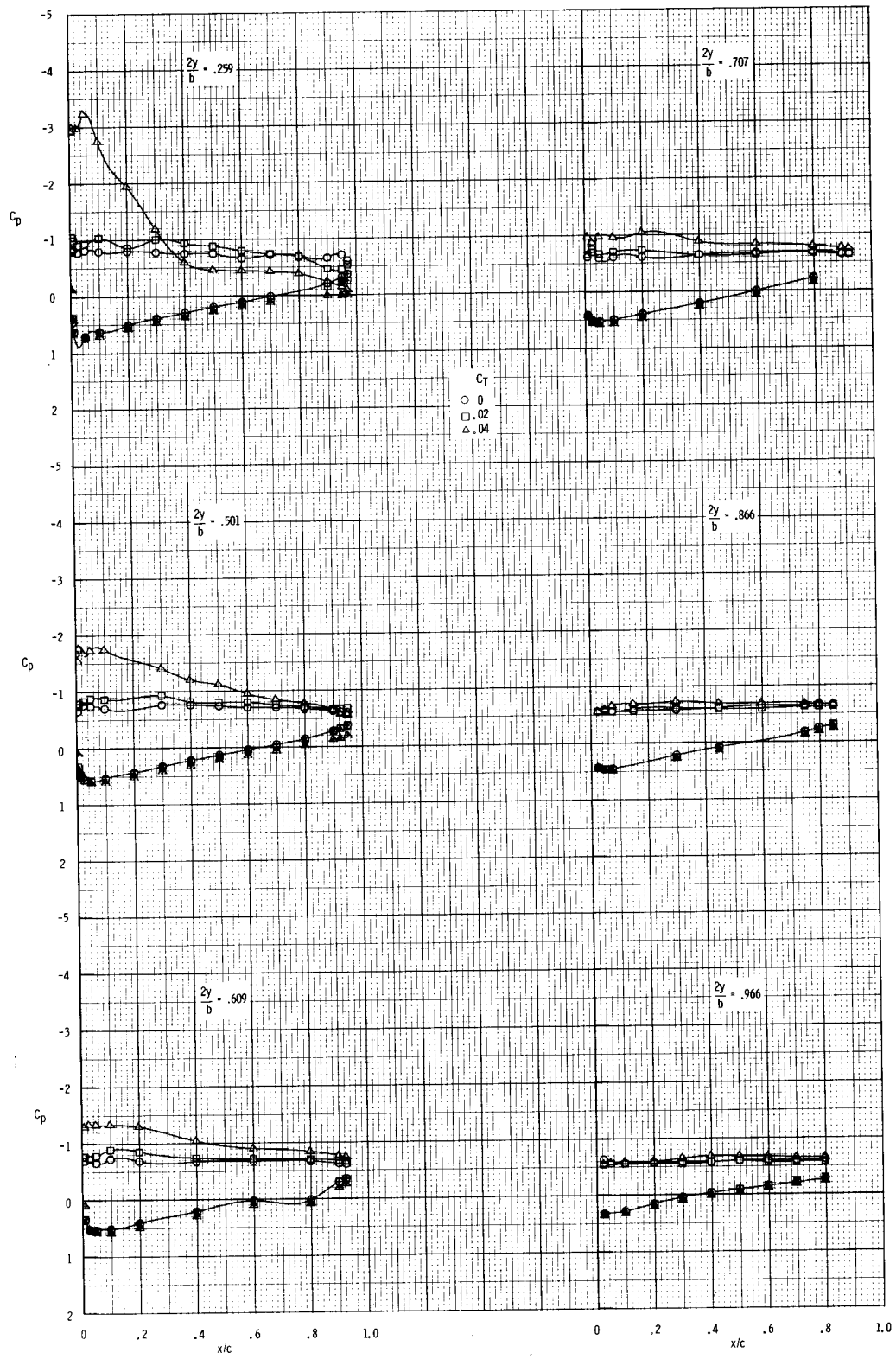

(a) C_T = 0, 0.02, and 0.04.

Figure 46.- Effect of nozzle thrust coefficient on wing-surface pressure distributions for $\alpha = 23.8^{o}$; $\overline{x_n/c_r} = 0.23$; $\Lambda_n = 33^{o}$; h/d = 0.835.

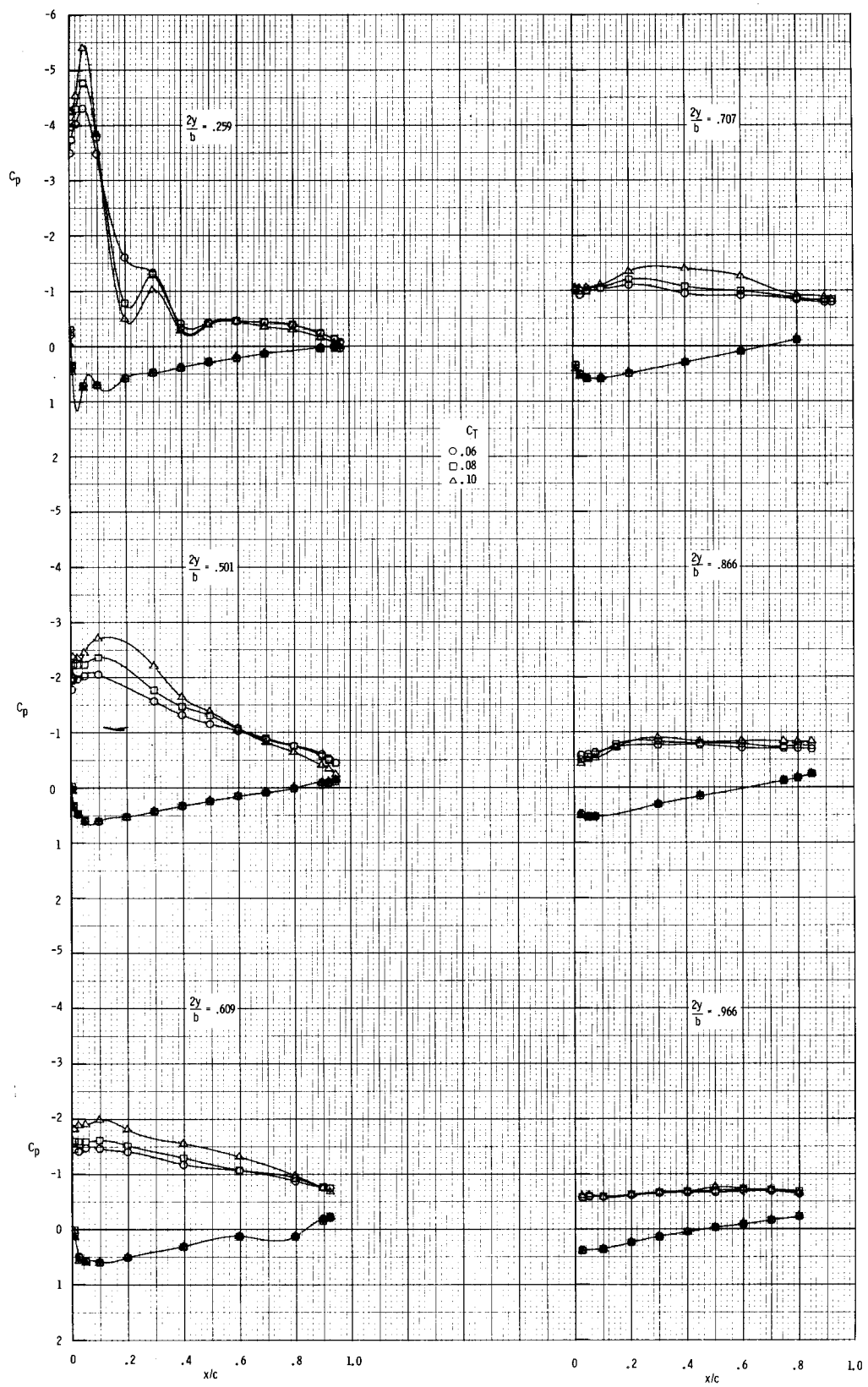

(b) C_T = 0.06, 0.08, and 0.10.

Figure 46.- Continued.

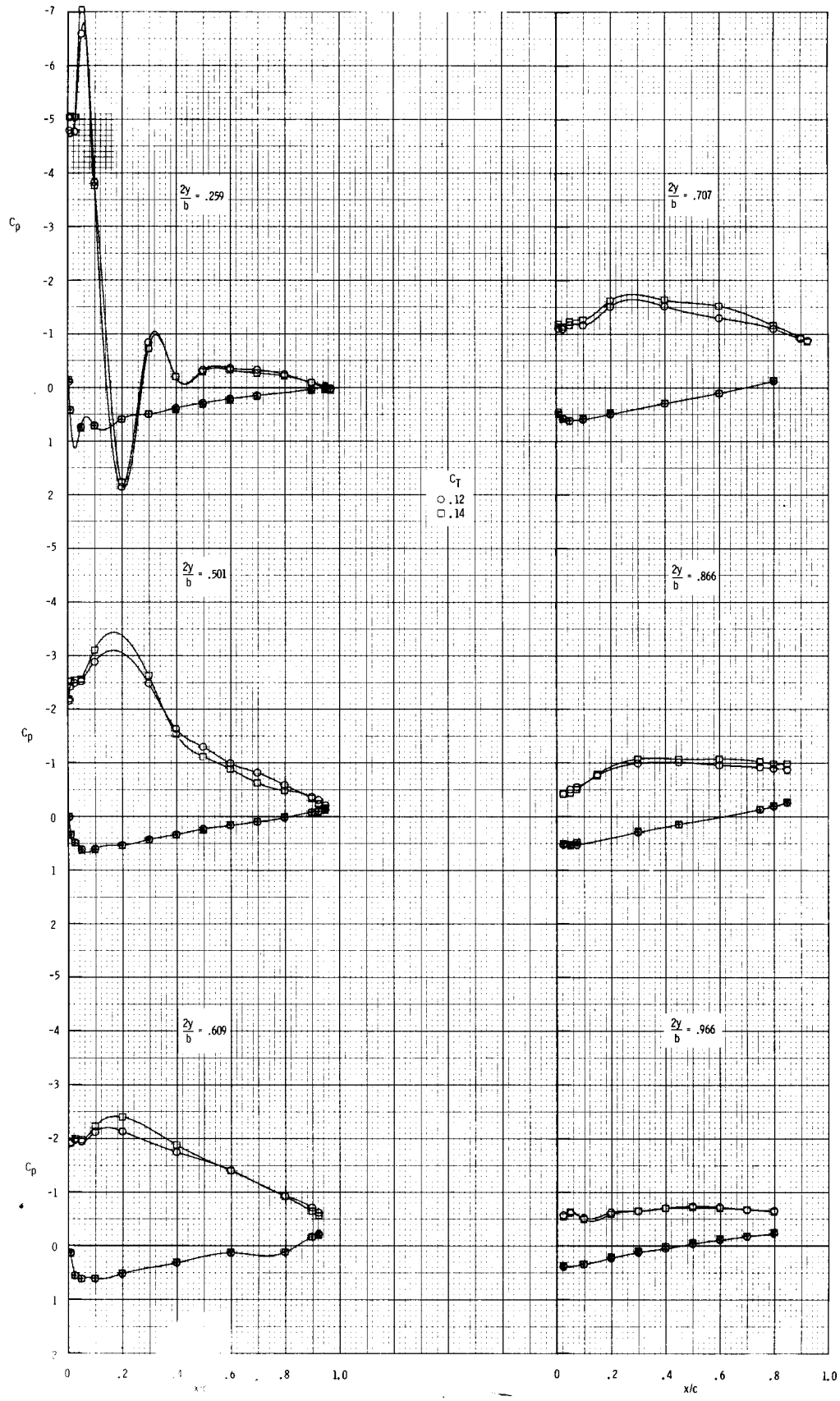

(c) C_T = 0.12 and 0.14.

Figure 46.- Continued.

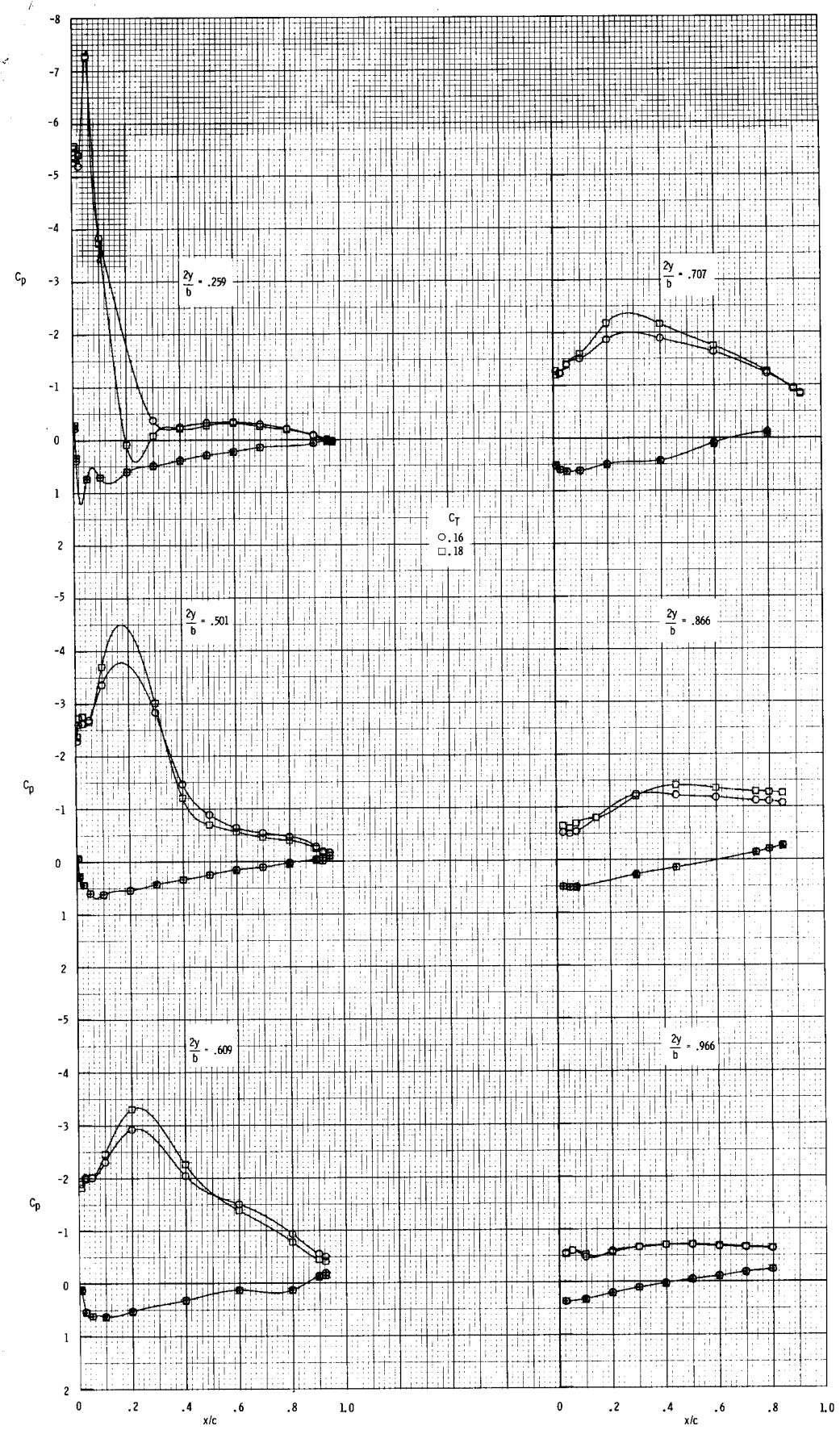

(d) C_T = 0.16 and 0.18.

Figure 46.- Concluded.

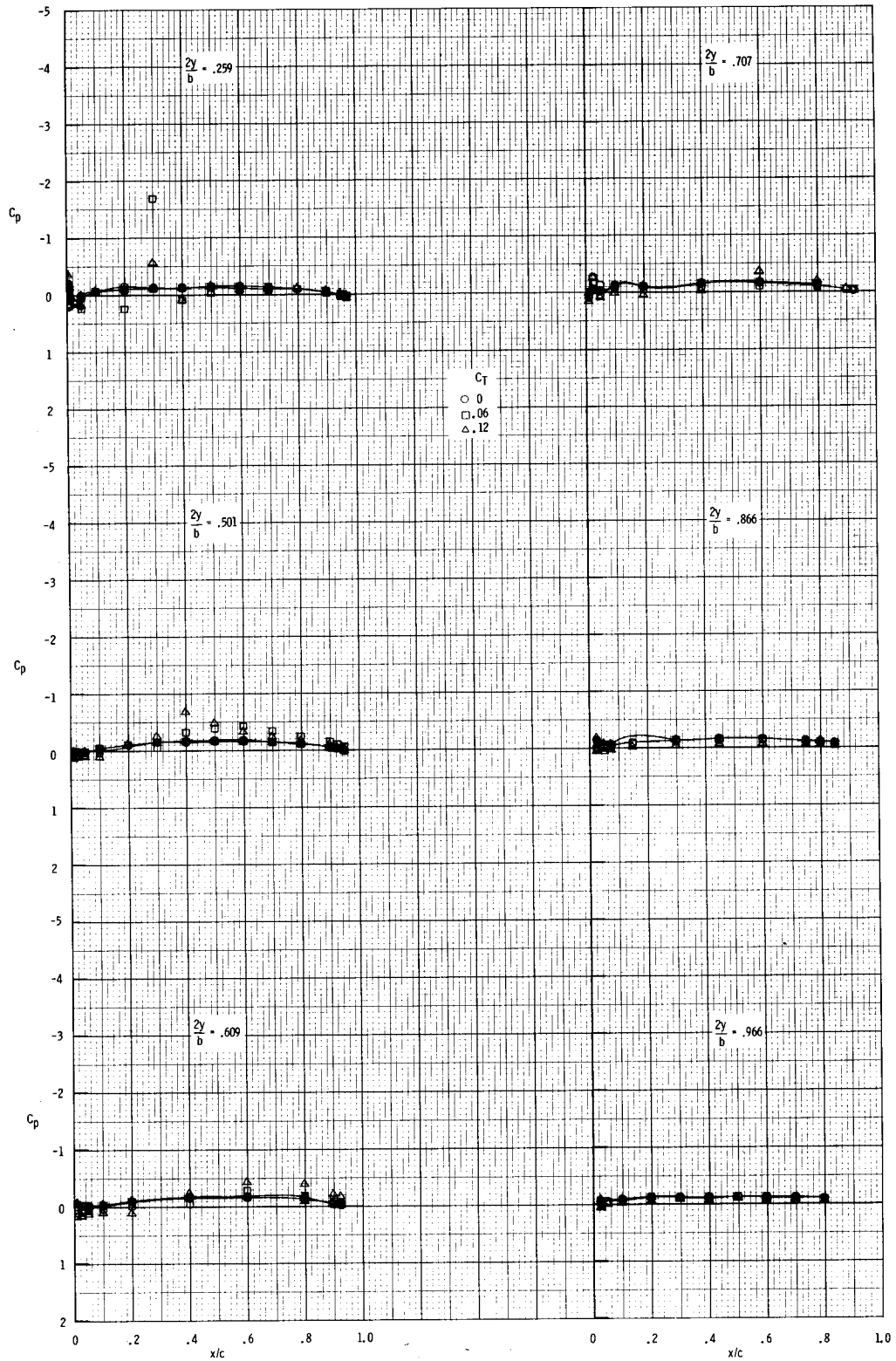

(a) $\alpha = 0.1^{\circ}$.

Figure 47.- Effect of nozzle thrust coefficient on wing-surface pressure distributions for a range of angle of attack. $\overline{x_n/c_r} = 0.23$; $\Lambda_n = 33^{\circ}$; $h/d = 0.835$; transition strips.

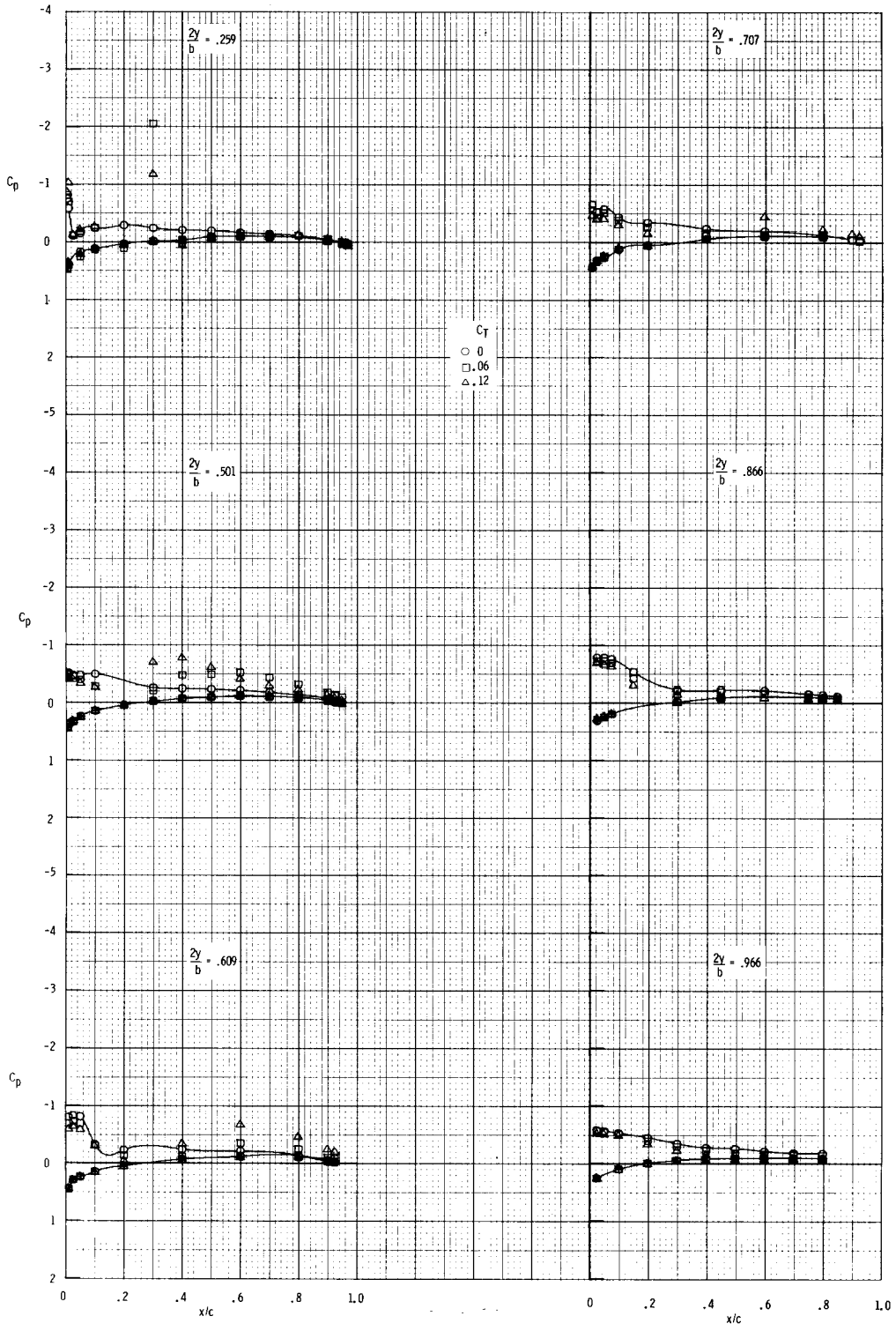

(b) $\alpha = 4.1^{o}$.

Figure 47.- Continued.

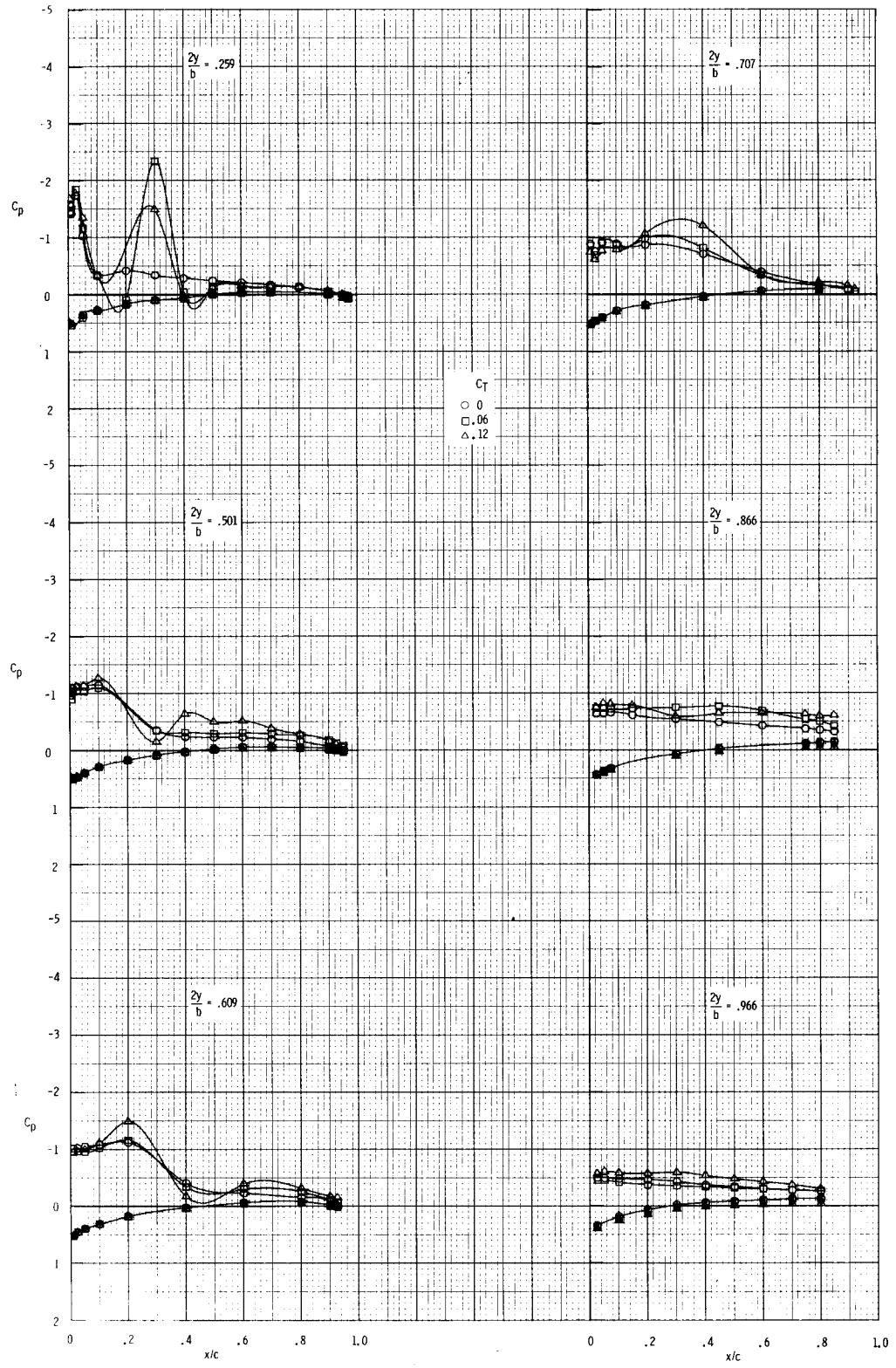

(c) $\alpha = 8.2^{\circ}$.

Figure 47.- Continued.

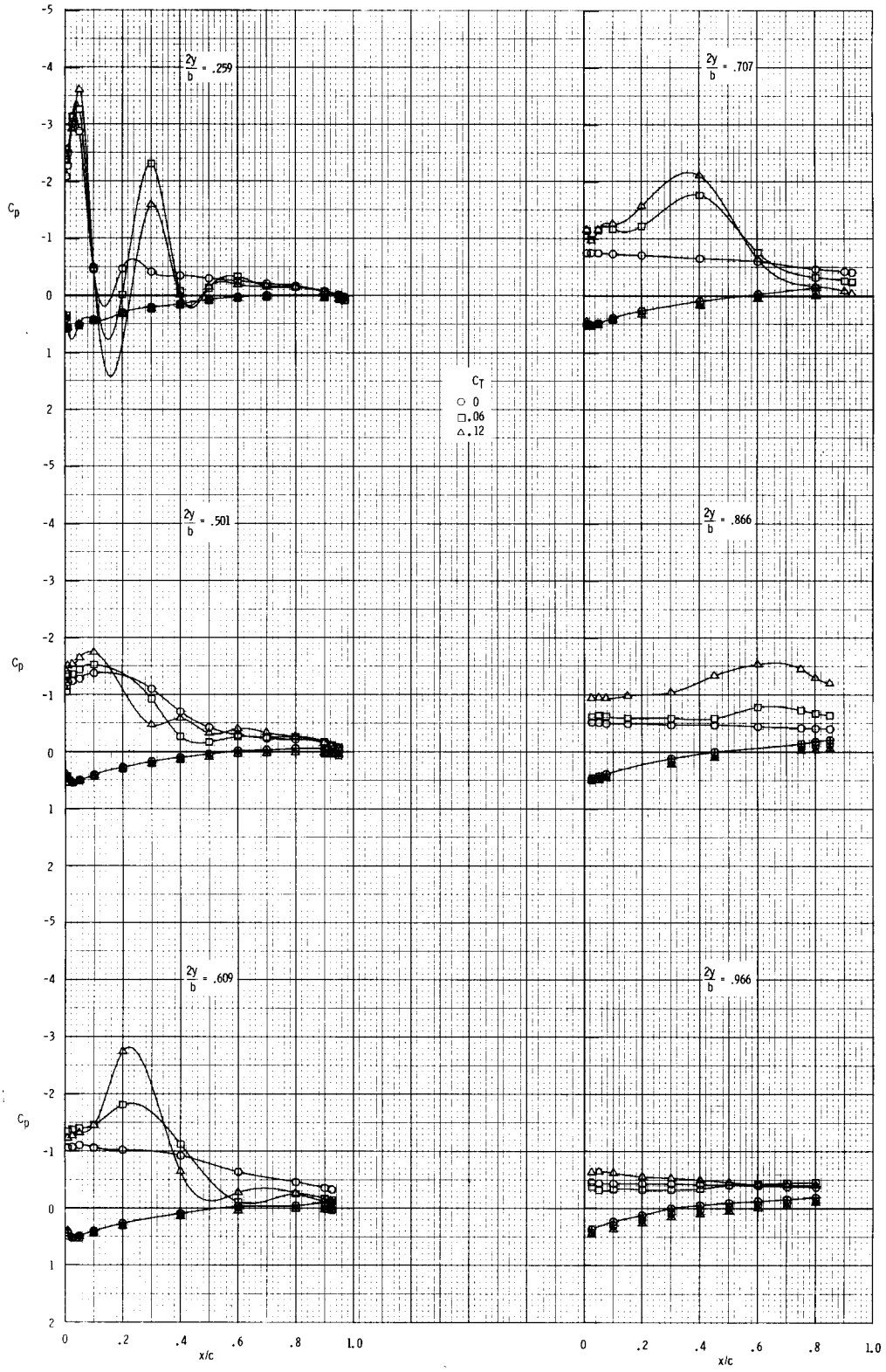

(d) $\alpha = 12.4^{o}$.

Figure 47.- Continued.

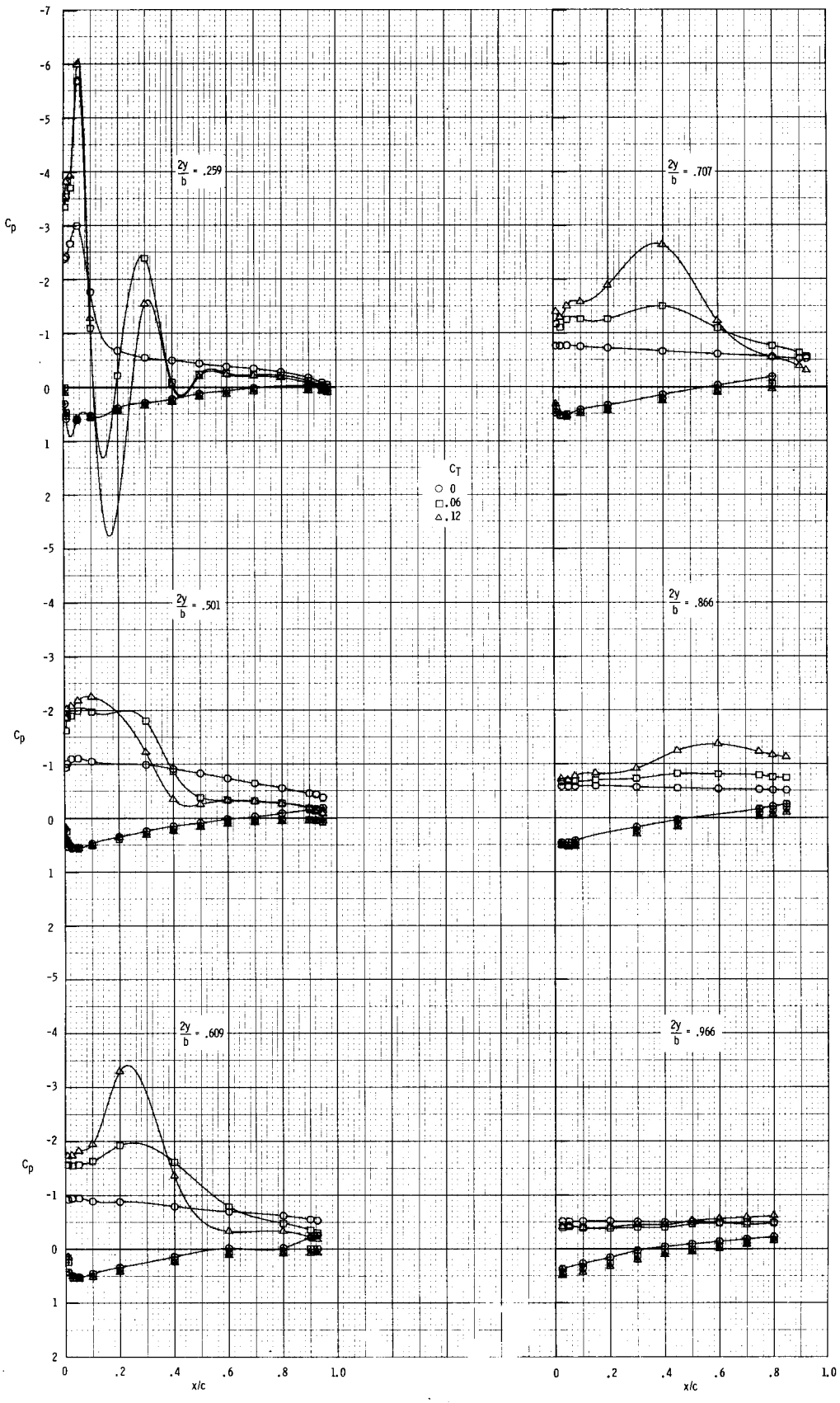

(e) $\alpha = 16.6^{o}$.

Figure 47.- Continued.

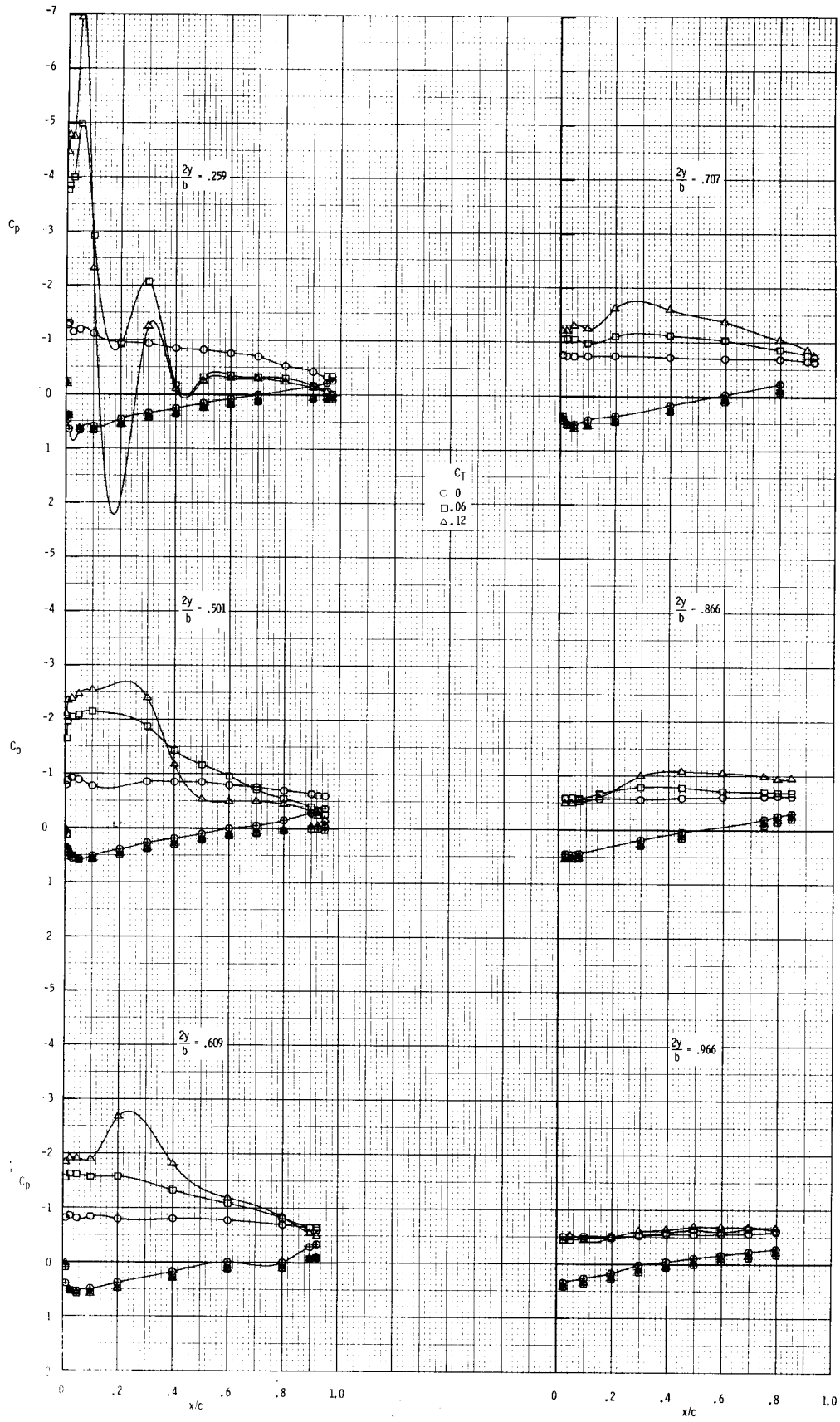

(f) $\alpha = 20.7^{o}$.

Figure 47.- Continued.

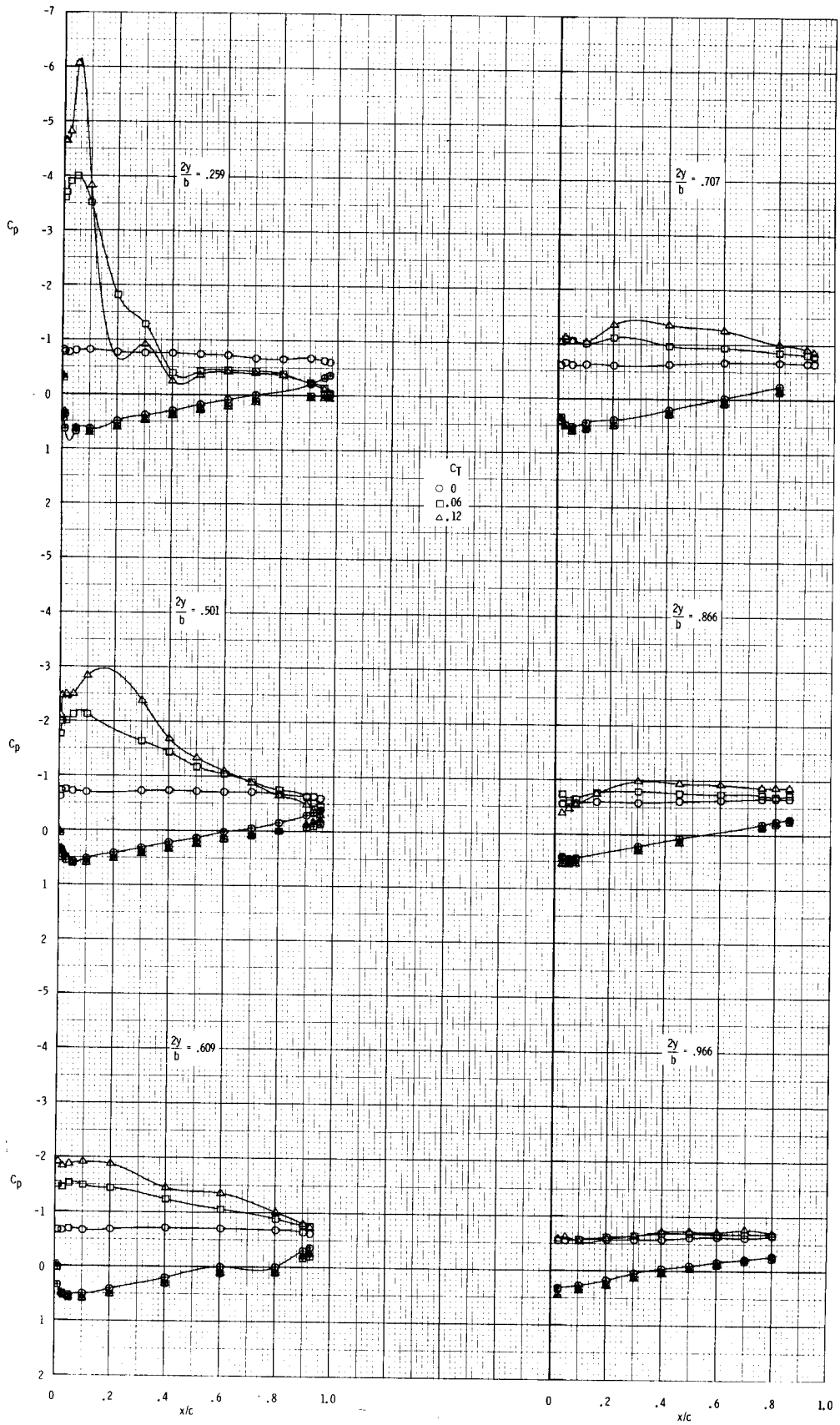

(g) $\alpha = 23.8^{\circ}$.

Figure 47.- Concluded.

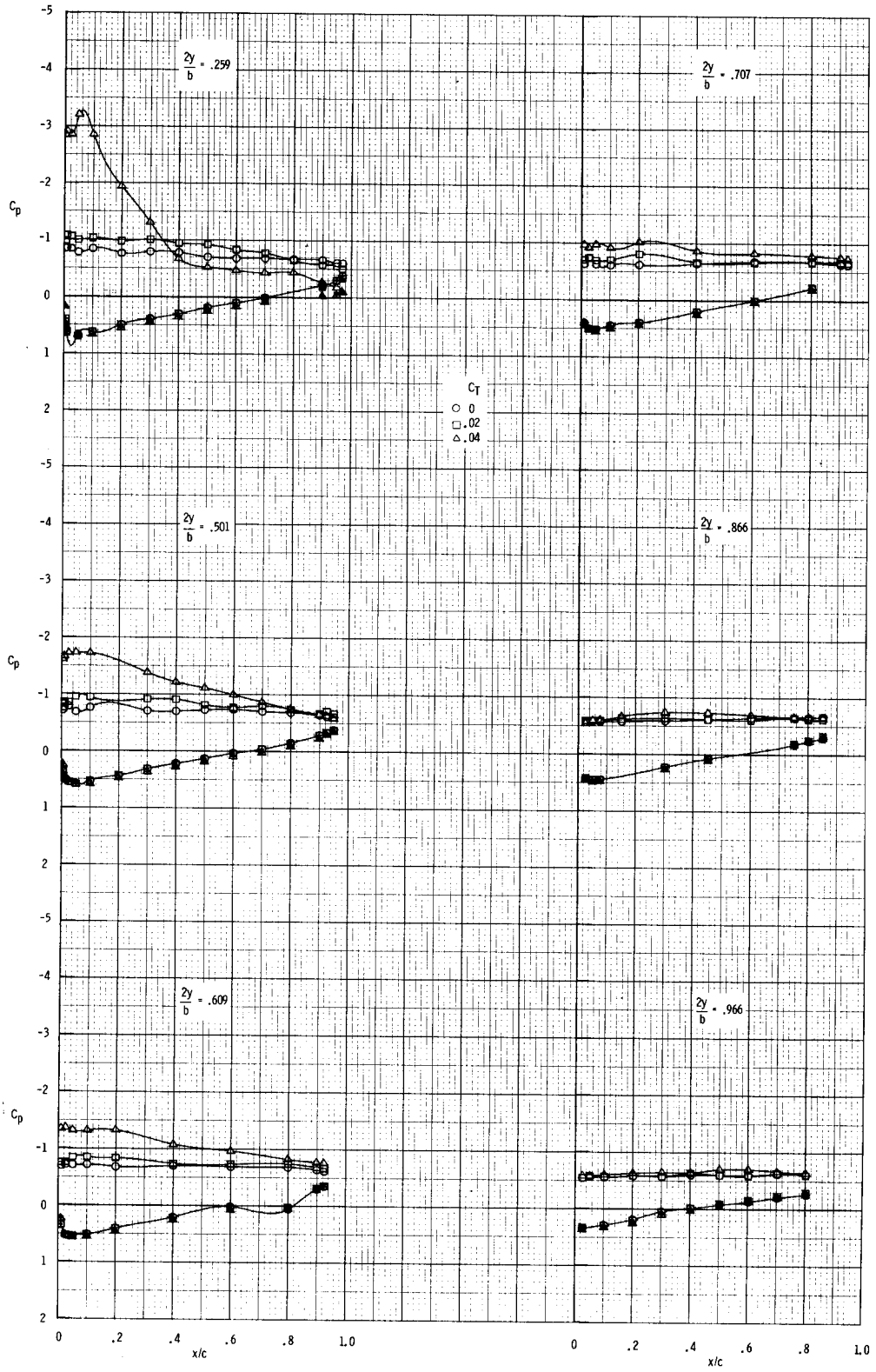

(a) C_T = 0, 0.02, and 0.04.

Figure 48.- Effect of nozzle thrust coefficient on wing-surface pressure distributions for $\alpha = 23.8^{\circ}$; $\overline{x_n/c_r} = 0.23$; $\Lambda_{\overline{n}} = 33^{\circ}$; h/d = 0.835; transition strips.

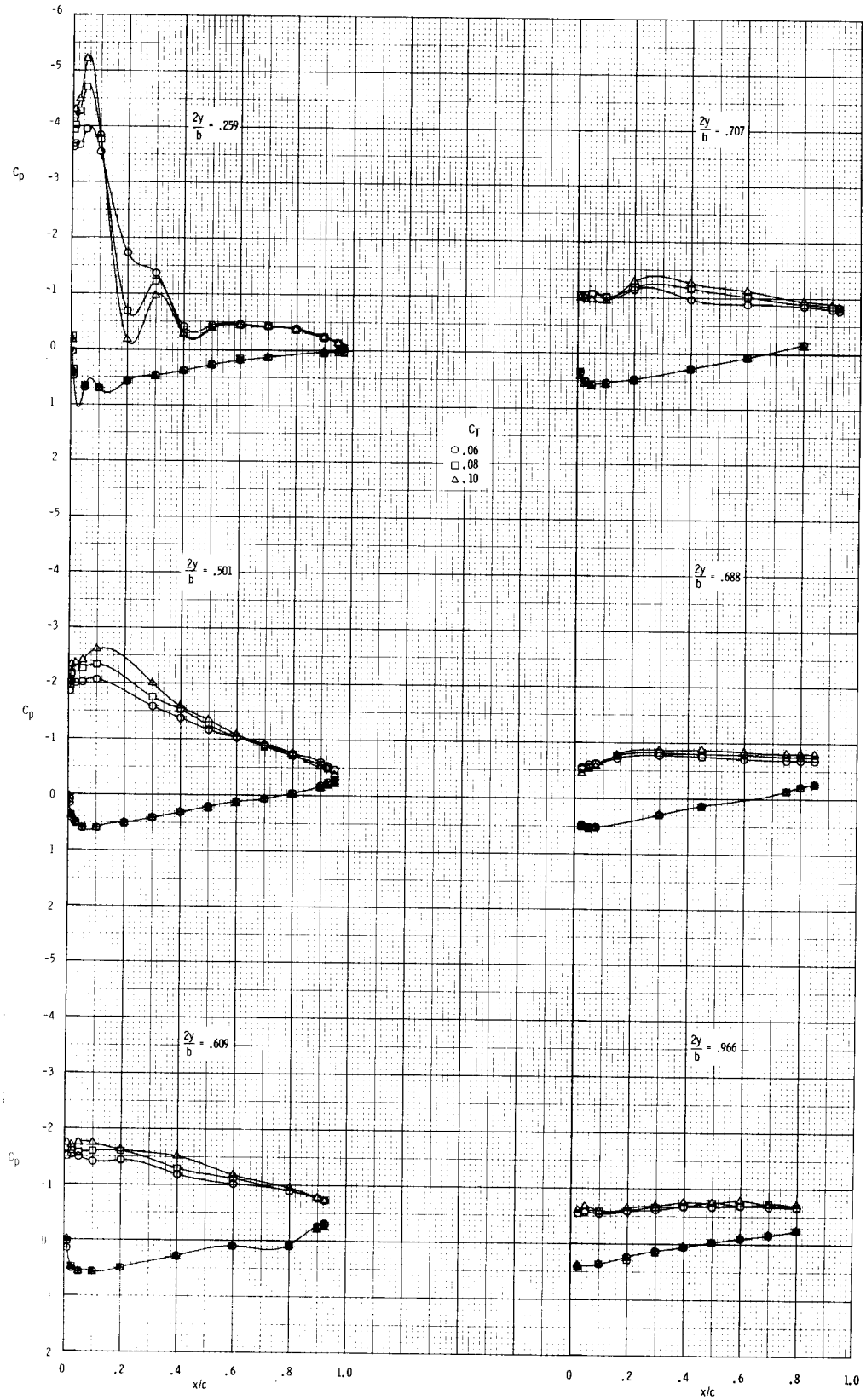

(b) C_T = 0.06, 0.08, and 0.10.

Figure 48.- Continued.

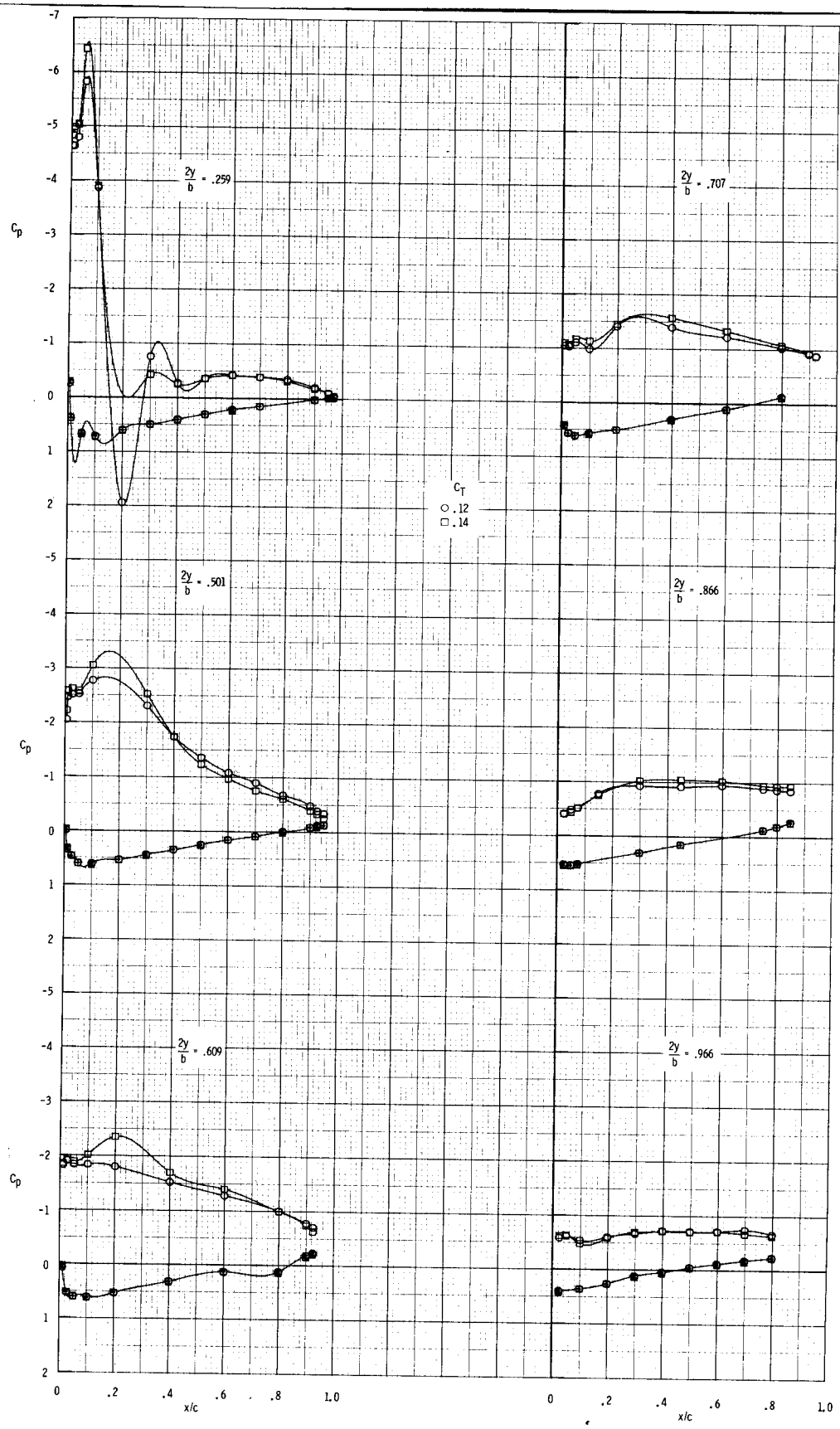

(c) C_T = 0.12 and 0.14.

Figure 48.- Continued.

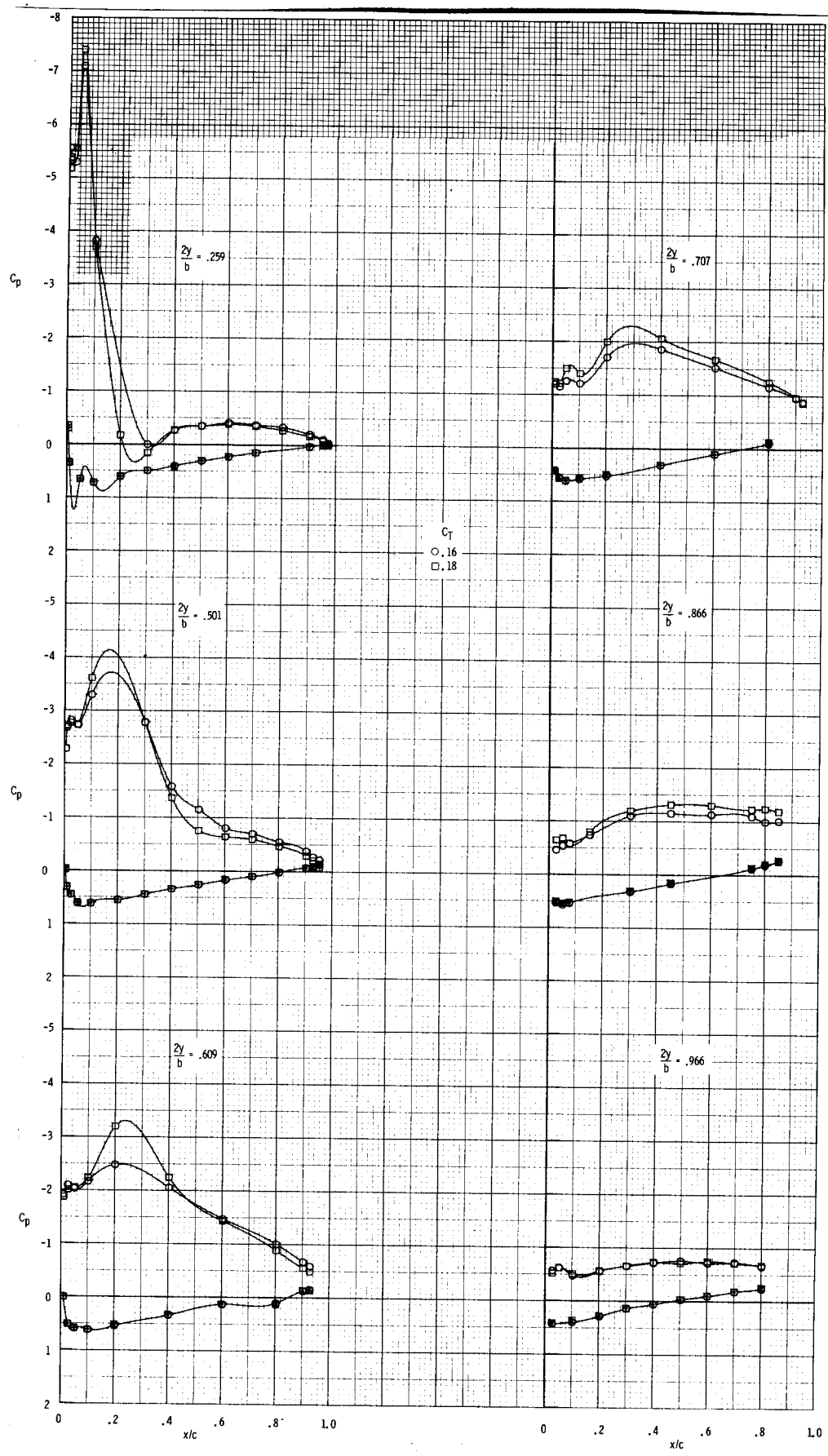

(d) C_T = 0.16 and 0.18.

Figure 48.- Concluded.